5-2016

Improving Droplet Interface Bilayers as Models for Cell Membranes

Graham Jeffery Taylor
University of Tennessee - Knoxville, gtaylor4@vols.utk.edu

To the Graduate Council:

I am submitting herewith a dissertation written by Graham Jeffery Taylor entitled "Improving Droplet Interface Bilayers as Models for Cell Membranes." I have examined the final electronic copy of this dissertation for form and content and recommend that it be accepted in partial fulfillment of the requirements for the degree of Doctor of Philosophy, with a major in Biomedical Engineering.

Stephen A. Sarles, Major Professor

We have read this dissertation and recommend its acceptance:

Eric Boder, Paul Dalhaimer, C. Patrick Collier, Francisco Barrera

Accepted for the Council:
Dixie L. Thompson

Vice Provost and Dean of the Graduate School

(Original signatures are on file with official student records.)

Improving Droplet Interface Bilayers as Models for Cell Membranes

A Dissertation Presented for the

Doctor of Philosophy

Degree

The University of Tennessee, Knoxville

Graham Jeffrey Taylor

May 2016

DEDICATION

To my son

Tatum

my parents

Randy and Vicki Taylor

my sister and two brothers

Jessica, Kevin, and Corey

and to Kelly and the rest of my family.

ACKNOWLEDGEMENTS

First and foremost, I am forever indebted to Andy Sarles for years of patient guidance and advice. Andy has significantly and positively influenced the way I write, the way I plan and perform experiments, the way I think critically about problems (scientific or otherwise), the way I look at literature, and the way I do many other things. I have learned a tremendous amount from Andy, both in and out of the lab, and can only hope to return the favor or pay it forward in some way.

I will cherish my time in the Bioinspired Materials and Transduction Laboratory for many reasons, three of which are my labmates, colleagues, and most importantly, lifelong friends; a sincere "thank you!" to Guru Venkatesan, Nima Tamaddoni, and Mary-Anne Nguyen for hours of conversation and deliberation, for good times, and for great memories.

The work described herein would not be possible without the assistance and advice from several key individuals along the way. I would like to acknowledge Guru Venkatesan, Max Pridgen, Jason Seinfeld, Fred Heberle, Eric Boder, Paul Dalhaimer, Pat Collier, Francisco Barrera, Francesco Stellacci, and Ahmet Bekdemir for their support. Thanks to UTK College of Engineering Dean Masoud Parang and ORNL CNMS/JINS Director Mike Simpson for personal advice and financial support. My work was also made possible through funding from the NSF, an ORNL Science Alliance JDRD, and an Air Force Office of Scientific Research (AFOSR) Basic Research Initiative (Les Lee's M^4 program).

ABSTRACT

This work describes research aimed at improving the droplet interface bilayer (DIB) platform for creating and characterizing biologically relevant model cell membranes. Improvements are made possible in part through the development of a portable, compact platform for controlling temperature with DIBs. Feedback-controlled heating allows studies to be conducted across a range of temperatures, from ambient up to at least 80°C, and also provides new understanding of methods to form DIBs using mixtures of total lipids extracted from bacterial and eukaryotic cells. The membranes formed from total lipid extracts (TLE) are introduced along with evidence that model membranes formed using lipid compositions mimicking natural biological membranes (here using total lipids extracted from *Escherichia coli* and from porcine brain) behave significantly different than simple single-component membranes. Results provided herein indicate TLE DIBs display high sensitivity to antimicrobial peptide (alamethicin) insertion at room temperature which is explained by evidence of thermotropic phase behavior not encountered with single-lipid DIBs. These results highlight the importance of considering lipid composition when using lipid bilayers as models of cell membranes, and new techniques are described that facilitate the study of composition-dependent phase transitions in model membranes.

The proposed research is also aimed at developing new non-ionic methods for characterizing membranes and the interactions of membrane-active molecules that do not necessarily affect membrane conductance and are thus difficult to study. A new tool is developed that utilizes the Young-Lippmann and Young-Dupre relations to enable measurement of membrane specific capacitance and surface tension in a single DIB experiment. The method is introduced, applied, and validated through studies of DPhPC DIBs incorporating various amounts of cholesterol and solvent molecules. The new method is also applied to provide insight toward the interactions of cell-penetrating mixed-monolayer protected nanoparticles in lipid bilayers. Lastly, the method is proven useful for tracking transitions in monolayer and bilayer surface tension that result from thermotropic phase transitions in total lipid extract DIBs.

TABLE OF CONTENTS

LIST OF TABLES

LIST OF FIGURES

CHAPTER 1

INTRODUCTION AND LITERATURE REVIEW

The overarching goal of this work is to elicit new understanding of the effects of membrane composition and heterogeneity on the biophysical properties and behavior of cell membranes. New knowledge of the mechanisms governing biological functions will provide new insights and tools to aide in the ongoing battle against diseases like cancer, diabetes, Alzheimer's, and more. We are currently lacking a full understanding due to the complexity of cells, their membranes, and the related fundamental biophysical processes that translate to larger physiological functions. The approach used here is to study artificial lipid bilayers formed at the interface of connected lipid-infused water droplets submerged in oil. This seemingly simple approach provides a physical model for cell membranes, and the tunability of the platform provides a means of "reverse engineering" the mechanisms of cellular function. This dissertation presents a step towards increasing the physiological relevance and practical utility of reverse engineered artificial membranes formed between aqueous volumes (i.e., droplet interface bilayers).

This chapter begins with a description of the function, structure, and organization of natural cell membranes; the second part of this chapter reviews prior literature regarding the formation of artificial models of cell membranes and methods for characterizing model membranes. The literature review highlights important findings from prior work as well as recognizable gaps and limitations hindering the utility and application of model membranes for the purpose of understanding natural membrane-mediated biological functions.

1.1 The Cell Membrane

1.1.1 Cell Membranes and Fundamental Functions

The cell membrane is a crucial multifunctional component of cellular architecture. Peering through the microscope into eukaryotic cells, we find a number of macromolecular structures ranging from the cell nucleus to Golgi apparatus, mitochondria, endoplasmic reticulum (ER), lysosomes, and others (Figure 1). While many of these organelles all perform different functions, there is one class of structural elements that is common to them all: membranes. The nucleus is surrounded by a nuclear envelope, the ER and Golgi are a dense highly folded network of membranes, and mitochondria have an outer membrane and an inner, densely folded membrane. The outer barrier of the entire cell is yet another membrane structure: the plasma membrane. Prokaryotic organisms, gram-negative and gram-positive bacteria for example, have similar outer membrane structures that help establish a clear boundary between the "inside" and the "outside" of the cell.

The membranes found throughout cells must perform a variety of functions, and they do so through the concerted implementation of the lipid bilayer and transmembrane proteins (Figure 1). [45] The lipid bilayer is the foundation of the membrane; it serves as a semi-permeable barrier between the

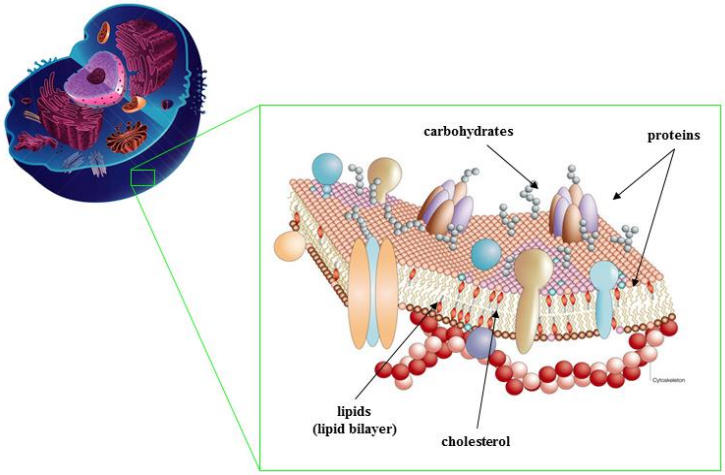

Figure 1. Cell membranes act as the outer barrier of the cell and organelles. Membranes can also be found inside organelles (i.e. inner mitochondrial membrane). Membranes serve as a two-dimensional liquid crystalline lattice in which transmembrane proteins, cholesterol, and other important biomolecules are anchored. (Reproduced from [44, 45])

aqueous solution on either side of the membrane, and it possesses a tri-layered hydrophilic-hydrophobic-hydrophilic two-dimensional matrix into which membrane proteins are able to insert or embed. Proteins then act as functional elements that play significant roles in cell-cell signaling and communication or transport, for example by transducing ions or water molecules or chemical species and signals.

Membranes and membrane proteins play pivotal roles in a number of important physiological processes. The cell membrane as a whole must act as a selectively permeable barrier that prevents unwanted species outside the cell from entering, allows nutrients and water in as needed, and simultaneously allows excretion of waste products and signaling molecules. There are many examples of physiological processes reliant on membrane or membrane-protein mediated processes. Mammalian muscle contraction involves the fusion of acetylcholine-rich liposomes with the membranes of neurons, and initial fusion event must then be followed by binding of acetylcholine molecules to membrane proteins (acetylcholine receptors) embedded in the membrane of the muscle cell that should contract. [112] Moving from the nervous system to the immune system, a proper immune response depends on the function of membranes and membrane proteins. Toll-like receptors (TLRs) are transmembrane receptor proteins [113] that are embedded in the membranes of immune cells, albeit with domains that reside in the aqueous region outside of the membrane where they bind to and recognize specific pathogens. Improper TLR function is implicated in immunodeficiencies, atherosclerosis, and asthma. [114] Yet another example of the significance of membranes and membrane-proteins in terms of normal physiological function: blood sugar control mechanisms involve insulin activation of insulin receptors (IRs) in the muscle cell plasma membrane, and then the insulin-signal propagates intracellularly to recruit liposomes rich in glucose transport proteins (GLUT) to the plasma membrane where the transporters can increase diffusion driven uptake of blood sugar. [115] Disruption of any of the membrane-mediated aspects of normal blood sugar control could thus play a role in diabetes which affects millions of people around the world. The examples provided here are only a few of the many membrane-mediated processes that affect physiological function of organisms.

1.1.2 Lipids and the Lipid Bilayer

The lipid bilayer is a fundamental element of cell membranes, providing barrier-like properties as well as an amphiphilic two-dimensional matrix to accommodate similarly amiphiliphilic membrane proteins. Lipid bilayers form through the self-assembly of lipids, amphiphilic molecules with hydrophilic and hydrophobic regions, placed in aqueous environments. While there are thousands of distinct lipid types known to exist in organisms [sud MAPS], every lipid generally has a hydrophilic region (referred to as a "headgroup") and a hydrophobic region comprised of one or more acyl chains (referred to as the "tails" in the case of phospholipids) or some other nonpolar moeiy. Figure 2 shows the chemical structure of several phosholipids, all of which include a polar headgroup region and a nonpolar acyl chain region. The phospholipids in Figure 2 all have identical acyl chains (14 carbons long – myristoyl), however there are differences in the chemical structure, and thus the net charge and steric size, of the polar headgroup regions. Each of the headgroup types shown in Figure 2 are common in natural membranes (note there are additional headgroup varations not included here); and the nomenclature for lipids includes different names for each of the headgroup types: phosphatidylcholine (PC), phosphatidylethanolamine (PE), phosphatidylserine (PS), phosphatidic acid (PA), and

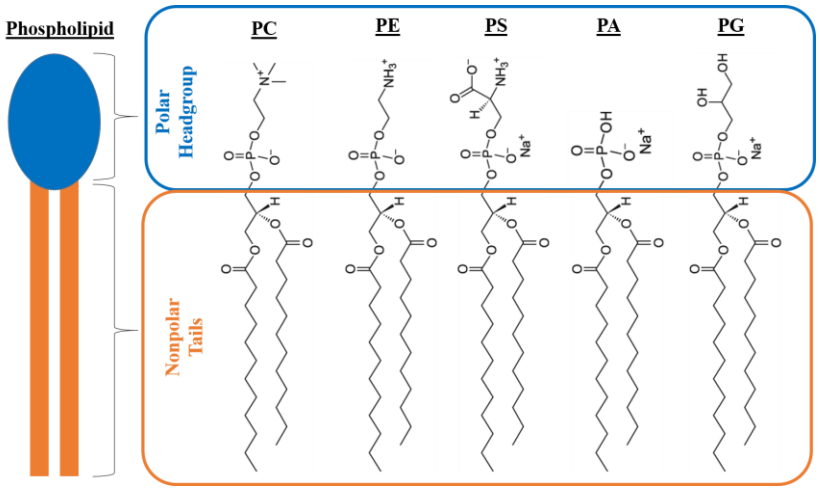

Figure 2. Typical phospholipid amphiphilic structure (polar headgroup and nonpolar tails) and headgroup types. PC – phosphatidylcholine, PE – phosphatidylethanolamine, PS – phosphatidylserine, PA – phosphatidic acid, PG – phosphatidyl glycerol.

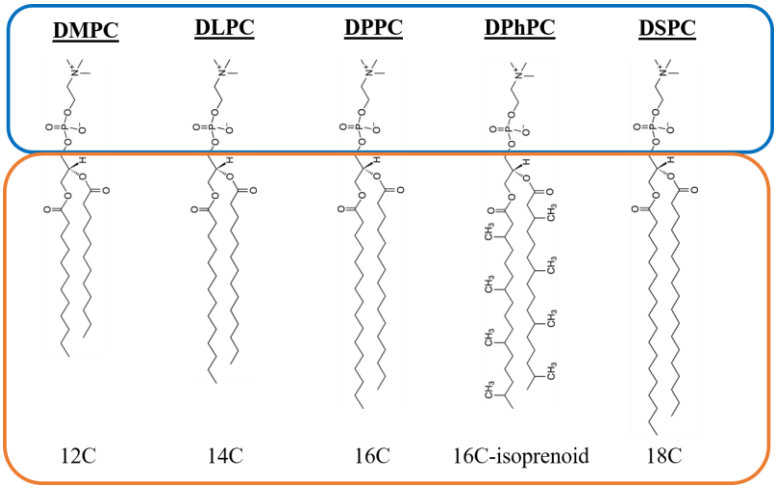

Figure 3. Variations in acyl chain length. DM – dimyristoyl, DL – dilauroyl, DP – diplamitoyl, DPh – diphytanoyl, DS – distearoyl. (PC – phoshpatidylcholine headgroup; see Figure 2)

phosphatidylglycerol (PG). PC and PE are zwitterionic: they display net charge neutrality despite the presence of positive charge on the phosphate group and a negative charge on the terminal amine. The other headgroups shown in Figure 2, PS, PA, and PG, are examples of lipids that possess a net charge in solution (and thus are shown complexed with a dissociated salt ion).

Figure 2 illustrates different common lipid headgroups, but an even greater number of lipid permutations are possible through the existence of various types of lipid acyl chains. Acyl chains can differ in their length, in their degree of hydrocarbon bond saturation, and through the possible presence of methyl sidegroups or cyclic moieties in the chains. Figure 3 depicts phosphatidylcholine lipids with two saturated acyl chains of varying length (12C - DMPC, 14C - DLPC, 16C - DPPC, 18 - DSPC). Figure 3 also shows a lipid with 16C acyl chains containing methyl sidegroups attached to every other carbon along the length of acyl chain: lipids of this type are referred to as isoprenoid (phytanic in the case of 16C long chains, i.e. DPhPC). Saturated and unsaturated acyl chains differ only in the types of bonds that exist between the carbon atoms that makes up the chain. Fully saturated acyl chains such as those in Figure 2 contain only single bonds between the carbon atoms. Figure 4 shows a PC lipid with fully saturated acyl chains as well as examples of PC lipids with unsaturated chains. Unsaturated acyl chains are those which contain a double bond between two of the carbon atoms in the chain. Acyl chains containing more than one

double bond are referred to as polyunsaturated acyl chains. Figure 4 depicts a "hybrid" lipid that contains one fully saturated acyl chain and one unsaturated acyl chain containing a single carbon-carbon double bond, a diunsaturated lipid with two acyl chains containing a single double bond, and a poly unsaturated lipid in which each acyl chain contains multiple carbon-carbon double bonds.

Sterols represent another class of membrane lipids that are commonly found in natural organisms. Figure 4 displays the structure of cholesterol and ergosterol, and in both cases, the polar region of the sterol molecule consists primarily of a single hydroxyl group. In contrast to the small polar "head", sterol molecules have bulky hydrophobic moieties containing numerous planar rings. The rigidity and bulkiness of sterol molecules is believed to play a key role in the ability of sterols to significantly alter membrane properties such as permeability and fluidity. [116, 117] A number of other two-tailed lipid types exist including the phospholipid sphingomyelin as well as non-phosphate containing gangliosides, sulfatides, cerebrosides, and ceramides. Additionally, natural membranes do contain single-tailed lipids such as sphingosine. Neutral lipids, i.e. lipids with no polar hydrophilic region, also exist. Monoacylglycerols (MAG), diacylglycerols (DAG), and triacylglycerols (TAG), and steryl esters (SE), however these types of lipids are fully nonpolar and

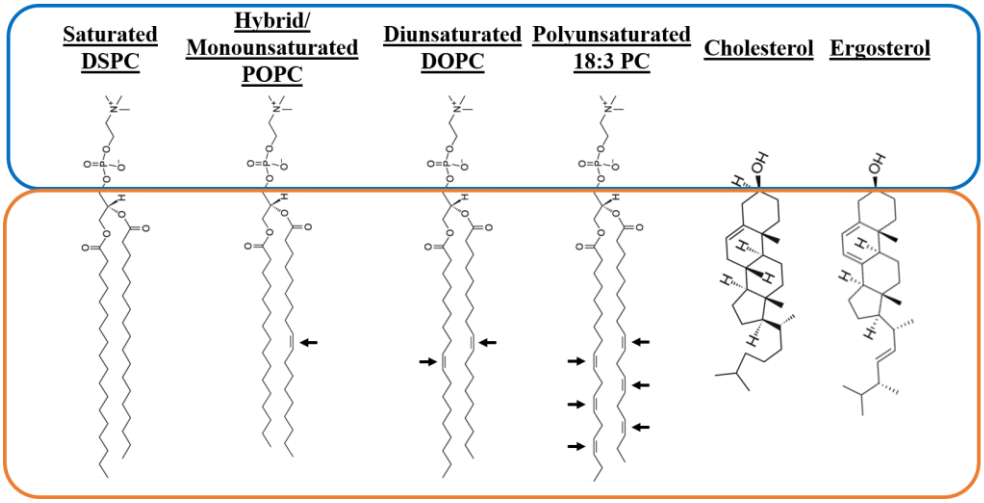

Figure 4. Variations in acyl chain saturation yield lipids with fully saturated chains, one saturated and one unsaturated chain, or two unsaturated chains. Unsaturated acyl chains may contain one or more double bonds. PO – palmitoyloleoyl, DO – dioleoyl. Many types of sterols exist: cholesterol and ergosterol are shown here.

reside in the core of lipid droplets or transiently in lenses or budding pockets in between leaflets of the bilayer. [118]

1.1.3 Membrane Proteins: Functional Membrane Biomolecules

Membrane proteins are often found inserted into or through the hydrophobic core of membranes in cells, and these membrane proteins perform specific microscopic functions that affect overarching macroscopic physiological functions. DNA in the human genome contains over 20,000 distinct genes that encode for proteins, and in humans, 20-30% of all protein encoding genes correspond to membrane proteins. [119] This amounts to between 5-6,000 different membrane proteins that perform a variety of functions including signaling, transport, and enzymatic activity. [120] Membrane proteins can be generally grouped into two categories: integral proteins span the entire thickness of the lipid bilayer while peripheral proteins are primarily associated with either an inserted integral membrane protein or the polar headgroup region of only one leaflet of the bilayer. [4] Figure 5 illustrates the difference between integral and peripheral proteins, and the figure also highlights the fact that many integral membrane proteins possess hydrophobic and hydrophilic domains. The bilayer-like amphiphilicity of certain proteins

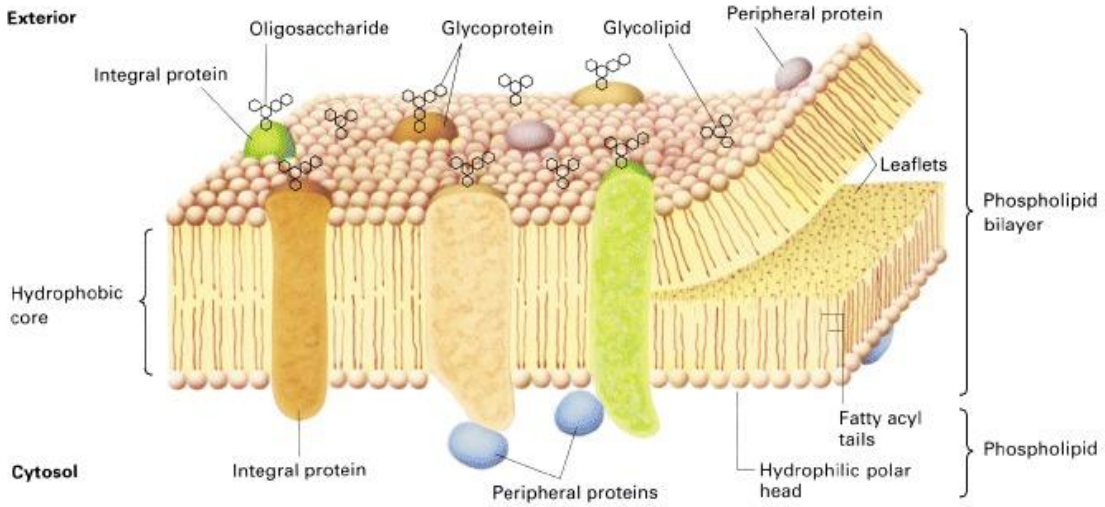

Figure 5. Illustration of membrane proteins associated with a lipid bilayer, including integral and peripheral proteins. (Reproduced from [4]).

drive or maintain protein positioning relative to the membrane (note: protein amphiphilicity is affected by the polarity of the amino acid chain sidegroups positioned along the length of the peptide).

Membrane proteins often perform tasks or functions, and many known membrane proteins can be grouped into one of three functional protein groups: receptors, transporters, and enzymes (presented in order of prevalence). [120] There are many different specific proteins within each of these three functional groups. Almen et al have identified over 1300 receptors, 800 transporters, and 500 enzymes. [120] Examples of receptors include G protein coupled receptors (GPCRs) like rhodopsin, a transmembrane protein that pumps protons across the membrane in response to stimulus by light. [120] The nervous system in mammals involves numerous other GPCRs that bind and respond to neurotransmitter molecules such as acetylcholine, γ-aminobutyirc acid (GABA), dopamine, and serotonin. Receptor proteins often undergo a change in shape or conformation upon activation by the appropriate ligand or input. Transporter membrane proteins perform roles in moving soluble and insoluble species across the membrane. Examples include ion pumps, ion channels, and even transporters of larger molecules like sugar molecules, nucleic acids, or lipid headgroups [120]. Ion pumps actively expend energy to pump ions across the membrane while channels act as passive pores that allow the passage of solutes through the membrane. It should be noted that some channels form constantly open static pores while others only form pores in the presence of sufficient electrical potential ("voltage-gated"), mechanical strain ("mechanosensitive"), or the appropriate soluble ligands ("ligand gated"). In addition to the movement of ions, some transporters move larger molecules and substrates. ATP-binding cassette (ABC) transporters, for example, promote movement of species like amino acids, peptides, and sugars across the membrane. [121] Floppases and flippases, other examples of transport proteins, are integral membrane proteins that aide in transporting the polar headgroups of lipids from one side of the membrane to the other in order to help maintain desired lipid composition asymmetry. Enzymatic membrane proteins catalyze chemical reactions. For example, protein kinase C is a member of the protein kinase family of enzyme proteins which are involved in signal transduction. Protein kinase C continuously moves between the cytosol and the inner cytosolic leaflet of the membrane in a cycle of chemical reactions. [4] There are additional membrane proteins that fall

outside of the classifications of receptors, transporters, and enzymes. For example, actin and spectrin are peripheral proteins that associate with the cytosolic leaflet of cell membranes where they play roles in binding or anchoring cytoskeletal filaments to the membrane. [4]

The microscopic functional abilities of proteins translates into higher level macroscopic physiological functions that are important to living organisms. For example, a mechanistic description of ion pump and ion channel function includes the proteins' ability to actively and passively transport ions across membranes, yet the higher level output might be an osmotic or electrochemical transmembrane potential that is essential to propagation of an action potential or membrane depolarization event related to nervous system signal conduction. In another example, T-cell receptor proteins change shape upon binding to pathogenic ligand; this simple binding-driven reorganization plays a pivotal role in triggering of the immune response to prevent further infection. Rhodopsin membrane proteins are found in cells in the eyes of mammals and animal, and these protein absorb intent radiant light and pump a proton (H^+) across the membrane in response. The seemingly basic ability of rhodopsin proteins to pump protons in response to light is, at a higher level, the first step in a signaling cascade that provides mammals with the sense of sight! Cyanobacteria also utilize the light-driven proton pumping function of rhodopsin-like proteins to generate chemical energy in a form of photosynthesis. These examples highlight the ways in which mechanistic functions of proteins translate into important higher-level functions.

Despite the vast amount of information obtained regarding the function and physics of membrane proteins, there are a number of scientists actively pursuing new information regarding the different types of proteins that exist and how they interact with and are modulated by lipid bilayers. The protein data bank of transmembrane proteins (PDBTM) has grown considerably over the last decade or more, for instance from 400 to 1700 known proteins between 2004 and 2012. [122] his means that only about 30-40% of the membrane proteins encoded in the human genome have been identified, and a full understanding of their function requires additional research. The development of new tools for studying interactions between membranes and membrane proteins would help in the efforts to obtain more information on both known and yet-to-be-discovered membrane proteins.

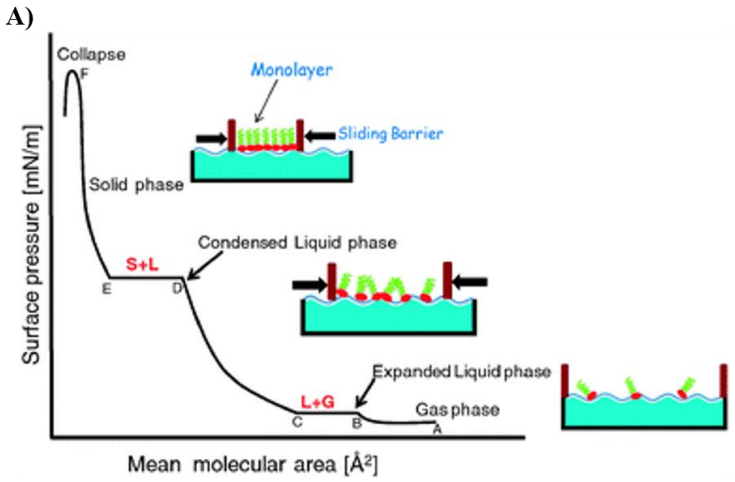

Figure 6. A) Lipid phases demonstrated through Langmuir trough experiments: G – gaseous, LE – liquid expanded, LC – liquid condensed, S - solid. (Reproduced from [7]).

1.1.4 Lipid Phase and Transitions

Lipid bilayers can exist in a number of different thermotropic phases, and these phase states are affected by a number of variables including the lipid packing, the temperature of the system, and the composition of the membrane. This section describes the effect of packing induced changes in lipid phase and ordering as well as temperature and composition dependent effects.

Lipid Packing

A straightforward demonstration of lipid phase behavior is enabled through the use of the Langmuir trough, and experimental tool developed by Irving Langmuir early in the 20th century. Figure 6A provides an illustration of a Langmuir trough filled with water to create an air-water interface. In a common approach, lipids or surfactants are deposited at the air-water interface via volatile solvent (which later evaporates). The Langmuir trough also has movable barriers that pass through the air-water interface, thus moving the barriers towards provides a means of corralling and compressing lipids adsorbed at the interface. By including one additional component with the trough, a Wilhelmy plate used to measure the surface tension at the interface, the effects of compressing the interfacial lipid monolayer can be studied in a quantitative fashion. Practically

speaking, the resulting measured changes in surface tension are often analyzed in terms of surface pressure (Π) which is equal to the difference between the surface tension of the fresh air-water interface ($\gamma_{a/w}$) and the surface tension of the interface with adsorbed lipid ($\gamma_{a/l/w}$) as given by

$$\Pi = \gamma_{a/w} - \gamma_{a/l/w}. \qquad \text{Equation 1}$$

Figure 6A shows the surface pressure at the air-water interface during a typical lipid-film compression experiment. Initially, the movable barriers are fully separated and thus adsorbed lipids are spaced far apart with a large allowable mean molecular area. This initial state corresponds to the lower right section of Figure 6A, and the lipids are in a very fluid "gaseous" (G) state with very little effect on the air-water surface tension (and thus low surface pressure). If the barriers are moved closer together so as to corral the lipids adsorbed at the interface, the lipids will eventually begin to physically contact each other and become slightly less disordered. The monolayer is still quite fluid in this "liquid-expanded" (LE) phase although the surface pressure begins to increase. Further compression of the lipid monolayer by movement of the trough barriers leads to progressively higher order, higher surface pressure, and eventual transition into a liquid-condensed (LC) phase where lipids are well-packed laterally but still display lateral and rotational diffusivity observed in the LE sate. Further compression leads to significant increases in surface pressure as the lipids are forced into a highly ordered and well-packed "solid" (S) phase. Surface pressure is a maximum at this point, and any additional compression leads to buckling or collapse of the monolayer accompanied by fluctuations and decreases in the measured surface pressure. Langmuir trough experiments such as the one described here help to provide insight into the fact that self-assembled layers of lipids can exhibit varying degrees of order and fluidity based on factors like spatial constraints, lipid type, and even the temperature or kinetic energy of the system.

Temperature and Thermotropic Phase Transitions

Unlike a monolayer used in Langmuir trough experiments, cell membranes have two leaflets, yet there is still strong evidence that even lipid bilayers exhibit various phases that are strongly affected by temperature and composition. Many methods have been employed to detect thermotropic transitions including NMR, [123-126] X-ray techniques, [127-131], fluorescence

anisotropy [131-133], and turbidity among others. Perhaps one of the most intuitive methods for observing thermotropic melting of lipid bilayers is calorimetry, an analytical method used for decades to study the exothermic and endothermic nature of chemical reactions and solid-liquid phase changes (i.e., the melting/freezing of ice/water). Differential scanning calorimetry (DSC) is a type of calorimetry that involves heating two separate samples, one being an inert reference and the other including the sample to be tested, at a constant rate in order to obtain the difference in power required to change the temperature of the sample alone. [6] The output of DSC is the excess specific heat or heat capacity of the sample as a function of temperature, and the excess specific heat of a sample undergoes a transition if changing temperature leads to a significant change in the ordering or phase of the sample. DSC has been heavily employed in the study of thermotropic behavior of lipid bilayers and the interactions of sterols, proteins, and small-molecules and therapeutics. [6, 134-147]

DSC of a single lipid component, often in the form of multilamellar or unilamellar liposomes in aqueous solution, yields a measure of the change in excess specific heat of the lipids as a function of temperature. When a lipid is heated or cooled through its T_m, DSC reveals evidence of changes in the lipid heat capacity that are consistent with endothermic or exothermic transitions, respectively. A representative thermogram obtained via DSC with a saturated lipid (DPPC) undergoing a melting transition is provided in Figure 7A, and the transition in excess specific heat capacity around 42°C is clearly observed. Single-lipid component liposomes often display sharp transitions that occur over a narrow temperature range like that shown in Figure 7. The thermogram in Figure 7A shows an example of the change in heat capacity that results from a heating induced gel-fluid melting transition, here in DPPC liposomes which display a main T_m around 41-42°C. . The sharpness of the peak is an indication of the highly cooperative nature of the melting transition. Another useful quantitative output of DSC is the enthalpy of the transition: the area under the excess specific heat curve provides a direct measure of the enthalpy associated with the melting transition (ΔH). Further, since the Gibbs free energy of the transition is zero at the midpoint of the transition (in ideal single-component liposomes), the entropy of the transition can also be calculated simply via $\Delta S = \Delta H / T_m$. DSC is a powerful tool for identifying the existence of, and quantitatively studying the thermodynamics associated with, lipid bilayer phase transitions.

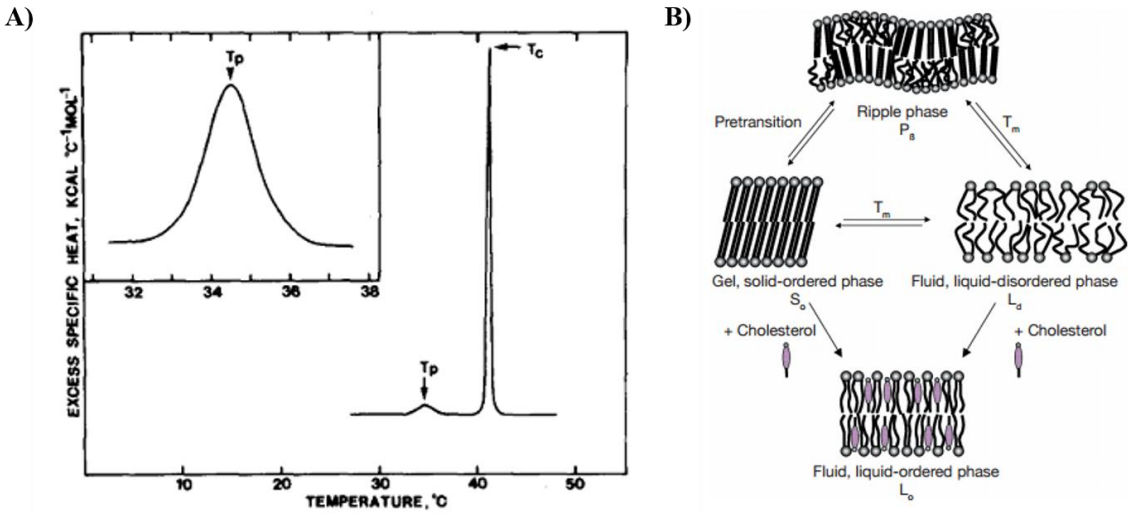

Figure 7. A) Representative thermogram obtained by high-sensitivity DSC using multilamellar DPPC liposomes dissolved in water. (Reproduced from [6]). B) Illustration of changing lipid bilayer phase upon changing temperature: heating through the melting temperature, T_m, leads to a transition from the solid or ordered phase to fluid, liquid-disordered phase. Some lipids transition through an intermediate rippled phase. Incorporation of cholesterol can also affect membrane phase, leading to a bilayer that is ordered but with properties of liquid crystalline bilayers, thus termed liquid-ordered. (Reproduced from [6] and [58]).

Figure 7B provides a graphical illustration of the effects of temperature on the phase, packing, and ordering of DPPC bilayers. At temperature well below T_M, the bilayer exists in a "gel" or solid-ordered (S_o) phase. Heating the DPPC bilayer leads to highly cooperative melting, [148] first through a pretransition (see the small peak labeled "T_p" and the inset in Figure 7A) into a rippled phase (P_β) where there are fractions of both ordered and disordered lipids, and then the bilayer transitions to a fully fluid, liquid-disordered (L_d) phase with sufficient heating to a temperature above T_m. [148] Similar transitions are observed for many of the saturated PC lipids, for instance DLPC, DMPC, DPPC, and DSPC all display highly cooperative melting transitions at T_m = -2°C, 23°C, 42°C, and 55°C respectively. [142, 148, 149] Generally, T_m increases with increasing acyl chain length. [148] Unsaturated lipids also undergo phase transitions, however the increased fluidity conferred by the presence of the double-bond(s) typically increase fluidity and decrease T_m (DOPC for instance has T_m = -18°C [150]). Another important factor that can affect phase is the presence or inclusion of sterol molecules whose large and bulky hydrophobic groups affect the

order and fluidity of neighboring lipid acyl chains. Cholesterol actually serves biphasic roles as it can fluidize solid-phase membranes and rigidify fluid-phase membranes [141, 142]. As a result, cholesterol yields bilayers that are of an intermediate liquid-ordered (L_o) phase (Figure 7B, bottom): the lipids display lateral and rotational diffusivity similar to that of the liquid phase, albeit with dense packing, order, and increased thickness associated with the ordered gel phase.

Despite the utility of DSC in studying and characterizing thermotropic phase transitions, it is limited in cases where membranes undergo low-enthalpy transitions. As will be discussed in Chapter 6, this type of situation may be encountered in complex mixtures of lipids such as those encountered in biological membranes, especially in the presence of large amount of cholesterol which typically reduce the enthalpy of the transition (thereby reducing the features that are detectable by DSC). As such, little is known regarding the possible occurrence and biophysical fundamentals of thermotropic transitions that occur in complex multi-component membranes. This shortcoming constitutes one of the major gaps addressed through the work in described this dissertation.

1.1.5 Cell Membrane Composition and Organization

Cell membranes are comprised of many different types of lipids (over 1000 distinct species have been recognized in the Lipid MAPS database [151]) and are densely crowded with membrane proteins, and there are specific modes by which these lipid and protein components are organized in the membrane. This section describes the heterogeneity found in natural membrane lipid composition, the non-random organization of lipids across leaflets of the bilayer (asymmetry) and laterally within each leaflet (subdomains or rafts), and the spatial localization of membrane proteins as modulated by lipid-bilayer organization (the Fluid-Mosaic Membrane Model).

Lipid Composition in Natural Membranes

Biomembranes possess astounding chemical complexity that is essential for the cell's ability to respond and adapt to the external environment. Complex compositions are observed in the membranes of both prokaryotic and eukaryotic species which is an evolutionary testament to the potential importance of such heterogeneity. Bacteria are primarily comprised of PE, PG, or

cardiolipin (CL, a PG dimer with a double net-negative charge). [152] Eukaryotic organisms display a greater diversity than prokaryotic organisms in terms of common phospholipid headgroups. Mammalian membranes contain appreciable fractions of PC, PE, PS, PI, PA, CL, and sphingolipids such as sphingomyelins (SM), cerebrosides, and gangliosides. [57, 153] The charts in Figure 8 illustrate the phospholipid compositions of prokaryotes (gram + and gram – bacteria, as examples) and eukaryotes (includes plasma membranes of *S. cerevisae* and human cells, as well as a breakdown by organelles in human cells), and it is clear that eukaryotic lipid composition is generally more diverse. Van Meer and de Kroon report that 65 mol % of mammalian lipids are glycerophospholipids (PC, PE, PS, or PI) while 10% are sphingolipids and the other 25% are sterols. Sterol content varies from organism to organism. For instance, cholesterol is abundant in humans and mammals, but it is not common to yeast (i.e., *S. cerevisae*) which is also member of the eukaryote family. The membranes of yeast do contain appreciable fractions of ergosterol, zymosterol, fecosterol, and episterol. [154] Conversely, bacterial organisms have little to no cholesterol, although there is evidence that bacterial membranes include hopanoids which are extremely similar to cholesterol. [155-157] Both prokaryotic and eukaryotic organisms contain a variety of saturated fatty acids and unsaturated acyl chains. [158] Table 12 in the appendix shows

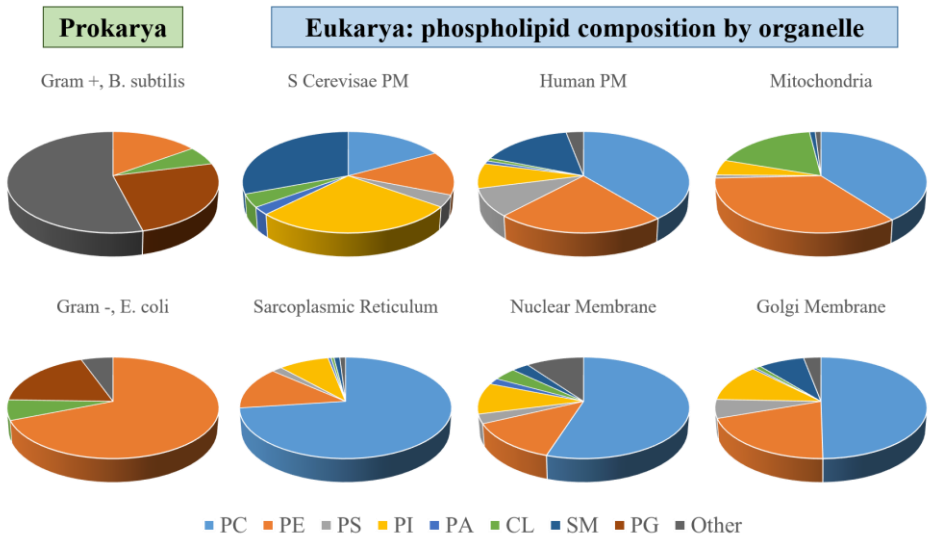

Figure 8. Lipid composition in prokaryotic and eukaryotic membranes. Compositional heterogeneity exists in both headgroup (shown) and acyl chain content (not shown). Refer to Table Table 12 (Appendix) for references and percentages.

some of the various types of fatty acids and acyl chains encountered which include 12:0, 14:0, 16:0, 16:1, 17:0, 18:0, 18:1, and even 18:3 and other polyunsaturated fatty acids. As illustrated in Figure 8, membrane composition varies not only from organism to organism, but from organelle to organelle within an individual cell. The organelle specific compositions are highly regulated by cells, most likely coordinated based on the specific functions of each organelle and associated membrane proteins, which is an indicator of their importance.

As discussed in Section 1.2.1, efforts employing artificial model membrane systems to study membranes, membrane proteins, and related biophysics would benefit from understanding and maintaining physiologically relevant features conferred by the complex compositions of natural membranes. Unfortunately, much of the work performed with model membranes to date has been performed with single lipid compositions or mixtures of between two to four components. As a result, there is still much to be learned about the effects of such diverse and complex composition on the properties and functions of membranes and interactions with membrane-active proteins, drugs, and other small molecules.

Non-Random Organization of Lipids: Subdomains and Asymmetry

The large number of different types of lipids found in cell membranes, both in terms of varying lipid headgroups (and thus steric size and charge) and acyl chains (thus hydrophobic length and fluidity), are known to be organized in a non-random fashion. [61, 159-164] Figure 9 illustrates two methods by which the lipid components of cell membranes are actively and passively reorganized both laterally within the plane of the membrane and across the leaflets of the bilayer to create asymmetry.

Lateral organization or phase separation of lipid components is, in many cases, a passive phenomenon that arises when the membrane contains multiple species with varying thickness or fluidity. [165, 166] Intense research over the last 10-20 years has elicited methods for recreating phase separation on demand, and one basic approach involves forming a lipid bilayer from at least three components: one lipid with a low T_m, one lipid with a high T_m or shingomyelin, and some fraction of cholesterol. [165-176] Commonly used mixtures include DSPC/POPC/cholesterol (T_m

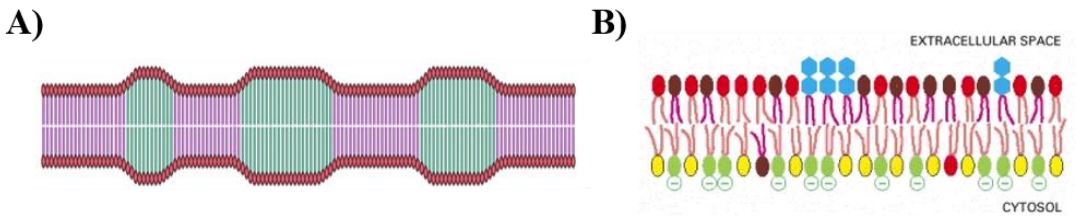

Figure 9. A) Phase separation occurs in lipid bilayers containing mixtures of lipids due to mismatches in the thickness and fluidity of lipid components. (Modified from [9]). B) Cell membranes often display asymmetric transbilayer distribution where each leaflet contains a different composition of lipids compared to the opposing leaflet. (Reproduced from [52]). Both lateral and transbilayer spatial organization of lipid components are believed to play fundamental roles in membrane-mediated processes such as signaling, protein sorting, and vesicle fusion.

is 53°C and -2°C for DSPC and POPC, respectively), DSPC/DOPC/cholesterol (T_m for DOPC is -18°C), or DPPC/DPhPC/cholesterol (Tm is 42°C for DPPC and below -120°C for DPhPC). [165-169, 171-176] As described in section 1.1.4 above, a single component membrane reversibly transitions from a disordered state to an ordered state upon cooling through the lipid's T_m. With this in mind, it is interesting to ask how phase transitions proceed when cycling the temperature of bilayers formed from mixtures of two or more types of lipids, especially when each of the lipid display significantly different transition temperatures if tested individually. Multi-component lipid mixtures often exist in a homogenously mixed, disordered state when heated to a temperature above the mixtures T_m, however, interesting mixing and miscibility behavior begin to emerge upon cooling the multi-component membrane through T_m. Upon approaching and passing through T_m, the lipid component with the highest T_m begins to become more ordered and more condensed. This ordering process begins at various spots or patches throughout the membrane which gives rise to domains of varying thickness and fluidity as illustrated in Figure 8. It is important to note, especially when considering thermoregulation of warm-blooded animals, that the size and fluidity of phase-separated domains can be controlled simply by altering the composition of the membrane [165, 166, 173, 176].

It is now well-known that compositional differences exist when comparing the two leaflets of a given section of cell-membrane, and this transbilayer asymmetry (Figure 8) is an important aspect of membrane-mediated signaling and cellular functions. Cells actively expend energy to maintain the asymmetry, and it is worth pointing out that a tremendous amount of energy should be required to flip the polar headgroup of a lipid across the nonpolar hydrophobic core of the membrane. While

the mechanisms that generate and maintain asymmetry are the subject of ongoing research, it is generally understood that there are families of membrane proteins responsible for "flipping" and "flopping" lipid headgroups from one leaflet to the other. Maintaining asymmetry is extremely important for cells. For example, normal cells typically have a larger fraction of anionic negatively charged PS lipid on the extracellular leaflet. Loss of PS asymmetry is associated with apoptosis or cell-death, and such loss of normal charged lipid asymmetry can trigger cytoskeletal reorganization critical to angiogenesis and vascular remodeling [177]. A cell that loses its ability to actively maintain normal asymmetry is thus signaling the need for attention, repair, or replacement, and such regulatory mechanisms are crucial to the hemeostasis of living organisms. This dissertation does not focus heavily on asymmetry, but this aspect of membrane organization is important enough to mention briefly.

Spatial Organization of Membrane Proteins: Evolution of the Fluid-Mosaic Model

Singer and Nicolson's 1972 Fluid-Mosaic Membrane Model [3], more recently referred to as the F-MMM [61], was an early advancement in our understanding and thinking of the structure and organization of cell membranes. Figure 10A shows a recently modernized [61] illustration of the original F-MMM [3] which describes the membrane as a fluid lipid matrix studded with globular transmembrane and peripheral proteins. The original F-MMM illustration shows a membrane comprised of a single-lipid as opposed to the complex mixture of lipids known to exist in cells. As described above, complex mixtures of lipids can potentially lead to lateral and transbilayer organization (i.e., phase separation and asymmetry) which are believed to play roles in determining the spatial organization of membrane proteins and other membrane-associating components. The illustration provided by Escriba et al. in 2008 is considerably more realistic (Figure 10B) than the initial F-MMM model provided by Singer and Nicholson in 1972. Escriba's version of the membrane includes numerous different types of lipids, transbilayer asymmetry, lateral separation into subdomains or rafts, and the interplay of these concurrent features with membrane protein insertion and association with cytoskeletal components inside the cell. Many of these advanced features resulting from the complexity of the membrane were carried over in 2014 when Garth Nicholson, one of the original authors of the 1972 F-MMM, published a review of the evolution of the F-MMM. [61] Nicholson's latest illustration is provided in Figure 10C, and it is clear that

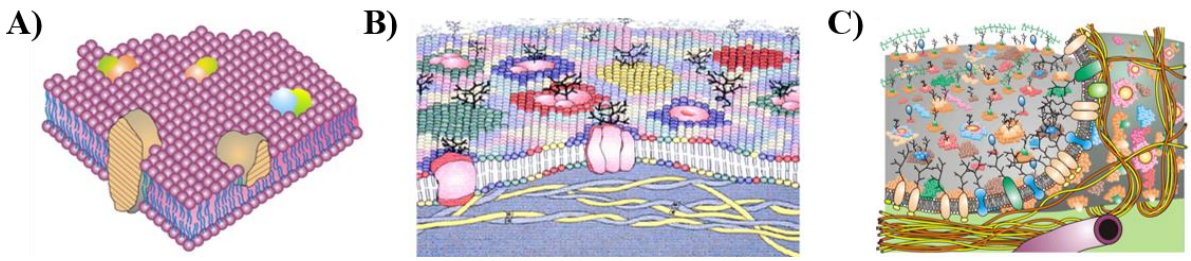

Figure 10. A) The original Fluid-Mosaic Membrane Model, including the lipid bilayer and globular integral or peripheral proteins, as illustrated in 1972. [3] B) An updated version of the model for membranes from 2008 includes lipid rafts, some of which help stabilize proteins, and lipid asymmetry across leaflets. [57] C) The latest (2014) update of Fluid-Mosaic Membrane Model, provided by one of the original authors of the 1972 model. [61]

models for the organization and structure of cell membranes is becoming increasingly more complex.

The literature review that follows highlights the history and evolution of model membrane systems, including ways in which model membranes, like the F-MMM, are still in the early stages of recreating and understanding the significance and influence of complex membrane composition.

1.2 Literature Review

This section provides a review of literature pertaining to the creation and characterization of artificial model membranes. Methods of forming model membranes have enabled detailed investigation of the properties, both physical and electrical, and function of membranes and membrane-proteins. However, there are a few key gaps to overcome in being able to recreate and understand physiologically relevant artificial models of cell membranes.

1.2.1 Model Membrane Systems

Given the importance and significance of membranes to greater physiological function, there are benefits of technologies that allow assembly and creation of model membranes that mimic the composition, organization, and function of natural membranes. A means of constructing and accessing physical model membranes could provide the ability to study membrane and membrane-protein mediated processes. Even more promising is the idea of using model membranes to study broken processes that result in disease, for instance diabetes or immunodeficiencies, and work on

finding ways to mitigate or stop the disease. For these reasons, scientists and engineers have been working for decades to form model membranes with the shared vision that they will serve as next generation tools to improve our understanding of membrane related biological and biophysical processes. A variety of approaches for creating model membranes exist, and each approach has its own advantages and disadvantages. This research proposal focuses on literature regarding droplet interface bilayers (DIBs) which can be classified as a type of freestanding planar lipid bilayer, and the usage of DIBs specifically provides the ability to characterize membrane biophysics via simultaneous electrophysiological and optical microscopy techniques. For comparison, Table 1 provides a summary of other methods to form model membranes which are extensively described elsewhere. [2]

Black Lipid Membranes

Black lipid membrane (BLM) films represent one of the earliest embodiments of artificial models of cell membranes, and there are several well-known variations of the methods used to form such films (see Figure 11). While Sir Isaac Newton noted the lack of light reflection, and thus the lack of any color, from lipid-stabilized films as early as 1704 [178], many scientists today credit Paul Mueller and Donald Rudin (co-authors Henry Tien and William Wescott should also be mentioned) [53, 54] and Mauricio Montale [60] for their seminal works establishing repeatable platforms for forming BLMs. One of the earliest methods, described briefly in 1962 by Mueller, Rudin, Tien, and Wescott, [53, 54] involved painting an "oily" solution of lipids dissolved in organic solvent over a small aperture (~100 μm diameter) in a hydrophobic solid support separating two aqueous compartments. Figure 11A provides an illustration of the formation of a painted BLM which was reviewed more thoroughly by Rudin et al. in 1969. [179]. Nearly a decade after the introduction of painted BLMs, Montale and Mueller provided a report of a modified technique for forming BLMs by first spreading lipid monolayers at an air-water interface, and then "folding" the monolayers over the two opposing sides of a small-hole in a hydrophobic solid support. Figure 11B illustrates the process of forming the monolayers and then folding them over the pore of a movable sliding solid-support to form a BLM over a hole in the solid support.

Table 1. Summary of methods used to form lipid bilayers as model cell membranes.

Method	Advantages	Disadvantages
Giant unilamellar vesicles (GUV, ≥ 500 nm diameter)	Various formation methods -Electroformation -Jetting through a BLM -Centrifugation Asymmetric Capability Suitable for tension measurements (LaPlace method)	Not suitable for electrophysiology, C_M Control over size polydispersity Fragile membranes
Liposomes/small and large unilamellar vesicles (SUV/LUV, <500 nm diameter)	Basic model for bilayers	Not suitable for electrophysiology Difficult to control asymmetry with small vesicles
Solid supported lipid bilayers (SLBs)	Suitable for AFM[51], QCM, TIRF, etc. Possibility for tethering Electrophysiology possible, but not common	
Black lipid membranes (BLM) – Montale, Montale-Mueller, Mueller-Rudin	Suitable for electrophysiology Asymmetric capability	Inherently unstable and rupture easily Poor view of bilayer area for C_M measurements Difficulty measuring θ
Droplet interface bilayer (DIB)	Suitable for electrophysiology Asymmetric capability Small size: portable, low resource cost Amenable to Cm, thickness, θ, tension measurements Supports use of fluorescent/chemiluminescent dyes and markers.	Limited options for lipids that can be dissolved as liposomes (to preserve asymmetric capability) and form stable asymmetric DIBs

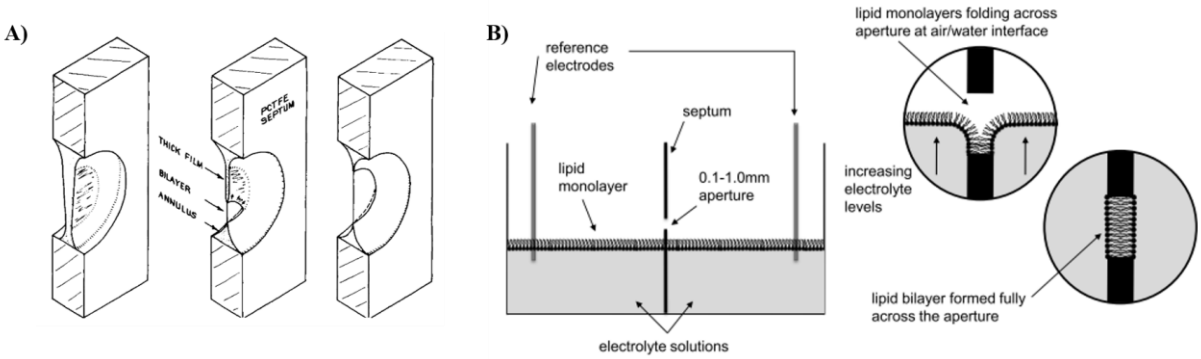

Figure 11. Illustrations of A) the thinning and formation of a "painted" BLM formed via the method of Mueller and Rudin, [53, 54] (Reproduced from [59]) B) the process of "folding" a BLM via the method of Montale and Mueller [60] (Modified from [2]).

Despite the differences in the early techniques used to form BLMs, there are some commonalities in the approaches used. A typical BLM setup includes aqueous compartments on either side that help promote self-assembly of the lipids while avoiding hydrophobic-hydrophilic-hydrophobic (i.e., the opposite of a cell membrane) style films formed by pioneers like Hooke and Newton [178, 180] who worked with soap or lipid stabilized films formed in wire hoops suspended *in air* (essentially forming the equivalent of bubbles that are so commonly enjoyed by children). The solid partition containing the small aperture is typically teflon or another suitably hydrophobic solid support, potentially modified by addition of petroleum jelly in solvent. Common solvents used for dispersing lipids and forming BLMs are often solvents with relatively high vapor pressures and include alkanes, alcohols, or chloroform, or mixtures thereof.

BLMs are a useful embodiment of artificial model membranes for a number of reasons. The ability to access each aqueous compartment allows for electrical measurements of ion transport, the currency of biological systems. Electrical measurements can also be used to measure membrane properties such as resistance, capacitance, specific capacitance and thus thickness, as well as the membrane's response to voltage (poration, electrocompression), and even the insertion and behavior of transmembrane proteins or pore-forming peptides. Scientists have used BLMs to study the interactions between membranes and a variety of membrane active biomolecules, small-molecules, and therapeutics. Drawbacks exist, however, with typical BLMs: the films formed are

anecdotally unstable and can be hard to work with for extended periods of time (in some cases for only a few minutes [59]; even recent BLM studies describe repeated failure and the need for reformation [181]). Further, many attempts to form BLMs using lipids with known phase transitions result in a high likelihood of membrane failure below the transition temperature (i.e., membranes in the "gel" phase). For these reasons, methods of quickly, easily, and repeatably forming stable lipid bilayers would serve as a preferred alternative to BLMs.

Droplet Interface Bilayers

Droplet interface bilayers, or DIBs, have been heavily pursued since their formal introduction around 2008. [77] DIBs are lipid bilayers that are formed at the interface between two aqueous droplets under oil. The main requirement, aside from placing aqueous droplets under oil, is that lipids are included in either the water or oil phase. The dissolved lipids begin to self-assemble at the oil-water interface surrounding an aqueous droplet placed into oil (see Figure 12A,B), and the droplets can be brought together after only a few minutes without coalescing and becoming one single droplet. Instead, the opposing monolayers on two adjacent droplets will spontaneously fuse and form a bimolecular layer of lipids (Figure 12A,B). The spontaneous formation of a lipid bilayer between droplets is driven both by a reduction in free energy of the system and the entropy driven exclusion [100] of solvent from the otherwise constraining acyl chains of the newly formed bilayer. The resulting interfacial film is stabilized by a balance of intermolecular forces (van der Waals, electrostatic, and steric interactions). [62] At equilibrium, the geometry of a DIB can be described by considering the surface tension of the monolayers (γ_m), the bilayer surface tension (γ_b), and the contact angle between them. The tensions and contact angle associated with a DIB are illustrated in Chapter 3 in Figure 17. A simple force balance yields the fact that $\gamma_b = 2\gamma_m \cos\theta$ which is a well-known relationship closely related to the Young-Dupre equation [43, 100-102, 182]. The reduction in Gibbs free energy mentioned above is also called the adhesion energy or free energy of formation (ΔF), and it can be calculated using the monolayer tension and the contact angle by

$$\Delta F = 2\gamma_m(\cos\theta - 1). \qquad \text{Equation 2}$$

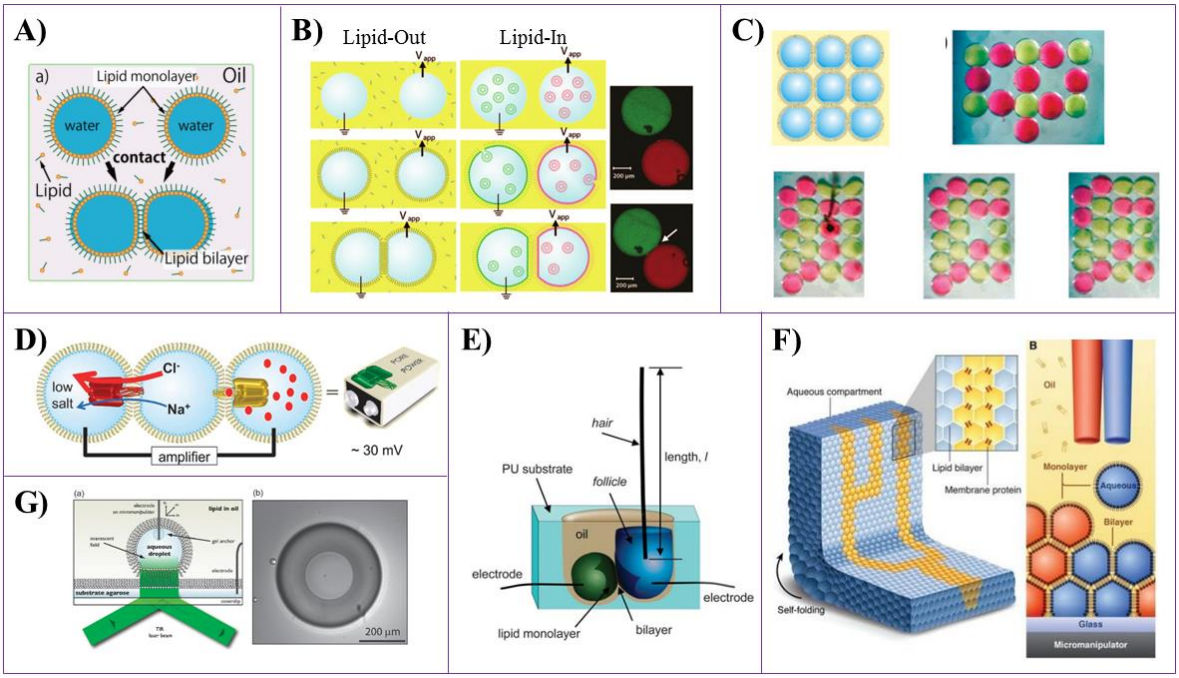

Figure 12. Droplet interface bilayers (DIBs). Images reproduced from previous works; refer to the text for appropriate citations.

The resulting ~3-5 nm thick [49, 50] lipid bilayer is an experimentally accessible model for cell membranes. Importantly, DIBs are formed quickly and easily using very low amounts of materials (i.e. on the order of µL of oil and water, only a few µg of lipid per trial) and are inherently more stable than traditional BLMs.

Methods for DIB formation provide the ability to control symmetry of biomolecules, salt concentration, pH, or other factors included on each side of the lipid bilayer (Figure 12B). [12] Multiple droplets can be connected in series or in parallel (Figure 12C) to create networks of droplets stabilized by lipid bilayers, [71] and this approach can be applied to create bioinspired devices using droplet networks and the collective functionality from embedded proteins and biomolecules. For instance, DIBs have been used to construct biobatteries that convert chemical energy into electrical energy (Figure 12D), [71] hair-cell inspired vibration sensors and energy harvesters (Figure 12E), [19] and recently even in the fabrication of tissue-like materials from a custom 3D droplet printing system (Figure 12F). [84] Another useful configuration is the droplet-

hydrogel-bilayer, or DHB, which allows formation of a bilayer directly over the objective of a microscope (Figure 12G). [183] The membrane formed with a DIB is capable of reconstituting proteins that form protein pores or channels, and in general there is a great deal of potential for the use of DIBs in studying and constructing biological systems. However, there are several obstacles that must be overcome before DIBs become the tool needed to recreate and study membrane and membrane-protein mediated processes. One such obstacle involves consideration of the lipid composition of the DIB and related important features of biological membranes.

Current practices for DIB formation are limited in their ability to create biologically relevant lipid bilayers as accurate models for studying membranes and membrane-protein interactions. However, it is theoretically possible to form DIBs using virtually any lipid or combination of lipids, and this capability would be particularly useful when attempting to recreate the complexity and heterogeneity found in the membranes of actual organisms and living cells. However, a clear majority of DIBs formed to date are formed using a single lipid, diphytanoyl phosphatidylcholine (DPhPC). Table 2 and Table 3 provide general and detailed reviews, respectively, of lipid selection in prior studies performed to date that involve either droplet interface bilayers (DIBs) or droplet hydrogel bilayers (DHBs).

There is a major gap between the lipid compositions found in real cell membranes and the lipid composition of typical DIBs. Considering the "lipid-in" approach required for asymmetric DIB formation, the lipid of choice from

Table 2. Summary of lipid usage in previous droplet supported bilayer studies. (Reproduced from [10])

Lipid Type	**Number of Published Papers**
DPhPC and DPhPC based mixtures	>55
Other lipid compositions	21
10:0 PG, SDS Span 80, other surfactant	4

Table 3. Detailed review of lipid selection in prior droplet-based bilayer studies. (Modified from [10])

Lipid Type	Lipid-In	Lipid-Out	Lipid Type	Lipid-In	Lipid-Out
DPhPC	H[11-43]; [55] M[62, 63] D[64-66] H:D[67] S:D [68] Hx[69]	H[12, 35-38, 41, 50, 64, 70-76] D[37, 66, 77-81] Sq[82]; D:Sq[83] So:H[41, 84] DD[85-87]; T[37]	DPhPC:DPPC, DPhPC: DSPC, other DPhPC mixtures	-	H[34, 37, 88] So:H[89] T,D[37]
DOPC	H[34, 90-94] So[91]	H[95]; D[85, 86] Sq[82]; So[91, 92] M[90]	Egg PC	-	D[79, 97-99] So:E[100]
DOPC:SM	-	H:So[96]			
DPPC	-	DD[87] M[90] So:C[101, 102]	Asolectin	-	D[78, 104-106]
			DPPC:cholesterol	M,So,Sq[103]	-
DMPC	-	M[90]	DOPG, DOPE, POPC, POPG, POPE mixtures	D[107]	H[37, 108] D[78, 104]; T,D[37]
Other/ Surfactants	-	D[62] DD[109]; Sq[110]; So:H[111]	Solvent abbreviations: H – hexadecane, D – decane, DD – dodecane, M – mineral oil, Sq - squalene, So – silicone oil, T – tetradecane, C - chloroform, E – ether, Hx – hexane, O – other		

Table 2 and Table 3 is almost unanimously DPhPC (and occasional fluorescently tagged lipids added to ~1% for visualization). One component of the gap

lies in the fact that the most commonly employed lipid for DIB studies, DPhPC, is a lipid of archaeal origin with very little relevance to studies of eukaryotic or prokaryotic processes. The physiological relevance of lipids in use is a major factor taken into consideration by biophysicists and scientists when designing experiments with bilayers, proteins, and other biomolecules. [184-188] As described above in Section 1.1.5, lipid composition potentially plays a key role in determining the dynamics and interactions of membrane and membrane-related phenomena. Moving forward, in order to create better model membranes that do not exclude the necessary diversity of species, asymmetry, and lateral organization that make cell membranes functional, there is a need for investigation of the ability to form DIBs using complex and physiologically relevant mixtures of lipids dissolved as liposomes in the aqueous phase. Further, there is a need for basic characterization, for instance of properties such as resistance, capacitance, specific capacitance, of droplet interface bilayers formed with increasingly physiologically relevant composition.

Droplet interface bilayers are not only useful for applications and for the study of membrane-protein interactions, but also for the characterization of membrane properties including osmotic permeability and electrical resistance and capacitance. Resistance and capacitance are more than just electrical properties: these quantities also reflect physical properties of the membrane as well. It should be noted that BLMs and DIBs both provide similar capabilities for measuring lipid bilayer resistance and capacitance. The ability to measure membrane resistance to water and ion transport provides a measure of membrane permeability. Permeability is an important quantity for biological membranes that must selectively block or allow the passage of specific solutes and solvents. Capacitance, as will be discussed in the following section, is dictated by the membrane hydrophobic region permittivity and thickness, thus means of measuring nominal capacitance provides a first step towards investigating properties and structure of the bilayer hydrophobic core.

1.2.2 Experimental Characterization of Planar Lipid Bilayers

Table 1 provides a summary of common methods used to form and characterize lipid bilayers including GUVs, sSLBs, SUVs, and LUVs. For the purposes of this review, the scope is narrowed to studies of planar lipid bilayers which provide electrical access to both sides of the membrane as

well as experimental control over the composition of each leaflet of the membrane. This section includes a description and review of the electrical properties of planar lipid bilayers, common methods for measuring bilayer electrical properties, and also methods for determining specific capacitance and tensions with lipids bilayers.

Electrical Measurements to Characterize Membrane Structure

A number of techniques exist that have been used to characterize lipid bilayer structure and properties (neutrons, x-ray, anisotropy, permeability). However, this dissertation focuses largely on electrical measurements with planar bilayers which are advantageous due to the ability to directly access both sides of the membrane and measure electrical and physical properties.

The electrical behavior of a lipid bilayer can be most simply represented as a parallel RC circuit. Figure 13A shows the representative electrical circuit for a BLM droplet interface bilayer, here including the nominal membrane resistance (R) and capacitance (C) as well as the resistance of the electrodes inserted into each of the aqueous droplets (R_{es}). It should be noted that the electrical properties of the lipid bilayer, R and C, represent physical aspects of the structure of the membrane. For instance, membrane resistance represents the portion of the membrane that acts as a barrier to ion transport. Alternatively, membrane capacitance stems from the layered structure of the membrane and the dielectric hydrophobic region which provides a means of storing charge or generating and propagating capacitive signals.

The complex impedance of a BLM or DIB, $Z_M(\omega)$, has been derived elsewhere and is given by: [2]

$$Z_M(\omega) = \frac{R}{1 + j\omega RC} + R_{es}. \qquad \text{Equation 3}$$

Equation 3 yields an impedance spectrum such as that shown in Figure 13B (here assuming R = 10 GΩ, C = 100 pF, R_{es} = 10k Ω). The circuit is comprised of three basic elements (electrode-electrolyte resistnace, membrane resistance, and membrane capacitance), and current through the membrane is frequency dependent whereby current follows the path of least resistance shown in Figure 13B. Application of zero-frequency dc voltage essentially leads to an open-circuit condition

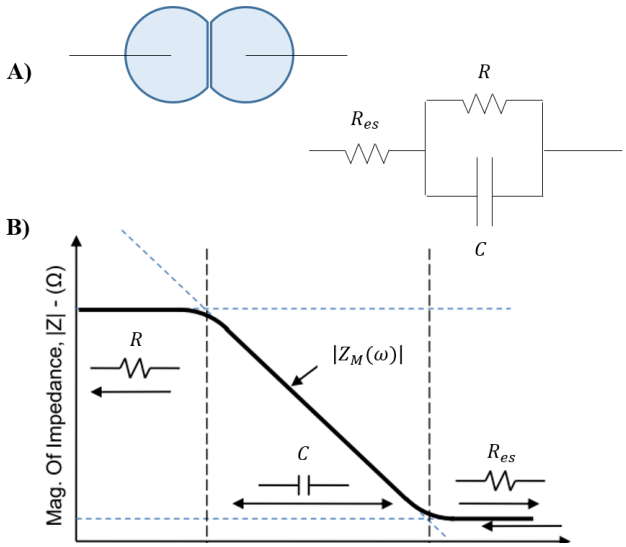

Figure 13. A) A DIB and its equivalent electrical circuit. B) The complex frequency dependent impedance of bilayers (DIBs or BLMs alike) based on the electrical circuit shown in (A). (Modified from [2]).

for the path involving membrane capacitance; dc current passes through the electrodes, the electrolyte, and the resistive portion of the membrane. Given that bilayer resistance, often on the order of gigaohms, is significantly higher than that of the electrode-electrolyte resistance (typically, $R_{es} \leq 10$ kΩ), current is determined via Ohm's law and the membrane resistance when applying dc voltage ($I=V/R$). Slightly more complex behavior emerges upon application of ac voltage signals, however, as a lower frequency exists at which current through the membrane begins to be dictated by the capacitance. This lower corner frequency (f_1 on Figure 13B) is the frequency at which the impedance of the membrane capacitance begins to fall below that of the membrane resistance. A common technique for measuring membrane capacitance involves application of an alternating triangle wave of constant amplitude (A_V) and frequency (f_V), and it can be shown that the membrane capacitance (C) results in square wave current amplitude (I_{sw}) given by

$$I_{SW} = 4A_V f_V C \,. \qquad \text{Equation 4}$$

As the frequency of the input ac voltage waveform is continually increased, the impedance of the membrane capacitance drops below that of the resistance at the electrode-electrolyte interface. At frequencies above this upper corner frequency (f_2 on Figure 13B), the impedance of the bilayer

remains constant at $Z_{BLM} = R_{es}$. In combination, the frequency-dependent impedance of the bilayer follows the path of the bold line drawn in Figure 13B. Knowledge of the electrical response of the bilayer proves to be useful in allowing precise measurements of the membrane resistance and the membrane capacitance by applying ac input voltages of an appropriate frequency. Refer to Chapter 2 for additional details and examples regarding how these types of measurements are performed in this dissertation.

Membrane Specific Capacitance

The ability to measure membrane resistance and capacitance is a useful tool when characterizing lipid bilayers, however, it is possible to gain additional insight my measuring the membrane specific capacitance. Unlike nominal membrane resistance and capacitance, which depend on the area of the membrane being tested, specific capacitance is an intrinsic property that depends only on the dielectric permittivity and thickness of hydrophobic core of the lipid bilayer. Specific capacitance could be expected to change with changes in the temperature or the composition of the membrane. Specific capacitance is applicable to the study of membranes via the treatment of a lipid bilayer as a parallel plate capacitor. Indeed, a lipid bilayer consists of a hydrophobic non-conductive layer (the lipid acyl chains) sandwiched between two opposing conductive layers (the lipid headgroups). Following convention for a parallel-plate capacitor, specific capacitance of the membrane (C_M), can be written as

$$C_M = \frac{C}{A_M}, \qquad \text{Equation 5}$$

or alternatively as

$$C_M = \frac{\varepsilon_r \varepsilon_0}{d_{HC}}, \qquad \text{Equation 6}$$

where ε_r represents the dielectric constant for the insulating hydrophobic region of the bilayer, ε_0 represents the dielectric permittivity of vacuum, and d_{HC} (sometimes also referred to as D_C in this dissertation) represents the thickness of the bilayer hydrophobic region. It is quite common to assume that the dielectric permittivity of the bilayer hydrophobic region, largely a mixtures of hydrocarbon lipid acyl chains, is similar to that of pure hydrocarbon (ε_r = 2.2). The dielectric

permittivity of vacuum is simply ε_0 =8.85x10^{-12} F/m. From Equation 6, it is clear that the ability to measure C_M for a lipid bilayer provides a means of directly measuring the thickness of the bilayer hydrophobic region. This was of particular interest in the early to mid-20th century when scientists were still working to understand the structure and physical properties of real and artificial cell membranes. As discussed below, numerous efforts have been made to measure specific capacitance of real cell membranes, as well as lipid bilayers through the use of BLMs and, more recently, DHBs.

Some of the earliest measurements of membrane specific capacitance were made almost 100 years ago using the real membranes of giant squid axons, but the advent of methods for forming BLMs led to a sharp increase in the amount of information available regarding the specific capacitance of lipid bilayers. Curtis and Cole were able to obtain an estimate of around 1 μF/cm^2 in 1938 by measuring the capacitance and area of the membrane of giant squid axons. [189] The large workable samples of such axons enabled relatively accurate estimation of membrane area while capacitance was measured directly via electrical measurements. Hodgkin and Huxley performed similar measurements on giant squid axons in 1952 as part of their work that was recognized in 1963 by the awarding of the Nobel Prize in Physiology and Medicine. [190] Mueller and Rudin provided initial estimates of C_M between 0.7-1.5 μF/cm^2 when they first formed BLMs in 1962. [53, 54] Shortly thereafter in 1965, Hanai and Haydon utilized measured capacitance and area of BLMs formed from lecithin, a mixture of lipids containing phospatidylcholine headgroups and mixed saturated and unsatured acyl chains. [191] Hanai and Haydon used an estimate for the bilayer hydrophobic region dielectric constant (2.05) to obtain the first C_M-based measurement of the thickness of lipid bilayers. The observed range of C_M values between 0.38-0.40 μF/cm^2 correspond to hydrophobic region thicknesses of 45-49 Å. Over the next ten years or more, a number of researchers performed C_M measurements with BLMs formed from a variety of different lipid types and under a number of environmental conditions (i.e. varying pH, temperature, salt concentration). [8, 46, 192-205] As research into the specific capacitance of BLMs emerged, typical C_M values fell between 0.3-1.0 μF/cm^2, thus the original estimates of Mueller et al., Hanai and Haydon, and even Curtis and Cole and Hodgkin and Huxley, were fairly accurate.

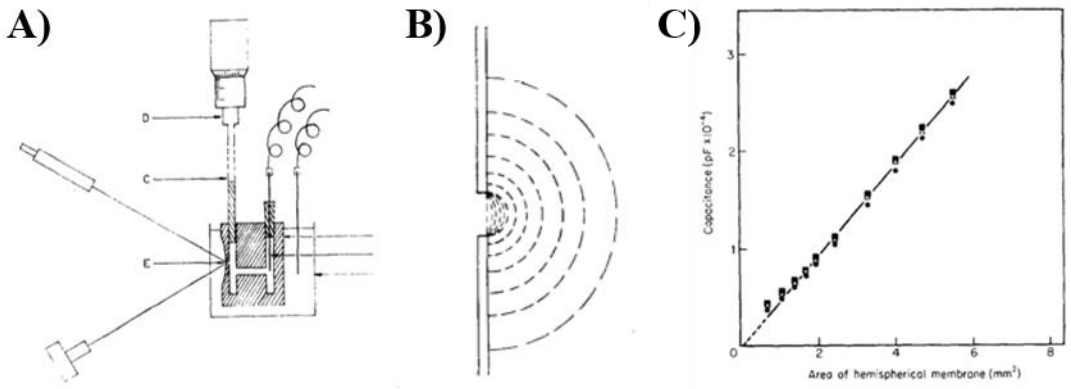

Figure 14. A) The setup of Hanai and Haydon (1965) for using hydrostatic pressure to "bulge" a BLM and vary its area while measuring capacitance. B) Illustration of a "bulged" BLM at varying area. C) Measured capacitance versus area for different steps in the "bulging" process shown in (B). (Reproduced from [46]).

One of the earliest experiments to measure specific capacitance with BLMs, a study performed by Hanai and Haydon in 1965, helped validate the relationship between the specific capacitance, capacitance, and area of lipid bilayers. [46] The experiment involved "painting" a Mueller-Rudin stlye BLM over a small aperture in a solid Teflon support, and the apparatus used included a means of applying asymmetry hydrostatic pressure across the membrane. Figure 14A shows the original diagram of the apparatus used in the experiment, and Figure 14B illustrates the effect of increasing hydrostatic pressure across the BLM; increasing pressure leads to an increase in the area of the lipid bilayer which essentially acts like a bubble being inflated or "blown up". By measuring electrical capacitance and membrane area at each step in pressure, Hanai and Haydon demonstrated the linearity of the relationship between lipid bilayer capacitance and its area (Figure 14C). Not only did their approach enable accurate determination of C_M by obtaining multiple capacitance-area data points, the established relationship between C_M and area enabled future estimation of membrane area (A_M) in cases when only the capacitance was measured (i.e., $A_M=C/C_M$, provided a value of C_M is known).

Despite the use of BLMs in a number of specific capacitance studies, as described above, the BLM technique is considered to a tedious and fragile platform for forming lipid bilayers. Further, the

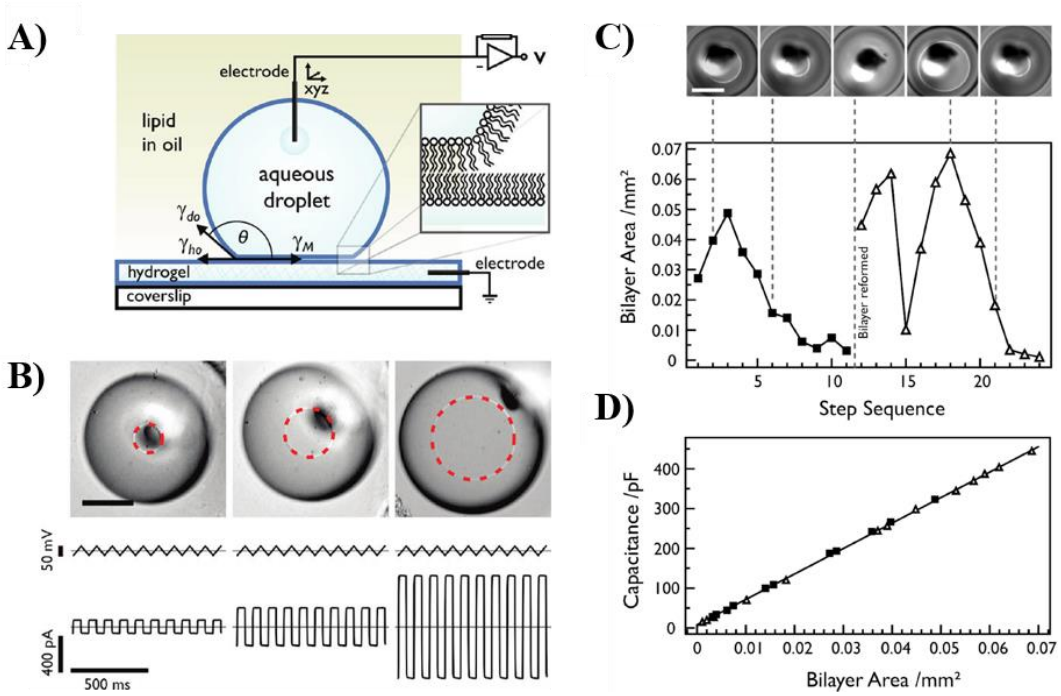

Figure 15. A) An illustration of the droplet hydrogel bilayer (DHB.) method. B) Actual images of a DHB at varying areas along with the applied triangle wave voltage and measured square wave current. The square wave current amplitude is proportional to capacitance. C) Images and corresponding measured bilayer area for a sequence of steps in which area is changed by pulling or pushing the droplet up or down (via mechanical manipulation of the electrode). D) Measured capacitance at each step potted versus the area measured at that step. The slope of the linear fit shown represents the membrane specific capacitance, or C_M. (Reproduced from [50]).

use of the opaque hydrophobic supports creates challenges for tracking the bilayer area in experiments not employing the "bulging" approach of Hanai and Haydon. Alternatively, DIBs present a means of forming robust, long-lasting lipid bilayers quickly and easily using relatively small experimental setups. Following this logic, Linda Gross and Mark Wallace recently investigated and established the ability to measure membrane specific capacitance using a variation of the DIB method for lipid bilayer formation. Instead of using two droplets, a single droplet is lowered onto a flat hydrated aqueous gel submerged in oil. Lipids can be placed in either phase, and provided the conditions are favorable for adequate lipid monolayer formation at the oil-water interface of the droplet and the hydrogel, a lipid bilayer is formed between the upper droplet and the lower planar hydrogel surface. The Droplet Hydrogel Bilayer (DHB) approach is illustrated in Figure 15A, and a series of actual images from a single DHB are shown in Figure 15B. In a process similar to that used by Hanai and Haydon in 1965, Gross et al. describe the

ability to mechanically tune the bilayer area, and thus capacitance, to obtain measurements of capacitance and area at a number of different areas. As opposed to using hydrostatic pressure to bulge a BLM, as in the case of Hanai and Haydon, Gross and Wallace simply move the electrode holding the droplet above the hydrated gel. Figure 15C shows additional images of a DHB and corresponding sequentially obtained values of the measured bilayer area. Figure 15D displays measured capacitance versus area throughout the trial, and as in the case of Hanai and Haydon, the capacitance-area curve is well approximated by a linear least squares regression. The slope of the linear fit in Figure 15D is the specific capacitance, and the ability to quickly and repeatedly form droplet-based bilayers enables relatively high-throughput measurements of lipid bilayer C_M.

Gross et al. describe a convenient and straightforward method of determining C_M and bilayer thickness, and in its entirety, the experiments for measuring C_M with a DHB can be conducted in a matter of minutes. One drawback to this method involve the requirement for manual analysis of each image to estimate the bilayer area; the manual analysis is both subjective and time-consuming which may be prohibitive in the context of high-throughput screening or studies of membrane specific capacitance. An additional challenge is presented by the fact that contact angle is not directly viewable with DHBs, and the angle can be useful in the determination of free energy of bilayer formation (adhesion energy) and even for the measurement of bilayer surface tensions (see Chapters 3-4).

Effects of Temperature on Planar Lipid Bilayer Specific Capacitance

The well-known thermotropic properties of lipids, similar to other liquid crystals, demand that attention be given to how the properties of the membrane are affected by temperature. Early measurements made by Stephen White demonstrated the ability to detect change in C_M, and thus bilayer thickness, at the expected T_m using BLMs formed from glycerolmonoleate (GMO). Figure 16 shows the results from White;s experiments cooling and heating GMO BLMs formed using tetradecane as the oil phase. C_M for the GMO bilayer generally increases with decreasing temperature, however a non-monotonic transition is observed around 16-18°C which is the expected T_m for GMO. Decreasing Cm would be caused by an increase in bilayer thickness, a result expected for a cooling induced transition from the fluid phase to the solid phase, assuming constant

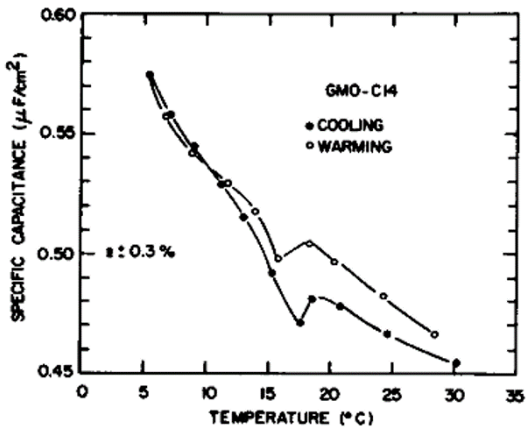

Figure 16. Specific capacitance of GMO BLMs (formed using C14 tetradecane as the nonpolar solvent) as a function of temperature. (Repreoduced from [8]).

dielectric permittivity (see Equation 6). A more recent report by Velikonja et al. [181] shows how the C_M values for painted DPPC BLMs undergo and increase at the pretransition (39°C < T < 42°C) and again at the main transition (T > 42°C). The results of Velikonja et al. further support White's conclusions that C_M measurements are capable of detecting changes in lipid bilayer thickness associated with thermotropic phase transitions.

A significant gap exists between the composition of real cell membranes and the single-component lipid bilayers used for the C_M studies of White and Velikonja et al. In light of their works, one looming question remains: how might measurements of the temperature dependence of C_M, now established as a quantitative method capable of detecting lipid phase transitions, vary when testing lipid bilayers formed using complex, multi-component, physiologically relevant mixtures of lipids? It is especially interesting to consider how C_M would change upon heating and cooling in membranes containing large fractions of cholesterol or sufficient heterogeneity to abolish the enthalpy changes associated with thermotropic phase transitions when tested via DSC. More directly, since C_M is inversely related to bilayer thickness which is known to change at T_m, C_M measurements may enable detection of phase transitions that occur in membranes possessing physiologically relevant compositional heterogeneity with different sensitivity than DSC. This

could be an important finding given that DSC of complex lipid mixtures might otherwise suggest there is no such phase transition.

Effects of Temperature on Droplet Interface Bilayers

There are only a few reports performed DIB studies performed at physiological temperature (37°C) or any temperature other than room temperature. Of the 80 publications included in Table 2 and 3, only three include studies of DIBs at temperatures other than room temperature. [62, 89, 90] As a result, there is little knowledge of the effects of heating and cooling on DIBs and DIB-protein interactions. Further, bilayers formed from saturated lipids are all reported to rupture while changing temperature for all three cases. Since membranes in nature do not simply rupture upon changes in environmental temperature, there must be mechanisms at play to allow organisms that ability to withstand temperature changes. Temperature is an important factor for lipid bilayers owing to the thermotropic phase behavior of lipids themselves. At high temperature or low packing density, lipids exist in an expanded liquid state. Conversely, the bilayer phase transitions to a solid phase as temperature drops. Actual cells regulate their lipid composition in response to the environmental temperature, and other factors, in order to maintain appropriate membrane fluidity. [206-209] Changes in lipid phase and composition are known to affect the behavior of membrane-proteins, [184-188] and the mechanisms involved could feasibly be studied with DIBs provided the ability to control temperature.

Lipid Bilayer Surface Tension

Cell membranes are soft materials that play critical roles in physiological processes both by acting as selectively permeable barriers and by providing a two-dimensional, liquid crystalline bilayer in which transmembrane proteins are anchored. The membrane is involved in physiological processes ranging from homeostasis to vesicle trafficking and many other forms of cellular signaling. For these reasons, methods to quantify physical properties of membranes provide direct insight into how their structures impact their functions.

Further, there is increasing evidence that biomacromolecules [210-212], cell-penetrating peptides [213, 214] and nanoparticles [48, 215, 216], and other small molecules such as anesthetics or drugs

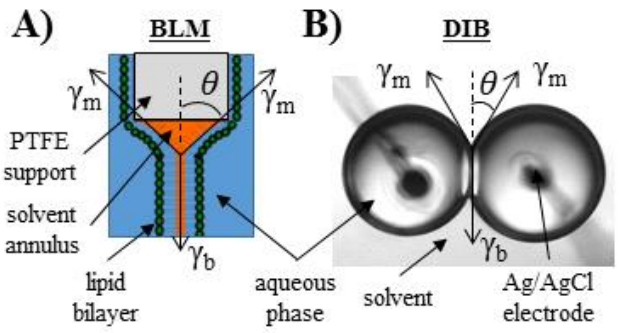

Figure 17. Common model membranes include the black lipid membrane (A) and the droplet interface bilayer (B). In both cases, the tension of the lipid bilayer that forms is in equilibrium with the vertical sum of the two opposing monolayer tensions.

[217-220] affect the packing and conformations of lipids in the membrane. For example, the bulk hydrophobic region of cholesterol is known to affect the structural order and fluidity of phospholipid bilayers by interdigitating between the acyl chains of neighboring lipids.[221-225] And because the interactions between lipid bilayers and cholesterol, transmembrane proteins, and membrane active pharmaceuticals can alter the tension of the membrane, methods for quantifying membrane tension can be applied to study the uptake and accumulation of a variety of important species into lipid bilayers. [210]

Motivated by many of the same reasons described above, scientific literature has produced several methods for measuring tension in synthetic model membranes known as lipid bilayers or black lipid membranes (BLM). [226-228] In many of these studies, the lipid bilayer was formed by spreading a lipid-oil mixture across a small aperture in a hydrophobic solid support submerged in water.[226, 228] As illustrated in Figure 17A, the suspended BLM consists of the thinned bilayer region of the painted film, which is stabilized at its perimeter by an annulus of excess solvent. Figure 17B also shows a DIB which is very similar to a BLM. In both cases, it is well known that the bilayer region and the annulus reach mechanical equilibrium through a balance of surface tensions, obeying Young's equation [86, 90, 102, 110]:

$$\gamma_b = 2\gamma_m \cos\theta. \qquad \text{Equation 7}$$

Specifically, the interfacial bilayer tension (γ_b) is balanced by the two lipid monolayer tensions (γ_m) at the annulus-water interface oriented away from the plane of the membrane by the contact

angle (θ). Knowledge of the contact angle and monolayer tension allows for direct calculation of bilayer tension, via the Young equation, as well as the specific free energy of bilayer adhesion via Equation 2 (also known as free energy of formation, ΔF) [63, 90, 102, 110, 226] Given a number of established methods for measuring monolayer tension (e.g. drop volume, pendant drop, Wilhelmy plate, etc.), the most difficult aspect of determining bilayer tension in a suspended BLM is obtaining an accurate measurement of the contact angle at the annulus.

Requena, Needham, and Haydon [226, 228] pioneered specialized techniques to measure the contact angle of suspended BLMs such that they could combine them with monolayer tension values obtained from separate drop volume experiments to calculate the interfacial tensions of glycerol monooleate and phospholipid bilayers. Via their technique, BLM contact angle measurements are made after introducing a lens of excess solvent into thinned lipid bilayer. Requena and Haydon's measurements of contact angle relied on imaging the concentric fringe patterns (visible rings created by constructive and destructive interference) cast by transmitted light passing through the solvent lens, [228] while Needham and Haydon imaged the lens directly to compute θ from the geometric relationship between the radius and volume of the lens. [226] In both cases, bilayer tension was computed using Young's equation by combining contact angles measured *in situ* with monolayer tension values obtained *a priori* via the drop-volume method. The approach is sufficiently quantitative, however, separate equipment and multiple experiments are required to determine monolayer and bilayer tensions. A method that provides simultaneous access to both monolayer tension and contact angle would thus enable *in situ* measurement of lipid bilayer tension and determination of free energy of formation.

Petelska, et al presented a different approach for measuring BLM tension, which they used to study the effects of cholesterol, [210, 229] charged lipids, [211] pH, [227] and the presence of amino acids on the tension state in membranes. [227] Petelska's method of bilayer tension measurement involves forming a planar bilayer and applying a differential hydrostatic pressure across the membrane, such that the Young-Laplace equation ($\Delta P = 2\gamma_b/R$) could be used to determine bilayer tension from the radius of curvature of the bulging bilayer (similar to the illustration in Figure 14B). [227] The Young-Laplace equation relates the pressure differential to the radius and

tension of the bilayer only. Thus, one drawback of this technique is that it does not allow for direct determination of contact angle, monolayer tension, or free energy of formation.

1.3 Gaps, Goals, and Research Plan

1.3.1 Scientific Gaps

The literature review provided thus far identifies several gaps in our understanding and knowledge of model membranes:

- Gap 1. There is a lack of knowledge of the partitioning and interaction of small-molecules into lipid bilayers in cases where the molecules interact with the membrane in a manner that does not form pores or otherwise exert measurable changes in membrane conductance (and thus measured current).
- Gap 2. Typical "lipid-in" DIBs are formed using liposomes containing a single lipid type, thus it is unclear whether or not it is possible to use complex multi-component lipid mixtures to form DIBs.
- Gap 3. Little is known regarding the specific effects, and possible temperature-dependence, of compositional heterogeneity on planar lipid bilayer resistance, specific capacitance, breakdown voltage, equilibrium surface tensions of the monolayers and the bilayer, and the interaction of membrane proteins or peptides.

1.3.2 Research Objectives

- Objective 1 (*addressing Gap 1)*. Develop new methods to directly measure physical properties of DIBs beyond resistance/conductance including specific capacitance (thus bilayer hydrophobic thickness) and monolayer and bilayer surface tensions (a measure of lipid packing and order).
- Objective 2 (*addressing Gap 1*). Apply and validate measurement capability of the method developed in Objective 1 by characterizing the effects of non-permeabilizing cholesterol and nonpolar solvent molecules, as well as mixed-monolayer protected cell-penetrating

nanoparticles, on DIB specific capacitance, thickness, equilibrium surface tensions, and lipid packing and order in the monolayers and bilayer.

- Objective 3 (*addressing Gap 2)*. Explore DIB formation methods using aqueous liposome solutions containing multi-component lipid mixtures and native cellular lipid extracts.
- Objective 4 (*addressing Gap 3)*. Apply methods and knowledge established via Objective 2 to study the effects of increasing compositional heterogeneity on DIB resistance, specific capacitance (thickness), monolayer and bilayer tensions (packing and order), and also the interactions of membrane-active peptides.
- Objective 5 (*addressing Gap 3).* Investigate temperature dependence of DIB resistance, specific capacitance, surface tensions, and membrane-active peptide interactions in simple and complex multicomponent DIBs.

CHAPTER 2

EXPERIMENTAL METHODS AND DATA ANALYSIS

This chapter describes experimental methods, as well as methods used in the analysis of data, that are generally applied throughout the work described in this dissertation.

2.1 Droplet Interface Bilayer Formation and Experimental Setups

2.1.1 Common Materials

Phospholipids were obtained in powder form from Avanti Polar Lipids (Alabaster, AL) and stored at -20°C until further use: DPhPC (1,2-diphytanoyl-*sn*-glycero-3-phosphocholine), DMPC (1,2-dimyristoyl-*sn*-glycero-3-phosphocholine), DPPC (1,2-dipalmitoyl-*sn*-glycero-3-phosphocholine), DSPC (1,2-distearoyl-*sn*-glycero-3-phosphocholine), DOPC (1,2-dioleoyl-*sn*-glycero-3-phosphocholine), POPC (1-palmitoyl-2-oleoyl-*sn*-glycero-3-phosphocholine), eTLE (*E. coli* total lipid extract), bTLE (brain total lipid extract, porcine), and cholesterol (ovine wool, >98%). Cholesterol used in GUV experiments was obtained from Nu Chek Prep (Elysian, NY). Fluorescent dyes: BoDIPY-PC (2-(4,4-difluoro-5,7-dimethyl-4-bora-3a,4a-diaza-s-indacene3-pentanoyl)-1-hexadecanoyl-sn-glycero-3-phosphocholine) and Fast DiI (1,1’-dilinoleyl-3,3,3’,3’-tetramethylindocarbocyanine perchlorate) were acquired from Invitrogen (Carlsbad, CA), C12:0-DiI (1,1’-didodecyl-3,3,3’,3’-tetramethylindocarbocyanine perchlorate) was purchased from Thermo Fisher Scientific (Waltham, MA), and naphtho[2,3a-]pyrene and DHE (Ergosta-5,7,9(11),22-tetraen3β-ol) was purchased from Sigma Aldrich (St. Louis, MO). Extracts of total

lipids carry a recommended 3 month shelf life, thus bTLE is used within 3 months after which a new lot is acquired. Alamethicin (Alm) from *Trichoderma viride* is obtained in powder form from A.G. Scientific (San Diego, CA).

Sodium chloride (NaCl), sodium hydroxide (NaOH), 2-(N-morpholino)propanesulfonic acid (MOPS), decane, hexadecane, AR 20 silicone oil (product number 10836), agarose (A9539), lidocaine hydrochloride (2% for injection), promethazine, isopropanol, ethanol, acetone, and chloroform are obtained from Sigma Aldrich. Unless indicated otherwise, aqueous buffer includes 10 mM MOPS, 100mM NaCl, and is buffered to pH 7.4 using NaOH. Solution pH is verified using a Fisher Scientific Accumet AP85 pH probe. Water used in the preparation of aqueous solutions is filtered to resistivity of at least 18MΩ*cm_2 via a Millipore Synergy water purification system.

Electrodes are fabricated using general purpose 22 gauge wire and either 125 μm silver wire from Goodfellow or 50 μm silver wool from Sigma Aldrich. As described in Section 2.1.3 below, larger diameter silver wire is used for tests involving the Regulated Attachment Method while smaller diameter silver wool is used when forming DIBs between droplets suspended on ball-ended, agarose-coated electrodes. Male D sub connector pins, used for connecting to the Axopatch headstage, are acquired from Newark element 14 (Chicago, IL).

2.1.2 Preparation of Stock Solutions of Liposome and Proteins

DIB formation involves the use of droplets from aqueous solutions containing large unilamellar vesicles (LUVs). Lipids and cholesterol are obtained in powder form from Avanti Polar Lipids. Unless stated otherwise, lipids are dissolved to a concentration of 2 mg/mL in aqueous buffer to create stock solutions of multilamellar vesicles (MLVs). When dissolving lipids with a T_m above room temperature, the buffer is first preheated to a temperature above the lipid T_m. Fresh MLV solutions are vigorously vortexed, aliquoted, and frozen at -20°C until further use. After a total of five cycles of freezing and thawing, aliquots of MLV stock solutions are extruded (T&T Scientific 100 nm LipX Extruder, or an Avanti MiniExtruder with Whatman 100 nm polycarbonate filters) or sonicated (Branson bath-style Sonicator) to create LUV solutions used in DIB experiments.

Freezing and thawing specifically helps reduce the degree of lamellarity of MLVs prior to extrusion [230, 231]. LUV suspensions are stored at 4°C and used within 2 weeks.

Solutions containing lipids and cholesterol are processed using a slight variation of the method just described. Lipids and cholesterol are obtained separately, and each is dissolved at a concentration in chloroform to create separate lipid and cholesterol stock solutions. Typical chloroform stock solution concentrations are 5mg of lipid per 1 mL of chloroform. When creating mixtures of lipids and mixtures of lipid and cholesterol, appropriate amounts from each chloroform stock are combined in a small vial, and the chloroform is removed by at least 2 hours of vacuum to obtain a dry mixed-lipid film. This film is rehydrated, frozen and thawed five times, and then sonicated until the solution becomes clear. Sonication is preferred over extrusion with cholesterol containing solutions to ensure cholesterol concentrations are not affected through the extrusion process (i.e. by filtration on the polycarbonate membrane). Sonication is also preferred over extrusion when forming unilamellar liposomes from with pure DPPC samples. As described elsewhere, [232] sonication for several hours above the transition temperature of DPPC (T_m = 42°C) yields stable suspensions of small unilamellar liposomes. In comparison, extrusion yields unstable solutions of liposomes that fuse and precipitate out over time if the solution is stored below T_m. Solutions containing cholesterol or DPPC are checked for optical clarity before testing and re-sonicated to clarity if there is any evidence of demixing.

Alamethicin, an antimicrobial peptide from *Trichoderma viride* is used extensively herein. Before mixing peptide with lipids or liposomes, the powdered form of the peptide is dissolved in ethanol at a concentration of 2.5 mg/mL to create an organic stock solution that is stored at -20°C. For DIB testing with Alm, the frozen peptide stock is thawed and diluted to 25 µg/mL (0.25% ethanol remaining) with buffer before adding it to 2 mg/mL unilamellar liposomes to achieve the desired final Alm concentration. This approach minimizes dilution of the liposomes while ensuring adequate dilution of the original ethanol solvent. Separately, for circular dichroism (CD) testing, alamethicin stock and liposome solutions are diluted and combined to create samples with 500 µg/mL lipid and 50 µg/mL Alm (peptide:lipid ratio ~1:46). All peptide/lipid stock solutions are stored at 4°C and used within 2 weeks.

2.1.3 Droplet Interface Bilayer Formation

DIBs are formed primarily using one of two approaches in our work, and both techniques rely on basic self-assembly of lipids at the interface of water droplets placed in oil. Typically, the experiments herein are conducted using the lipid-in approach (lipids dissolved in the water phase as opposed to the oil phase). Figure 18 shows a representation of the two approaches used; 1) the Regulated Attachment Method[17] (RAM) and 2) the suspended droplet method with droplets pipetted onto agarose-coated ball-ended electrodes submerged in oil. Micromanipulators are used either to control compression of the RAM and resulting droplet contact, or to hold and position the gel-coated electrodes. Electrodes used with the RAM are typically 125 μm and do not need a ball-end or agarose. The hanging drop approach utilizes smaller, 50 μm diameter wire to help minimize the effects of the electrode on droplet shape. 50 μm electrodes are held briefly over a flame to create a ball end before chloriding the electrodes with bleach and dipping them in molten agarose to acquire the gel-coat. In either the RAM or suspended droplet methods, 200-800 nL droplets of aqueous solution are pipetted into the oil, several minutes are allowed for monolayer formation, and then droplets are either allowed to come into contact (RAM) or moved into contact (suspended droplets). Droplets are created manually by pipetting them directly into oil-filled PDMS substrates. Droplets are pipetted directly into the compartments when using the RAM substrate, and they are pipetted onto the gel-coated electrodes tips in suspended droplet tests. Typically, 2-5 minutes are

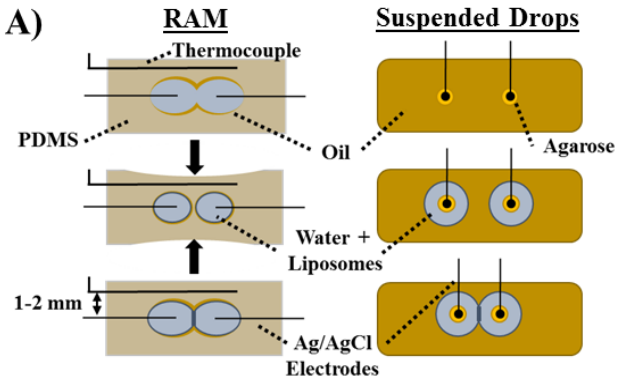

Figure 18. A) The two techniques used for DIB formation and tests described in this work are 1) the regulated attachment method (RAM, left) or 2) droplets suspended on gel-coated electrode tips ("suspended droplets", right). (Modified from [10]).

allowed for sufficient lipid monolayer formation before bringing droplets into contact for DIB formation. Subsequent bilayer formation, as well as any peptide insertion or gating, is monitored using electrical measurements as described in Section 2.2.

2.1.4 Fabrication of PDMS Substrates and Electrodes

Flexible elastomeric and hydrophobic substrates are constructed using Sylgard 184 poly(dimethylsiloxane) (PDMS) acquired from Dow-Corning (Midland, MI) as described previously[10, 17, 49]. Briefly, double-molding techniques are used to fabricate desired PDMS substrate geometries: a negative of the desired substrate shape is machined in acrylic to form a template, two-part polyurethane (PU; ClearFlex 50 from Smooth-On Inc.) is cast into the negative template, and then the PU negative is removed and placed in a separate machined acrylic template defining the final outer geometry of the PDMS substrate. The use of PU helps ensure that the negative does not crosslink or bond to the PDMS which allows for straightforward removal of the negative after the PDMS is cured. Once the negative is removed, the cured PDMS substrates are trimmed as needed (to remove flash and excess material that may absorb alkane solvent in later testing), cleaned with mild soap and water, and rinsed thoroughly with DI water before use.

Electrodes used in the tests herein, including both RAM and suspended droplet style experiments, are prepared using a similar process. In either case, a 10-20 cm long section of 22 gauge wire is taken from the stock spool of wire. The insulation is removed from each end of the wire to expose approximately 1-2 cm of the metal core at each end. A metal male D sub pin is soldered onto one of the exposed ends of the wire. The other end of the wire is attached to either 125 μm silver wire by soldering, or to 50 μm silver wool using conductive silver paint (Ted Pella, Inc., Redding, CA). For both types of electrodes, the silver wire attached is trimmed to leave approximately 2 cm of free wire. The silver wire is then submerged in bleach for at least one hour to obtain a silver/silver-chloride (Ag/AgCl) coating. It should be noted that in experiments with ball-ended 50 μm electrode tips, the wire is briefly held over a flame to create the ball-end *before* the electrodes are chloride in bleach. Further, the ball-ended, chlorided electrodes are often coated in a layer of agarose by dipping them approximately 10 times in molten agarose (melted and stirred on a hot-plate set to 140-160°C). After completing the steps described thus far, any exposed 22 gauge wire

and soldered or painted connections are covered with heat-shrink to protect and insulate the connections and to mitigate motion or vibration during DIB experiments.

2.2 Electrical Measurements to Monitor Bilayer Formation and Quantify Membrane Properties

2.2.1 Lipid Bilayers as RC Circuits: Membrane Resistance and Capacitance

The equivalent electrical circuit for a single lipid bilayer is a simple RC circuit. As illustrated and described in Section 1.2.2, the bilayer can be modeled as a resistor and a capacitor in parallel.

Electrical measurements are used to monitor the formation of a DIB between droplets suspended or impaled by Ag/AgCl electrodes. Specifically, current across the interface is measured using an Axopatch 200B patch clamp amplifier. As a DIB begins to form and approach equilibrium, capacitance of the interface also begins to increase and stabilize. Continuous application of a 10 mV, 10 Hz triangular voltage waveform results in a square current waveform whose amplitude is

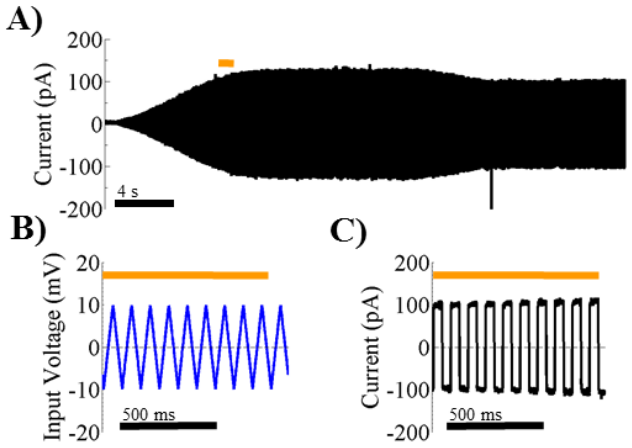

Figure 19. A) A typical current response during bilayer formation and subsequent adjustment of bilayer area before further characterization. The orange bar corresponds to the portion of the trace associated with (B) and (C). B) The triangular input voltage waveform with 10mV amplitude and frequency of 10Hz used to continually elicit bilayer capacitance while forming a DIB, or while adjusting or monitoring bilayer area. C) The actual current recorded in the region with the orange bar in (A). The "square" nature of the current waveform is a result of the bilayer capacitance, with the amplitude of the current waveform relating directly to the magnitude of bilayer capacitance and thus its area.

proportional to the area of the bilayer ($C=I/(4A_V f)$; C-capacitance, I-current, A_V-triangle waveform amplitude, f-input waveform frequency). Thus, square-wave measurements confirm bilayer formation and provide a measure of the bilayer area. Examples of the triangle wave and typical current response through a DIB are shown in Figure 19. The capacitive current amplitude is proportional to bilayer area and is monitored in real-time while adjusting substrate compression (RAM) or droplet positioning (droplets suspended on electrodes) to achieve a desired bilayer area (Figure 19). Bilayer area (A) can be computed using a known value for the membrane specific capacitance (C_M) and the fact that $A=C/C_M$.

2.2.2 DC Voltage Step Routines for Measuring Rupture Potential and Resistance

Membrane resistance and rupture potential are measured to assess the sealing quality of the membrane and the threshold for electroporation. [10] Resistance is determined by measuring current for 15-30 seconds at various DC voltages, for instance from -150mV to 150 mV in 25 mV increments.[10] Plotting average current at each voltage step as a function of voltage provides access to membrane conductance through Ohm's Law: $I/V=G=1/R$, where I-average current, V-applied DC voltage, G-membrane conductance, R-membrane resistance. The slope of a linear fit of the I-V curve is thus the inverse of the membrane resistance. An automated DC step voltage routine is used to perform tests for rupture potential in a repeatable fashion, typically increasing the applied holding potential by 12.5 mV every 15 seconds until the membrane ruptures and droplets coalesce. The potential at which the membrane ruptures is taken as the rupture potential, or V_{rup}.

With a DIB formed, bilayer resistance is characterized by applying a DC step voltage routine that consists of a positive (increasing) and negative (decreasing) voltage step scan (Figure 20A,C). The input voltage waveforms are generated using a custom LabVIEW routine, which allows control of the step size (mV), duration (sec), and maximum voltage (mV) applied to the membrane. For DC step tests employed to obtain bilayer resistance, voltage is typically adjusted in 12.5 mV increments from 0 to 100 mV (or -100 mV for the decreasing sweep) with 10-15 seconds of holding time at each step. Pursuing the ohmic resistance of the bilayer, average current at each DC step is

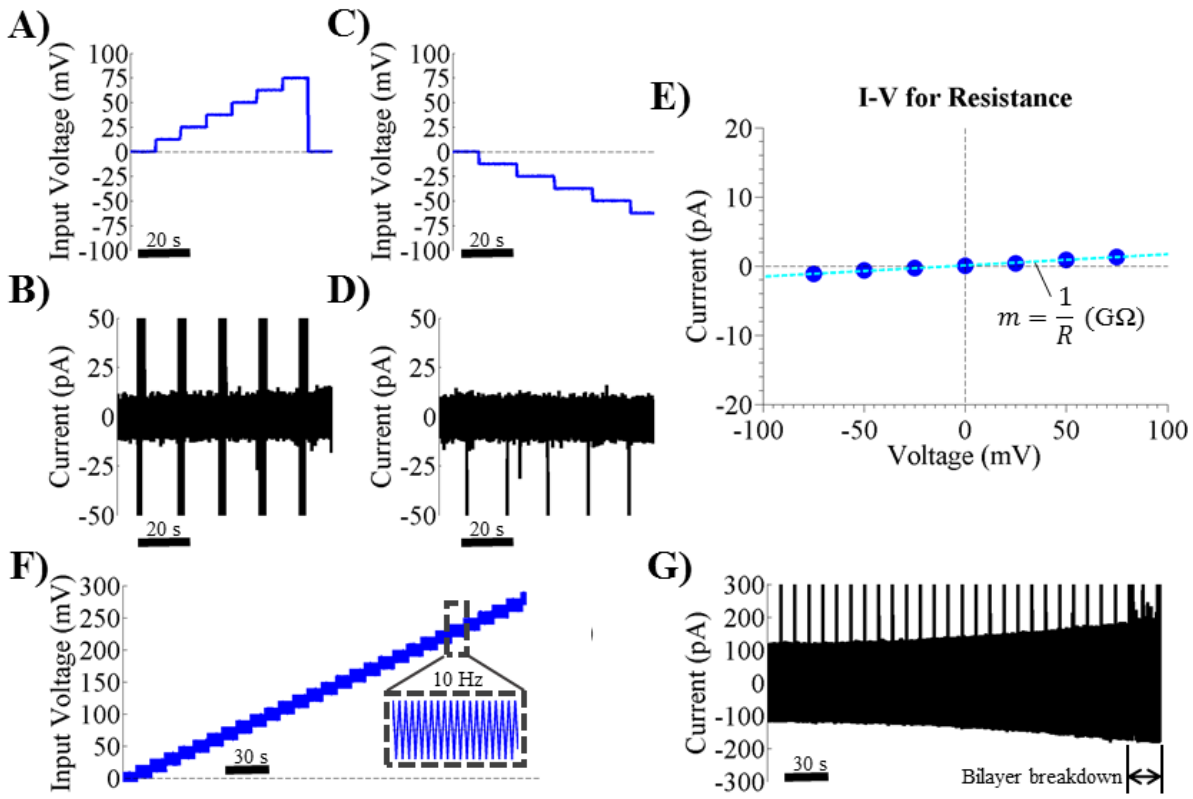

Figure 20. DC step routines used to measure bilayer resistance and rupture potential. To obtain bilayer resistance, applied voltage is increased via an automated routine with prescribed step size (mV) and time (s) up to a final voltage (typically 12.5 mV and 10-15 seconds per step from 0mV to +75 or +100 mV). A) Voltage applied during the positive sweep of a DC step routine to +75 mV. B) Current is measured during the DC step routine. C-D) Voltage and current during DC steps to -75 mV. E) Average current measured at each voltage step as shown in (B) and (D) is plotted as a function of the applied voltage. Via an Ohmic relationship, bilayer resistance is obtained as the inverse of the slope of a first order linear regression. F) The same DC step routine is used to elicit bilayer rupture potential. Typical step size and step time is 10 mV and 10 seconds, respectively, with final voltage set to 350 mV. In these tests, the triangular voltage waveform is applied on top of the DC step routine to monitor bilayer size. G) Current measured during a DC step routine for rupture potential. Bilayer area increases with applied voltage due to electrowetting, and ultimately the bilayer begins to breakdown and ruptures. The voltage at which the membrane ruptures is taken as $V_{rupture}$, the rupture potential.

plotted against the applied step voltage to allow calculation of bilayer resistance, taken as the inverse of the slope of a linear fit (Figure 20E). After executing DC step scans to obtain bilayer resistance, the scan is repeated with a high upper voltage limit (Figure 20F) to identify the rupture potential, $V_{rupture}$, which is the voltage level at which the DIB ruptures and droplets coalesce (Figure 20G).

2.2.3 Membrane Specific Capacitance

The suspended-droplet method of DIB formation is the most common setup used for C_M measurements in this work. For reference, equations related to C_M are provided in Section 1.2.2. To facilitate imaging of the DIB, the PDMS substrate is modified to obtain an optically clear bottom surface. When using the heat-distributing shell for feedback-controlled heating studies, the shell must include a hole or port to allow visualization of the droplets while suspended over the objective of the microscope. Bilayers are formed with droplets fully suspended in oil on the tips of ball-ended, gel-coated electrodes. Agarose-tipped electrodes are mounted above the microscope stage using micromanipulators or clamps and lowered into the oil reservoir of the PDMS substrate before being hydrated with aqueous buffer or lipid solution. For DIB formation, one droplet (typically 200-500 nL) of aqeuous lipid solution is placed onto each electrode, and the droplets are allowed to form monolayers. After the appropriate amount of time for monolayer formation, one or both electrodes are moved such that droplets come into contact, after which a DIB spontaneously forms. As described further below, capacitance measurements are made in sync with capture of images, and bilayer area can be manipulated by additional stepwise movements of one electrode.

Figure 21A shows typical images of a DIB between droplets suspended on electrodes at various area steps. Dynamic area control is achieved through manipulation of one or both of the electrodes. Figure 21B shows the square wave current measured over the course of a single experiment (15-20 minutes in this example). Figure 21C-D display sections of the current at shorter time scales. Figure 21E shows the capacitance at each area step associated with an arrow in Figure 21B, and we see no signs of any hysteresis as expected.[50] In sync with capacitance measurements, images are simultaneously acquired using a QIClick Digital CCD camera (operated via Qcapture Pro 7 or μManager[233]) mounted on an Olympus IX51 inverted microscope with a 4x objective installed

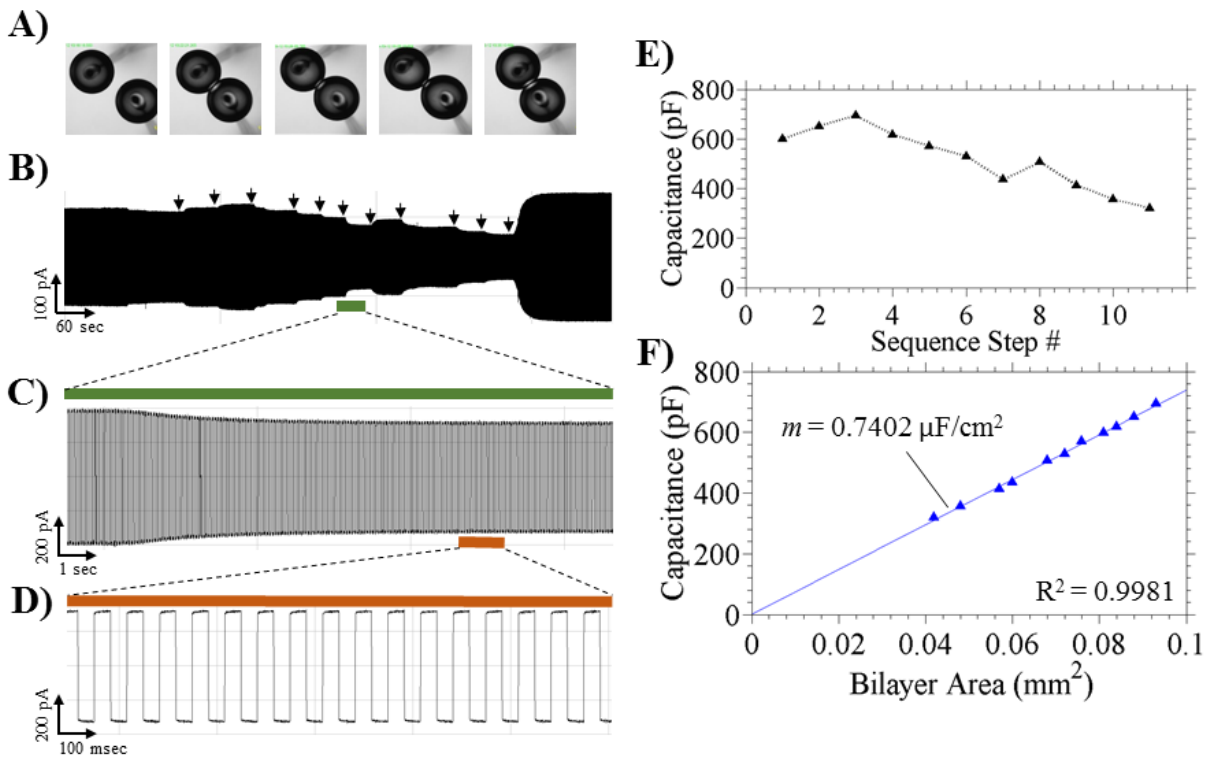

Figure 21. A) Images of droplets with purposefully varied amounts of contact (including one image of drops before they are connected). B) Capacitive square wave current measured during a single experiment to obtain specific capacitance, C_M. Arrows indicate the end of each step or the time at which area and capacitance data are simultaneously acquired. C-D) Measured current from part (B) at decreasing time scales show changing current amplitude as area is adjusted, although the signal remains square as a result of bilayer capacitance. E) Capacitance measured at each area step indicated by an arrow in (B). F) Capacitance as a function of area including a linear fit to obtain the slope, or specific capacitance.

(bright-field, intent light at 50% with 7 ms exposure time). Area is calculated after using an automated image processing routine to extract the effective diameter of the bilayer based on the distance between vertices where the two droplets are in contact. Chapter 3 provides additional details regarding area calculations and assumptions regarding the circularity of the bilayer interface. Figure 21F shows capacitance plotted versus its area for this representative experiment, and the slope of the linear fit is taken as C_M.

Error is estimated based on the normally distributed residuals from the linear fit of capacitance as a function of area following the method of Gross and Wallace.[50] For the example shown in Figure 21 with mean capacitance of 466 pF and mean area of 64000 μm^2, residual standard deviations are 5.86 pF or 722 μm^2 which represent measurement errors of 1.26% or %1.13 , respectively, for any single A_M vs C_T point.

2.3 Electrical Measurements to Quantify Membrane Protein Insertion in Droplet Interface Bilayers

Alamethicin (Alm) insertion is observed in response to applied transmembrane voltage using electrical measurements of current through the membrane. Alamethicin measurements are conducted using DIBs formed via the RAM platform to allow control of the bilayer size, and alamethicin is added to the liposome solution before placing droplets into oil. Tests herein are either performed using high concentrations (≥ 500 nM) that yield macroscopic currents (≥ 1 nA) or low concentrations (≤ 500 nM) that yield stochastic bursts of current through a single or few peptide channels (see Section 5.3.6 or Section 6.3.5 as examples). The following section is included to provide additional detail regarding the Cyclic Voltammetry (CV) methods used extensively in this work.

2.3.1 Macroscopic – Cyclic Voltammetry with Alamethicin Insertion

Alamethicin insertion at the macroscopic level is quantified via cyclic voltammetry (CV), a method that involves linearly ramping the applied voltage while measuring current. The voltage waveform used for CV scans is generated from a LabView program and routed through the

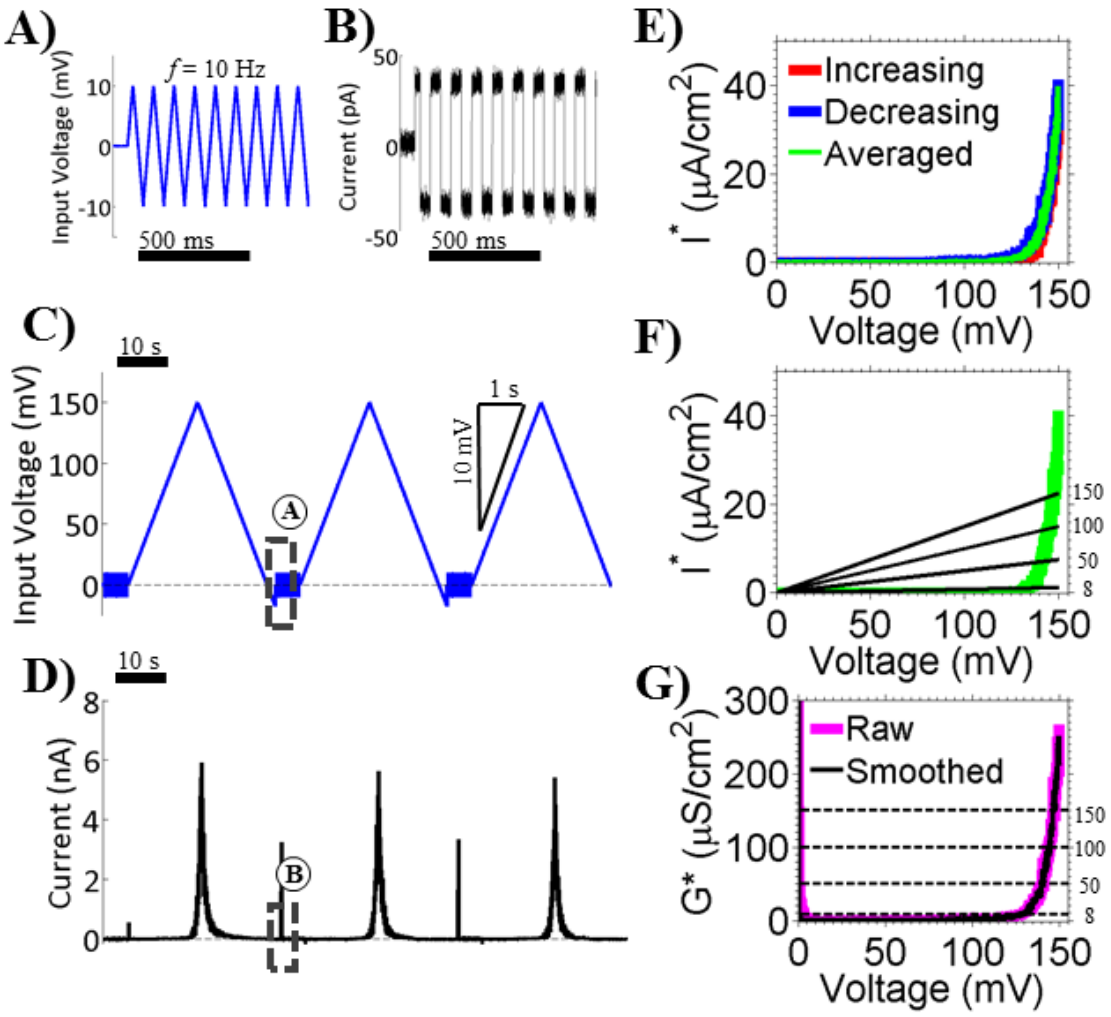

Figure 22. Cyclic voltammetry for characterizing interactions between alamethicin and DIBs. A-B) The typical triangular voltage waveform and corresponding square current wave (with a bilayer formed) is applied for 5 seconds at the beginning of each CV cycle. C) CV testing involves multiple cycles (typically 10 cycles per test). In a single cycle, voltage increases at a constant rate of 10 mV/sec up to the maximum applied voltage before decreasing at the same rate to 0mV. D) As voltage becomes more positive in the droplet containing alamethicin, current begins to increase exponentially with voltage above a certain characteristic threshold voltage, V^*. E) For each cycle, the steady-state current response to applied voltage is approximated by averaging current measured during the increasing and decreasing voltage segments of the CV scan, respectively. F) The averaged current response is normalized by membrane area for each scan and is divided by the applied voltage to determine specific conductance shown in (G). G) Specific conductance (G^*) during the CV scan is used to determine the voltage threshold, V^*, which depends on the specific value used for the threshold (dashed lines showing example thresholds). After smoothing G^* to further reduce noise effects, V* is taken as the voltage at which G^* first crosses the selected threshold. The selected threshold value is 8 μS/cm^2 (as used elsewhere [56]) in all instances of this work. (Figure reproduced from [10]).

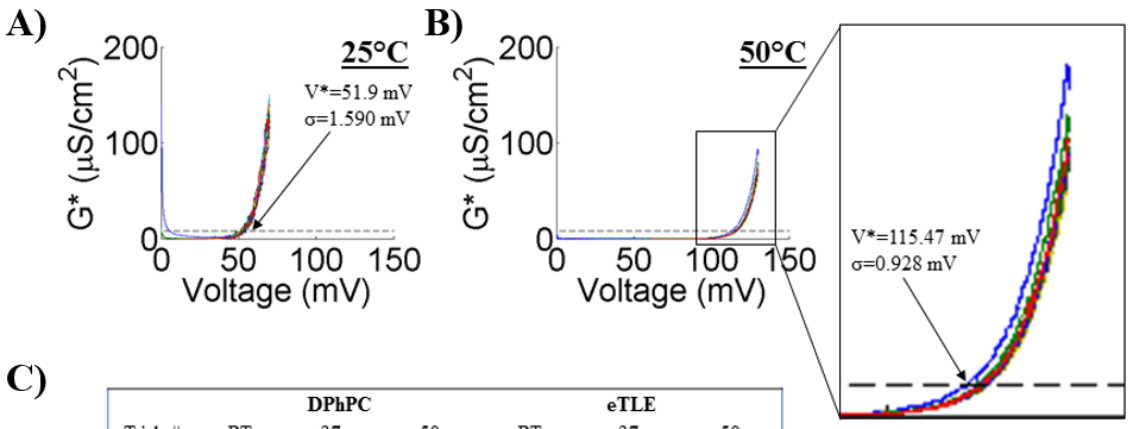

C)

	DPhPC			eTLE		
Trial #	RT	37	50	RT	37	50
1	129.99	138.97	152.96	51.91	103.15	119.75
2	131.48		139.25	57.01	73.33	124.05
3	127.03		139.43	49.68	94.64	115.47
4	129.68		147.82	60.52	93.03	113.55
5	134.56		142.59	61.71	94.62	111.37
6	129.88		141.61	67.15	97.05	136.77
7	130.34		151.96		91.05	119.18
8	132.72					132.35
9						130.91
10						
Avg (across trials)	130.7	139.0	145.1	58.0	92.4	122.6
Std	2.104	-	5.360	5.931	8.561	8.470

Figure 23. Repeatability and reproducibility of CV sweeps. A-B) Each plot includes 10 stacked conductance-voltage traces. Each of the 10 traces is the raw conductance signal for a single sweep, calculated as shown in Figure 22E-G. A) Room temperature, B) 50°C. Both) The 10 sweeps are obtained during a single trial with a single DIB via continuous CV scanning. As described in Section 5.3.6, CV sweeps with eTLE at higher temperatures require a higher maximum voltage to elicit enough current to cross the conductance threshold (dashed line). For the 10 traces within a single test, each trace is a different color, although the high within test repeatability makes it difficult to discern the different signals: see inset in (B). *V** is calculated for each sweep, and the values from each sweep are averaged to provide the final *V** value for the single trial. Typical standard deviation within a trial is <1-2 mV (σ as shown). C) *V** values obtained in all trials which are used to compute average *V** values shown in Figure 57C. The low standard deviations of 2.1-8.6 mV demonstrate the reproducibility of *V** calculations across trials. (Figure modified from [10]).

Axopatch to the DIB. Figure 22 shows the applied voltage (Figure 22A) and measured current (Figure 22B) during three sweeps of a typical CV measurement (DPhPC, 1 μM Alm). Each CV test involves forming a new DIB, adjusting the size to around 250 pF (100 pA square wave current with the selected triangle waveform input voltage), and then starting the CV scan. Each scan consists of $n \geq 10$ voltage sweeps where each sweep includes 5 seconds of the 10 mV/10 Hz triangular waveform (to monitor bilayer capacitance) followed by a triangular ramp at a rate of 10 mV/sec as used elsewhere [234] (Figure 22C). The maximum voltage used in CV tests is adjusted as needed (high concentrations of Alm require lower maximum voltage and vice versa). Current is measured throughout the CV sweep, and in the presence of alamethicin, current begins to increase exponentially (Figure 22D) with respect to voltage as the voltage exceeds a critical voltage referred to as the voltage threshold (V^*). Figure 22E shows the current-voltage curves measured during the increasing and decreasing legs of a CV sweep, as well as an averaged current-voltage curve. Alamethicin insertion is thermodynamically reversible, thus current begins to decrease as voltage begins to decrease in the second half of a CV sweep. Note that current is displayed as specific current ($I^*=I/A$) which accounts for variations in bilayer area from test to test. Area, A, is tracked and calculated for each sweep based on the magnitude of the square wave (i.e., Figure 22B) and a value of C_M for the membrane being tested. The single averaged I^* signal is then smoothed using a 100-point median filter (MATLAB, Figure 22F) before being converted to specific conductance ($G^*=I^*/V^*$, Figure 22G) using the applied voltage. V^* is the voltage at which current exceeds the conductance threshold. Specifically, V^* is determined as the voltage at which specific membrane conductance reaches a constant threshold value of conductance. The conductance threshold used throughout this work is 8 μS/cm^2.[10, 56] After performing 10 sweeps, V^* is calculated for each sweep and averaged to provide a single value for the trial before forming a new DIB and repeating the process for a new trial. Typically, $n \geq 5$ trials are conducted for a given case to obtain a representative average V^*.

CV measurements of alamethicin insertion are considered to be a robust method for quantitatively investigating membrane-protein interactions due to the repeatability and reproducibility of results within a single experiment and across multiple experiments. Figure 23A displays CV scans obtained during 10 consecutive sweeps in a single experiment at 25°C (here with an eTLE DIB,

see Chapter 5). Each of the 10 current-voltage curves are very similar which demonstrates the repeatability of the CV method within an experiment, and this robustness hold at elevated temperatures as well (Figure 23B). The table in Figure 23C lists average values of *V**, taken as the average of V* values obtained from each of the 10 sweeps such as those shown in Figure 23A,B, for multiple DIBs. The table also lists the standard deviation of *V** values across multiple DIBs, and the low standard deviations ($\sigma < 10$ mV for all cases) demonstrates the reproducibility of CV and determination of *V**.

2.4 Differential Scanning Calorimetry with Lipid Vesicles

DSC measurements are made using a NanoDSC calorimeter from Thermal Analysis Instruments. In each DSC run, the sample contained MLV suspension while the reference contained DI water. Sample lipid concentration is 2 mg/mL unless otherwise noted. The MLV solutions used for DSC were frozen once after initial reconstitution in water then thawed prior to desiccation and loading in the DSC instrument. Before loading the samples or DI water references, solutions are placed in vials and vacuumed for 15 minutes with a stir bar rotating at 600 rpm to remove air bubbles. The volume of the sample and reference cells are 0.5 mL each. A fixed pressure of 3 atm is used in DSC scans to further reduce bubble formation and provide initial feedback on the potential

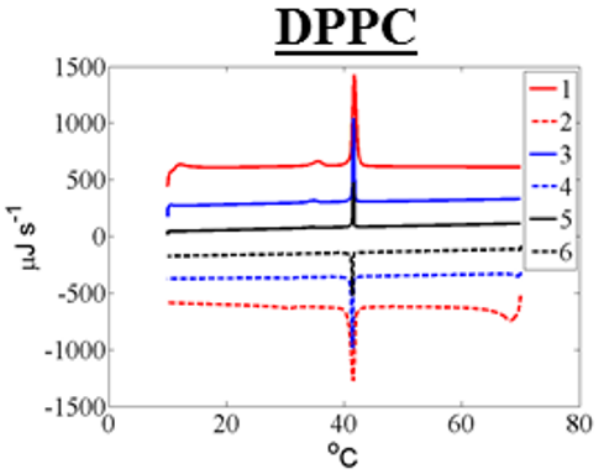

Figure 24. Representative thermograms obtained from DSC with DPPC MLV. Legend: 1 – heating at 1°C/m, 2 – cooling at 1°C/m, 3 – heating at 0.25°C/m, 4 – cooling at 0.25°C/m, 5 – heating at 0.1°C/m, 6 – cooling at 0.1°C/m.

presence of air bubbles. The DSC scan protocol is as follows: cooling and equilibrating at 0 or 10°C for 10 minutes, then three heating and cooling cycles to 70°C and back. The first, second, and third cycles have progressively slower scan rates of 1, 0.25, and 0.1°C/min, respectively. Temperature is held for a 10 minute equilibration period at each temperature endpoint during heating and cooling cycles. To avoid subjectivity with baseline correction or subtraction, DSC scans presented here are often shown as raw power versus temperature (see Figure 24 for DPPC, a lipid with known T_m = 42°C). This does, however, introduce "startup hooks" at the beginning of each heating or cooling cycle as the system equilibrates to the linearly changing temperature. Slower scan rates yield shorter startup hooks.

2.5 Pendant Drop Monolayer Tension Measurements

A pendant drop goniometer is useful for studying the self-assembly of lipids or other amphiphilic molecules at an oil-water interface. Self-assembly of lipids at an oil-water interface is an important initial step (i.e., monolayer formation) for BLM and DIB formation. Due to the extremely low interfacial tension (≤1 mN/m) achieved by lipid monolayer self-assembly, a pendant drop of aqueous lipid solution formed at the tip of a needle in oil often falls off, making it hard to measure the equilibrium tension. This is particularly problematic when the effects of gravity are significant, for instance when testing with hexadecane which has a much lower density than the aqueous phase ($\rho_{hexadecane}$=0.77 g/mL compared to ρ_{buffer}=1.00 g/mL). To circumvent this problem, a J-shaped needle is often used to form an "inverted" oil drop in the lipid aqueous solution as shown in Figure 25A. A glass cuvette is thoroughly cleaned by rinsing in acetone, IPA, and then deionized water before placing the cuvette in an oven (80°C) for several minutes or until it is fully dry. Clean, dry cuvettes are filled with 2 mL of liposome solution (ρ = 1.0007 g/mL). A clean 23 gauge steel needle (Ramé-Hart) is bent to form the J-shaped dispensing tip, taking care to ensure that the tip of the needle will be vertically oriented once assembled onto the goniometer. After fitting the needle on the automatic dispenser, few µL of the appropriate oil mixture is drawn into the needle. In order to prevent wetting of oil on the needle's exterior surface, the tip of the needle is dabbed with a clean wipe (Kimwipe) to remove residual oil before lowering the needle into the cuvette such that the tip is fully submerged into the aqueous solution. A 1 µL drop of the oil mixture is dispensed at the tip of the needle and the interfacial tension measurement begins. Example tension

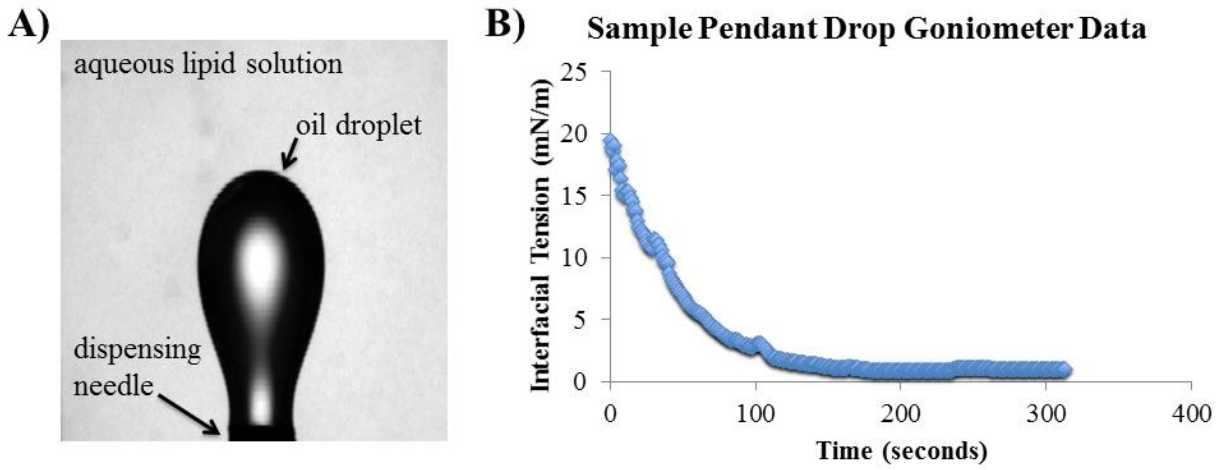

Figure 25. A) Representative image of the pendant droplet formed during goniometer measurements of lipid monolayer surface tension. An inverted 1 μL droplet of oil (the less dense liquid phase) is dispensed at the tip of a J-shaped needle submerged in aqueous solution containing small unilamellar liposomes (DPhPC or DPhPC:cholesterol). The droplet "floats" upwards as a result of the difference in the oil and aqueous phase densities. B) Typical response of monolayer tension upon creating of a new clean, lipid-free oil droplet at the tip of the dispensing needle. Tension decreases instantaneously upon droplet formation, settling to a steady state value as lipid self-assembly and packing reach equilibrium. Steady state monolayer tensions are typically near 1 mN/m. Typical test results resemble the example shown in which 62% of the overall tension decrease occurs over a period of 30-40 seconds.

data from a representative experiment is shown in Figure 25B. Measurements are taken at a rate of 60 samples per minute until an equilibrium value is reached. All measurements are performed at room temperature.

CHAPTER 3

DIRECT *IN SITU* MEASUREMENT OF SPECIFIC CAPACITANCE AND SURFACE TENSIONS IN DROPLET INTERFACE BILAYERS

As described in Section 1.2.2, thickness and tension are important physical parameters of model cell membranes. However, traditional methods to measure these quantities require multiple experiments using separate equipment. This chapter introduces a new multi-step procedure for directly accessing *in situ* multiple physical properties of droplet interface bilayers (DIB), including specific capacitance (related to thickness), lipid monolayer tension in the Plateau-Gibbs border, and bilayer tension. The work described herein addresses Objective 1 from Section 1.3.2. The DIB-based procedure is based on the Young-Dupre and Young-Lippmann relationships for adhesive droplets in the presence of applied electric fields. The procedure employs a combination of mechanical manipulation of bilayer area followed by electrowetting of the capacitive interface to examine the sensitivities of bilayer capacitance to area and contact angle (external angle between droplets) to voltage, respectively. Analyzing these data allows determination of membrane specific capacitance and the surface tension of the lipid monolayer, which are then used to compute bilayer thickness and tension, respectively. This chapter presents the theory behind the measurement technique, initial demonstration of the method for assessing DPhPC DIBs, and detailed uncertainty analysis and practical details associated with the method.

Note: This chapter presents a modified portion of the published paper “Direct In Situ Measurement of Specific Capacitance, Monolayer Tension, and Bilayer Tension in a Droplet Interface Bilayer " [49].

3.1 Theory and Approach of Electrowetting-Based Measurements of Droplet Interface Bilayer Surface Tensions

It is well known that applying voltage across a BLM affects the equilibrium interfacial geometry of the suspended film through a process known as electrowetting.[50, 86, 228, 235] Specifically, an applied electric field increases the external contact angle at the annulus, which drives a subsequent increase in area of the bilayer. The relationship between the contact angle and the applied electric field is described by the Young-Lippmann equation that relates the change in contact angle at the edge of the bilayer to the specific capacitance of the membrane and monolayer tension. When the membrane specific capacitance and monolayer tension are themselves not functions of voltage, the change in contact angle is described by

$$\cos\theta_0 - \cos\theta_V = \frac{C_M}{4\gamma_m}V^2. \qquad \text{Equation 8}$$

Equation 8 includes the contact angle measured at a nonzero applied voltage (θ_V), the zero-volt contact angle (θ_0), the capacitance per unit area of the membrane (C_M), the monolayer surface tension, and the voltage applied across the membrane (V). shows that if C_M is known, γ_m can be determined experimentally by measuring the voltage dependent change in the cosine of the contact angle. Requena and Haydon[228] were the first to verify that this relationship could provide access to γ_b, though they suggested that either C_M or γ_m would be known ahead of time from a separate experiment. Their work also highlighted the difficulty in determining an accurate value for the area of a suspended BLM, which is required to precisely determine C_M. Consequently, rather than using Equation 8 to extract monolayer or bilayer tensions, they used this relationship and separate measurements of γ_m as a way to determine C_M from the electrowetting response.[228] This approach contrasts the more commonly used discrete measurements of electrical capacitance and bilayer area to determine specific capacitance.[8, 46, 196-200, 204, 205, 228, 235-243] Yet, if C_M and θ_V can be measured *in situ*, then the Young-Lippmann relationship and Young's equation show that γ_m, γ_b, and the free energy of bilayer formation can be comprehensively and simultaneously determined.

The droplet interface bilayer (DIB) method is an elegant technique for assembling planar lipid bilayers to study membrane properties and membrane protein activity.[10, 12, 17, 50, 66, 80, 81, 83, 84, 89, 183, 244, 245] Droplet interface bilayers form spontaneously between lipid-coated aqueous volumes immersed in oil. DIBs offer several advantages to other methods for bilayer formation, including long lifetimes (hours-days),[71] low-volume, tunable bilayer area,[10, 17, 50, 70, 71, 86, 245] control over the composition of each leaflet and of each droplet,[12] and potential for scale-up by forming multi-membrane networks with many droplets.[66, 80, 81, 83, 84, 89, 244] DIBs have been successfully used as soft functional building blocks for bottom-up synthetic biology, for example in the construction of tissue-like materials[84] and in the construction of spatially arranged artificial cells.[246, 247] As illustrated in Figure 17B, a DIB is energetically balanced by lipid monolayer tensions that oppose bilayer tension in the same manner as a suspended BLM. DIBs also possess the appropriate thickness and amphiphilic, two-dimensional liquid crystalline structure to reconstitute transmembrane proteins and peptides while retaining their natural function.[36, 71, 75] However, unlike suspended BLMs, the DIB allows for optically tracking both the contact angle and the interfacial area between droplets, in addition to permitting electrical measurements of membrane capacitance.

Thus, we propose that DIBs could be employed to study the effects of proteins, cell-penetrating peptides, and other biomolecules and lipophilic species on bilayer capacitance, tension, and free energy of formation by combining methods for determining membrane specific capacitance with a technique to measure contact angle. Using a coupled approach, we demonstrate that both monolayer and bilayer tensions can be measured *in situ* by tracking changes in C_M and θ with a droplet interface bilayer (DIB) at varying bias voltages. The specific advantages of DIBs for this type of experiment include: 1) control of droplet positions relative to one another allows for direct tuning of the area of the interface,[70, 71] which allows for accurate determination of C_M,[10, 50] and 2) simple optical imaging of the adjoined pair can be used to determine both membrane area and θ across a range of applied electric fields.[86, 90, 110]

In the following sections, we demonstrate the accuracy and sensitivity of a multi-step tuning technique that allows for measurement of monolayer and bilayer tension in a DIB. First,

mechanical tuning of the interfacial area is used to determine specific membrane capacitance. Then, an electrical tuning routine is performed to determine lipid monolayer tension via C_M and θ values obtained at various applied voltages. Bilayer tension is subsequently determined from values of γ_m and θ using Equation 7 (Young's equation). *In situ* measurements of monolayer tension are compared to separate measurements of monolayer tension obtained via the pendant drop method. After confirming that monolayer tensions can be accurately obtained via measurements of C_M and θ, we showcase the utility of this method for measuring changes in membrane capacitance, monolayer tension, and bilayer tension (via the Young's equation) caused by the addition of cholesterol, known to affect lipid packing and order and, separately, the incorporation of silicone oil into the oil phase surrounding the droplets. The ability to detect cholesterol-induced changes in thickness help validate the method for future use in studies of the effects of other biomolecules, while measurements using different mixtures of oils confirms what is known about size-selectivity of oil retention versus exclusion in a BLM. These oil mixtures also represent commonly used oils in DIB assembly.[33, 84]

3.2 Measurement Methodology

3.2.1 Specific Capacitance, Monolayer Tension, and Bilayer Tension Measurement with a DIB

Figure 26A illustrates the three-part process for measuring C_M, γ_m, and γ_b on a DIB. In Part 1, a DIB is formed between two aqueous droplets suspended on agarose tipped ball-ended electrodes in oil. The initial thinning of the bilayer occurs generally within 1-2 minutes of initial contact and results in a rapid increase in the amplitude of the capacitive current signal due to the formation of a thinned bilayer region between droplets. The area of the thinned region and the angle between droplets stabilize to constant values when the total energy of the connected droplets reaches a local minimum.[84]

Part 2 of the process involves incrementally changing the bilayer area, and thus the nominal capacitance of the interface, by moving one electrode in a stepwise fashion relative to the other. As others have shown,[50] returning the mobile electrode to its original position results in a

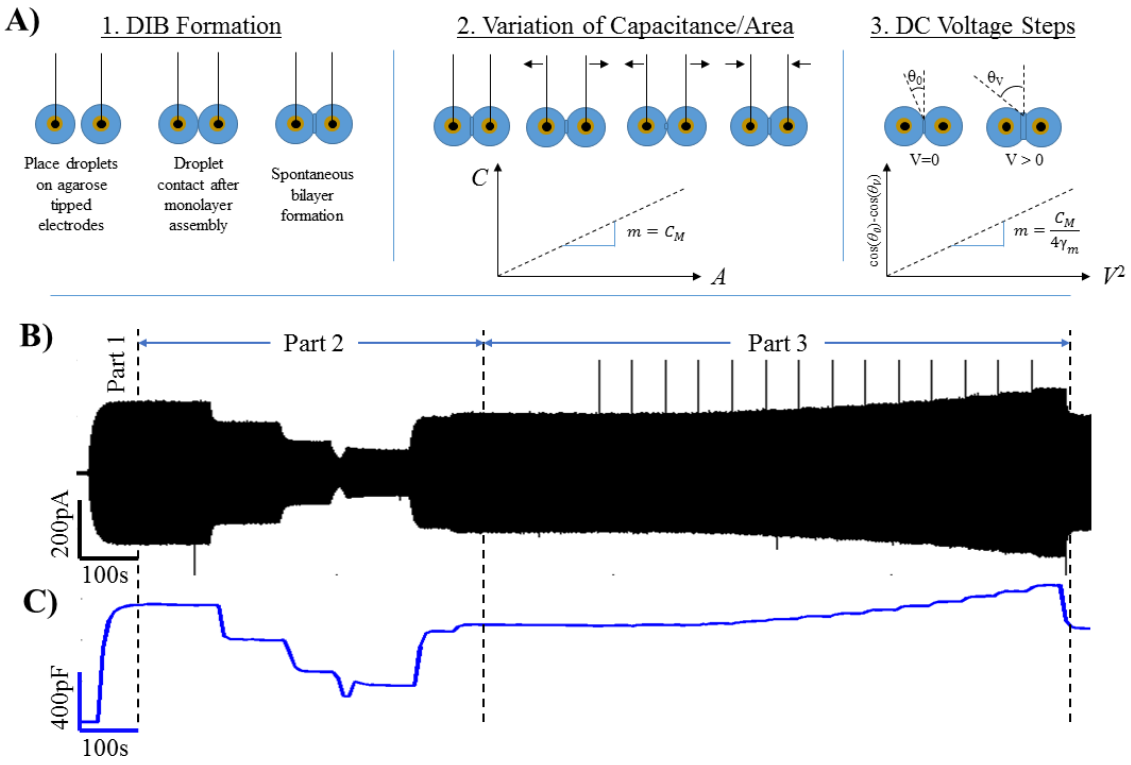

Figure 26. A) A three-part process is used to characterize DIBs: Part I represents bilayer formation; Part II represents the mechanical tuning of the bilayer area to determine specific capacitance; and Part III represents electrical tuning of the contact angle to determine monolayer tension via the Young-Lippmann equation (Equation 8). B) A typical current trace recorded during the course of an experiment in which all three parts are performed. C) Membrane capacitance versus time computed from the raw square current waveform shown in (B).

reversible change in the capacitive current and bilayer area. The size of the bilayer at each position stabilizes within about 30 s of the electrode positioning. At each level of contact area (typically >5 contact areas are prescribed), the steady-state amplitude of the square-waveform current signal is recorded and an image of the DIB is acquired simultaneously. Nominal capacitance is computed using $C=i/(4Af)$, where i is the amplitude of the current waveform measured at steady state and A and f are the amplitude and frequency, respectively, of the applied triangular waveform voltage. Specific capacitance is obtained simply from the slope of a linear least squares regression of nominal capacitance versus area data from all electrode positions (Figure 26A, center).[10, 50]

Part 3 requires an applied dc transmembrane voltage that increases in a stepwise fashion in addition to the ac triangular voltage required for capacitance measurement. This procedure begins by fixing

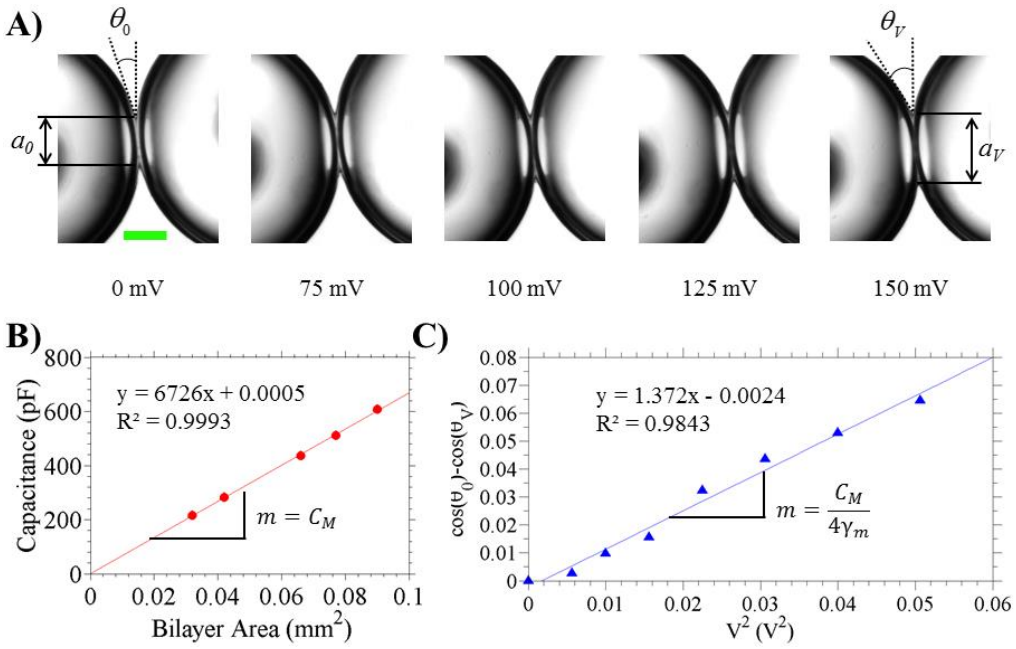

Figure 27. A) Representative images of a DPhPC DIB in decane during a Young-Lippmann test for monolayer and bilayer tensions (bottom-view images, scale bar represents 100 μm). The DIB is allowed to equilibrate at each voltage before capturing any images used for contact angle measurements. The contact angle and the contact area increase with increasing voltage. This behavior is a result of reduction in bilayer surface tension by an amount equal to the energy stored on the capacitor. B) Results from specific capacitance measurement (V=0 mV, Part II in Figure 26) C) The Young-Lippmann equation describes the linear relationship between applied bias voltage and the resulting change in the cosine of the contact angle. Experimental observation of contact angle at various applied voltages then allows for calculation of the monolayer tension. Parts B and C represent data obtained from a DPhPC DIB in hexadecane.

the electrode (i.e. droplet) positions, setting the bias voltage to zero, and allowing the DIB to equilibrate for several minutes to ensure the droplets reach a steady contact area and angle. Images are taken at the 0 mV equilibrium point to allow measurement of θ_0 before voltage is increased in a stepwise fashion. The bilayer is held at each new voltage for 15-30 seconds, during which electrowetting causes the external bilayer contact angle to increase as predicted by the Equation 3 (Young-Lippmann equation). Images ($n \geq 10$) of the contact angle (θ_V) are obtained at the end of each voltage step and the process is repeated at successively higher voltage levels. This part of the experiment takes only a few minutes to perform. Using the average contact angle from each voltage level, the change in the cosine of the contact angle is plotted versus the square of the applied bias voltage (Figure 26A, right). As noted above with Equation 8, the change in the cosine of the contact angle is recorded with respect to the cosine of θ_0.

3.2.2 Representative Measurements on DPhPC DIBs in Hexadecane

Figure 26B shows the square current waveform induced by the ac triangular voltage applied to a DPhPC DIB formed in hexadecane during all three parts of the experiment. Figure 26C shows the corresponding bilayer capacitance, computed from the same current response, versus time. During Part 1 of the experiment, the amplitude of square current waveform stabilizes at ~240pA. Images of the connected droplet pair show that θ_0 is 29.3 ° for this type of lipid and oil.

The second and third parts of the measurement process result in stepwise changes to bilayer capacitance, caused by mechanical and electrical tuning, respectively. During Part 2, the measurement shows that at each successive electrode position (i.e. farther apart), the square wave current stabilizes to smaller amplitude, which corresponds to smaller area of contact and thus capacitance. Conversely, the application of an increasing dc bias (of either polarity) drives the square wave current and bilayer capacitance to successively higher levels in Part 3.

The micrographs of a DPhPC DIB in hexadecane in Figure 27A show that increasing levels of electrowetting lead to increases in the external contact angle, θ, as well as the projected length of the interface, a. Figure 27B presents the capacitance versus area data obtained in Part 2 of the same test on this DIB, and the change in the cosine of the contact angle versus voltage data from Part 3 are shown in graphical form in Figure 27C. Typically, tests to measure γ_m conclude when the bilayer ruptures at voltages between |200-350| mV. In this test, θ increased from 28.8° at 0 mV to 35.9° at +225 mV. The change in cosine of the contact angle is well represented by a linear least squares regression with respect to V^2 across the range from 0 to 225 mV with an R-squared value >0.98. From Equation 8, it can be seen that the slope of the regression (m) is related to both C_M and γ_m, as given by

$$m = \frac{C_M}{4\gamma_m}. \qquad \text{Equation 9}$$

Equation 9 is rearranged to solve for monolayer tension using the value of C_M obtained in Part 2 and the value of m obtained in Part 3. The specific data shown in Figure 27C yield a slope of m=1.372 which, combined with the C_M value (slope from Figure 27B) of 0.673 μF/cm^2, yields a computed value of monolayer tension, γ_m, equal to 1.23 mN/m. For a group of eight DPhPC DIBs

formed in hexadecane, this method results in an average (± one standard deviation) monolayer tension of 1.18±0.136 mN/m, which is in excellent agreement with prior results[63] and the results of our own independent pendant drop measurements of DPhPC monolayer tension (1.19±0.067 mN/m, n=3). A student t-test confirms that there is no significant difference ($p<0.005$) between the values obtained with either tension measurement method, which serves to validate an approach that leverages the electrowetting response of DIBs to determine the tension state. In summary, the measurement method introduced herein is capable of determining lipid monolayer tensions at the surfaces of the droplets that are consistent with those obtained using accepted techniques such as pendant drop goniometry.

After computing monolayer tension, the bilayer tension at zero volts is readily computed for each trial using Young's equation (Equation 7) along with the measured contact angle at 0 mV.[101, 102, 226] For the example shown in Figure 27, the calculated monolayer tension (1.197 mN/m) and zero-volt contact angle of 28.7° results in a calculated value for γ_b of 2.10 mN/m. For the pool of eight different DPhPC DIBs in hexadecane that are tested, we obtain an average value of 2.04±0.222 mN/m for the tension of DPhPC bilayers in hexadecane. Prior studies obtained values of 1.62 mN/m and 1.9±0.3 mN/m for planar lecithin bilayers[227, 248] and DPhPC DIBs, [63] respectively. The latter value, provided by Dixit et al., was obtained using Equation 7 along with the monolayer tension determined via independent goniometer measurements and the contact angle estimated using images of connected droplets. It is possible to calculate bilayer tension via Equation 7 using the data herein: the average value of monolayer tension obtained from the goniometer and the average contact angle in DIB measurements (29.3°, see Table 7) yields an estimate of 2.08±0.198 mN/m for bilayer tension. All of these results are in strong agreement with one another, and there is no significant difference ($p<0.005$) between bilayer tensions computed from monolayer tensions obtained via the pendant drop and DIB methods.

It is also possible to use Equation 7 to discretely compute bilayer tension as a function of bias voltage using the measured values of γ_m (fixed) and DIB contact angle at each voltage applied during Part 3 of the experiment. Additionally, the average bilayer tension can be empirically projected in a continuous fashion versus voltage using experimentally determined values of C_M,

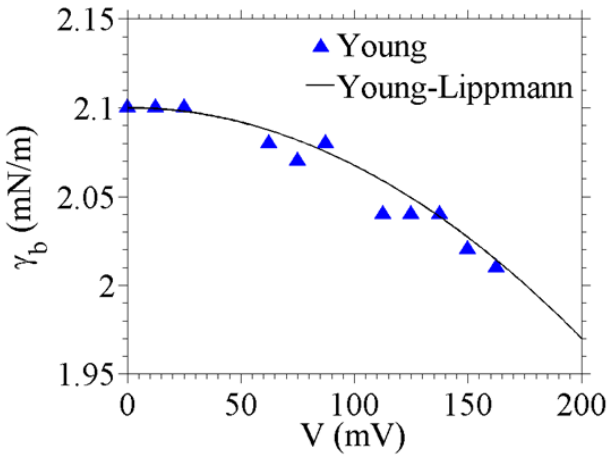

Figure 28. Bilayer tension (γ_b) as a function of applied voltage (V) for a DIB, calculated using the representative data presented in Figure 27.

γ_m, and θ_0. This second method evaluates bilayer tension versus voltage using a rearranged form of Equation 8,

$$\gamma_{b,V}(V) = \gamma_{b,0} - \frac{C_M}{2}V^2, \qquad \text{Equation 10}$$

along with the bilayer tension at 0 mV ($\gamma_{b,0}$) computed using Equation 7. Figure 28 compares γ_b as a function of voltage computed discretely and continuously using the values of θ, C_M, γ_m, and V obtained for the data presented in Figure 27B-C. Clearly, γ_b decreases with increasing voltage, which illustrates that the stored electrical energy across the bilayer acts to mechanically relax the interface. Further, close agreement between the discrete data points and the continuous curve show that the measured contact angles and thus the computed bilayer tension, conform to the Young-Lippmann relationship for bilayer tension at voltages between |0-175| mV. This agreement suggests that bilayer tension can also be computed accurately at a non-zero voltage provided the contact angle is measured at that potential and the monolayer tension is known. Monolayer tension is assumed to be independent of applied potential due to the fact that the thinned bilayer contributes the dominant electrical impedance between droplets. This occurs because of the presence of nonconductive oil in the Plateau-Gibbs border that is much thicker and has a lower capacitance per unit area than the bilayer. As a result, the applied voltage produces an electric field predominantly across the membrane.

For further comparison of the DIB Young-Lippmann equation with prior studies, it is possible to evaluate the reduction in free energy obtained upon droplet adhesion (Equation 2). For a DPhPC DIB formed in hexadecane, the calculated monolayer tension and average contact angle at 0 mV (29.3°) yield 0.301 mJ/m^2 as the free energy of bilayer formation. As further validation of the accuracy of the approach, our estimated free energy of formation is in direct agreement with the value of 0.31±0.02 mN/m for DPhPC bilayers formed in squalene,[110] as well as other reported values which fall between 0-2 mN/m.[63, 90, 102, 226]

3.2.3 Analysis of Uncertainty of Specific Capacitance and Tension Measurement

Error in determining specific capacitance and tensions arises from uncertainties in measuring capacitance and area (for C_M) and in determining the contact angle (for γ_m, γ_b), respectively. Nominal capacitance is determined directly via electrical measurement as described previously[10] where it is shown that there is <1.3% error in any C versus A data point used for C_M determination[10]. Therefore, we focus instead on the accuracy and repeatability of bilayer area and contact angle measurements, which are obtained via a two-step process: 1) an image acquisition step, and 2) image processing (MATLAB) to determine the angle and projected length (diameter) of the bilayer. To determine uncertainties introduced from image acquisition, we look at repeatability of measurements taken from 10 images of a DIB at a fixed equilibrium condition. The images are acquired rapidly within a few seconds (10Hz). Estimation of bilayer area begins in MATLAB by extracting the projected diameter of the bilayer from images taken through the inverted microscope objective. These "bottom-view" images are analyzed via a custom image processing routine to calculate the horizontal distance, a, between the intersection points of the two droplets and the external half angle (i.e. contact angle), θ, that exists at the waist of the interface (as shown in Figure 27A). Area estimation requires an assumption regarding the shape of the interface. Dixit, et al outlined the geometrical relationships that govern DIB formation for spherical droplets of identical size in an equally dense oil phase. This analysis predicts a perfectly flat, circular interface.[63] However, the shape of the interface becomes more elliptical when gravitational effects cause the water droplets to sag vertically from the wire-type electrodes in a less dense oil phase (Refer to Figure 38). With droplets hanging on electrodes, the minor axis of

the elliptical interface (*a*) is the horizontal distance obtained from microscope images whereas the longer major axis (*b*, Figure 38) is oriented vertically and cannot be determined from a bottom-view image. Analysis of bilayer shape under increasing levels of sagging enables estimation of correct bilayer area using only *a*. However, since the contact angle is measured in the horizontal plane at the waist of the connected droplet pair (i.e. the force balance at the contact point does not have a vertical component), we do not correct the measured contact angle for effects of droplet sagging.

The average and standard deviation of bilayer area and contact angle are calculated from the 10 images acquired with zero applied voltage to assess the repeatability. Furthermore, the average group standard deviation of bilayer area using images acquired from 11 unique DPhPC bilayers (110 images total) is 458 μm^2. Similarly, contact angles measurements from 14 different DPhPC DIBs (140 images total) provide an average group standard deviation of only 0.763°. With a typical zero-volt area of 30000 μm^2 for a DPhPC DIB in hexadecane, the average standard deviation in measured bilayer area corresponds to an error of less than 0.002%. For the average contact angle of 29.3°, the average standard deviation represents an error of 2.6% for the angle measured at a given area step. These results present a lower standard deviation than previously reported for contact angle measurements in DIBs (σ = 3-6°) in DIBs. [90, 102] The comparison here shows that the automated image processing routine and the use of multiple images at each voltage level provide an order of magnitude lower variation in average angle measurements. Separate analysis for quantifying error propagation within the multi-step technique, described in the following section, yields uncertainties of ± 0.32 mN/m and ± 0.51 mN/m in monolayer and bilayer tension measurements, respectively.

3.2.4 Uncertainty and Error Propagation in Tension Measurements

Monolayer tension (γ_m) measurement requires independently obtained values for both C_M and m (refer to Equation 8 for additional context).

$$\gamma_m = \frac{C_M}{4m} \qquad \text{Equation 11}$$

The uncertainty in tension measurement thus involves uncertainty of both specific capacitance measurements and the measured values of *m*. We are able to define the sensitivity index Ω for each contributor.

$$\Omega_{C_M} = \frac{\partial \gamma_m}{\partial C_M} \qquad \text{Equation 12}$$

$$\Omega_m = \frac{\partial \gamma_m}{\partial m} \qquad \text{Equation 13}$$

Total uncertainty, u_R, is obtained as the square root of the sum of the square of each contributing sensitivity index multiplied by the uncertainty in the respective independent variable (u_{C_M} and u_m) .

$$u_{\gamma_m} = \pm\sqrt{(\Omega_{C_M} u_{C_M})^2 + (\Omega_m u_m)^2} \qquad \text{Equation 14}$$

The uncertainty in each independent variable is computed using the student t-test factor ($t_{n,p;}$ *n* is the number of samples and *p* is the probability level) and the standard deviation (σ) for each respective measurement method.

$$u_{C_M} = \pm t_{n,95}\sigma_{C_M}$$
$$u_m = \pm t_{n,95}\sigma_m \qquad \text{Equation 15}$$

The overall uncertainty of monolayer tension measurements is then calculated using Equation 14, Equation 15, and differentiating Equation 1 to obtain expressions for Ω (per Equation 11).

$$u_{\gamma_m} = \pm\sqrt{\left(\frac{1}{4m}u_{C_M}\right)^2 + \left(\frac{-C_M}{4m^2}u_m\right)^2} \qquad \text{Equation 16}$$

The average and standard deviation from C_M and *m* calculations are 0.652±0.027 μF/cm^2 and 1.41±0.158 V^{-2}, respectively (DPhPC in hexadecane data). The resulting value for overall uncertainty in measuring monolayer tension is u_{γ_m} = ±0.316 mN/m. This is roughly equivalent to the uncertainty estimated simply by $u_{\gamma m} = \pm t_{n,95}\sigma_{\gamma m}$ (standard deviation for DPhPC monolayer tension is 0.136 mN/m).

Uncertainty in bilayer tension (u_{γ_b}) can be approximated using the same approach described for monolayer tension, although Equation 7 is replaced by the Young equation defining bilayer tension. The independent variables are γ_m and θ. The contribution from monolayer tension measurements, u_{γ_m}, is calculated above. The standard deviation of θ measurements made on a group of images is found to be 0.768°. Using the average angle of 29.3°, the overall uncertainty including propagation of error in γ_m and θ is 1.813 mN/m. Clearly this is greater than the standard deviation observed with bilayer tension values provided in Table 7. As with monolayer tension above, a more reasonable estimate of bilayer tension measurement uncertainty is obtained by $u_{\gamma b} = \pm t_{n,95}\sigma_{\gamma b}$ = (2.306)(0.222) = ±0.512 mN/m (n=8).

3.2.5 Effects of Mechanical Manipulation of Droplet Positions on Electrowetting and Tension Measurements

In analyzing images obtained during specific capacitance measurements of DIBs (Figure 26A, Part 2), we observe that the zero-Volt contact angle at equilibrium is directly affected by mechanical manipulation (i.e. positioning) of the droplets, which is used to intentionally vary the area of the bilayer. To explore this relationship, Figure 30A-B shows the results of a representative experiment in droplets were successively pulled apart in 3 steps and then sequentially pushed back together in 3 area steps (refer to Figure 29 for sequential presentation of area and angle data). The

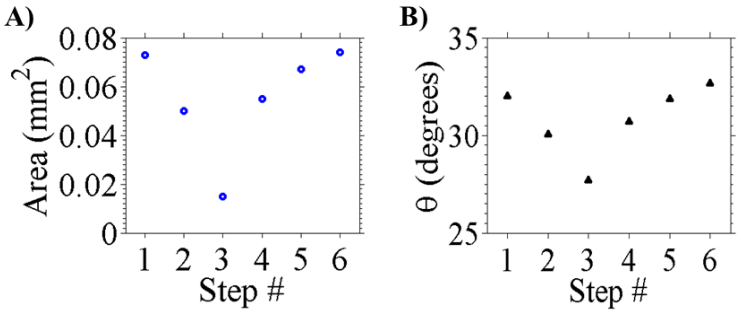

Figure 29. (A) Area and (B) contact angle at each step during Part 2 of the DPhPC DIB experiment shown in Figure 26A-B. With each step, area is either decreased or increased by changing the distance between electrodes. Generally, contact angle is seen to increase with increasing bilayer area and vice versa (see also Figure 26 and related discussion in the text).

data in Figure 30B shows that the contact angle reversibly increases by as much as 5-6° as 300 nL droplets are pushed together to yield a larger interfacial area. To further test this response, Figure 30C shows zero-Volt contact angle versus bilayer area obtained from n = 115 various measurements made via Part 2 of the method on 13 different DPhPC DIBs. The larger population of data confirms that contact angle increases with mechanically driven increases in bilayer area. While the precise mechanism for this change in angle remains undetermined, the data suggest that pushing or pulling the droplets in a direction perpendicular to the interface reversibly alters the equilibrium tension balance that establishes the contact angle.

The fact that changing the electrode separation distance alters droplet contact angle begs the question: how much does mechanical manipulation required for Part 2 affect the accuracy of the electrowetting-based method in Part 3 for determining monolayer tension in a DIB? To examine this possibility, we consider the role of the zero-Volt starting contact angle, which was shown in Figure 30A-B to be a function of droplet positioning. Based on Equation 8, tuning or altering the initial wetting condition (θ_0) should not affect the magnitude of the change in the cosine of the contact angle across a range of voltage assuming fixed C_M and γ_m. However, the nominal change in contact angle does depend on θ_0 since the cosine of an angle varies nonlinearly. Such behavior is observed experimentally as portrayed in Figure 30D and Figure 30E, which show the theoretical and experimentally observed values for $\cos(\theta_0) - \cos(\theta_V)$ and θ_V, respectively, with increasing applied voltage. The data portrayed is from two different electrowetting trials where the zero-Volt contact angle is varied (θ_0 = 29° and θ_0 = 25°) by mechanical manipulation between trials. The data in Figure 30D provides slope values of m = 1.548 and m = 1.579. With a specific capacitance value of 0.652 μF/cm^2, the resulting calculated monolayer tensions are 1.05/1.03 mN/m for (θ_0 = 29°/25°) and the Young equation is used to calculate bilayer tension of 1.84/1.87 mN/m). The variation in θ_0 causes <2% change to the slope, monolayer tension, and bilayer tension. Thus while mechanical manipulation can affect the zero-Volt contact angle, it does not significantly affect the

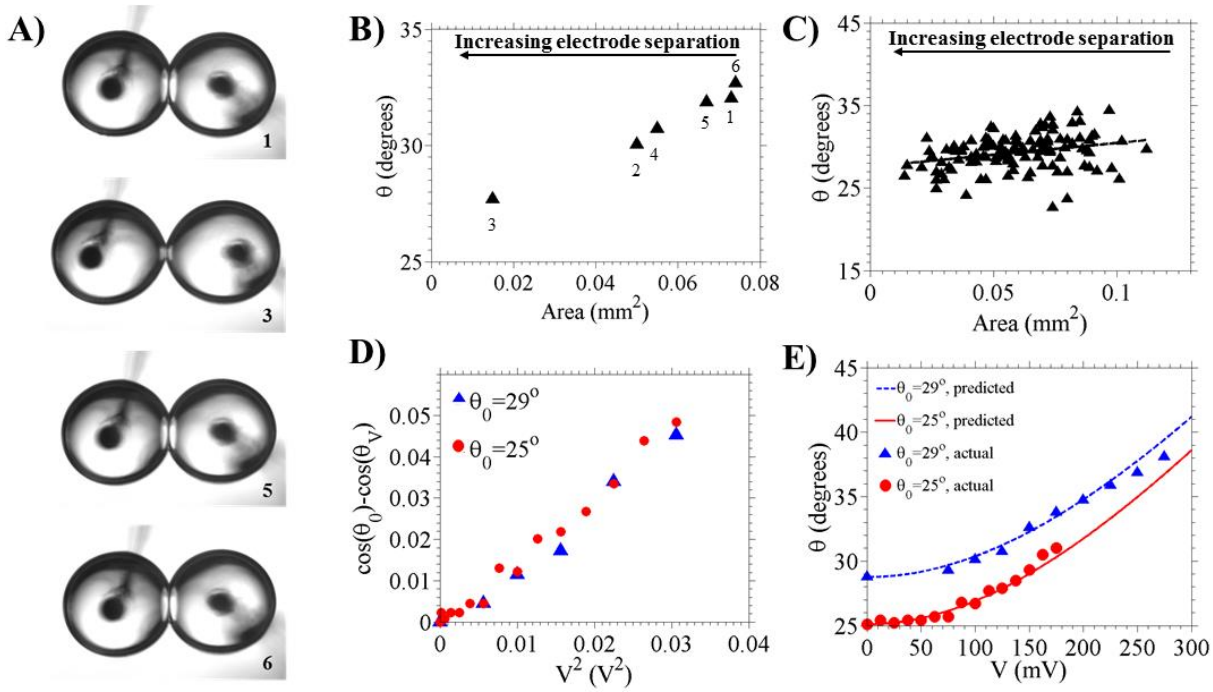

Figure 30. A) A DPhPC DIB at varying steps during Part 2 of an experiment where DIB area is mechanically varied by moving one electrode and changing the distance between droplets. B) θ measured from images of the DIB at each area step. B) θ measured from $n > 100$ images obtained at varying area steps with 13 separate DPhPC DIBs during C_M measurements. D) The change in the cosine of θ as a function of voltage for a DPhPC DIB mechanically manipulated to obtain two different zero-volt contact angles: θ_0 = 29° and 25°. E) Theoretical ("predicted") and experimentally observed ("actual") nominal θ as a function of voltage for the trials shown in (D).

ability to correctly determine monolayer and bilayer tension in the electrowetting-based method used in Part 3.

While varying θ_0 does not affect the magnitude of the change in the cosine of the contact angle, the magnitude of the nominal voltage-dependent change in angle is expected to increase with decreasing zero-Volt contact angle due to the nonlinearity of the cosine function (Refer to Section 3.2.6). This behavior is seen with both predicted and experimentally observed values for θ_v shown in Figure 30E, which show that contact angles for DIBs starting at different contact angles appear be on converging trajectories at increasing voltage. These data also confirm that DIB contact angle follows the Young-Lippmann equation up to 175 mV, regardless of starting angle. At higher voltages, the data obtained from the DIB with θ_0 = 29° indicates that the change in the contact angle saturates. The saturation issue will be discussed later, but the immediate point to be made is that the lower initial θ_0 incurs a larger nominal angle change as voltage increases. Thus, while a given amount of electrical energy (for fixed values of V, C_M and γ_m) produces a fixed change in the cosine of the contact angle, the corresponding change in the nominal value of θ is greater when starting from a lower θ_0 (closer to unity on the cosine curve, refer to Figure 31). Because we demonstrated that our method for measuring monolayer and bilayer tensions in a DIB is limited most by the resolution of contact angle measurement, the nonlinear relationship between angle

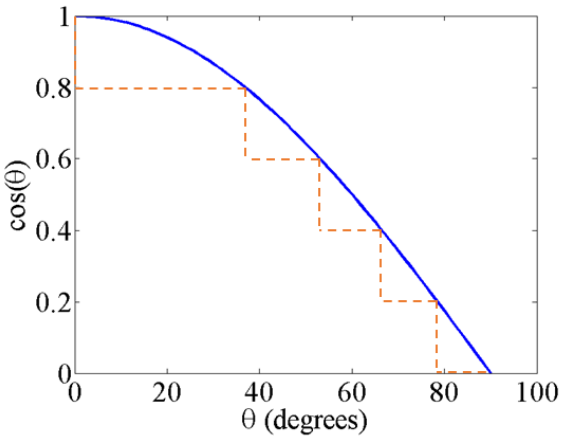

Figure 31. The solid line shows cos(θ) across the range of θ = 0° to 90°. The dashed line shows unitary stepwise (vertical) decreases in cos(θ) and the associated (horizontal) increase in nominal θ.

change and applied voltage suggests that achieving a small θ_0 (e.g. via mechanical manipulation or even through oil selection) could be used to maximize the nominal change in contact angle and improve the accuracy of this technique. This approach is also common to other electrowetting-based applications, including single droplet electrowetting on dielectric (EWOD) experiments,[249] where tuning the initial wetting condition to make θ_0 small can be used to enhance angle change in response to voltage.[249]

Nonetheless, it is necessary to remember that the nominal contact angle is used in the Young Equation to compute bilayer tension. Thus, while the two membranes characterized in Figure 30D-E exhibited bilayer tensions within 2% of each other, the amplitude of error in determining bilayer tension also varies nonlinearly with starting contact angle. Thus, it is advisable to initiate Part 3 of the method at a location where the droplets are minimally deformed by electrode separation in order to reduce the effects of mechanical manipulation on the accuracy of determining bilayer tension.

3.2.6 Effects of Initial, Zero-Volt Contact Angle with Young-Lippmann

For completeness, we also investigated the effect of starting contact angle on the voltage-induced change in membrane capacitance (Figure 32). The Young-Lippmann equation can be used to predict the contact angle in response to applied voltage assuming that specific capacitance (C_M), monolayer tension (γ_m), and the zero-volt contact angle (θ_0) are known. Rearranging Equation 8 yields

$$\theta_V(V) = \cos^{-1}\left(cos(\theta_0) - \frac{C_M}{4\gamma_m}V^2\right). \qquad \text{Equation 17}$$

Figure 32A shows theoretical θ_V as a function of voltage across the range of 0-300 mV for various initial contact angles (θ_0 = 5°, 15°, 25°, 35°, 45°). C_M and γ_m values used in the calculations are taken from Table 7 (for DPhPC in hexadecane). The data in Figure 32A can be used to compute the nominal change in the contact angle ($\Delta\theta$) in response to voltage for each zero-volt angle case using

$$\Delta\theta(V) = \theta_V(V) - \theta_0. \qquad \text{Equation 18}$$

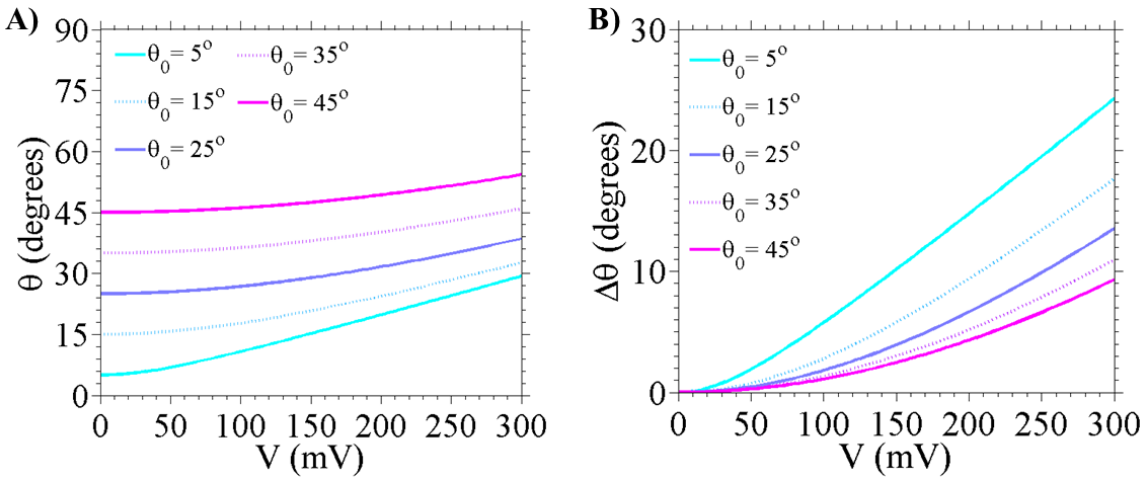

Figure 32. A) Theoretical contact angle predicted by the Young-Lippmann equation for various hypothetical zero-volt contact angles (θ_0) with a DPhPC DIB formed in hexadecane (C_M = 0.65 μF/cm^2, γ_m = 1.18 mN/m). The simulated input voltage is linearly varied across the range from 0-300 mV. B) Data in (A) converted to show the change in contact angle ($\Delta\theta$) with increasing applied voltage.

Figure 32B shows $\Delta\theta$ for each zero-volt angle case shown in Figure 32A. For a given applied voltage, the magnitude of the nominal change in θ depends on θ_0. For instance, 300mV results in a 24° change when θ_0 = 5° while the same voltage results in <10° change when θ_0 = 45°. Notably with DIBs, typical values for θ_0 are closer to 25-35°, although it is clear that the zero-volt contact angle can be an important parameter affecting the electrowetting response described by the Young-Lippmann equation.

Figure 33A-B shows actual capacitance and area data collected at 12.5 mV intervals between 0 and 175 mV in electrowetting trials beginning from one of two zero-Volt contact angles. The variation in θ_0, as before, is achieved via mechanical manipulation. The data in Figure 33A-B can be reduced to a single plot for comparison by normalizing capacitance and area by their initial zero-Volt values. The resulting behavior can be described by

$$C/C_0 = 1 + \alpha V^2, \qquad \text{Equation 19}$$

and

$$A/A_0 = 1 + \beta V^2, \qquad \text{Equation 20}$$

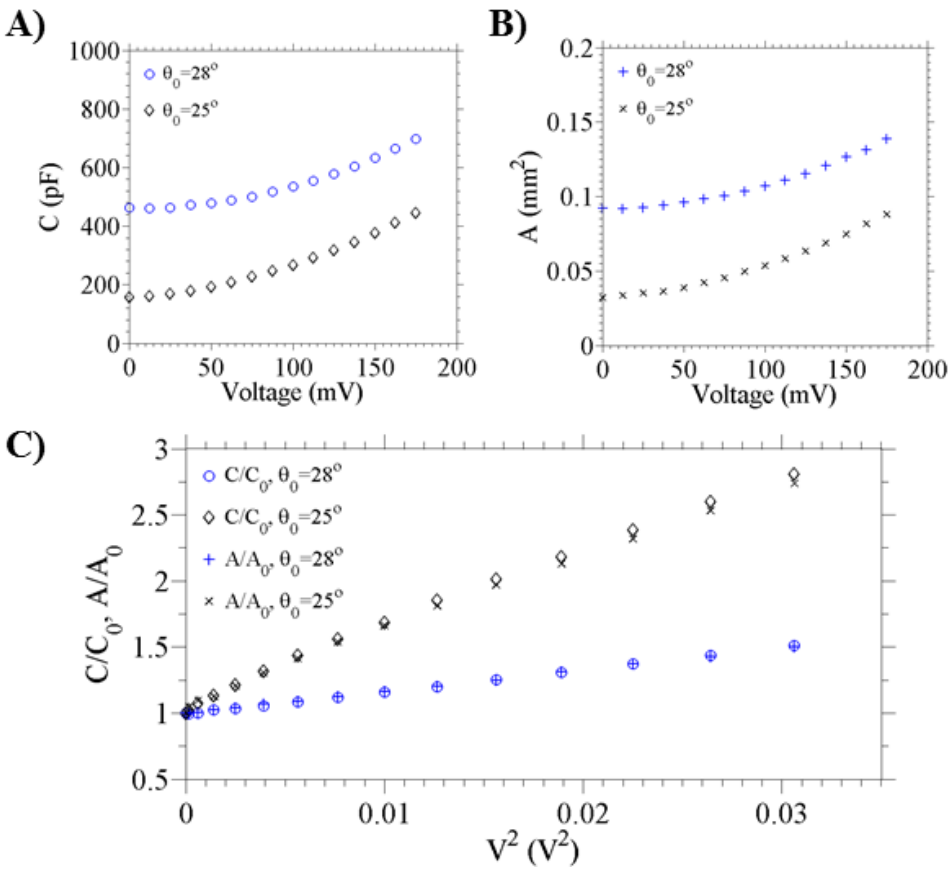

Figure 33. A-B) Capacitance and area, respectively, as a function of voltage with two DIBs with varying initial, zero-Volt contact angle. C) Capacitance and area data in (A-B), normalized by the zero-volt capacitance and area, respectively, and plotted against the square of applied voltage.

where α and β are parameters that describe the sensitivity of interface to capacitance and area increases, respectively, in response to increasing applied voltage and electrowetting. The data in Figure 33A-B can be normalized by the zero-Volt C and A values and plotted as a function of the square of applied voltage as presented in Figure 33C. Linear least squares regression of the curves in Figure 33C return slope values equal to α and β for each case. For both initial contact angle cases, we see that capacitance and area are linear with respect to the square of applied voltage as expected from Equation 19 and Equation 20. The fact that C/C_0 and A/A_0 curves (Figure 33C) for a given initial contact angle are almost overlapping is a result of the fact that C_M is not significantly affected by voltage. [50] However, the data in Figure 33A-B shows that α and β are affected by initial contact angle imposed by varying electrode separation and droplet positioning. Specifically, we see higher values for both α and β when beginning at lower zero-Volt contact angles (i.e.

droplets pulled apart slightly from equilibrium) which is in direct agreement with larger theoretical and experimentally observed changes in the nominal contact angle when starting at lower zero-Volt angles.

The analysis presented in this section shows that the sensitivities of nominal bilayer capacitance and area to voltage are affected by the starting angle. However, the linear relationship between capacitance and area (i.e., Figure 27B), and thus the determination of C_M, holds across a wide range of areas obtained via mechanical manipulation as we [10] and others [50] have shown previously. Section 3.2.8 includes addition analysis of the possibility that specific capacitance varies under an applied dc voltage.

3.2.7 Limits of electrowetting in DPhPC DIBs

Numerous studies of electrowetting have shown that the change in the wetting angle saturates at high voltage, falling short of the expected angle change predicted by the Young-Lippmann equation. [249-252] With a single sessile droplet placed on a dielectric, common in many EWOD systems, the saturation limit is believed to be the result of dielectric charging or breakdown, charging of the insulating fluid surrounding the droplet, formation of instabilities and/or microdroplet ejection, or reduction of interfacial tension to zero. [250] The zero-tension theory, which states that the maximum angle change occurs at a voltage where the interfacial tension is zero, [250, 252] is capable of predicting the saturation angle for single droplet EWOD cases. [250] Applying this concept to a DPhPC DIB, the Young-Lippmann equation predicts that an applied voltage of nearly |800| mV is required to reduce a bilayer tension to zero (calculated using Equation 10 and values of C_M and $\gamma_{b,0}$ for DPhPC DIBs in hexadecane, Table 7). However, because the typical rupture potential of DPhPC DIBs occurs at |200-300| mV,[10] it is unlikely that saturation of the contact angle could be caused by reducing tension to zero. Rather, the observed contact angle saturation at voltages above |175|mV is likely due dielectric breakdown and electroporation which typically precede bilayer rupture. [10, 253]

3.2.8 Effect of Increasing Voltage on C_M

When using specific capacitance to determine monolayer tensions in Equation 8, it is important to understand how much C_M varies when an electric field is applied to induce changes in the contact angle. The effect of voltage on C_M has been shown previously to follow the experimental relation [50, 199, 205]

$$C_M = C_{M,0}(1 + BV^2), \qquad \text{Equation 21}$$

which involves the specific capacitance at 0 mV ($C_{M,0}$), the magnitude of applied dc bias (V), and a parameter (B) describing the voltage dependence of C_M. While electrostriction of the membrane is a possible mechanism for voltage affecting C_M, prior works have shown that planar lipid bilayers formed in the presence of solvents can exhibit voltage-dependent specific capacitance due to the electric field exerting a compressive force that excludes trapped oil from the membrane, thereby reducing the thickness of the hydrophobic core. [50, 199, 205] This effect is particularly significant when membranes are formed in the presence of organic solvents with high solubility in the hydrophobic region of the bilayer, and less in "solvent-free" membranes formed in the presence of large-molecule solvents that are more easily excluded from the hydrophobic region. [226, 254, 255]

Figure 34 shows values obtained for C_M normalized by $C_{M,0}$ at each voltage step with a DPhPC DIB in hexadecane. Discrete values of C_M at each voltage step are calculated (Figure 35) using the capacitance and area at that voltage step (as opposed to dynamically varying area at each voltage step to determine C_M). Slight nonzero offset (Figure 35) in the total measured capacitance is obtained from mechanical tuning and is used to correct the instantaneous calculated C_M. From Equation 21, a linear least squares regression of $C_M/C_{M,0}$ as a function of V^2 yields a straight line with an intercept of 1 and a slope of 0.27 V^{-2} representing the value for parameter B. The resulting value of B indicates that C_M would only increase by 0.01 μF/cm^2 at a voltage of |200|mV, a deviation that is approximately 1.6% of the value of specific capacitance measured at zero volts for DPhPC DIBs in hexadecane (0.67 μF/cm^2). Compared to the larger B values measured for planar bilayers formed with decane as the oil-phase (4 V^{-2}), [50] our result is much lower as expected due to the decreased solubility of hexadecane in the bilayer. Our results are agreement

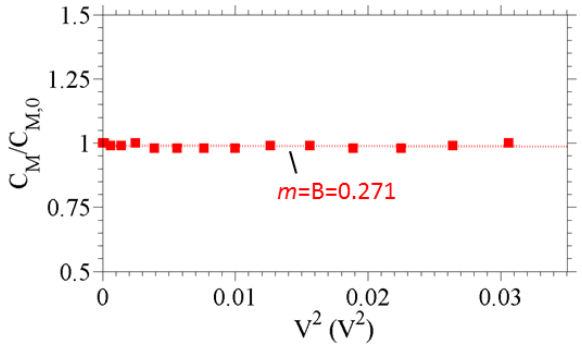

Figure 34. Normalized specific capacitance for a DPhPC DIB (hexadecane oil phase) as a function of applied voltage. $C_{M,0}$ is the specific capacitance measured via dynamic capacitance/area changes with voltage clamped at 0mV (see Figure 26, part II).

with previously reported values of *B* in tests with solvent-free supported bilayers. [50, 200, 228] As a result, small values of *B* in solvent-free membranes allow for monolayer and bilayer tensions based on contact angle and specific capacitance to be accurately determined using a value of specific capacitance obtained with zero bias applied. This approach is supported by previous reports that the Young-Lippmann equation accurately predicts the response of lipid bilayers subject to applied voltage when using a constant value for $C_{M,0}$. [50, 87, 228]

3.2.9 Effects of Droplet Deformation Due to Gravity

Specific capacitance measurements involve area calculations that are affected by the shape and circularity of a DIB interface. The extent of gravity-driven droplet deformation is investigated experimentally by performing specific capacitance measurements in hexadecane with pipetted droplets of different sizes. Droplets are pipetted onto the agarose-coated ball-ended electrodes as usual in these experiments, and specific capacitance measurements made on multiple newly formed (symmetric) DIBs with droplet volumes ranging from 200 nL to 500 nL. Figure 36A shows images of DIBs formed from aqueous droplets of varying volume in hexadecane. These "bottom view" images are obtained through the microscope objective directly below the drops.

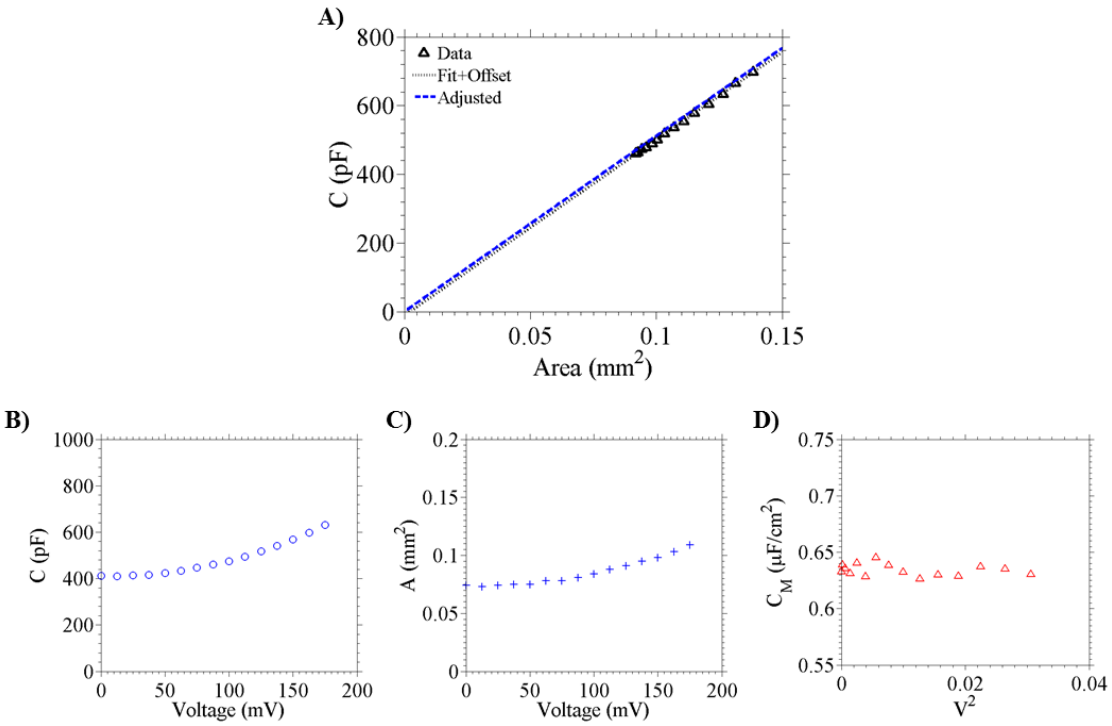

Figure 35. A) Actual C versus A data obtained during specific capacitance measurement along with the fit obtained from linear least squares regression (dotted, black) of C versus A. The raw fit displays a small capacitance offset (y intercept) when A=0. Removing the -11.7 pF offset adjusts the fit (dashed, blue) and can be used to correct. B-D) Electrowetting to measure voltage-dependence of C_M from 0-175mV. (B) and (C) show capacitance (offset removed) and area measured at each voltage step, respectively. D) C_M at each voltage step calculated discretely using C and A data in (B-C).

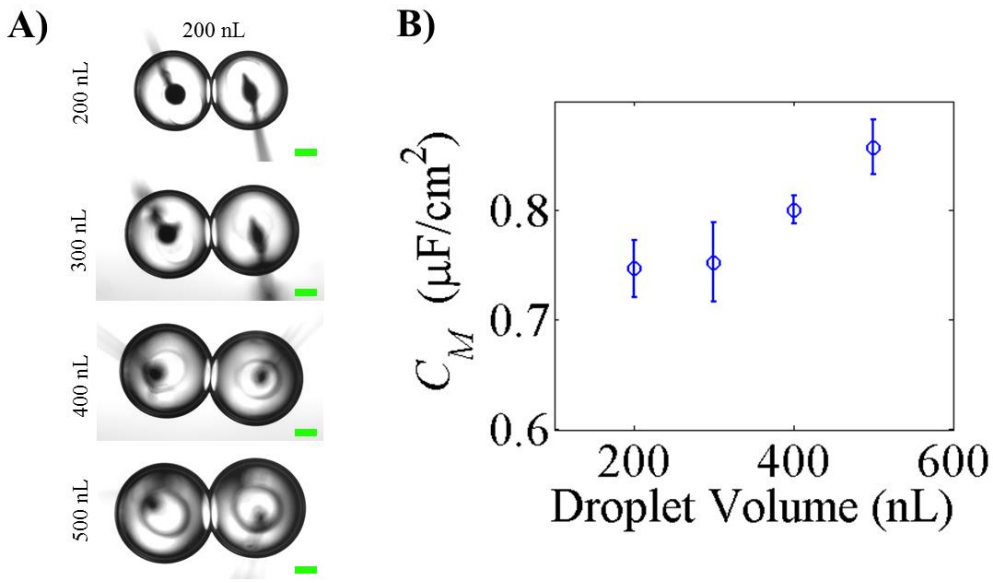

Figure 36. A) DPhPC DIBs formed in hexadecane using droplets with volumes of 200, 300, 400, and 500 nL. Images are used to determine the bilayer contact length *a*. Green scale bars represent 100 μm. B) Specific capacitance (C_M) as a function of droplet size, calculated via the method of dynamically varying area (error bars represent ± one standard deviation; see Table S1). For the results shown here, the bilayer is assumed to be circular with area determined by $A=\pi a^2/4$.

Images are processed to determine the bilayer contact length which is a principal diameter, *a*. If the interface is assumed to be circular, the area of the interface is then calculated by:

$$A = \pi a^2 / 4 \qquad \text{Equation 22}$$

C_M values are calculated for each trial using a circular area assumption. Figure 36B shows the average specific capacitance value as a function of droplet volume (error bars represent ± one standard deviation, n >3 for all volume cases except the 200 nL case where n = 2). It is clear that specific capacitance values are increasing with droplet volume despite the fact that the thickness and dielectric permittivity of the lipid bilayer should be insensitive to the macroscale droplet size. However, the observed increase in C_M with droplet size is explained by considering droplet deformation due to gravity. There are two dominant forces that determine droplet shape: gravity and surface tension. For small droplets with low Bond numbers, the effects of gravity become negligible and surface tensions typically dominate. However, when interfacial tensions are also very low or when droplets are large, the droplet shape is affected by surface tension and gravity. It should be noted that with our method as described, the bottom-up view through the microscope

provides viewing access of the bilayer diameter from only one direction. If droplets are contained in a less dense oil phase, then they will sag in the vertical direction. Thus, the contact length obtained from bottom view images represents the minor axis (*a*) of an ellipse whose major axis is being stretched by gravity. In these cases, the actual bilayer area is in fact larger than what would be calculated if the bottom-up diameter is used along with the assumption that the bilayer profile is circular. The result is that specific capacitance, taken as capacitance divided by area, is artificially high when droplets sag and circular area equations are employed.

3.2.10 Experimental and Computational Determination of Ellipticity Factors

Previously reported values for C_M can be used to calculate a correction factor for each droplet volume based on the experimentally observed values in Table 4. The correction factor is derived from the geometry of the interface as it assumes a non-circular profile due to droplet deformation. A sagging droplet has a major axis diameter that is longer than the minor axis diameter obtained from images. Assuming the interface to take the form of an ellipse, the area is now calculated by:

$$A = \pi ab/4 \qquad \text{Equation 23}$$

We introduce an ellipticity factor, ε, that represents the ratio of the major axis diameter (*b*) to the minor axis diameter (*a*).

$$\varepsilon = \frac{b}{a} \qquad \text{Equation 24}$$

Table 4**.** Summary of C_M values obtained in DPhPC DIB trials with varying droplet volume assuming a perfectly circular interface.

	Drop Volume			
	200 nL	**300 nL**	**400 nL**	**500 nL**
C_M	0.741 (0.028) *n*=8	0.753 (0.036) *n*=13	0.801 (0.013) *n*=7	0.828 (0.017) *n*=2
correction factor	1.1585	1.1773	1.2519	1.3413

*values from tests performed using DPhPC in pure hexadecane

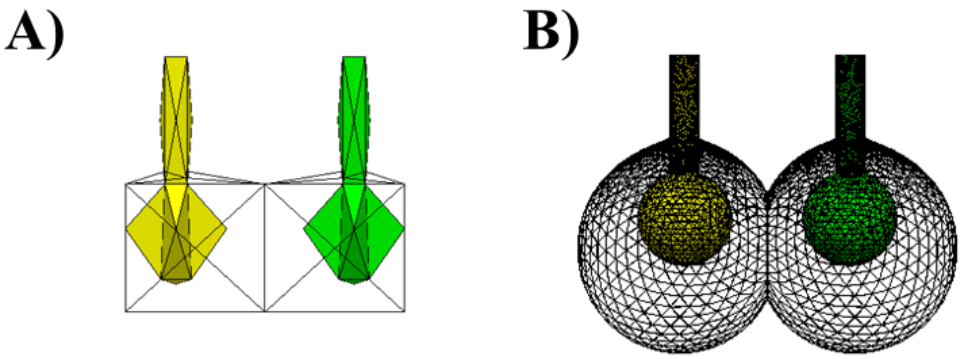

Figure 37. Representative images showing a DIB (A) before, and (B) after evolving. The simulation is performed using Surface Evolver, a computer program that simulates interfacial behavior by minimizing the free energy of defined surfaces. A) Initial surface structure defining the electrodes (one yellow and one green) and the water droplets. B) An image saved after evolving the DIB with monolayer tension set to 1 mN/m, bilayer contact angle at 25°, electrode spacing of 0.7 mm, and 300 nL droplet volumes.

Rearranging and substituting Equation 24 into Equation 23 yields the area of the elliptical interface in terms of only the minor axis diameter and the ellipticity factor.

$$A = \pi a(\varepsilon a)/4 = \varepsilon(\pi a^2/4) \qquad \text{Equation 25}$$

While we do not directly observe the major axis diameter of sagging droplets, we are able to calculate ellipticity factors by dividing our artificially high values of C_M by an accepted value (0.64 μF/cm^2, DPhPC, hexadecane). [50, 256] The resulting volume-specific ellipticity factors are shown in Table 4.

Surface Evolver [257] is a computer program that has been used to simulate the behavior of droplets and foams. [258] The program operates by minimizing the free energy of surfaces created using defined vertices, edges, and facets, and it is employed here to further quantify droplet deformation as a function of the difference in droplet and oil densities. Figure 37 shows the results of an evolution from initially defined surfaces (Figure 37A) to a suspended DIB (Figure 37B) with the droplets in wireframe and the electrodes colored green and yellow. The model used includes gravity and allows for changing the density of the droplet and the oil phase. Certain parameters are fixed during each evolution including the monolayer tension at the oil-water interface (1 mN/m for all), the tension between the electrode and the oil (5mN/m for all), the droplet volume, and the

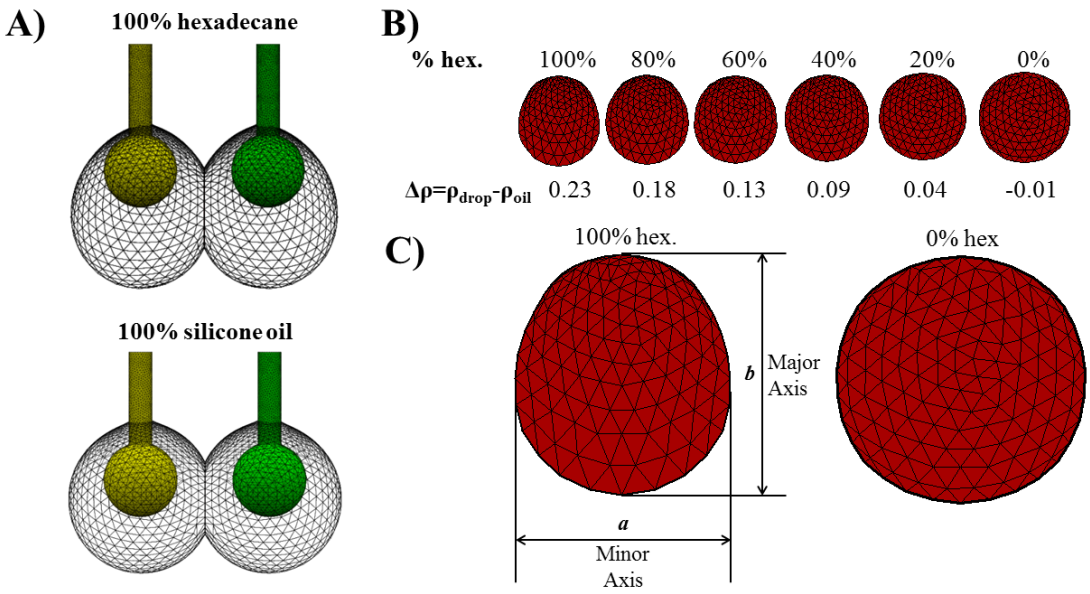

Figure 38. A) DIBs after evolution in Surface Evolver. Top – the oil phase is pure hexadecane, and droplets are seen to sag downwards. Bottom – the oil phase is pure AR 20 which is more dense than water. B) Images of the bilayer region alone after Surface Evolver trials with 300 nL droplets and varying ratios of silicone oil: hexadecane. The difference between the density of the aqueous droplet and the oil mixture is shown. C) Magnified versions of the images in (B) representing pure hexadecane (left) and AR 20 silicone oil (right).

equilibrium contact angle. Each droplet is confined to the electrode along the cylindrical portion such that the ball tip remains fully encapsulated by the droplet.

To assist determination of shape ellipticity factors for specific capacitance area calculations, we investigate the effects of varying density differences by performing a series of evolutions while changing the density difference to represent fractions of silicone oil ranging from 0 to 100%. Figure 38A-B shows images saved after separate evolutions with varying oil compositions. Figure 38A shows a side view of the DIB at each extreme: pure hexadecane (top) and pure silicone oil (bottom). Figure 38B shows the bilayer region for 100%, 80%, 60%, 40%, 20%, and 0 % hexadecane volume fractions as indicated above each image. Similarly, the density difference between the water and oil mixture for each case is displayed below each respective image. The interface formed in pure hexadecane ($\rho_{hexadecane}$=0.77 g/mL) is clearly sagging in the vertical direction. As expected, this ellipticity diminishes as the oil mixture is loaded with dense silicone oil. The coordinates of the equilibrium bilayer are exported to MATLAB to further analyze bilayer

Table 5. Table of Ellipticity Factors by Oil Type

Oil	Correction Factor, Ellipticity (b/a)
Decane	1.232
Hexadecane	1.158
1-1 AR20:Hexadecane	1.045
9-1 AR20:Hexadecane	0.990

area and its geometry. Ellipticity is quantified by extracting the minor (*a*) and major (*b*) axis diameters as illustrated in Figure 38C. Ellipticity can then be monitored as a function of oil composition by evaluating the quantity $\varepsilon_{b/a}=b/a$ which increases from unity as the droplets sag and extend the bilayer major axis. Figure 39A shows calculated values of $\varepsilon_{b/a}$ as a function of the difference in the density of the droplet and the oil mixture with evolutions using 300 nL droplets and a 25° equilibrium contact angle (half-bilayer angle). Clearly, the interface transitions from being vertically distended and elliptical to nearly circular as the silicone oil content increases and the density difference decrease. Identical results are obtained in other evolution trials using a 45° contact angle (Figure 39B), thus it is not expected that conclusions drawn from Surface Evolver analysis are heavily affected by the selection of contact angle (at least in the typical range of around 25-45°).

The values obtained for $\varepsilon_{b/a}$ provide both a) information regarding the shape of the bilayer, and also b) the ellipticity factors required to confidently estimate the bilayer area using the minor axis diameter alone. The ability to calculate area using the minor axis diameter enables more accurate estimation of area in experiments with images taken from beneath the suspended droplets through an inverted microscope. All experimental tests described in Chapter 3 and Chapter 4 are performed using 300 nL drops, and the same pipette is used for consistency. To calibrate Surface Evolver calculations, we compared the volume-specific ellipticity factor (Table 4) obtained from DIBS formed with 300nL droplets to values of ellipticity for varying droplet volumes computed in Surface Evolver. This comparison shows that the experimentally observed ellipticity is most

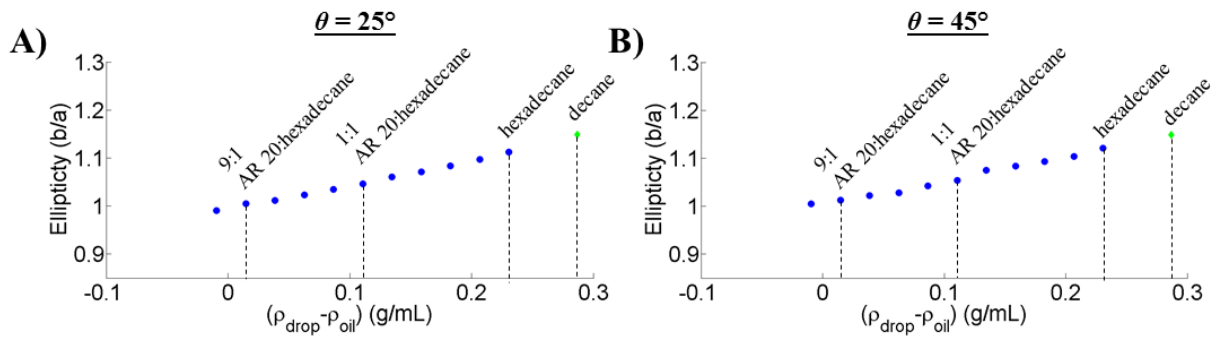

Figure 39. Ellipticity as a function of the difference in droplet and oil density. Ellipticity values are computed based on the major and minor axis diameters calculated using coordinates of the interface after Surface Evolver trials. (A) and (B) are drawn from Surface Evolver trials using identical parameters except for the equilibrium contact angle. A) θ=25°. B) θ=45°. The density differences associated with oil compositions commonly used in literature and in Chapter 4 are labeled. Blue circles represent values obtained by varying the volume fraction (% vol) of AR 20 in an AR 20:hexadecane mixture. The green diamond represents pure decane.

closely reproduced by Surface Evolver calculations when using 400nL droplets. To our knowledge, there are no published values of C_M for planar bilayers or DIBs formed in mixtures of hexadecane and AR20 silicone oil, thus Surface Evolver is used to compute ellipticity factors for 400 nL droplets with the density difference adjusted to match each oil combination tested. The final ellipticity factors used in area calculations for specific capacitance measurements provided in this Chapter 3 and Chapter 4 are listed in Table 5.

3.2.11 Effects of Surface Tension on Ellipticity

Monolayer tension values provided in Table 7 fall between 1.03 and 1.42 mN/m. These results are based on specific capacitance trials in which area is corrected by the factors in Table 5, and these factors were obtained from Surface Evolver trials using a value of 1 mN/m as the input monolayer tension. To investigate the possibility that ellipticity changes significantly with increasing monolayer tension, Surface Evolver trials are performed for a range of monolayer tension values. The droplet volume is set to 300 nL, and the oil type is set as pure hexadecane where gravitational effects are most significant. Figure 40 shows calculated values for ellipticity as a function of the input monolayer tension. Figure 40 shows that the major axis of the interface is about 11% longer than the minor axis at 1 mN/m (ε = 1.11). Increasing tension to 1.5 mN/m reduces the ratio $\varepsilon=b/a$ to 1.07, thus the cases with 1.4 mN/m tensions would require < 3-4 % change in the ellipticity

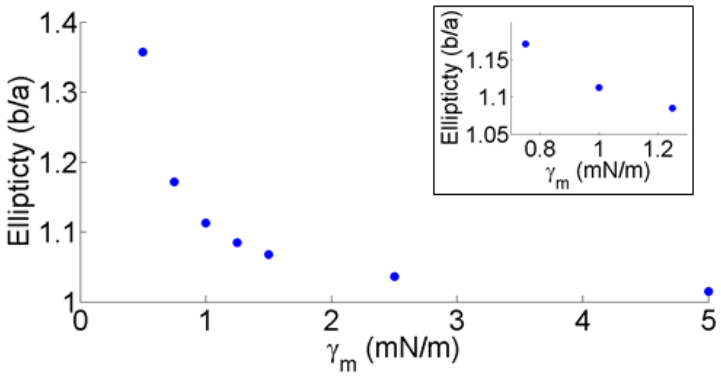

Figure 40. Ellipticity as a function of input monolayer tension obtained from Surface Evolver trials with 300 nL droplets in pure hexadecane. The inset highlights the region of monolayer tension values encountered experimentally in this work (~1.0 mN/m).

factor. For the cases tested here, it thus seems reasonable to use the single set of ellipticity factors obtained from the Surface Evolver data using 1 mN/m as the input monolayer tension.

3.3 Chapter Summary and Conclusions

The Young-Lippmann equation relates changes in contact angle to the applied voltage which affects the interfacial tension. In the DIB platform, where mechanical manipulation can be used to accurately measure C_M, and applied bias voltage induces measurable changes in contact angle, the Young-Lipmann relation provides a framework for simultaneous measurements of both monolayer and bilayer tension. The method is simple and involves measuring changes in the contact angle between droplets as applied bias voltage is increased. Contact angle alone is not sufficient for tension calculations as the Young-Lippmann equation includes membrane specific capacitance. However, specific capacitance is easily and precisely determined during the same test for tensions with droplets suspended on agarose-tipped electrodes. Knowledge of the shape (i.e. the circularity) of the interface is crucial to the accuracy of the measurement, particularly in light of observed droplet deformation due to gravity when there is a difference in densities of the oil and aqueous phases. Such density differences are encountered here with ≥ 200 nL droplets in tests using pure hexadecane or mixtures of hexadecane and silicone oil. Further, we learned that the zero-Volt contact angle between droplets increases with increasing droplet area (as droplets are pushed

together). However, while it was shown that values of monolayer tension are not affected by manipulation-induced changes to θ_0, the nominal contact angle does affect the caculation of bilayer tension In both theory and practice, larger angle changes are obtained for lower θ_0. This conclusion allows tuning of the system (targeting $\theta_0 \leq \theta_{eq}$) to achieve greater angle changes for the same voltage, which increases the signal-to-noise ratio of angle measurement.

With appropriate understanding of the shape of the interface, we demonstrated that this procedure exhibits comparable or better accuracy in measuring values of specific capacitance, bilayer tension, monolayer tension, and free energy of formation to methods described in prior literature. Further, all four physical properties can be measured in a single test over the course of 30 minutes or less. There are several advantages of the DIB-Young-Lippmann approach over supported or painted lipid bilayer techniques: [226, 228] 1) forming bilayers between lipid coated droplets allows the area of the bilayer to be easily manipulated, which has been shown to enable accurate determination of specific capacitance; 2) bilayer formation in a liquid environment (versus on a solid support) provides direct visual access to bilayer contact length and contact angle.

CHAPTER 4

APPLICATION OF SPECIFIC CAPACITANCE AND TENSION MEASUREMENTS IN DROPLET INTERFACE BILAYERS

In Chapter 3, a multi-part experiment for determining monolayer and bilayer tension is presented and validated with data obtained from DPhPC DIBs in hexadecane. This chapter address Objective 2 as described in Section 1.3.2. To demonstrate the value of the multi-part method and begin using it to acquire new information regarding the effects of non-lipid species in the membrane, the method is been applied to study the effects of oil (solvent) type used for DIB formation, the addition of cholesterol, and the incorporation of mixed-monolayer protected cell-penetrating nanoparticles on the specific capacitance and tension state of DIBs. As with DPhPC DIBs in hexadecane, equilibrium monolayer tensions are compared to values obtained from a pendant drop goniometer. The results provided by specific capacitance and tension measurements are used to help understand the molecular level organization of various solvents, cholesterol molecules, and cell-penetrating nanoparticles in a lipid bilayer. It is important to recognize that the information obtained via measurements of C_M and tension is not easily obtained by measurements of conductance alone, as is more typical with ion-channels and pore-forming peptides, as the three types of membrane-active species tested here do not necessarily affect the conductance.

4.1 Materials and Experimental Methods

4.1.1 Mixed-Monolayer Protected Nanoparticles

The nanoparticles (NP) used in this chapter contain gold cores and are modified through the attachment of lipid-like ligands. The main class of NPs used herein is coated with two types of

Note: This chapter presents a modified portion of the published paper “Direct In Situ Measurement of Specific Capacitance, Monolayer Tension, and Bilayer Tension in a Droplet Interface Bilayer " [49].

ligands: one ligand type is hydrophilic (11-mercapto-1undecanesulphoniate, MUS) and that is hydrophobic (1-octanethil, OT). Specifically, these mixed-monolayer protected NPs are coated with a 50:50 (mol:mol) ratio of MUS and OT ligands. In addition to the 50:50 MUS:OT mixed-monolayer protected NPs which have been shown to adopt a "striped" ligand pattern, [259] DIB experiments are also performed including NPs coated entirely (100%) in hydrophilic MUS ligands (i.e., no OT included). Both NP types are synthesized by collaborators (Ahmet Bekedemir and Francesco Stellacci) using methods described elsewhere.

A series of prior investigations have established the fact that MUS:OT NPs are capable of translocating through cell membranes, thus rendering them as a promising candidate for applications like drug delivery or gene transfection. [48, 215, 216, 260] In contrast to the cell-penetrating properties of the amphiphilic NPs coated with a mixture of MUS and OT ligands, NP coated entirely in hydrophilic MUS (100 MUS) do not readily translocate through cell membranes. [215] The interactions of these MUS:OT and MUS NPs with real cell membranes prompted a study of NP interaction with model membranes using a planar lipid bilayer approach. [47] In a study using painted BLMs, Carney et al. observed concentration dependent increases in membrane

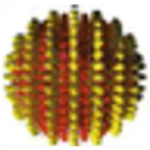

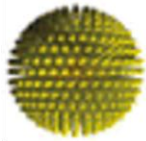

Type	"Striped" MUS:OT NPs	MUS NPs
Core	Gold (Au)	Gold (Au)
Hydrophilic ligand (abbrev.)	11-mercapto-1-undecanesulhponate (MUS)	MUS
Hydrophobic ligand	1-octanethiol (OT)	none
Particle size	~2-10 nm	~2-10 nm

Figure 41. Details regarding the two types of NPs used in this work (see also Section 14.2.3). The mixed-monolayer protected "striped" NPs are coated with a mixture of hydrophilic and hydrophobic ligands. 100 MUS NP are coated entirely in hydrophilic ligands. (Images reproduced from [48]).

Table 6. Molar Volumes of DPhPC Acyl Chains, Decane, Hexadecane

Species	Molar Volume [cm^3/mol]	Ref.
DPhPC acyl chains (tetramethyl hexadecanoic acid)	444.8	[1]
Decane	194.7	-
Hexadecane	294.1	[5]

capacitance upon addition of the 50:50 mixed MUS:OT NPs while addition of 100 MUS ("control") NPs elicited no such increase in capacitance. The concentration dependent changes in BLM capacitance were well described by a Langmuir adsorption model, but the mechanism explaining the increase in capacitance is not completely clear. The authors concluded at that time that the MUS:OT NPs accumulate in the lipid bilayer, thus the goal in this work is to use DIB-based measurements of C_M and monolayer and bilayer surface tensions to a) quantitatively probe for the occurrence of NP accumulation in the bilayer, nd b) provide mechanistic level insight as to the cause of previously observed NP induced changes in BLM capacitance. [47]

4.1.2 Lipid/Solvent Molar Volume Ratio Calculations

Estimation of the molar volume ratio of lipid acyl chains to solvent molecules involves the molar volumes of the lipids and solvents as displayed in Table 6. Where available, a source for each value is included in the table. The referenced value for hexadecane is in close agreement with the value obtained simply by dividing the solvent molecular weight by the solvent density to obtain a molar volume with units of [cm^3/mol]. Thus the value listed for decane is calculated simply using the density (0.731 g/cm^3) and molecular weight (226.45 g/mol) of decane. Note that the value listed for DPhPC, based on the molecular volume provided by the LIPID MAPS database[1] for a single tetramethyl hexadecanoic acid molecule, is converted to molar volume and doubled to account for two acyl chains on each DPhPC lipid molecule.

Results provided in Chapter 4 are based on previous estimates[50] that with DPhPC DIBs formed in hexadecane solvent, approximately 10% of the hydrophobic region volume consists of the hexadecane solvent. Thus, for any given volume of the hydrophobic bilayer region, a volume ratio of 9:1 exists for lipid acyl chains:solvent. Dividing each value in the ratio by the molar volume then provides a molar ratio of acyl chains: solvent (note: the calculations here include the assumption of two acyl chains per lipid). It then follows that if 10% of the hydrophobic region volume consists of hexadecane solvent, the molar ratio of lipid:solvent falls around 6:1, which means that there is one solvent molecule for every 6 lipids. Consistent with previous findings, results provided in Section 4.2.1 below suggest that DPhPC DIBs formed in decane contain 43% decane solvent by volume. Conversion from a 53:47 volume ratio of lipid:decane to percent molar volume provides an estimate of 0.58:1 (or 1:1.7). Thus it appears that when DPhPC DIBs are formed in decane, the hydrophobic region contains approximately two solvent molecules for every lipid molecule. These calculations assume that the molar volumes of each component are fixed quantities.

4.2 Results and Discussion

4.2.1 Effects of Solvent on Membrane Thickness and Lipid Packing

First, tests are performed to determine monolayer and bilayer tensions for DPhPC DIBs formed in a mixed solvent phase containing silicone oil (AR 20) and hexadecane. Prior to performing contact angle measurements versus voltage, values of specific capacitance are measured separately for DPhPC DIBs formed in pure hexadecane, in a 1:1 (vol:vol ratio) AR 20:hexadecane mixture, and in a 9:1 mixture of AR 20:hexadecane. Values obtained for C_M (average ± standard deviation) are shown in Figure 42A as a function of the volume percentage of silicone oil. These values are then used in calculations of monolayer tension obtained via Part 3 of the experiment (Figure 42B) and are combined with measured values of θ_0 for each to estimate bilayer tension at 0 mV (Figure 42C). Table 7 presents average values, standard deviations, and the number of trials included for each case tested, as well as for DPhPC DIBs assembled in decane.

Table 7. Specific capacitance, thickness, and tension values obtained for DPhPC DIBs formed at 25°C.

Lipid Type	C_M [μF/cm²]	D_C [Å]	γ_m [mN/m] *	γ_m [mN/m] **	γ_b [mN/m]	$\theta_{0,eq}$ [°]	ΔF [mN/m] [mJ/m²]
DPhPC hexadecane	0.652 (0.027) *n*=13	29.9	1.18 (0.136) *n*=8	1.19 (0.067) *n*=3	2.04 (0.222) *n*=8	29.31 (2.13) *n*=116	0.302
DPhPC, 1:1 AR20:hex	0.667 (0.022) *n*=9	29.2	1.03 (0.115) *n*=4	1.01 (0.041) *n*=3	1.54 (0.198) *n*=4	41.63 (2.21) *n*=37	0.520
DPhPC, 9:1 AR20:hex	0.701 (0.027) *n*=9	27.8	-	-	-	42.15 (7.39) *n*=84	-
DPhPC, decane	0.488 (0.043) *n*=7	39.9	1.09 (0.095) *n*=7	-	2.11 (0.173) *n*=7	15.40 (1.06) *n*=43	0.078
DPhPC, 20% Chol. hexadecane	0.655 (0.030) *n*=8	29.7	1.42 (0.051) *n*=6	1.40 (0.111) *n*=3	2.50 (0.095) *n*=6	27.10 (1.65) n=80	0.312
DPhPC, 20% Chol. 1:1 AR20:hex	0.713 (0.045) *n*=3	27.3	1.24 (0.056) *n*=4	1.15 (0.045) *n*=3	1.92 (0.056) *n*=4	38.85 (2.34) *n*=128	0.548

*: DIB-electrowetting/Young-Lippman method
**: Pendant drop with goniometer
-: not measured
D_C: hydrophobic thickness, $D_C = (\varepsilon_r\ \varepsilon_0)/C_M$

It is well established that C_M varies strongly with the amount of solvent in the hydrophobic region. [50, 199, 254, 255] The solubility of solvent in the bilayer region generally increases with decreasing solvent molecule size. [226, 254, 255] As a result, techniques for measuring the thickness of the hydrophobic region are used to probe the amount of solvent trapped or dissolved in the bilayer. [50, 196] C_M is related to the thickness of the hydrophobic region (D_C) and permittivity (ε_r) of the hydrophobic region of the bilayer, as well as the permittivity of vacuum (ε_0) by

$$C_M = \frac{\varepsilon_r \varepsilon_0}{D_C}. \qquad \text{Equation 26}$$

The minimum value of C_M for the three oil cases tested is obtained for DIBs formed in pure decane (0.488 μF/cm^2), and the result is in close agreement with the value of 0.445 μF/cm^2 obtained elsewhere. [50]. C_M increases by 33% to 0.65 μF/cm^2 upon changing the solvent from decane to hexadecane, and the result is again consistent with previously reported values around 0.64 μF/cm^2. [50, 256] Compared to DIBs in hexadecane, C_M increases by 3.1% to 0.67 μF/cm^2 for 1:1 AR 20:hexadecane and by 7.7% to 0.70 μF/cm^2 for 9:1 AR 20:hexadecane, respectively. The increase

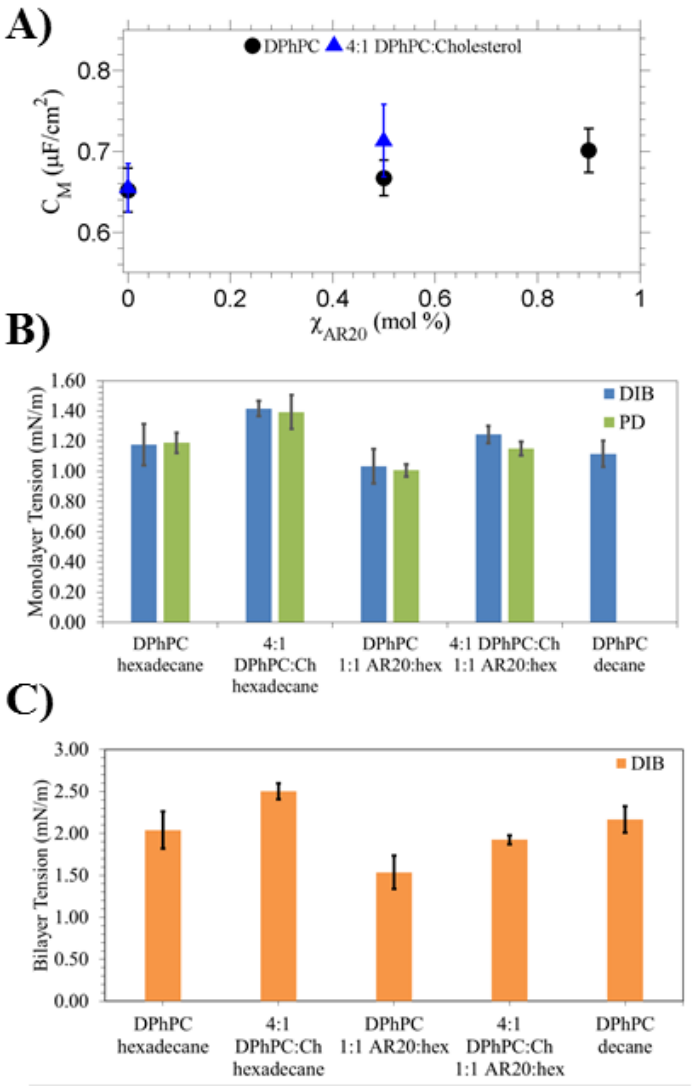

Figure 42. A) Values obtained from measurements of specific capacitance for bilayers as a function of the fraction of silicone oil added to the hexadecane oil phase. Error bars show ± one standard deviation. Two lipid compositions are tested in the various oil mixtures: pure DPhPC, and DPhPC containing 20% (mol %) cholesterol. B) "DIB-YL" –monolayer tensions measured by monitoring Young-Lippmann related changes in DIB contact angle as voltage is increased. "PD" – monolayer tensions measured using the pendant drop method with a goniometer. C) Bilayer tensions for each lipid-oil combination, calculated using average observed contact angle (case specific) and the monolayer tension measured via the DIB-YL method.

in C_M with increasing silicone oil in the oil phase indicates a thinner, more solvent-free bilayer, while the reduced value of C_M in decane indicates a thicker, oil-rich bilayer. Assuming a constant dielectric of ε_r = 2.2 for the hydrocarbon-rich hydrophobic region of the bilayer, our values of C_M yield thickness values of 29.9, 29.2, and 27.8 Å for DPhPC DIBs in 1:0, 1:1, and 9:1 mixtures of silicone oil:hexadecane, respectively. The 9:1 mixture thus results in bilayers that are 7.3% thinner than those in pure hexadecane. Gross et al. reported that the hydrophobic region of DPhPC-hexadecane DIBs is 10% oil by volume, leading us to believe that with DIBs formed in the 9:1 mixture, the bilayer hydrophobic region consists of only 2.7% (10%-7.3%) solvent by volume. The 1:1 mixture invokes a similar effect, although the thickness reduces by only 2.7% leading to hydrophobic regions containing approximately 7.3% (10%-2.7%) oil by volume. These estimates assume that the changes in volume, based on C_M measurements, are equal to the changes in membrane thickness (i.e. oil distributes evenly across the membrane area and the permittivity is unchanged). Converting percent volume oil to molar volume ratio provides a rough estimate of 6:1 for lipids:hexadecane in the hydrophobic region (refer to Section 4.1.2). The average thickness of DPhPC DIBs in decane is 39.9 Å. Based on the calculated thickness values, DIBs formed in decane are 33.4% thicker than those formed in hexadecane as a result of the increased solubility of small decane molecules in the hydrophobic region. [50] DPhPC bilayers formed in decane are expected to contain around 43% (10% +33.4%) oil by volume which is in close agreement with the estimate of 38% by Gross and Wallace. [50] Conversion of the volume ratio of lipid:decane to a molar volume ratio suggests that there are 1.7 decane solvent molecules for every lipid molecule present (refer to Section 4.1.2).

In addition to thickness, the oil used to form a DIB affects the tension state of a DIB. [226] Of the oils studied, bilayer tension is highest for DPhPC DIBs formed in decane. The data in Figure 42 and Table 7 show that the presence of silicone oil has the opposite effect. The average monolayer tension decreases by 17% from 1.18 mN/m in pure hexadecane to 1.03 mN/m in the 1:1 mixture. Meanwhile, bilayer tension decreases by 29% from 2.04 mN/m in hexadecane to 1.54 mN/m in the 1:1 mixture. Note that for 0:1 and 1:1 AR 20:hexadecane mixtures, the monolayer tension values obtained via the multi-step technique introduced herein are not significantly different than the values obtained via pendant drop measurements with a goniometer. Tension values are not

calculated for DIBs formed in the 9:1 AR20:hexadecane mixture, because these bilayers consistently ruptured at voltages near 100mV which prevented us from recording the increases in contact angle as applied bias voltage increases.

The free energy of formation is also a metric that can be used to understand the same phenomenon of oil-exclusion. Needham and Haydon [226] and Bibette et al. [100-102] reported that more solvent-free bilayers exhibit higher free energies of adhesion. Our results show that ΔF is nearly doubled in the 1:1 AR 20:hexadecane mixture compared to pure hexadecane, which itself has a ΔF value nearly four times that for decane-rich DIBs. Collectively, the DIB-electrowetting method appears to be a valid approach for measuring γ_m, γ_b, and ΔF, which serve as metrics for detecting solvent the presence of solvent and associated effects on lipid packing. The results of both C_M and ΔF measurements herein support the understanding that addition of AR 20 silicone oil to the hexadecane oil phase surrounding the droplets reduces the amount of remaining solvent in a DPhPC DIB, resulting in a thinner, more relaxed interface. The fact that monolayer tension also decreases with increasing silicone oil content, demonstrates that the hydrophobic regions of the lipid tails in monolayer are also better able to exclude silicone oil than pure hexadecane.

4.2.2 Effects of Cholesterol on Membrane Thickness and Lipid Packing

In a second study, we applied the multi-step procedure introduced in Chapter 3 to quantify the effects of cholesterol on C_M and tensions in DPhPC DIBs formed in various organic solvents. We study incorporation of 20 mol% cholesterol and do not pursue higher cholesterol levels due to its reduced solubility in DPhPC bilayers (40 mol% is the maximum for DPhPC,[261] compared with 50-60% across a range of acyl chain compositions (12:0, 16:0, and 22:0) and headgroup types (PC, PG, PE, and PS)[261]. When droplets containing DPhPC liposomes with 20 mol% cholesterol are used to form DIBs in pure hexadecane, we obtain a C_M of 0.655±0.030 μF/cm^2, γ_m equal to 1.42±0.051 mN/m, and γ_b of 2.50±0.095 mN/m. In comparison, DIBs formed in 1:1 AR20:hexadecane from droplets of 20% cholesterol-DPhPC solution yield C_M of 0.713±0.045 μF/cm^2, γ_m equal to 1.24±0.056 mN/m, and γ_b of 1.92±0.056 mN/m. The results for measured specific capacitance and tensions are illustrated in Figure 42 and listed in Table 7.

The average value of C_M is higher for DPhPC with 20% cholesterol compared to pure DPhPC in both oil cases tested. Assuming the effective dielectric constant of the interface is unchanged by the incorporation of cholesterol (ε_r=2.2)[262], Equation 26 shows that the increase in C_M must instead be attributed to thinning of the bilayer hydrophobic region. While numerous studies have identified lipid bilayer thickening upon incorporation of cholesterol,[221-224] the effect depends greatly on the length (relative to cholesterol) and degree of saturation of the lipid being used.[223, 225] For instance, McIntosh reports that bilayers comprised of phospholipids with up to 16-carbon acyl chains are thickened by the introduction of cholesterol, whereas 18-carbon chain bilayers in the solid phase (i.e. $T<T_m$) exhibit a reduction in thickness upon incorporation of cholesterol.[225] The effects of cholesterol on bilayer thickness are explained by comparing the hydrophobic lengths of the cholesterol and lipid chains[225]. Similar biphasic behavior regarding the effects of cholesterol on lipid transition temperature is also attributed to hydrophobic mismatch.[142] The cholesterol-induced decrease in thickness (Figure 42) measured herein suggests that a length mismatch exists between the DPhPC acyl chains and the embedded cholesterol. As encountered by McIntosh with 18-carbon acyl chains, the mismatch between rigid DPhPC tails and cholesterol hydrophobic lengths may create voids near the bilayer mid-plane that prompt the free ends of the acyl chains to bend or kink around embedded cholesterol molecules in an attempt to fill this space. The result is a net shortening of the lipid length and thinning of the bilayer hydrophobic region. This effect is also supported by molecular dynamics simulations showing flexible lipid acyl chains packing tightly around cholesterol molecules.[263]

The fact that C_M increases with the addition of cholesterol in both pure hexadecane and the 1:1 AR20:hexadecane mixture shows that DPhPC bilayers containing cholesterol are thinner than those without cholesterol in each solvent case. Equation 26 allows calculation of bilayer thickness, again using ε_r=2.2 as the dielectric constant, which reveals that bilayers containing 20% cholesterol possess a hydrophobic thickness of 29.7 Å or 27.3 Å when droplets are submerged in hexadecane or 1:1 AR20:hexadecane, respectively. Cholesterol reduces the thickness of bilayers in hexadecane by 0.14 Å (<0.5% of nominal value without cholesterol), however when DIBs are formed in a 1-1 AR20:hexadecane oil phase, cholesterol decreases bilayer thickness to 1.88 Å (a 6.4% reduction). This finding is consistent with prior studies that observed increased sensitivity of

membrane specific capacitance to small molecules when bilayers are more solvent free, i.e. using solvents that are well-excluded from the hydrophobic region.[217, 220].

Additionally, our technique allows us to determine that doping a DPhPC bilayer with cholesterol results in an increase in both monolayer and bilayer tension. This result is consistent with the observations of previous studies[248, 264] and is explained by the fact that cholesterol interdigitation decreases packing in gel-phase bilayers,[265] such as those formed from DPhPC, which would drive increased interaction between water and the solvent or hydrophobic region of the bilayer. Incorporation of 20% cholesterol increases monolayer and bilayer tension by 0.24 mN/m and 0.21 mN/m in pure hexadecane and 1:1 AR20:hexadecane, respectively. The nominal changes to monolayer tension represent a 20.3% spike, while bilayer tension changes by 22.6% or 24.7% in hexadecane or the 1:1 AR20:hexadecane mixture. As with specific capacitance described above, bilayer tension is more significantly affected by cholesterol when the membrane is solvent-free.

Free energy of adhesion (ΔF) also increases nominally through the incorporation of cholesterol into the bilayer. Raising cholesterol content to 20% increases ΔF of DPhPC DIBs formed in hexadecane by 0.010 mN/m (+3.3%). For DPhPC DIBs formed in the 1:1 AR20:hexadecane mixture, inclusion of 20% cholesterol causes ΔF to increase by +0.028 mN/m (+5.4%). It is interesting to consider the mechanism by which cholesterol increases free energy of adhesion. Evidenced by the equation for free energy (Equation 2, Section 1.2.1), ΔF increases with increases in either tension or contact angle. Our measurements demonstrate the cholesterol increases bilayer and monolayer tensions while causing the contact angle to decrease. To achieve such changes in all three parameters, Equation 7 verifies that the ratio $\gamma_b/2\gamma_m$ must in fact increase in response to the addition of cholesterol. Based on the experimentally obtained values in Table 7, increasing cholesterol content is accompanied by an increase in the ratio of $\gamma_b/2\gamma_m$ (0.853 and 0.880 at 0 and 20% cholesterol, respectively). The data here suggests that cholesterol causes less distortion of lipids positioned in the monolayers around the droplets compared to lipids in the bilayer interface, possibly due to the presence of bulk solvent molecules near the monolayers that fill voids between the sterol and lipid molecules. These results simultaneously support the notion that cholesterol

affects bilayer tension more than monolayer tension through the same mechanism that results in membrane thinning: i.e. kinking and bending of the lipid acyl chains to "wrap" cholesterol molecules and fill sterol-induced voids in the hydrophobic region.

Collectively, results from our measurements of C_M, γ_m, γ_b, and ΔF confirm that the multi-step process is suitably capable for measuring changes to bilayer thickness and tension caused by changes in membrane composition or oil content. Interestingly, solvent-free DIBs formed in 1:1 AR20:hexadecane displayed a heightened sensitivity in terms of the effects of cholesterol on C_M, D_C, γ_b, and ΔF. These takeaways provide guidance for future studies aimed at investigating the effects of biomolecules, peptides, pharmaceutics, and other species on lipid bilayer thickness and tensions. Specifically, such studies could use 1:1 AR 20:hexadecane mixtures to amplify the effects on membrane thickness and tension caused by accumulation of a species of interest.

4.2.3 Effects of Mixed-Monolayer Protected Nanoparticles on Membrane Thickness and Lipid Packing

In addition to studying the effects of nonpolar solvent and cholesterol, the multi-step procedure introduced in Chapter 3 is applied to investigate the effects of mixed-monolayer protected nanoparticles on DPhPC DIB C_M and tensions. As illustrated in Figure 43A, nanoparticles are incorporated into each of the two droplets used to form a DIB. In the case of the mixed 50:50 MUS:OT (hydrophilic:hydrophobic) ligand protected nanoparticles (NPs), DPhPC DIBs rupture frequently during formation, or shortly after, at NP concentrations above ~5 μM. In contrast, stable DIBs were formed with concentrations of the 100 MUS (fully hydrophilic) NPs at concentrations as high as 10 μM. C_M was measured for DIBs incorporating 0, 0.5, 1, or 2.7 μM 50:50 MUS:OT NPs and also with 10 μM 100 MUS NPs. Figure 43B shows C_M values obtained as a function of the concentration of 50:50 MUT:OT NPs included in the droplets. In the case of 10 μM 100 MUS NPs, C_M is measured to be 0.655 μF/cm^2. Figure 43C provides representative images of actual DIBs incorporating the various concentrations and types of NPs tested. It should be noted that when 50:50 MUST:OT NPs were included in DIB, attempts to use the electrowetting method of measuring tension (described in Chapter 3) were complicated by a decrease in the voltage at which

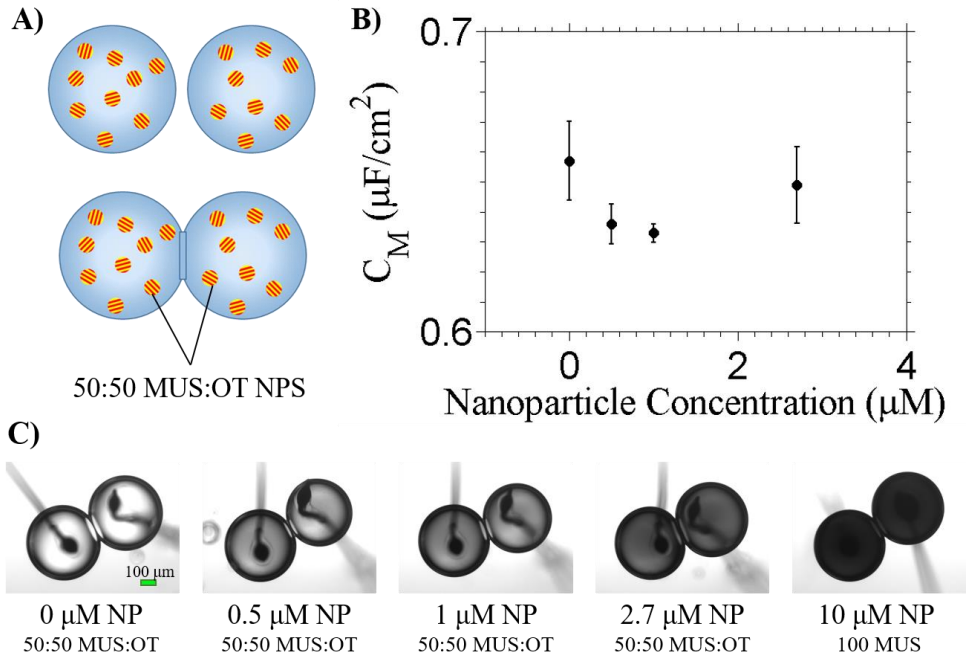

Figure 43. A) Approach for testing effects of mixed-monolayer protected nanoparticles on DPhPC bilayer C_M. NPs are included in each droplet at an identical concentration before DIB formation. B) C_M measured as a function of NP concentration for multiple DIBs incorporating 50:50 MUS:OT NPs in each droplet. Error bars show ± 1 std. dev. C) Images of DIBs including various concentrations of 50:50 MUS:OT NPs, and one image of a DIB including a high concentration of 100 MUS.

bilayer breakdown begins to occur (breakdown was encountered between 50-100 mV in these tests). Voltage induced electroporation causes contact angle change to deviate from the relationship predicted by the Young-Lippmann equation, thus surface monolayer and bilayer tension values were not measured using the electrowetting-based DIB method. The resulting measured values of C_M and corresponding calculated hydrophobic region thicknesses (calculated via Equation 26 assuming ε_r=2.2) are tabulated in Table 8.

DPhPC DIB C_M values are lower in the presence of the mixed-monolayer protected MUS:OT NPs, although not significantly across the concentration range tested ($p<0.005$ only with 0.5 μM and 1.0 μM NPs). The minimum C_M obtained is 0.633 μF/cm^2 (at 0.5 μM NPs) which, compared to the value of 0.657 μF/cm^2 obtained in cases without NPs, represents a 3.6 % decrease (-0.024 μF/cm^2). In comparison, the previous report by Carney et al shows a 10-15% increase in

Table 8. Specific capacitance and bilayer hydrophobic thickness values obtained for NP-infused DPhPC DIBs formed at 25°C.

NP Concentration (μM), Type	C_M **[μF/cm²]**	D_C **[Å]**
0 μM 50:50 MUS:OT	0.657 (0.013) *n*=2	29.6
0.5 μM 50:50 MUS:OT	0.636 (0.007) *n*=4	30.6
1.0 μM 50:50 MUS:OT	0.633 (0.003) *n*=2	30.8
2.7 μM 50:50 MUS:OT	0.649 (0.013) *n*=3	30.0
10 μM 100 MUS	0.655 *n*=1	29.7

D_C: hydrophobic thickness, $D_C = (\varepsilon_r\ \varepsilon_0)/C_M$
All DIBs formed using DPhPC and hexadecane as the oil phase

capacitance upon addition of 5 μM hydrophilic:hydrophobic NPs. The results provided here are inconsistent with those of Carney et al. both in terms of the magnitude and the direction of change. [47] Further, Figure 43B shows that C_M does not change monotonically with increasing concentration of the 50:50 MUST:OT NPs. In other words, the measured values of C_M do not follow the NP concentration-dependent Langmuir-adsorption style trend observed previously. [47]

Thus one question arises: is it possible that Carney et al. observed real NP-driven changes in capacitance that were accompanied by changing area. Unfortunately, it is challenging to track the area of the bilayer in BLM experiments due to the opacity of the solid substrates employed. For both BLMs and DIBs, increases in capacitance due to increasing area would be expected to be a result of a shift in the surface tension balance governing the equilibrium bilayer geometry (i.e. the Young-Dupre equation, $\gamma_b = 2\gamma_m \cos\theta$ as shown in Section 1.2.1). From the Young-Dupre equation, an increase in contact angle (between the range of 0 and 90°) would be the result of a decrease in the quantity ($\gamma_b / 2\gamma_m$). This quantity could decrease through the addition of NPs if the NP incorporation leads to either a) a relative decrease in bilayer tension compared to a fixed monolayer tension, or b) an increase in monolayer tension relative to fixed bilayer tension. The

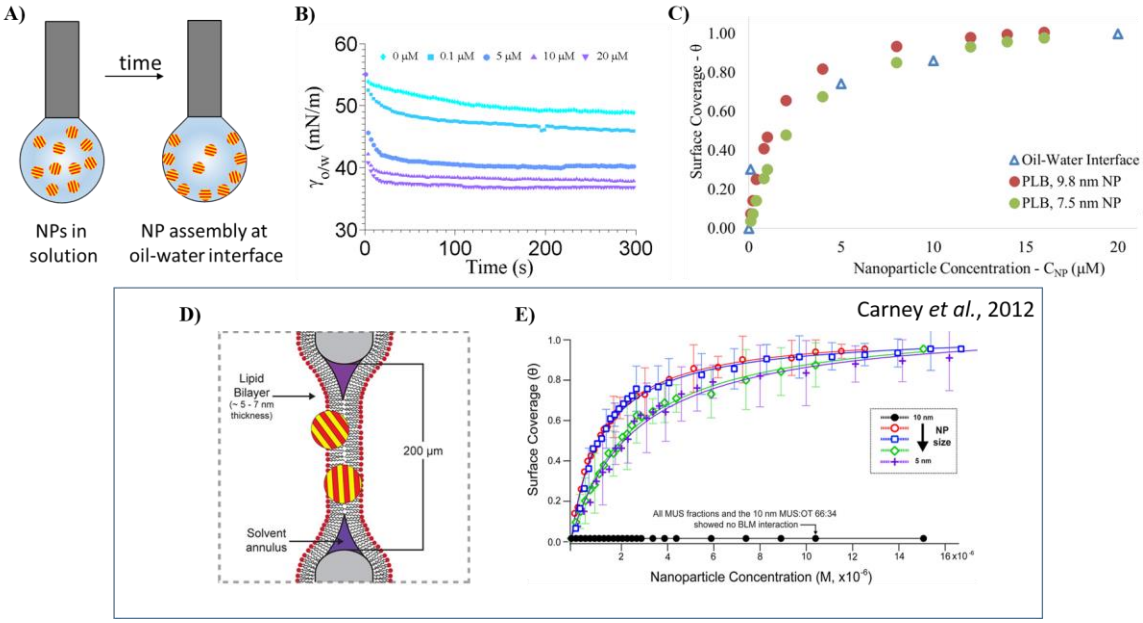

Figure 44. A) Illustration of pendant drop goniometer measurements to study NP adsorption at oil-water interfaces. B) Measured surface tension as a function of time with varying concentrations of NPs (concentrations shown in the legend). C) Fractional surface coverage calculated based on steady-state surface tension values (refer to text for details) (D-E) Illustrations from a prior study by Carney et al. into NP association in BLMs (D) and the resulting measured Langmuir adsorption isotherm (E). (D-E reproduced from [47]).

fact that NP adsorption does not affect bilayer thickness (as determined by C_M measurements) a) indicates that that NPs do not accumulate within the membrane, and b) suggests that NP adsorption affects monolayer tension as opposed to the bilayer tension. The ability to measure the effects of the 50:50 MUS:OT NPs at the monolayer would provide a way to investigate the hypothesis that monolayer tension is affected by NP adsorption at the oil-water interface. As mentioned above, 50:50 MUS:OT NPs created challenges for electrowetting based measurements of DIB surface tensions, thus a set of pendant drop goniometer experiments were performed to investigate the possibility, and the kinetics, of 50:50 MUS:OT NP adsorption at an oil-water interface.

Figure 44A illustrates the experimental approach for using pendant drop measurements of surface tension to study the adsorption of 50:50 MUS:OT NPs at a hexadecane water interface (no lipids are included). At a start time considered t = 0, a ~ 1μL droplet of aqueous-NP solution is ejected from an otherwise clean steel needle into a bath of oil, and the surface tension of the oil-water

interface is measured for 10-20 minutes at a rate of 1Hz. Figure 44B shows representative measured values of surface tension as a function of time (the first five minutes of each experiment) with varying concentrations of NPs included in the aqueous droplet (0, 0.1, 5, 10, and 20 μM 50:50 MUS:OT NPs). The initial surface tension of the clean oil-water interface is around 55 mN/m as expected, however the tension begins decreasing within seconds, ultimately approaching a minimum steady-state value of tension, in all cases. Tension drops even without NPs present due to impurities in the hexadecane (these impurities have been described elsewhere [33] and remained in our tests despite filtering the hexadecane over aluminum), and we allow the NP-free tension to reach steady-state to obtain a measure of the equilibrium tension of the hexadecane-water interface alone. Figure 44B shows that steady-state surface tension decreases with increasing nanoparticle concentration, thus the 50:50 MUS:OT NPs demonstrate the capability of self-assembling at an oil water interface. Given the prior application of a Langmuir adsorption model [47] to describe NP-induced changes in BLM capacitance, it seems appropriate to consider the possibility that NP-adsorption at the oil-water interface could be described by the same model. The proposed model provides the fractional surface coverage, θ, as

$$\theta = \alpha \frac{K_L C_{NP}}{1+K_L C_{NP}}, \qquad \text{Equation 27}$$

Where K_L is the Langmuir adsorption equilibrium constant, c_{NP} is the concentration of the nanoparticles, and α is a scaling factor. Using the steady-state surface tension value obtained from the data shown in Figure 44B (actual values used for θ calculations were taken as the average steady-state tension from at least 5 separate pendant drop experiments for each concentration), an experimentally observed fractional coverage was determined by

$$\theta = \frac{\gamma(c_{NP})-\gamma_0}{\gamma_{sat}-\gamma_0}, \qquad \text{Equation 28}$$

Where γ_0 is the surface tension of the bare oil-water interface, γ_{sat} is the surface tension of an interface saturated with NPs (assumed to be the case with 20 μM NPs), and $\gamma(c_{NP})$ is the steady-state tension measured at each NP concentration. Figure 44C shows the resulting values of θ obtained at each NP concentration based on the surface tension measurements (blue triangles), and Figure 44C also includes representative value of θ calculated using previously published values of K_L and α (for c_{NP} ranging from 1 to about 16 μM). Qualitatively, the θ isotherm obtained from surface tension measurements of NP adsorption at an oil-water interface aligns closely with the

isotherms obtained with prior measurements of NP-induced changes in BLM capacitance. Rearranging Equation 29 yields

$$\frac{1}{\theta} = \frac{1+K_L C_{NP}}{\alpha K_L C_{NP}} = \left(\frac{1}{\alpha K_L}\right)\frac{1}{c_{NP}} + \frac{1}{\alpha}. \qquad \text{Equation 29}$$

Via the relation in Equation 29, the reciprocal of θ is a linear function of the reciprocal of c_{NP}. As such, and returning to our experimentally obtained values for θ as a function c_{NP}, a least-squares linear regression of $1/\theta$ versus $1/c_{NP}$ yields a linear function with coefficients that allow solving for K_L and α. Having performed this procedure with θ values obtained herein, values for the Langmuir equilibrium constant and scaling factor are listed in the first row of Table 9. The adsorption model parameters obtained with pendant drop monolayer tension measurements, despite the lack of lipids or any lipid bilayer, are in striking agreement with the parameters derived from experimentally observed changes in BLM capacitance. The strong agreement here implies that changes observed with prior BLM measurements were most likely a result of NP accumulation that oil-water monolayer interface (and not due to accumulation in the lipid bilayer).

The prior work of Carney et al. established the fact that MUS:OT NPs interact with BLM style lipid bilayers, but the mechanism of increased capacitance was attributed to NP association with the lipid bilayer. [47] Based on the results presented here, the previously observed increase in BLM capacitance can now be attributed to NP adsorption at the monolayers and not the bilayer. This conclusion is based on the several observations: 1) C_M measurements of DIBs exposed to NPs show no signs of a concentration-dependent, NP-induced increase in capacitance, 2) C_M does not

Table 9. Langmuir adsorption model parameters obtained herein and elsewhere with MUS:OT NPs.

NP Diameter	**Equilibrium Constant, K_L [M^{-1}]**	**Scaling Factor α**	***Ref***
1-10 nm	4.0 x 10^5	1.10	This study
7.5 nm	3.6 x 10^5	1.15	[47]
9.8 nm	7.6 x 10^5	1.09	[47]

change significantly as a function of NP concentration, thus it is unlikely that NPs are accumulating in the lipid bilayer, 3) pendant-drop monolayer tension measurements show that NP adsorption at an oil-water interface follow the Langmuir adsorption isotherm established in prior BLM measurements (including remarkably similar experimentally obtained values for the model parameters K_L and α), and 4) an NP-induced, concentration-dependent increase in monolayer tension would drive an increase in bilayer capacitance (*and area, although this would be unobserved in a typical BLM experiment)* like that observed performed previously. What the work herein does not descibe is the possible means by which these cell-penetrating mixed-monolayer protected gold nanoparticles translocate through cell membranes. Future work with DIBs will likely need to explore alternative to C_M, for instance simultaneous electrical and optical measurements, to track NP transport through lipid bilayers. It is possible, also, that the ability of these NPs to pass quickly through real cell-membranes is largely affected by the lipid and protein content, or even higher-level features, of real cell membranes. Continuing avances in the ability to recreate complex and physiologically relevant droplet interface bilayers may prove useful for these reasons.

4.3 Chapter Summary and Conclusions

The proposed and validated method of measuring capacitance and tensions in a DIB opens the door to being able to study a wide variety of lipidic and non-lipidic species and their effects on membranes. Measurements of C_M (and thus D_C), γ_b, and ΔF support the conclusion that DPhPC DIBs formed in silicone oil:hexadecane mixtures are more solvent-free than DIBs formed in pure hexadecane or decane. Further, the solvent-free bilayers formed in silicone oil:hexadecane mixtures show an increased sensitivity to the effects of cholesterol on C_M, D_C, γ_b and ΔF. This conclusion suggests that, in future works, tuning oil composition to yield solvent-free bilayers could improve the ability to detect and quantify the effects of biomolecules, nanoparticles, peptides, or other species accumulating in lipid bilayers.

A key application of this procedure is the ability to characterize changes in bilayer physical properties driven by the incorporation of species (e.g. cholesterol) that, unlike transmembrane ion

channels, do not elicit changes in membrane conductance. The initial embodiment of the method is ready for studies aimed at characterizing, monitoring, or sensing the interactions of a number of small molecules, peptides, pharmaceutic and therapeutic agents, or other lipophilic species with droplet interface bilayers.

CHAPTER 5

HEATING ASSISTED FORMATION OF TOTAL LIPID EXTRACT DROPLET INTERFACE BILAYERS

Droplet interface bilayers (DIBs) serve as a convenient platform to study interactions between synthetic lipid membranes and proteins. However, a majority of DIBs have been assembled using a single lipid type, diphytanoyl phosphatidylcholine (DPhPC). As a direct response to Objective 3 in Section 1.3.2, the work described in this chapter establishes the use of controlled heating to enable assembly of DIBs using liposomes comprised of natural total lipid extract derived from *Escherichia coli* (eTLE). This chapter also begins to address Objective 4 and Objective 5 through efforts to study the effects of increasing compositional heterogeneity on DIB resistance, specific capacitance (thickness), the interactions of membrane proteins, and the effects of changing temperature on these properties.

5.1 Introduction

Droplet interface bilayers (DIBs)[183] are gaining momentum as a tool for researching lipid bilayers and membrane-associating proteins from bacterial and eukaryotic organisms.[12, 16, 17, 36, 66, 67, 74, 75, 77] Using this platform, a lipid bilayer is formed between two lipid monolayer-encased water droplets submerged in oil. The ability to independently control the contents of each droplet allows symmetric or asymmetric tailoring of the bilayer composition as well as

Note: This chapter presents a modified version of the published paper "Heating-Enabled Formation of Droplet Interface Bilayers Using *Escherichia coli* Total Lipid Extract " [10].

independent tuning of the aqueous solutions on either side of the membrane.[12] As illustrated in Figure 45, studies have utilized DIBs to capture and study membrane-active proteins such as ion-channels, pore-forming peptides,[12, 35] and even toxins.[36, 75] Demonstrating potential for drug development, DIBs have also been used to monitor the ability of drugs or blocking agents to modulate transmembrane protein behavior.[67, 97]

The majority of DIBs have been formed using diphytanoyl phosphatidylcholine (DPhPC), a single lipid type of archeal origin. The reader is referred to Section 1.2.1 for a review of lipid selection in DIB studies published to date. Yet, it is well known that cell membranes *in vivo* are comprised of many types of lipids and other molecules (Appendix, Table 12 for details on natural lipid composition) and that the structures and functions of transmembrane proteins are influenced by membrane composition.[185, 186, 266] It is also known that many organisms, such as *E. coli* bacteria, actively regulate their lipid compositions in response to environmental conditions like temperature.[206, 207, 209] Thus, to be certain that relevant model membranes are available for studying the functions of bacterial and eukaryotic proteins, there is a need for the ability to use complex, naturally occurring lipid mixtures for forming DIBs.

A truly mimetic bacterial model membrane could be used to study the natural functions of antimicrobial peptides. For example, it is known that antibiotic resistance in bacteria is partially enforced through increases in membrane rigidity via alteration of fatty acid content, a response that modulates membrane permeation by alamethicin peptides.[267] These types of changes could be studied *in vitro* by using total lipids extracted from antibiotic resistant bacteria to form DIBs, which could lead to improved understanding of bacterial resistance and the development of more effective antibiotics. Furthermore, the ability to create DIBs using natural extracts from bacterial or eukaryotic organisms could provide a means to study complex transmembrane proteins such as G protein-coupled receptors (GPCR) and other proteins with 7 or 12 transmembrane spanning domains.[268, 269] Processes such as receptor-ligand mediated signaling or liposome-mediated trafficking could also be studied in bilayers that mimic the mechanical properties, charge distribution, and fluidity of membranes found in living organisms.[270, 271] Until now, however,

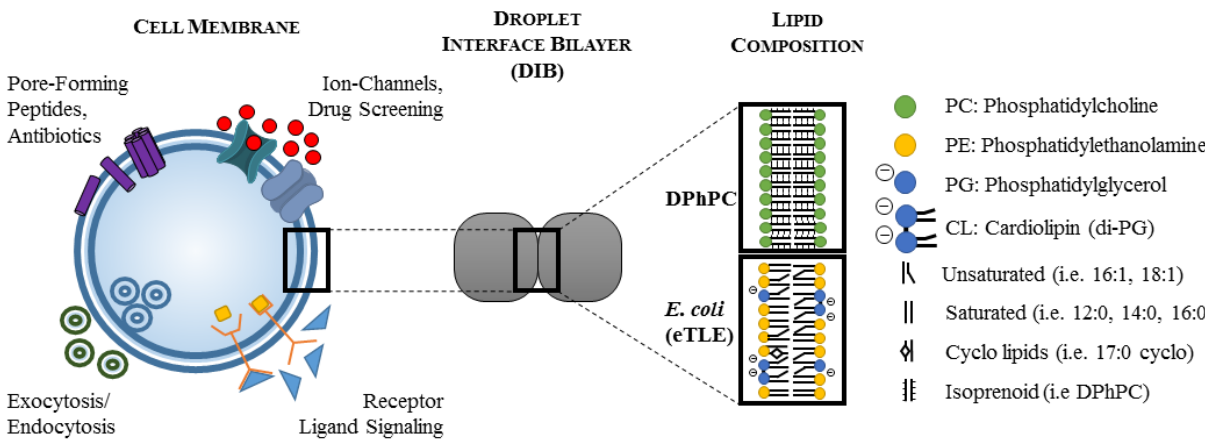

Figure 45. (*left*) DIBs have been used to create model membranes for studying antimicrobial pore-forming peptides, ion-channels, and drugs or blocking agents interacting with transmembrane proteins. DIBs could potentially be used to study other membrane-mediated processes including receptor-ligand associated signaling, basic vesicle fusion/fission, or higher level trafficking and exo/endocytosis. (*right*) The majority of DIB research utilizes DPhPC to create single lipid-type bilayers, as shown. A current challenge lies in mimicking the complex composition of natural lipid membranes comprised of multiple lipid types. Total lipid extracts such as the eTLE used herein feature a diverse selection of lipid headgroups and acyl chains, including charged species such as PG and cardiolipin (di-PG).

there is no clearly defined method for forming droplet interface bilayers with total lipid extract obtained from cells.

In contrast to reconstituting cellular membrane fragments into a DIB formed with DPhPC,[74] this work focuses on the assembly and characterization of bilayers from naturally occurring lipid mixtures without the need for added synthetic lipids. Total lipid extract is preferred over assembling model membranes using a mixture of synthetic lipids for two reasons: 1) obtaining a ready-to-use total extract is easier and less subjective than selecting and then carefully mixing synthetic lipids, and 2) it is desired to mimic the full lipid composition of the membrane, including "unknown" components that may play crucial roles in membrane-protein interactions. For example, the "unknown" fraction of brain total lipid extract contains novel membrane lipids and signaling molecules that are vital in neural membrane communication.[272]

Herein, we report that regulated heating allows formation of DIBs using total lipid extract from gram-negative *Escherichia coli* bacteria. Forming bilayers with *E. coli* total lipid extract (eTLE) is enabled using a recently designed platform for controlled heating of DIBs, and we examine the

effects of temperature to determine why heating is required for eTLE DIBs and how temperature affects the bilayer. The eTLE mixture is expected to result in DIBs constructed with a symmetric lipid composition that mimics the inner cytoplasmic membrane of *E. coli* (refer to Appendix, Table 12*)*. The composition of the inner membrane is largely representative of the total phospholipid composition for total lipids in *E. coli*[209, 273] as depicted in Figure 45 (adapted from *E. coli* composition data in Table 12). Phospholipids in *E. coli* are distributed between three main classes in terms of lipid headgroups: neutral phosphatidylethanolamine (PE), negatively charged phosphatidylglycerol (PG), and cardiolipin (CL), which is a PG dimer carrying a double-negative charge. Acyl chains in lipids of *E. coli* consist largely of monounsaturated (UFA), saturated (SFA), or cyclopropane (CFA) fatty acids. As illustrated in Figure 45, the complexity of a bilayer with natural lipid composition is significantly greater than that of a DPhPC-only membrane.

As with prior DIB studies, we show that bilayers formed using eTLE are capable of reconstituting proteins or peptides.[12, 17, 35, 36, 75] Specifically, we use single channel current recordings, cyclic voltammetry measurements, and circular dichroism to compare the insertion of alamethicin (Alm), a naturally occurring and well-characterized antibiotic peptide produced by *Trichoderma viride* fungus,[274] into eTLE bilayers to that for DPhPC membranes. Single channel recordings are performed at low peptide concentrations, while cyclic voltammetry (CV) is used to examine macroscopic voltage- and temperature-dependent effects of Alm-associated permeation at moderate peptide concentrations in both eTLE and DPhPC DIBs. Circular dichroism (CD) is also used to monitor temperature-dependent changes in the secondary structures of peptides incubated at high concentration with eTLE and DPhPC liposomes.

5.2 Feedback Controlled Heating of Droplet Interface Bilayers

Figure 46A shows an isometric view of the heating platform including the polydimethyl siloxane (PDMS) regulated attachment (RAM) substrate used for regulating droplet attachment as described previously (Figure 47 shows a full setup).[17] The RAM substrate (Figure 46A,B) is used in all DIB experiments except for those in which submerged droplets suspended on agarose-coated

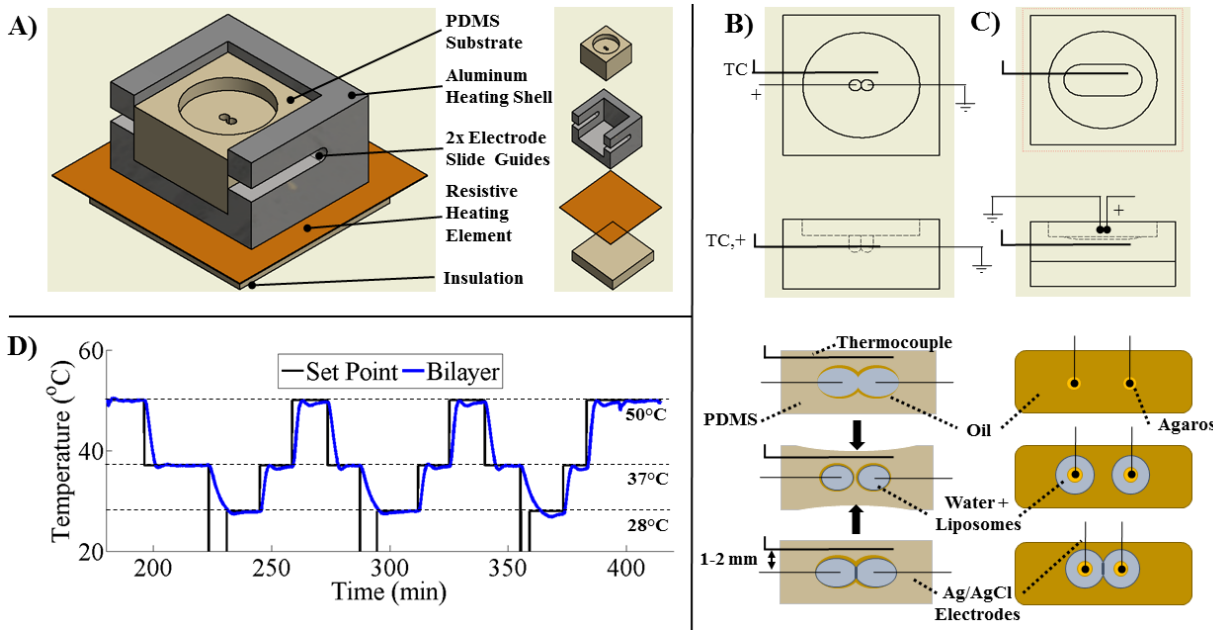

Figure 46. A) The experimental platform for temperature-controlled heating of DIBs utilizes a PDMS substrate to hold oil and droplets, a resistive heating element, and a heat distributing shell assembled as shown. B-C) Top and front views of two types of PDMS substrates used for DIB formation (B) via the regulated attachment method or (C) between suspended droplets on movable electrodes. The outer geometry of both substrates is identical, and the thermocouple (TC) is inserted into the same location within both PDMS substrates (refer to the text for more details). D) Representative measurements of temperature tracking within the substrate using on-off, PI feedback temperature control.

electrodes are used for measuring specific bilayer capacitance. Typical droplet sizes for RAM and suspended droplet tests are 700 nL and 300 nL, respectively. The PDMS substrate is placed within an aluminum shell that rests on top of a 30 mm x 30 mm resistive polyimide flexible heating element (Omega, KHLV-101/10). An insulating PDMS wafer is placed beneath the heater to reduce heat loss in the downward direction. The 4-wall design of the heating shell preserves access to one side of the substrate for lateral compression during bilayer formation[17], while the shell itself allows for faster, more even heating of the PDMS substrate. A silver-silver chloride (Ag/AgCl) electrode made from 120µm diameter silver wire soaked in bleach is inserted through the substrate into each compartment. A thermocouple inserted into the PDMS substrate measures temperature near the bilayer region. The 152 mm-long, 2.4 mm-diameter steel-encased thermocouple probe (Omega P/N JMTSS-020U-6) allows direct insertion and fixation within the flexible substrate. When placed parallel to the electrodes at a distance < 2 mm from the droplet compartments, the thermocouple records temperature within 1°C (+1/-0°C) of the temperature of

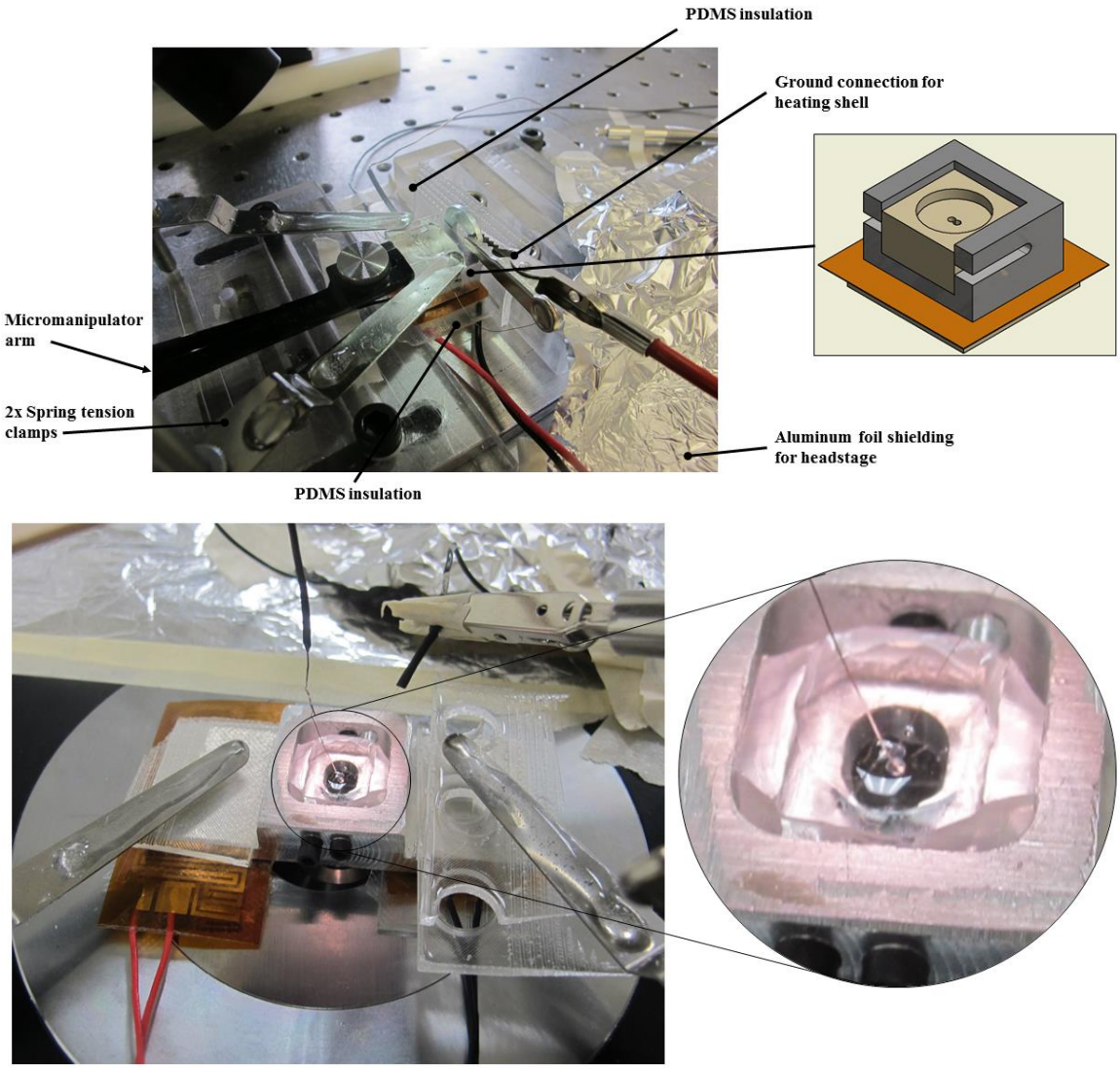

Figure 47. Top – Typical setup for feedback controlled heating with the regulated attachment method (Note: the thermoelectric module shown is not in use here). Bottom - Substrate and setup for temperature controlled testing of suspended DIBs and specific capacitance measurements. Both setups employ an aluminum heating shell clamped (two aluminum tension clamps shown, coated in PDMS to prevent heat transfer from the substrate) on top of flexible Kapton heat pads. PDMS is included as insulation to reduce unwanted heat loss. Slots or holes in the heating shell provide access points for the thermocouple and electrodes. For specific capacitance measurements, the electrodes hang from above where they are clamped or fixed with alligator clips or a micromanipulator arm (not shown).

the bilayer region (confirmed in separate tests) without directly interfering with the droplets or bilayer. Temperature is recorded using a custom LabVIEW Virtual Instrument (VI) in communication with a National Instruments (NI) 4-channel thermocouple input module (NI 9211) within a NI CompactDAQ (cDAQ-9174). On-off, proportional-integral (PI) feedback temperature control is implemented within the same VI to enable controlled heating and passive cooling of the bilayer temperature to within +/-0.3°C of a desired value. Figure 46D shows the bilayer region temperature and system response to discrete changes (via the VI) in the desired temperature (set point).

5.3 Results and Discussion

5.3.1 Differential Scanning Calorimetry with E. Coli Total Lipid Extract

Attempts to form DIBs using lipids extracted from *E. coli* were guided by two facts: 1) membranes of living organisms display thermotropic phases,[206, 207, 209, 275] and 2) lipid monolayer assembly at a polar-nonpolar liquid-liquid interface is affected by temperature-dependent phase transitions of liposomes.[276] DSC is first used to identify transition temperatures in liposomes made from *E. coli* total lipid extract, as well as DPhPC and DPPC synthetic phospholipids. DPPC lipids are included as a reference since they are known to undergo a gel-to-liquid phase transition

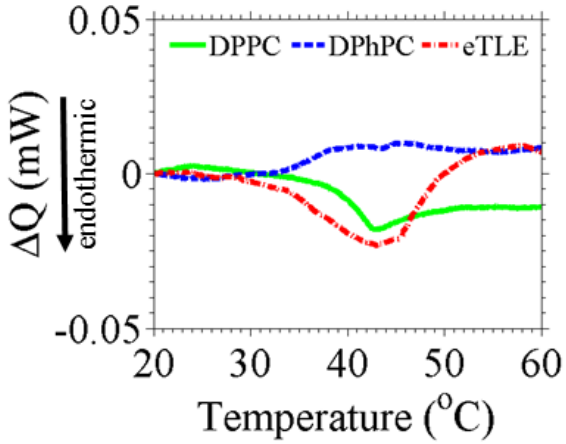

Figure 48. Differential scanning calorimetry (DSC) thermograms obtained from heating aqueous unilamellar liposomes of DPPC, DPhPC, and eTLE between 10-80°C at a rate of 5°C/min. Data is presented as change in heat (ΔQ). Downward deflections indicate endothermic heat absorption.

at a temperature of 41-43°C. The resulting thermograms for eTLE, DPhPC, and DPPC are provided in Figure 48. As expected, the negative change in heat measured by the instrument near 42°C confirms that DPPC liposomes undergo an endothermic melting transition from gel to fluid phase. DPhPC, a lipid expected to exist in a single gel phase between -120°C and 120°C,[277] does not exhibit a similar melting transition upon heating from 20-60°C. In contrast, eTLE displays a broad endothermic transition centered about 44°C. This result suggests that heterogeneous eTLE bilayers undergo a gel-to-fluid melting transition when heated from 40°C to 50°C. The center of this endothermic range is in agreement with a reported transition at 41-43°C that was observed in fluorescence anisotropy and DLS experiments with eTLE.[278]

5.3.2 Enabling Total Lipid Extract Bilayer Formation through Heating Enabled Monolayer Assembly

The DSC results provide knowledge about the temperature-dependence of eTLE bilayers in an aqueous environment. However, the goal of this research is to form DIBs using eTLE lipids, which first requires liposomes present inside the droplets to facilitate the assembly of a well-packed lipid monolayer at the oil-water interface. Therefore, a series of experiments was performed to test DIB formation between two droplets containing eTLE liposomes in hexadecane (Appendix, Figure Figure 77). Similar trials using DPhPC are included for comparison. Both the time allowed for monolayer formation (t_m) at the droplet surfaces and the temperature of the liquid environment were varied. Droplets are introduced separately into the adjacent compartments of the RAM substrate at $t_m = 0$, and the volumes are kept apart by compressing the flexible substrate. The time at which the substrate is opened to allow droplet contact is recorded as t_m. Current measurements are used to monitor bilayer formation upon initiating droplet contact. Highly resistive lipid bilayers produce a stable, square current waveform, leaky membranes yield an ohmic triangular current response, and coalesced droplets yield a saturated current in response to the continuously applied triangular voltage waveform (examples of the current response for each state are provided in Figure 77 in the Appendix).

The general results from this experiment are illustrated in Figure 49. While DPhPC DIBs form after 3-5 minutes (Figure 77F) of droplet incubation in oil at room temperature, we found that

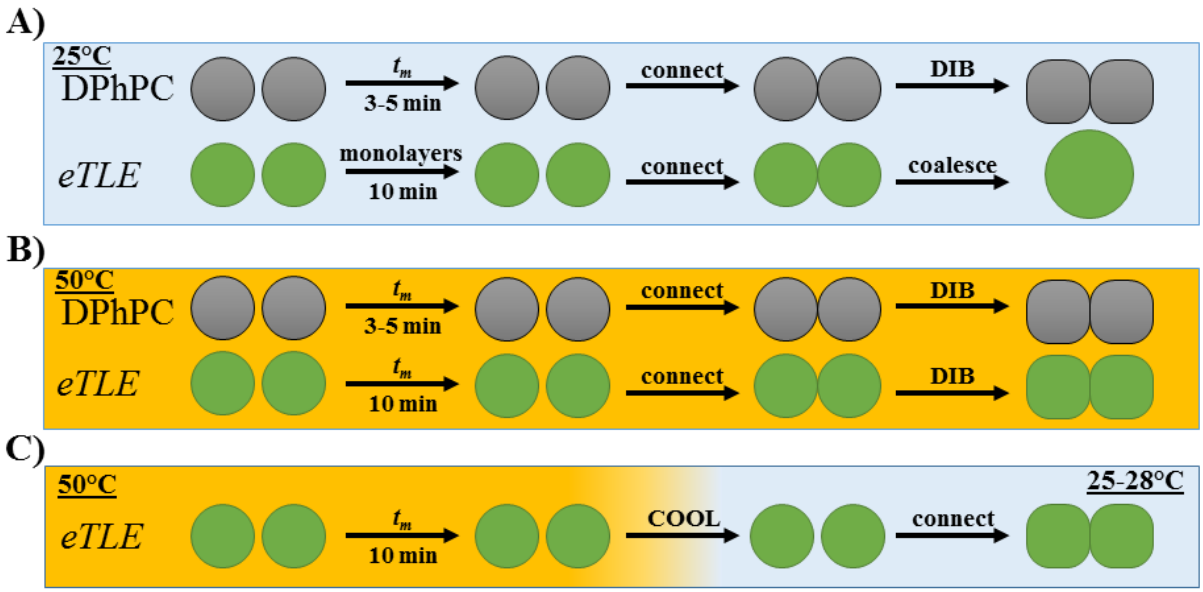

Figure 49. Approaches taken to attempt bilayer formation in hexadecane using aqueous droplets containing 2mg/mL DPhPC or eTLE lipids: A) At 25°C, DPhPC droplets resist coalescing when connected after only 3-5 minutes for monolayer assembly. In contrast, eTLE droplets coalesce at room temperature even after an hour for monolayer assembly. B) With the system (oil, substrate, and droplets) heated to 50°C, droplets containing DPhPC enable bilayer formation after 3-5 minutes for monolayer assembly, and eTLE droplets allow bilayer formation after 10 minutes for monolayer assembly. C) eTLE droplets can be introduced at 50°C with 10 minutes for monolayer assembly before cooling the entire system to room temperature and then connecting the droplets. In contrast to coalescence as observed in (A), eTLE droplets allow for DIB formation at room temperature via this treatment, confirming that heating to a temperature above T_m promotes self-assembly of lipid monolayers.

droplets containing eTLE liposomes do not form a DIB at room temperature. Instead, eTLE-doped droplets coalesce upon contact, even in tests allowing up to 1 hour of incubation time for monolayer formation (Figure 49A, Figure 77C). This result indicates that a well-packed lipid monolayer does not assemble at the droplet surfaces at room temperature with eTLE liposomes. The oil temperature was then gradually increased to determine if monolayer assembly and DIB formation could instead occur at an elevated temperature. The current recordings (Figure 77C) demonstrate that not until the temperature reached 50°C did we observe two droplets containing *E. coli* liposomes form a stable interface bilayer as indicated by a square current response. Additional trials at this temperature were performed to determine that an incubation time of 10 minutes at 50°C allows for consistent DIB formation with eTLE (Figure 49B, Figure 77E). We

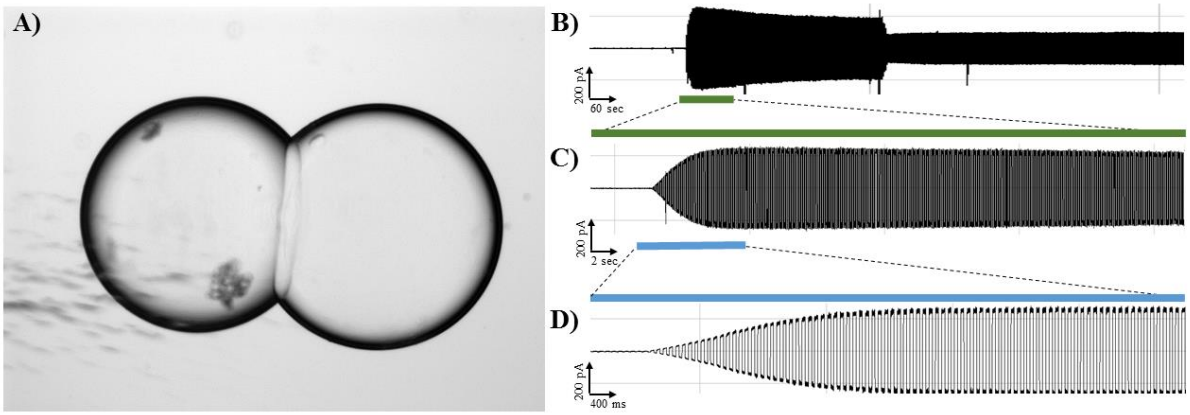

Figure 50. A) DPPC DIB formed at 51°C after 10 minutes of incubation (at 51°C). DPPC is dissolved in the aqueous phase as sonicated small unilamellar liposomes with hexadecane as the oil phase. These droplets are in a shallow heated oil reservoir, without any electrodes, positioned over an inverted microscope (4x, droplet diameters ~ 1mm). B-D) Current measured during formation and size adjustment of a DPPC DIB (tested in the RAM substrate, not shown) performed at 51°C.

confirmed that droplet diameter remains unchanged over the course of an hour at 50°C to rule out the possibility of evaporation induced monolayer assembly and packing.

A final series of DIB formation tests was performed at room temperature (25°C) after a 10-minute incubation period at 50°C (illustrated in Figure 49C) to determine if heating is required for both monolayer assembly and bilayer formation. Like those that were incubated and connected at 50°C, we found that eTLE DIBs readily form after cooling to room temperature following incubation at 50°C. These results suggest that: 1) heating above T_m enables improved monolayer assembly at the oil-water interface from fluid-phase liposomes, which more readily assemble to reduce surface tension;[276] and 2) that DIBs can be formed with lipids in the gel phase, so long as the opposing lipid monolayers are well-packed.

To test this idea, we attempted DIB formation with two types of saturated synthetic lipids, DMPC (T_m = 25°C) and DPPC (T_m = 41-43°C), which display transition temperatures above room temperature. To our knowledge, these lipid types have not been incorporated as liposomes into droplets to form DIBs. Instead, previous attempts to form DMPC or DPPC bilayers between water droplets incorporated lipids into the organic phase,[87, 90, 101, 102] where the phase behavior of

inverse lipid micelles in oil may not correlate to that for bilayers in an aqueous environment. In numerous trials at room temperature, DMPC or DPPC liposome-infused droplets coalesce (100% failure rate) when brought into contact. Coalescence is encountered even in tests allowing 30 minutes or more for monolayer formation, much like droplets containing eTLE at room temperature described above. A long-lasting lipid bilayer can be assembled by heating DMPC droplets to 35-45°C and DPPC droplets to 50-60°C (Figure 50) for 10 minutes before bringing droplets together. However, unlike eTLE DIBs, we observe these single component membranes to rupture when cooled through T_m - a result that has been reported by others. [89, 279]

The combined result from DIB formation and DSC measurements is that monolayer assembly and thus bilayer formation improves drastically when the mixed lipids are heated above their effective T_m. This finding is in close agreement with Lee and Needham's study of homogenous monolayer assembly using saturated phosphatidylcholine lipids supplied to the interface as liposomes, which showed that maximum monolayer surface pressure is reached only when the system temperature is above T_m. [276] What our results add is that the phase behavior of the liposomes is an important factor in DIB formation for lipids with transition temperatures above room temperature and that *in situ* heating control can be used to enable monolayer formation for lipids with high transition temperatures.

5.3.3 E. coli TLE DIBs as Model Bacterial Membranes

The entire lipid content of *Escherichia coli* is found in its cell envelope, consisting mainly of phospholipids. [273, 280] *E. coli* and other gram negative bacteria contain two membranes, an outer and an inner membrane, [280] while gram positive bacteria are encapsulated by a single outer membrane. [281] The process of extracting total lipids from bacteria results in a mixture that includes lipids from the inner leaflet of outer membrane (OM) and both leaflets of the inner cytoplasmic membrane (CM). With eTLE dissolved in water, frozen and thawed, and extruded through 100 nm polycarbonate membranes, it expected that the resulting vesicles consist of homogeneously mixed lipids. In our tests, the same lipids are present in each droplets and thus each leaflet is expected to be identical resulting in bilayer with symmetric lipid composition.

The outer leaflet of the OM of natural bacteria is rich in lipopolysaccharides (LPS), [282, 283] giving rise to an asymmetry in natural *E. coli* that is not expected to be recreated with eTLE DIBs described in this study. The majority of phospholipids of the OM is contained in its inner leaflet[282, 283] which is extracted as part of the process of lipid extraction. White shows that the three major headgroups of the OM and CM include PE, PG, and CL[284] which is consistent with overall total lipid extract headgroup composition as described by Avanti and elsewhere.[152]

eTLE DIBs most closely represent the CM of E. coli. The CM is the source of the majority of the lipids in TLE, and the CM composition is considered to be relatively simple compared to that of the OM.[281] Considering each leaflet of the CM, there are only minor differences in terms of lipid composition.[284] It seems reasonable then to assume that a symmetric bilayer constructed from homogenously distributed total lipids extracted from *E. coli* closely mimics natural bacterial CM.

5.3.4 E. Coli Total Lipid Extract Membrane Specific Capacitance as a Function of Temperature

Measurements of capacitance per unit area are used to confirm that the interface between non-coalescing droplets containing eTLE is a bilayer. Specific capacitance of DPhPC bilayers assembled from liposomes in the droplets is also measured. C_M is determined for bilayers assembled from each lipid type at 25, 37, and 50°C, and the results from these measurements are provided in Figure 51A. At 25°C, we find C_M to be 0.74±0.022 μF/cm^2 for DPhPC DIBs, a value that is in close agreement with previously reported values of 0.65±0.2 μF/cm^2 [239] and 0.64±0.025 μF/cm^2 [80] for DIBs formed using DPhPC in hexadecane. The measured C_M value of 0.66±0.021 μF/cm^2 for eTLE DIBs at 25°C shows that the capacitance per unit membrane area of these interfaces is close to that for DPhPC DIBs. [50] Measurements at 37 and 50°C yield similar values of C_M for both membranes. Yet, while DPhPC exhibits a consistent decrease in specific capacitance with rising temperature, eTLE membranes exhibit a peak specific capacitance of c.a. 0.68 μF/cm^2 at 37°C, before falling back to c.a. 0.62 μF/cm^2 at 50°C. Given that synthetic lipid bilayers are known to exhibit specific capacitances between 0.5-1.0 μF/cm^2, [86] these data

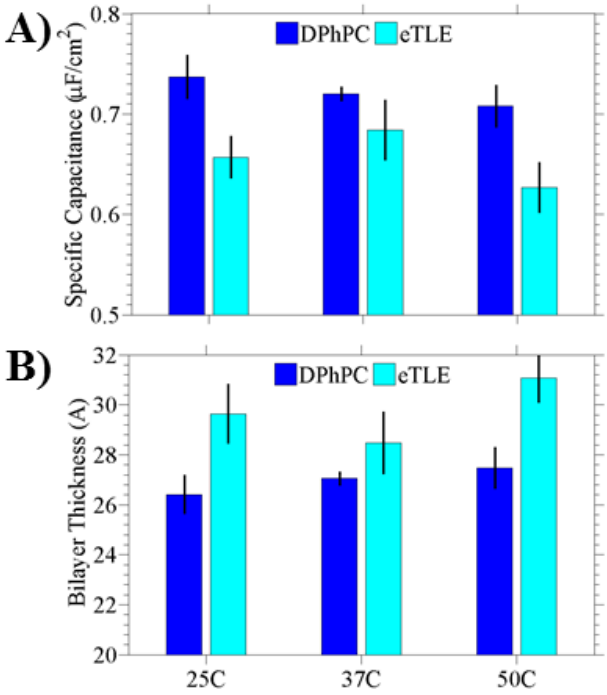

Figure 51. (A) Specific capacitance (C_M) and (B) hydrophobic region thickness (d_{HC}) of eTLE and DPhPC bilayers formed at 25, 37, and 50°C. Bars represent the average values for each case with lines showing ± one standard deviation. Actual values, including standard deviation and number of trials for each case, are included in Table 10.

provide strong evidence that the interface formed between non-coalescing eTLE-doped droplets is that of a thinned, lipid bilayer, [77] regardless of the temperature at which the membrane forms.

The specific capacitance of a bilayer is related to the thickness of the hydrophobic bilayer interior (d_{HC}) as given by $C_M = \varepsilon \cdot \varepsilon_0 / d_{HC}$, where ε and ε_0 are the dielectric coefficient of the hydrophobic region and the permittivity of free space, respectively. Hydrophobic thicknesses for eTLE and DPhPC bilayers (Figure 51B) formed across the range of 25-50°C are estimated using the measured values of C_M and a value of 2.2 for the dielectric coefficient. [256, 285] These data reveal that the hydrophobic thickness of a DPhPC bilayer is approximately 26 Å at 25°C, whereas an eTLE membrane at the same temperature has a hydrophobic thickness closer to 30 Å. This comparison suggests that eTLE membranes are nearly 12% thicker than DPhPC bilayers at 25°C, despite the fact that both membranes contain large fractions of 16-carbon acyl chains (Table 12)

and are expected to have a similar dielectric constant. Estimates of thickness at elevated temperatures show that the thickness of the membrane is sensitive to temperature. DPhPC membranes steadily thicken, from 26.4 Å to 27.5Å, as the droplets are heated from 25°C to 50°C, while eTLE exhibit thicknesses ranging from 28.4-31.0Å.

The temperature dependence of membrane capacitance and thickness for a synthetic lipid bilayer depends greatly on the presence and amount of trapped hydrocarbon solvent in the membrane. In cases where a membrane is completely *solvent-free*, experiments and theory confirm that the thickness of a solvent-free membrane increases upon cooling.[286, 287] At temperatures above the gel-liquid phase transition for the membrane, the membrane is relatively thinner due to a reduced length and higher area per lipid in the bilayer. The lipids elongate and the area per lipid reduces as it cools from the more-disordered liquid state to the more-packed gel state. These types of thickness changes relative to the T_m have been observed via AFM [286] or SANS/x-ray scattering data [287, 288] on solvent-free bilayers, where one would expect a lower C_M in the gel phase as a result. However, the dependence of membrane capacitance and thickness on temperature has been shown to be opposite for synthetic lipid bilayers in which equilibrium between the thinned bilayer region and the surrounding annulus results in oil trapped in the membrane. In the *solvent-containing case*, increasing the temperature results in changes to the lipid phase that are consistent with those for a solvent-free membrane, but also changes in the net amount of oil in the bilayer (the entropic penalty for excluding oil decreases with higher temperature leading to more solvent in the membrane). [8] As a result, a shortening of the lipid lengths as the membrane is heated from the gel-to-liquid phase is counteracted by an increase in the amount of oil trapped in the bilayer. White showed that the net effect is a thickening of the bilayer, as shown by a decrease in specific capacitance, with increasing temperature. [8]

Our results on eTLE bilayers using hexadecane, which is known to remain in DPhPC bilayers,[50] show a temperature-dependence for membrane capacitance that agrees in both magnitude and direction with White's results[8] on suspended planar bilayers in the presence of alkane solvents. The fact that we do not observe an increase in C_M upon heating eTLE through the phase transition indicates that the membrane is not completely *solvent-free*. Conversely, the subtle decrease in C_M

upon heating denotes a slight increase in the oil fraction in the bilayer. While DPhPC bilayers have been shown to contain c.a. 10% hexadecane by volume,[50] it is unknown from our data alone how much the thickness of an eTLE membrane corresponds to solvent. Follow up measurements on solvent-free eTLE membranes achieved with a different oil are required to estimate the hydrophobic thickness of the mixed-lipid membrane. Interestingly, the higher value of C_M measured at 37°C, which aligns well with the phase transition region for eTLE bilayers (Figure 48), may indicate that oil is excluded to a greater degree near the phase transition. However, this result is not conclusive with few measurements of C_M at widely spaced values of temperature.

5.3.5 Effects of Temperature on E. Coli Total Lipid Extract Membrane Resistance and Rupture Potential

A high electrical resistance (>1GΩ) is important in synthetic lipid bilayers because it shows that the membrane creates an effective seal between the two aqueous phases, which minimizes unwanted diffusion of species and reduces leakage current in single channel measurements of transmembrane proteins.[36, 74] Measuring the voltage-induced rupture potential provides an idea of the practical range of voltages that can be applied to study membranes and membrane-associating proteins.[36, 74] Rupture potential tests also provide information regarding membrane sensitivity to electroporation and lipid ion-channel formation.[289] Thus in addition to specific capacitance measurements described above, experiments are performed to characterize the electrical resistance and rupture potential of both eTLE and DPhPC membranes at two bilayer formation temperatures: room temperature (25°C) and 50°C.

In these tests, eTLE DIBs are formed at either 25°C or 50°C between droplets incubated for 10 minutes in oil at 50°C, while DPhPC DIBs are formed at either temperature after 3-5 minutes for monolayer formation. Membrane resistance and rupture potential are extracted from current measurements obtained using the DC step voltage routines described in Chapter 2. Figure 52 provides a summary of measured resistance, specific resistance, and rupture potential measured for eTLE and DPhPC DIBs formed at both temperatures. At 25°C, eTLE and DPhPC DIBs exhibit statistically similar nominal (Figure 52A) and specific resistances (Figure 52B) on the order of 100GΩ and 70MΩ·cm^2, respectively. These levels of resistance are consistent with values reported

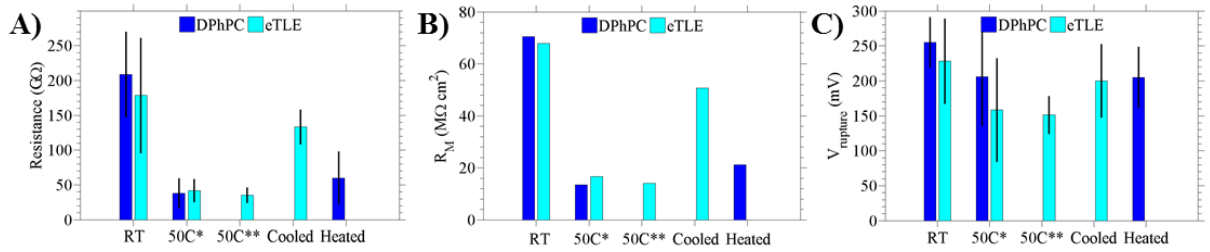

Figure 52. (A) Nominal bilayer resistance, (B) membrane resistance (resistance x area), and (C) rupture potential obtained for the various combinations of lipid type and temperature tested herein. Bars represent the average values for each case, with lines showing +/- one standard deviation. Actual values, including standard deviation and the number of trials for each case, are included in Table 10. For (B), resistance is taken from (A), while area is computed based on a bilayer capacitance of 250 pF established in all tests and an appropriate value of C_M as determined above (Figure 5) for each lipid/temperature combination. *t_m = 10 minutes. **t_m = 30 minutes.

for other DIBs[36, 74] tested at room temperature. The data also reveal that both eTLE and DPhPC bilayers formed at 50°C exhibit lower values of resistance; specific resistance for both drops from approximately 70MΩ·cm^2 to <20MΩ·cm^2. Independent-sample *t*-tests confirm that for each lipid type bilayer resistance is significantly lower (i.e. $p<0.05$) at 50°C versus 25°C. This result suggests that bilayer conductivity, and thus permeability to ions, increases with temperature with bilayers of DPhPC and eTLE as well. Nonetheless, both membrane compositions exhibit nominal resistances greater than 20GΩ across the temperature range tested (25-50°C) and neither exhibit leakage currents in response to an applied voltage. Similar to resistance, the data in Figure 52C show that eTLE and DPhPC exhibit similar values of rupture potential, and that rupture tends to occur at a lower voltage for DIBs assembled and tested at 50°C. More specifically, rupture potentials are found to be greater than 150mV for all lipid and temperature combinations, even though there is no significant difference in rupture potential as a function of temperature ($p>0.05$) for either lipid type.

Given reports of droplet coalescence during heating of DIBs,[62, 89, 90] we are also motivated to determine if the bilayer can withstand a dynamic change in temperature and understand how this change in condition affects bilayer resistance and rupture potential. Thus, a group of tests is conducted to examine the effects of dynamically cooling an eTLE DIB formed at 50°C as illustrated in Figure 53A. (Raw capacitance and temperature data acquired during heating and

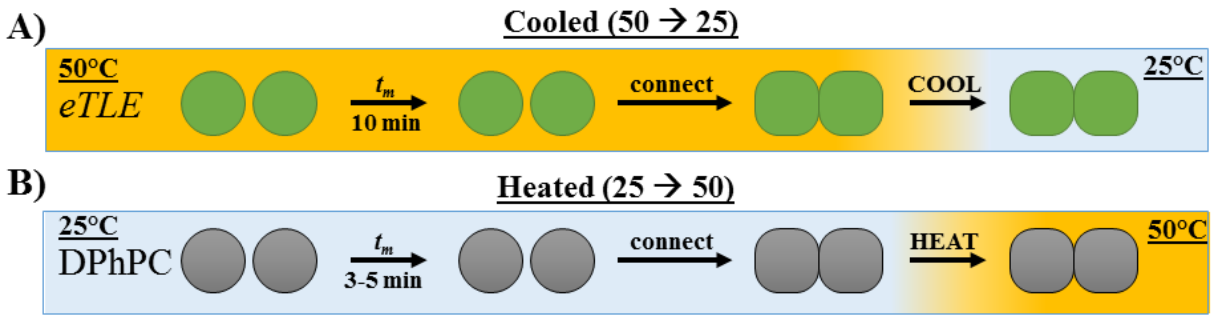

Figure 53. A) Approach for forming an eTLE DIB at 50°C before cooling it to room temperature. B) Similarly, the approach to assemble a DPhPC DIB at room temperature followed by heating to 50°C. Refer to the text for descriptions of test results and electrical properties of heated/cooled DIBs.

cooling tests is provided in Figure 54). To do so, the system temperature set point is changed to 25°C after a DIB formation to allow the bilayer and adjoining droplets to passively cool from 50°C to <28°C in about 15 minutes, at a maximum cooling rate of 3-4°C per minute (Figure 54F). We found that eTLE bilayers were able withstand the decrease in temperature without rupturing in 11 of 11 separate cooling trials. Nominal resistance, specific resistance, and rupture potential measured for the "cooled" eTLE DIBs after cooling to room temperature are provided in Figure 52.

Conversely, we examine the effects of increasing temperature on DPhPC bilayers formed at room temperature by controllably heating them to 50°C (Figure 53B, Figure 54G). Similar to eTLE DIBs, heated DPhPC bilayers remain intact (in 9 of 9 trials) during the temperature change, even with heating rates greater than 10°C per minute (Figure 54J). The active heating provided by the temperature controller is responsible for the increased rate of temperature change with heating compared to cooling, achieving the prescribed increase from room temperature to 50°C in just a few minutes. Values for the electrical properties of "heated" DPhPC DIBs formed at room temperature and warmed to 50°C are shown in Figure 52 (see Table 10 also). Like those formed and tested at 50°C, DPhPC membranes heated to 50°C after assembly at 25°C exhibit statistically lower values of resistance than is measured for DPhPC membranes formed and tested at room temperature.

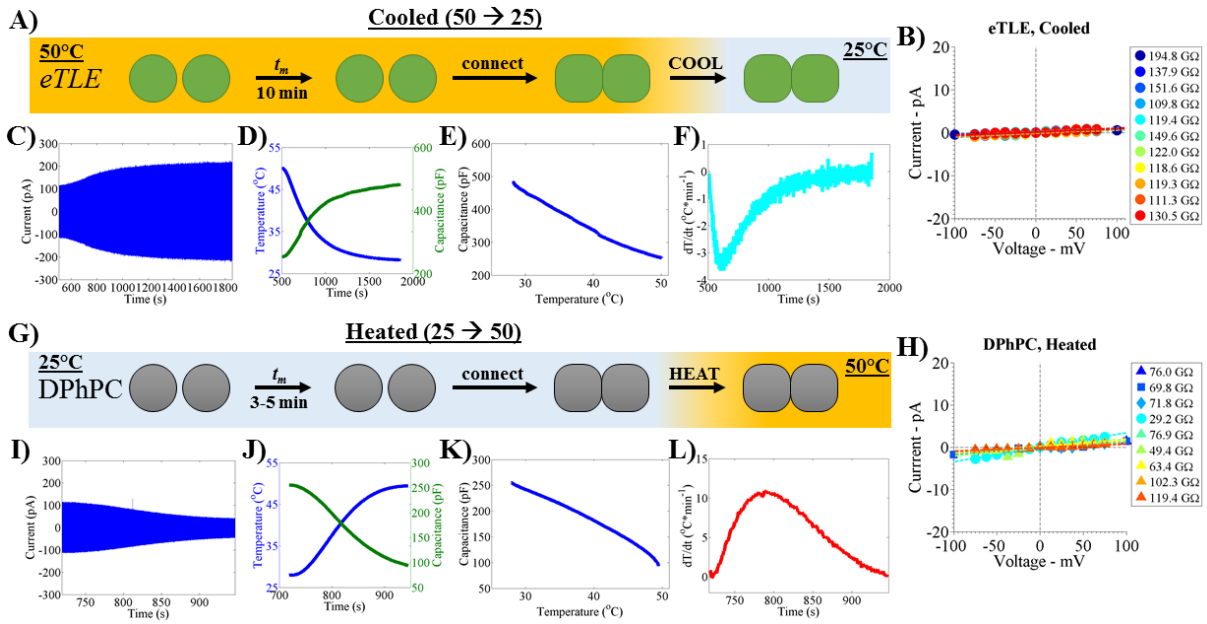

Figure 54. Cooling and heating formed DIBs. A) A pair of eTLE liposome infused droplets are connected at 50°C after 10 minutes of incubation time under oil, the size is adjusted to attain 100 pA SW via compression of the RAM substrate, and then the temperature set point is changed to 25°C to enact a cooling step. B) I-V curves obtained via DC step routines for multiple bilayers formed and cooled to 25°C. C) The square wave current as a function of time during the cooling step which shows increasing amplitude. The increasing amplitude corresponds to increasing capacitance, either via increased bilayer area or decreased bilayer thickness. D) Capacitance, calculated from the current, and temperature as a function of time while cooling. E) Capacitance as a function of temperature during the cooling step. F) Rate of temperature change during the cooling step, obtained as the derivative of the temperature signal with respect to time. G-H) Similar to (A-F) above except now for a pair of DPhPC liposome infused droplets connected at room temperature and heated to 50°C. I) The square wave current amplitude, and thus capacitance, decrease as a function of time while heating. J) Capacitance and temperature as a function of time while heating. K) Capacitance as a function of temperature. L) The rate of temperature change during the heating cycle, now increased compared to (E) above due to the active heating capability provided by the temperature controlled DIB platform. G) I-V curves for DPhPC bilayers formed and heated to 50°C.

Table 10. Summary of electrical properties measured with eTLE and DPhPC DIBs.

	DPhPC					E. coli TLE				
Temperature Group	R (GΩ)	R_M (MΩ·cm^2)	$V_{rupture}$ (mV)	C_M (μF/cm^2)	d (Å)	R (GΩ)	R_M (MΩ·cm^2)	$V_{rupture}$ (mV)	C_M (μF/cm^2)	d (Å)
Room Temp (RT)	208.7 σ=61.20 *n*=7	70.51	255.0 σ=36.20 *n*=7	0.74 σ=0.022 *n*=6	26.4	178.4 σ=82.60 *n*=12	67.88	228.2 σ=60.80 *n*=12	0.657 σ=0.021 *n*=6	29.64
50°C (10 minutes)	38.1 σ=21.30 *n*=12	13.45	205.8 σ=70.50 *n*=12	0.708 σ=0.021 *n*=7	27.48	41.8 σ=16.40 *n*=10	16.67	158.2 σ=73.90 *n*=10	0.627 σ=0.025 *n*=6	28.47
50°C (30 minutes)	n/a	n/a	n/a	n/a	n/a	35.2 σ=10.70 *n*=8	14.04	151.1 σ=26.85 *n*=9	n/a	n/a
Cooled (50°C→RT)	n/a	n/a	n/a	n/a	n/a	133.1 σ=24.70 *n*=11	50.65	200.0 σ=52.30 *n*=6	n/a	n/a
Heated (RT→50°C)	59.8 σ=37.90 *n*=9	21.12	205.0 σ=43.40 *n*=4	n/a	n/a	n/a	n/a	n/a	n/a	n/a
37°C	n/a	n/a	n/a	0.720 σ=0.007 *n*=4	27.05	n/a	n/a	n/a	0.684 σ=0.030 *n*=6	31.07

These findings prove that DIBs formed from DPhPC or eTLE can withstand temperature changes without rupturing. Yanagisawa, et al[90] reported that DIBs made from saturated dimyristoyl or dipalmitoyl phosphocholine (DMPC or DPPC) lipids (incorporated as inverse micelles into the organic phase) rupture during heating from 20-50°C. Dixit, et al (DPhPC liposome solution)[62] and Villar, et al (a 3:1 DSPC:DPhPC mixture in oil)[89] also separately observed droplet coalescence and bilayer rupture while heating intradroplet bilayers, the latter at a heating rate of only 1°C/minute. We report here that DIBs made from both eTLE and DPhPC phospholipids incorporated as liposomes within the droplets remain intact while heating between 20-50°C at rates as high as 10-11°C/minute. The key difference here is that DIBs are formed from either a complex mixture of lipids (eTLE) or lipids that do not undergo a phase transition (DPhPC). Single-component membranes are known to exhibit increased permeability and inherent stability near the phase transition due to having a sharp maximum in heat capacity at the transition.[289] As a result, bilayers formed from single lipids and binary mixtures are inherently weak and rupture easily upon cooling through T_m. The cited reports showing rupture near T_m with DMPC, DPPC, and

DSPC:DPhPC bilayers are good examples of this outcome. In contrast, membranes consisting of many lipid types exhibit broader transitions with lower susceptibility to rupture. The fact that eTLE survives heating and cooling through its T_m is attributed to its diverse lipid profile that preserves fluidity and a low permeability through the transition. On the other hand, our DPhPC DIBs are believed to survive for the reason that they do not pass through a transition in the temperature range tested. While this finding contrasts a prior study showing DPhPC failure, [62] we note that the authors of that work induced localized heating via an infrared laser and temperature and heating rate were not measured or controlled.

5.3.6 Lipid Composition Affects Membrane-Protein Interactions

Having a reliable method to construct lipid bilayers from *E. coli* total lipid extract enables the study of interactions between transmembrane proteins and bilayers possessing natural and heterogeneous lipid composition. A series of experiments are performed to determine how the insertion of alamethicin (Alm), a well-characterized antimicrobial peptide, differs between eTLE and DPhPC DIBs. First, it is necessary to ensure that no channel-like activity exists in eTLE DIBs formed in the absence of Alm. This control is especially important considering that almost 20% of the mixture is "unknown" (Avanti). In control tests without Alm, we observe no channel-like currents across a wide range of applied voltages and bilayer lifetimes. Even large eTLE bilayers exhibit no transient current with voltage clamped for several minutes at 150 mV (Appendix Figure 78). Control tests with DPhPC also result in quiet baselines at voltages below the rupture potential. In contrast, the addition of Alm to the *cis* droplet (+ electrode) of either DPhPC or eTLE DIBs introduces significant voltage-dependent changes in membrane conductance, giving rise to either microscopic single-channel or macroscopic aggregate-channel currents depending on Alm concentration.

Figure 55A and Figure 55B show representative alamethicin activity measured at room temperature (25°C) in both DPhPC and eTLE DIBs with 500 nM Alm in the *cis* droplet. In bilayers of either lipid type, the current (conductance) signal stochastically fluctuates between discrete levels signifying single channel pore formation, as previously established.[290, 291] Yet, voltage-dependent gating events occur at much lower voltages for eTLE bilayers. For example, Figure 55A

shows gating with DPhPC held near 160 mV. In this test, voltages <160 mV induce little to no activity, while voltages >160 mV lead to higher currents via the insertion of additional channels. In contrast, measurements of alamethicin gating in eTLE DIBs at 25°C show single-channel activity near 85 mV (Figure 55B), roughly half of the potential required to promote gating with DPhPC under the same conditions. In separate tests of eTLE DIBs with 5 μM Alm incorporated into the droplet, single-channel events are observed at voltages between 30-40mV. This trend agrees with prior reports[291] of the concentration-dependence of Alm, where increasing peptide concentration reduces the voltage required to attain insertion. The first five unit conductance levels (including the sub-conductance level at 15-20pS) for Alm with each lipid type at 25°C are determined from histograms of many single channel events and summarized in Figure 55C. The ratios of alamethicin conductance levels relative to the sub-conductance level in DPhPC bilayers are found to be 1, 4.3, 12.2, and 21.6, and 32.8, and for eTLE, we obtain ratios of 1, 5.1, 14.6, 25.3, and 33.0. These values for both lipid types compare well with previously reported values,[292] and there appear to be no significant differences in the conductance states between lipid types or for different measurement temperatures, which is consistent with prior findings regarding the effects of membrane composition on Alm conductance levels.[292]

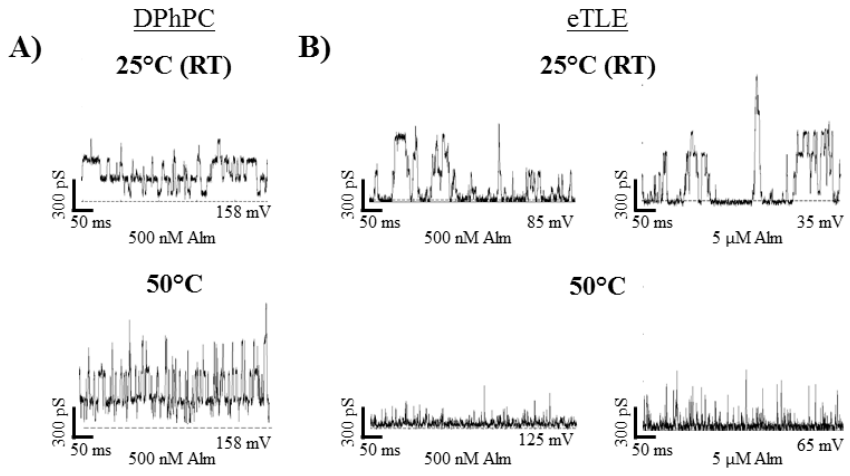

C)

	DPhPC	*E. Coli* TLE	
Alm Conc.	500nM	500nM	5uM
Level	G (pS)	G (pS)	G (pS)
0	0.0	0.0	0.0
1	18.3	17.3	-
2	78.8	87.8	90.5
3	226.1	252.1	266.9
4	398.8	437.1	463.0
5	606.0	570.49	615.7

Measured at 25°C

Figure 55. Single channel alamethicin (Alm) gating with: A) DPhPC and B) eTLE DIBs incorporating Alm in the cis (+ electrode) droplet. Concentrations tested include 500 nM and 5 μM, and tests are performed at 25 and 50°C which is below and above, respectively, T_m for the eTLE lipid mixture. The applied voltage is indicated with each trace. C) Single-channel conductance levels for DPhPC and eTLE bilayers at 25°C, computed from multiple gating events (all data not shown) at different Alm concentrations.

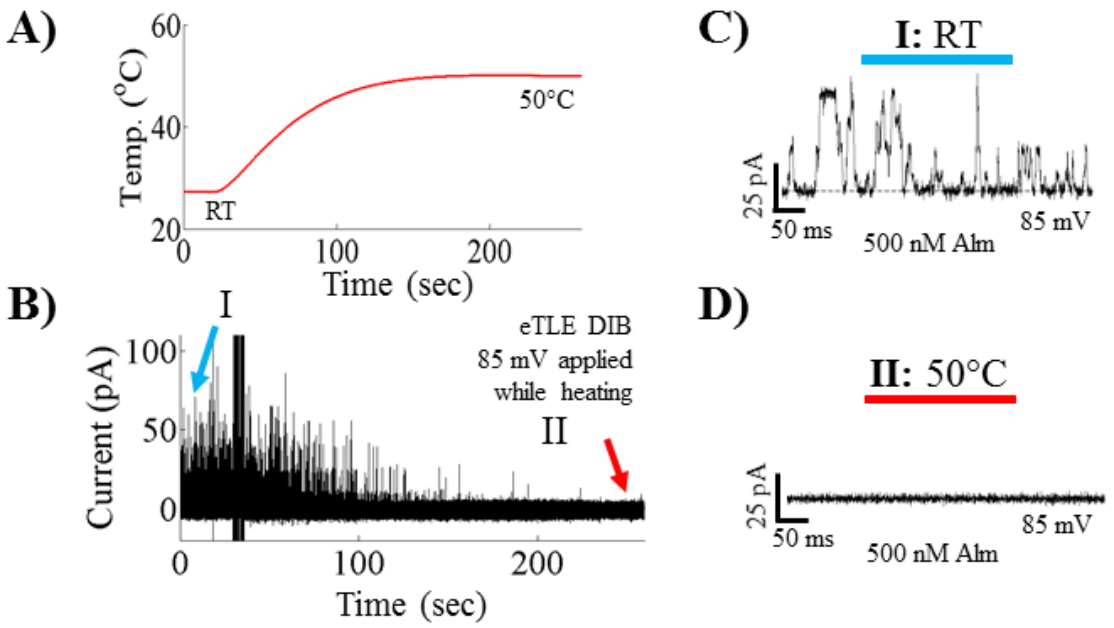

Figure 56. Test of dynamic changes in single channel currents while heating an eTLE DIB from 28 to 50°C. A) Temperature throughout the heating cycle. B) Current measured throughout the heating cycle. Applied voltage is fixed at +65mV with an initial bilayer size of ~250 pF (the large black bar in (B) is actually the square wave current response, ~ 100 pA amplitude). The blue (I) and red (II) arrows correspond to the insets shown in (C) and (D), respectively. (B) shows the gradual decrease in the frequency and magnitude of Alm associated current bursts while heating through T_m of the eTLE mixture. C) Single channel activity at room temperature before heating. D) After heating, activity has ceased while at the same applied voltage. The bilayer is confirmed to have remained intact throughout the heating cycle.

The lower panels of Figure 55A-B show the results of single channel recordings in DPhPC and eTLE DIBs at 50°C. Discrete stepwise changes in current at the same conductance levels are again observed with DPhPC DIBs at the same voltage shown for room temperature (158 mV). However these transitions occur at a noticeably higher frequency, a result that is in agreement with previous reports of temperature-induced changes in the rates of channel closing.**[290]** In the case of eTLE at 50°C with 500nM Alm, very quick bursts in current are observed when the voltage is increased to 125mV. Current through the same bilayer shows no channel activity at an applied voltage of 85 mV (i.e the voltage used to elicit channel activity at 25°C). The lifetime of a given burst at 125 mV is significantly shorter than gating events in eTLE at room temperature or even in DPhPC at 50°C. As voltage is increased above 125mV, the bursts become more frequent. The dynamic change in channel gating during heating is displayed in full in Figure 56. The nature of the heated-

state activity is similar for a higher peptide concentration of 5 μM with eTLE DIBs held at 50°C. Like at 25°C, we again observe a reduction in both the voltage required to elicit Alm-associated currents (65 mV as opposed to 125mV with 500 nM Alm) as well as the lifetime of Alm associated gating events.

The voltage-dependent insertion of alamethicin is confirmed and characterized further versus lipid type and temperature using CV measurements. For a lipid bilayer in the presence of Alm, macroscopic conductance (and thus current) is known to increase exponentially as a function of voltage above a critical voltage threshold (V^*). Figure 57A shows representative current-voltage sweeps for eTLE and DIB DIBs containing 1μM Alm in the aqueous lipid solution at 25, 37 and 50°C. For both membrane compositions and at all temperatures, the data show the expected exponential current response (confirmed via plotting in Figure 58), a result that further validates

Alm insertion in bilayers of both lipid types. V^* is determined as the voltage at which conductance exceeds a threshold conductance, G^*_{thresh}, of 8μS/cm^2 (see Section 2.3.1 for V^* calculation details). At each temperature tested, V^* is higher for alamethicin in DPhPC membranes than in eTLE membranes. For example, 1μM Alm exhibits voltage thresholds of 58mV and 122mV at 25°C and 50°C, respectively, in eTLE, while the same concentration of peptide requires voltages of 130mV and 145mV, respectively, to reach the conductance threshold in DPhPC. Combining these data with the single channel observations, we conclude that Alm inserts into eTLE bilayers at lower voltages than DPhPC bilayers within the range tested of 25-50°C. The CV data also show clearly that V^* increases with increasing temperature in both membranes. This trend is reflected by the rightward shifts in the representative exponential current traces as shown in Figure 57A, and also in the calculated values of V^* and ΔV^* (change in V^* relative to RT for each lipid) summarized in Figure 57B,C. Plotting the voltage threshold versus temperature for the two membranes (Figure 57B) reveals that V^* for alamethicin insertion in eTLE bilayers is more sensitive to temperature increases compared to insertion in DPhPC bilayers. This result is in direct agreement with the single-channel gating that was shown to occur at significantly lower voltages in eTLE membranes at 25°C versus 50°C.

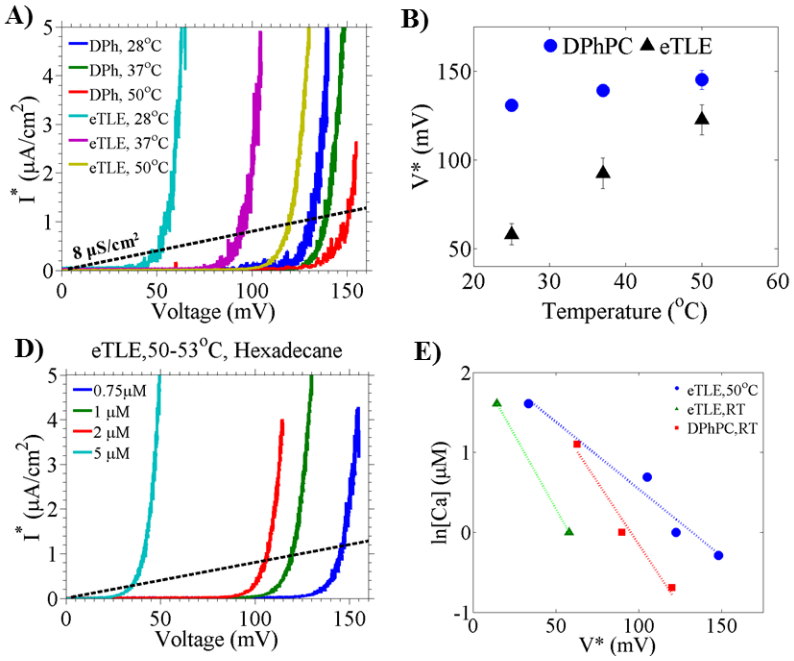

C)

Temp. Group	DPhPC V* (mV)	DPhPC ΔV* (mV)	*E. coli* TLE V* (mV)	*E. coli* TLE ΔV* (mV)
RT	130.7 (2.104) *n*=8	0	58.0 (5.931) *n*=6	0
37°C	139.0 *n*=1	+8.3	92.4 (8.561) *n*=7	+34.4
50°C	145.1 (5.360) *n*=7	+14.4	122.6 (8.470) *n*=9	+64.6

F)

Lipid/ Temp.	V_a (mV)	C_0 (µM)
DPhPC, RT	31.95	19.72
eTLE RT	26.95	8.59
eTLE, 50°C	59.52	9.24

Figure 57. (A) Specific current (I*, normalized by membrane area) from one of 10 repeated scans during CV testing at varying temperatures with either DPhPC or eTLE DIBs. The trace shown is an average of I* recorded during the increasing and decreasing portions of a single scan, resulting in a single I* signal associated with the linear voltage ramp from 0-150 mV. In these tests, the cis (+) droplet contains 1µM alamethicin (Alm). For each lipid case shown, a bilayer is formed at 50°C, tested via CV, cooled to 37°C, tested via CV again, and then finally cooled to 28°C before a third and final round of CV scans. The dashed line represents the conductance threshold (G^*_{thresh}) used to determine voltage threshold (V*): the voltage at which I* exceeds G^*_{thresh}. B) V* as a function of temperature from part (A). Error bars show ± one standard deviation (σ). (C) Summary of cyclic voltammetry (CV) testing, including V* and relative change in voltage threshold (ΔV*) versus temperature. The value in parenthesis is σ. D) Current-voltage sweeps for an eTLE DIB above T_m with 0.75, 1, 2, and 5µM Alm. E) Plot of the logarithmic relationship between V* and alamethicin concentration, C_a, used to compute the conductance parameters V_a and C_0 shown in (F).

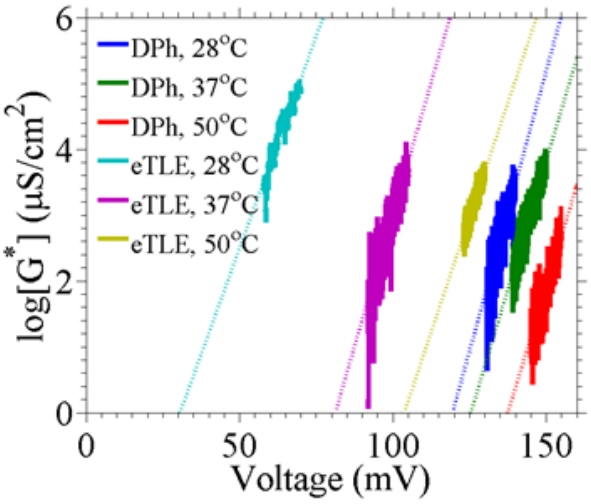

Figure 58. Data from Figure 57A, converted from current into conductance before plotting ln(G^*) against the voltage. Note, only current from the exponentially increasing region ($V>V^*$) is utilized for fitting. Dashed lines show the fit for each lipid and temperature case.

The effects of temperature and lipid type on peptide insertion are examined quantitatively by computing other macroscopic Alm conductance parameters. V^* follows an experimental relation to the aqueous alamethicin concentration (C_a) as follows: [56, 291, 293]

$$V^* = -V_a \ln(C_a/C_0) \qquad \text{Equation 30}$$

Here, V_a describes the shift in V^* (and thus the current-voltage curve) that results from an e-fold increase in C_a. Physically, V_a provides a measure of the sensitivity of membrane conductance to Alm concentration and is known to change with lipid type and temperature. [293] C_0 is a constant, representing the concentration at which Alm inserts spontaneously into the bilayer without an applied voltage. Figure 57D shows the current-voltage curves of eTLE bilayers tested at 50°C with alamethicin concentrations ranging from 0.75-5 μM, and it is clear that the curves shift towards lower voltage (left) as peptide concentration increases. Figure 57E is a plot of ln(C_a) versus V^* obtained from data in Figure 57D (eTLE at 50°C) as well as eTLE and DPhPC at 25°C. Similar measurements on the effect of Alm concentration in DPhPC are not performed at 50°C, although little change is expected due to the reduced sensitivity of V^* to temperature. Rearranging Equation 30 yields:

$$\ln(C_a) = -(1/V_a)V^* + \ln(C_0) \qquad \text{Equation 31}$$

Via the relation described by Equation 31, the slope and intercept of a linear fit of the series in Figure 57E provide access to V_a and C_0 for each lipid and temperature (Figure 57F). At 25°C, V_a is 32 mV for DPhPC and 27 mV for eTLE. Upon heating eTLE through T_m to 50°C, V_a increases significantly to almost 60 mV, indicating that heating results in a considerable change to the membrane environment that reduces its susceptibility to Alm insertion at a given concentration. The near doubling of V_a from 25°C to 50°C provides additional support that the gel-fluid phase transition in eTLE bilayers is the cause for reduced alamethicin activity in the heated state. Further, higher values of C_0 for DPhPC versus eTLE and for eTLE at 50°C versus 25°C indicate that a higher concentration of Alm is required to promote insertion without applied voltage in DPhPC bilayers and heated eTLE bilayers. These results allow us to conclude that Alm inserts into eTLE membranes below its T_m at lower voltages and concentrations compared to both DPhPC bilayers at the same temperature and fluid-phase eTLE DIBs (above T_m).

CD experiments at 28, 37, and 50°C also provide structural evidence that alamethicin insertion into lipid bilayers decreases with increasing temperature. The spectra obtained for Alm bound to eTLE and DPhPC liposomes are converted to molar ellipticity and shown in Figure 59A-B, respectively. Figure 59C shows the molar ellipticity at 224nm, a wavelength associated with alpha-helical conformation,[56] as a function of lipid type and temperature. For both lipid types, the

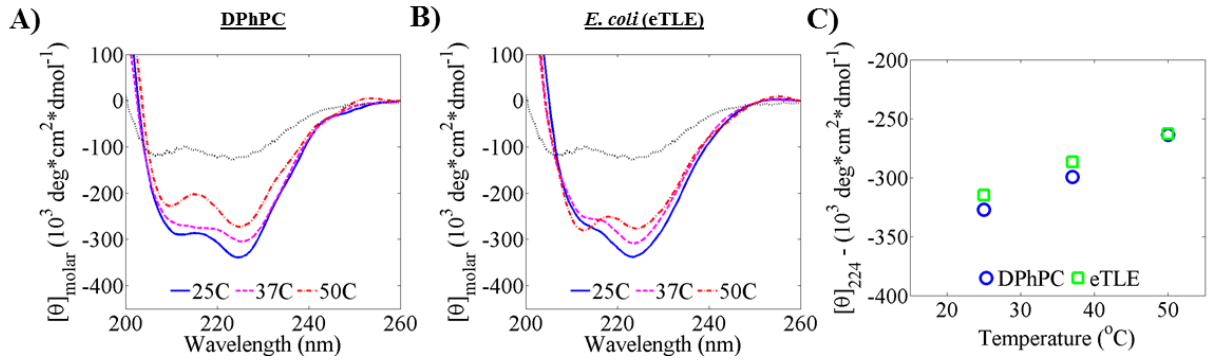

Figure 59. Molar ellipticity of alamethicin incubated with DPhpC (A) and eTLE (B) liposomes at a peptide:lipid ratio of 1:46. Samples are tested initially at 25°C. The light dashed line shows molar ellipticity of pure Alm in aqueous buffer solution at 25°C. Temperature is increased to 37°C and 50°C after 10 minutes of equilibration before each measurement. Total lipid and Alm concentrations are 500 µg/mL and 50 µg/mL, respectively. C) Molar ellipticity at 224 nm for both DPhPC and eTLE as a function of temperature.

magnitude of ellipticity decreases with increasing temperature, which suggests decreasing alpha helical content upon heating. The alpha helical content is believed to correlate to the amount of inserted, transmembrane spanning alamethicin.[56] Thus, it appears here that the amount of inserted Alm is inversely related to the temperature. This result holds for both eTLE and DPhPC bilayers, is consistent with previous research into effects of temperature on secondary structure,[294] and is also in line with finding that V^* increases with temperature for DIBs of both lipid types.

5.3.7 Discussion of Alamethicin Insertion into eTLE Membranes

There are several possible reasons as to why eTLE DIBs exposed to Alm exhibit lower voltage thresholds compared to DPhPC. Without the bulky isoprenoid methyl groups present in DPhPC,[295] an eTLE bilayer may exhibit higher fluidity and present a lower barrier to entry for Alm insertion. Phase separation and the presence of subdomains within an eTLE[296, 297] may laterally concentrate regions of Alm, thereby increasing the probability of channel formation in concentrated regions. Additionally, alamethicin may itself induce local melting in the membrane that leads to peptide-rich fluid regions even below the effective T_m for the membrane.[279] While the specifics of this mechanism are unclear from our data alone, the measurements provide strong evidence that eTLE membranes allow for Alm channel formation to occur at lower voltage and lower concentration compared to DPhPC bilayers.

Aside from differences in composition, the increases in voltage threshold (CD) and decreases in alpha-helical content (CV) suggest that the likelihood of Alm insertion decreases upon heating. The trend is consistent for both DPhPC and eTLE, however alamethicin insertion in eTLE exhibits a greater sensitivity to increases in temperature, as indicated by the larger change in voltage threshold (Figure 57A-C) and the more drastic changes to single channel currents (Figure 55B). These data suggest that the gel-to-liquid phase transition of eTLE versus heating of DPhPC within the liquid phase is the cause for the difference in temperature sensitivity for alamethicin peptide insertion between the two membranes. The results obtained from CD testing show less of a difference, however these tests were performed at much higher alamethicin concentrations required to induce spontaneous insertion without voltage. At such a high concentration needed for

CD measurements, the additional peptide may have also reduced the membrane phase transition below room temperature. An increase in alamethicin activity below T_m in a mixed-lipid membrane is supported by a prior study by Boheim, et al[279] that showed increased conductance (at a fixed voltage) upon cooling into the gel state of a binary phospholipid mixture. The authors of that work hypothesized that peptide does not prefer to insert into a gel-phase membrane, rather that cooling below the phase transition creates phase-separate subdomains in the bilayer that effectively increase the concentration of alamethicin in the fluid portions of the bilayer.[279] Our results with heterogeneous eTLE DIBs show a similar trend, and we too believe that the phase transition may drive an increase in local concentration of peptides in the membrane, which agrees with the trend for single channel lifetimes (Figure 55A-B) and voltage threshold versus alamethicin concentration (Figure 57C).

It is important, too, to put the observed temperature sensitivity of Alm insertion in context to the fact that heating *solvent-containing* DIBs results in an increased amount of oil in the membrane. The comparable magnitudes of solvent-associated changes in C_M and d_{HC} (Figure 51) suggest eTLE and DPhPC bilayers undergo similar increases in thickness upon heating. Thus it seems unlikely that thickness or temperature-dependent solubility of oil in the membranes are solely responsible for the changes in V^*, which were shown to be significantly larger for eTLE membranes. To help eliminate oil as the cause of the significant changes to V^* with eTLE as a function of temperature, we performed separate CV measurements on eTLE DIBs in squalene instead of hexadecane (Figure 60). This substitution was made since it is known that larger-molecule oils are known to yield more *solvent-free* bilayers.[226] In the presence of squalene, V^* for an Alm concentration of 2 μM shifts from 86.2 mV at 25°C to 49.0 mV at 50°C after heating the bilayer from the gel phase to the fluid phase. Thus, while oil in the membrane may affect the thickness of the bilayer, and can depress the transition temperature (believed to be less than 10°C),[298] we conclude that the effective phase change of the eTLE membrane is the dominant cause for the changes in alamethicin insertion upon heating.

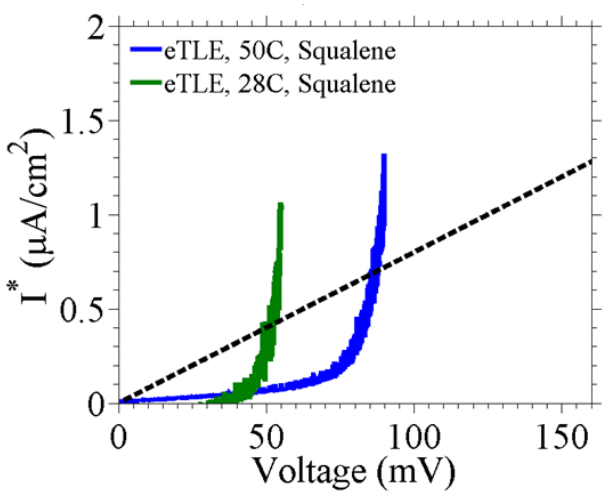

Figure 60. Representative current-voltage sweep from CV tests of an eTLE DIB incorporating 2 μM Alm in one droplet in tests using squalene as the oil phase. Each curve corresponds to a different temperature (28°C, 50°C). V* decreases from 86.2 mV to 49.0 mV upon cooling through T_m, even in these essentially *solvent-free* DIBs obtained through oil selection (squalene as opposed to hexadecane). Dashed line represents the conductance threshold, 8 μS/cm^2, used for *V** calculation throughout the work.

5.4 Chapter Summary and Conclusions

DIB formation using total lipid extract from gram negative *E. coli* is enabled by heating droplets containing eTLE liposomes to 50°C to promote monolayer formation at the oil-water interface. Through parallel measurements, we found that this temperature corresponds to the upper limit of a gel-to-liquid phase transition for the mixed liposomes. Nonetheless, bacterial model membranes comprised of eTLE lipids can be formed at cooler temperatures too, so long as heating is used to first promote adequate monolayer formation. These findings suggest that the formation of DIBs using liposomes with gel-to-liquid transition temperatures above room temperature can be performed in either the gel or liquid phase by using heat to first aid in monolayer assembly. Electrical measurements of specific capacitance confirm that like DPhPC, the interface between droplets containing eLTE liposomes is that of a lipid bilayer. Hydrophobic thicknesses for both are comparable (~26-31Å), although the bacterial variant exhibits slightly thicker interfaces than its DPhPC counterpart. Electrical measurements reveal that eTLE DIBs are comparable to those formed using DPhPC at both room temperature and 50°C in terms of resistance, specific resistance,

and rupture potential. Plus, DIBs comprised of either DPhPC or eTLE exhibit low leakage currents under applied voltage, making them suitable for electrical measurements of single or few ion channels as well as higher peptide concentrations. With the capability to vary temperature, we demonstrated that the electrical resistance and rupture potential of DPhPC and eTLE DIBs both decrease with increasing temperature. However, mixed-lipid compositions of eTLE enable reversible cycling through T_m without leakage or rupture, unlike single and binary lipid compositions that often coalesce during the transition. Specific capacitance of membranes from either lipid type decreases with increasing temperature, indicating a slight increase in thickness, which is attributed to a temperature-dependent increase in hexadecane solubility in the bilayer.

In the second part of the work, the ability to construct DIBs from *E. coli* total lipid extract enabled study of alamethicin interactions with bilayers possessing natural and heterogeneous lipid composition. The ability to control temperature allowed investigation of the role of gel-fluid phase transitions in peptide-membrane interactions. Alm inserts at lower concentrations and voltages in eTLE, likely the result of increased membrane fluidity compared to ordered structure of gel-phase DPhPC membranes. We also determined that the phase change exhibited by eTLE is a dominant cause for the greater temperature sensitivity of eTLE bilayers to alamethicin insertion. Our results show that upon cooling through T_m, the voltage required to induce channel formation drops by more than a factor of 2 (compared to a ~10% decrease in voltage threshold for DPhPC). An increase in alamethicin activity in the effective gel-phase for eTLE bilayers is thought to occur due to localized phase separation that concentrates alamethicin within the remaining fluid regions of the bilayer, leading to lower voltage threshold and longer single channel lifetimes. The temperature-dependent transition and resulting phase separation is a result of the complexity and heterogeneity of the natural total lipid extract. The output of this work advances DIB technology by providing methods to fabricate better biomimetic model membranes that could be used to study other antimicrobial peptides and many other membrane mediated processes. Given that eukaryotic TLEs are commercially available (i.e. yeast, heart, brain, and liver), the lessons learned here may also enable rapid advances in assembling natural, biologically relevant model membranes to benefit human medical technology.

CHAPTER 6

DETECTING WEAK-ENTHALPY PHASE TRANSITIONS IN BRAIN TOTAL LIPID EXTRACT DROPLET INTERFACE BILAYERS

Chapter 5 established knowledge of the requirements for consistently forming DIBs using liposomes comprised of complex, physiologically relevant mixtures of lipids derived from *E. coli*. This chapter seeks to continue to build on the newly established methods by exploring the formation of DIBs using eukaryotic mixtures of total lipids extracted form porcine brain. This chapter addresses Objective 4 through efforts to study the effects of increasing compositional heterogeneity on DIB resistance, specific capacitance (thickness), surface tension, and the interactions of membrane-active peptides. In direct response to Objective 5, this chapter describes extensive analysis of the thermotropic behavior of DIBs and the effects of changing temperature on bilayer electrical and physical properties and the behavior of membrane-active peptides. This chapter includes comparative measurements on three major classes of membranes: 1) lipid bilayers comprised of a single lipid type that are known to undergo no phase transition, and 2) lipid bilayers comprised of a single lipid or lipid mixture that are known to undergo a phase transition (in the temperature range tested), and 3) lipid bilayers formed from brain total lipid extract (bTLE) whose thermotropic properties are not well understood.

6.1 Introduction

Chapter 5 describes efforts to enable DIB formation using total lipid extract from *E. coli* (eTLE). Previous attempts conducted at room temperature failed when neighboring droplets coalesced soon

after being brought into contact with each other, an indication that eTLE monolayer self-assembly did not achieve sufficient steady-state packing levels for DIB formation. However, by heating the oil and the submerged aqueous droplet above the lipid mixture's transition temperature (T_m) – thereby promoting adequate monolayer assembly at the oil-water interface – stable DIBs could be formed from the complex lipid mixture. Importantly, total lipid extracts preserve the heterogeneity found in cell membranes, including the different types of naturally occurring hydrocarbon chains and headgroups. For example, eTLE contains charged phosphatidylglycerol (PG) and uncharged phosphatidylethanolamine (PE) headgroups [299], as well as a diverse assortment of acyl chain types (e.g., 12:0, 14:0, 16:0, 16:1, 18:1, 17:0-cyclopropanic, and partially methylated 14:0) [158]. The lipid extract is also rich in cardiolipin [299], a unique lipid possessing a net double negative charge and four acyl chains comprised of one or more types of acyl chains [300]. Compared to DPhPC, eTLE better represents the chemical complexity of the inner cytoplasmic membranes of gram negative bacteria. eTLE DIBs are therefore a promising new model system for studies of antimicrobial resistance, mechanisms of antibiotic action, and prokaryotic membrane functions.

The successful formation of eTLE DIBs represents an important step forward toward droplet-based bilayers with a physiologically relevant lipid heterogeneity [10]. It is now important to ask: can DIBs be constructed from other complex lipid mixtures, such as those found in eukaryotic organisms? Comparing the bacterial and mammalian lipidomes, several significant differences are apparent. Bacterial membranes are rich in PE and the charged lipids PG and cardiolipin (typically with unsaturated, low-melting chains), and they contain no sterol, although many bacteria produce hopanoids that are believed to play a similar role [155]. In contrast, mammalian membranes contain a diverse mixture of saturated and unsaturated species, and as much as 50 mol% cholesterol [153]. Schiller *et al.* used MALDI-TOF mass spectrometry and HPLC to identify 36 different lipid species in porcine brain total lipid extract (bTLE), including nine distinct types of headgroups [301]. NMR data indicated that ~ 46 mol% of the mixture consisted of phospholipids (PL), with the remaining ~ 50 mol% comprised of cholesterol, cerebrosides, gangliosides, and other non-phospholipid species [301]. Sphingomyelin and cholesterol are known to play an important role in lipid raft formation [168, 176, 302, 303], the targeting of toxic pore-forming membrane peptides [304], and nervous system endocytosis and intracellular processing within cells [305, 306].

A droplet-based model membrane system incorporating bTLE would therefore be an attractive platform for the systematic study of mammalian neural membranes, including neurological conditions and their underlying membrane-associated phenomena, such as: 1) the interactions between membranes, amyloid-beta and tau proteins that play key roles in diseases such as Alzheimer's, Huntington's, Parkinson's, and Down Syndrome [307-309]; 2) studies of myelinated cell membranes and the mechanisms responsible for their degradation in neuropathy, diabetes, or general aging [309]; 3) the behavior of the blood brain barrier [310]; and 4) the properties of raft-like domains. A DIB approach for assembling multiple synthetic bTLE membranes using an array of droplets [84] could also support the development and high-throughput screening of drugs targeting the central nervous system.

This chapter provides a report of the ability to form bTLE DIBs with heating-assisted monolayer formation at temperatures ≥ 50°C. Heating is found essential for adequate monolayer packing and stable DIB formation when using bTLE, in contrast to DPhPC and DOPC. Once formed, bTLE DIBs survive cooling and heating, which allows us to investigate their temperature-dependent electrical and physical properties. Nominal resistance (R) and specific membrane resistance (R_M) provide a measure of the membrane's integrity and permeability to ions, while specific capacitance (C_M) measurements [10, 49, 50] allow calculation of bTLE membrane thickness. C_M of solvent-containing bTLE DIBs reveals an abrupt change in bilayer thickness at 42°C, reminiscent of a phase transition. A similar transition is observed in DIBs formed from three component lipid mixtures known to separate into coexisting fluid phases, but not in single component DIBs prepared from either dioleoylphosphocholine (DOPC) or DPhPC. Differential scanning calorimetry (DSC) is used to examine the thermotropic behavior of bTLE multilamellar vesicles (MLVs). No thermotropic events are observed in the range of 10-70°C, suggesting that the transition observed at 42°C with electrical measurements is of low enthalpy and cooperativity.

Via a similar approach to that used in the study of eTLE DIBs (see chapter 5 and [10]), the antimicrobial pore-forming peptide alamethicin (Alm) is used as a tool to further compare the properties of simple and complex lipid bilayers. Microscopic (single-channel) and macroscopic (cyclic voltammetry, CV) electrical measurements are used to quantify Alm insertion into bTLE

DIBs. Specifically, the known empirical relation between Alm concentration and the voltage threshold for insertion (V^*) is used to extract thermodynamic parameters for Alm-bTLE membrane interactions between 20°C and 60°C. Tracking V^* while cooling DIBs is used to investigate effects of the bTLE thermotropic phase transition on peptide insertion; we discuss the possibility of lateral reorganization of the Alm peptide in response to temperature-induced changes in membrane structure. Fluorescence microscopy of bTLE giant unilamellar vesicles (GUVs) and FRET measurements with bTLE large unilamellar vesicles (LUVs) are utilized to inspect further for the presence of lateral organization at both the micro- (> 1 μm) and nanoscale (i.e., length scales <10 nm).

6.2 Experimental Methods

6.2.1 Single Channel and CV Measurements with Alm

Single channel measurements of Alm insertion into DPhPC and bTLE DIBs include symmetric DIBs: both droplets contain 2 mg/mL total lipid and 100 nM Alm peptide. Applied dc voltage is varied manually via the patch clamp amplifier in voltage clamp mode. CV scans are performed with symmetric Alm concentrations of 0.25, 0.5, or 1 μM (L/P ratios of 8000/1, 4000/1, or 2000/1 respectively). Details of the CV method and analysis are described in detail in Chapter 1 and elsewhere [10]. For measurements of V^* while cooling bTLE DIBs, a single bipolar CV sweep was initiated manually at timed intervals during the cooling cycle which results in one V^*-temperature pair per sweep (temperature taken as the temperature at the start of the sweep). V^* values shown (Figure 74) are the average V^* from multiple DIBs where the V^* value for each DIB is the average of V^* values determined from $n \geq 4$ consecutive CV sweeps.

6.2.2 Fluorescence Microscopy with GUVs

GUVs were prepared using the electroformation method [311], modified as follows. Lipid mixtures (300 nmoles total) were prepared in 200 μL chloroform, deposited onto indium tin oxide (ITO)-coated glass slides (Delta Technologies, Loveland, CO) preheated to 50°C, and uniformly spread across one end of the slide. Residual chloroform was then removed by placing slides under vacuum for 2 h. An electroformation chamber was formed by separating two slides with an O-ring

filled with 30 mM sucrose. The assembled chamber was stabilized in a custom built aluminum block that was heated to 55°C in a dry block heater. Lipid films were swelled at 55°C in a 10 Hz, 1 volt (peak-to-peak) ac field for 2 h, then cooled to room temperature over 3 h. The ac waveform was generated from a waveform generator. Samples were harvested into microcentrifuge tubes using large orifice pipet tips and imaged using a 100x lens on a confocal fluorescent microscope).

6.2.3 FRET Spectroscopy Measurements

Mixtures of lipids in chloroform were prepared in glass culture tubes using a glass syringe and repeating dispenser (Hamilton USA, Reno, NV). Fluorescent probe/lipid mole ratios used are 1:200 (DHE), 1:1500 (BoDIPY-PC), and 1:3000 (FastDiI). Samples contain final total lipid mass of 1 mg which is transferred to 1 mL of buffer via reverse solvent exchange (RSE) [312] which yields MLVs. FRET measurements are conducted with 100 μL of MLV stock diluted with 1.9 mL of buffer in a sample cuvette. Fluorescence data were collected between 20-60°C using a F7000 Spectroflourimeter (Hitachi high Technologies). Additional details regarding the fluorescence data collection and analysis are described elsewhere [167].

6.2.4 GCMS Sample Preparation and Analysis

GCMS experiments were performed using lipid mixtures subjected to a protocol for conversion to fatty acid methyl esters (FAMEs) via acid catalyzed methanolysis as described elsewhere. [313] GC analysis was performed on an Agilent 5890A gas chromatograph (Santa Clara, CA) with a 5975C mass-sensitive detector operating in electron-impact mode. Helum was used as the carrier with a flow rate of 1 mL/min. The column used was an HP-5MS capillary column (30 m × 0.25 mm, 0.25 μm film thickness). The inlet temperature was 300 °C. 1 μL aliquots of FAME samples in hexane were injected, using splitless mode, via an Agilent 7693A automatic sampler. Assignment and integration of total ion chromatogram peaks was performed using GC/MSD ChemStation Enhanced Data Analysis software (Agilent Technologies, Santa Clara, CA)

6.3 Results and Discussion

6.3.1 DSC and DIB Formation with bTLE

Differential scanning calorimetry (DSC) is used to investigate the thermotropic behavior of liposomes made from either bTLE, DPPC, DPhPC, or DOPC. Figure 61 shows resulting thermograms from DSC scans of MLVs formed with bTLE (Figure 61A-B), DPhPC (Figure 61C-D), DOPC (Figure 61E-F), and DPPC (Figure 61G-H). The curves obtained with DPhPC and DOPC are featureless, without any signs of a first-order phase transition, as expected. On the other hand, the scans collected with DPPC MLVs display a sharp peak at 41-42°C that corresponds to the first-order, highly cooperative gel-fluid transition [142, 314]. The thermograms for bTLE show no signs of a reversible first-order phase transition such as that seen with DPPC. Prior studies were similarly unable to detect lipid phase transitions via DSC with total lipid extracts from mammalian membranes (erythrocytes and myelin) [6]. In these studies, however, removal of the cholesterol produced a measurable peak in the thermograms [6]. This result suggests that cholesterol reduces the enthalpy of the transition to a point that it is difficult to observe and study the transition using calorimetry. GCMS analysis of the bTLE used herein confirms the presence of a large fraction of cholesterol (~50 mol%), and the remaining fatty acid distribution is found to slightly favor

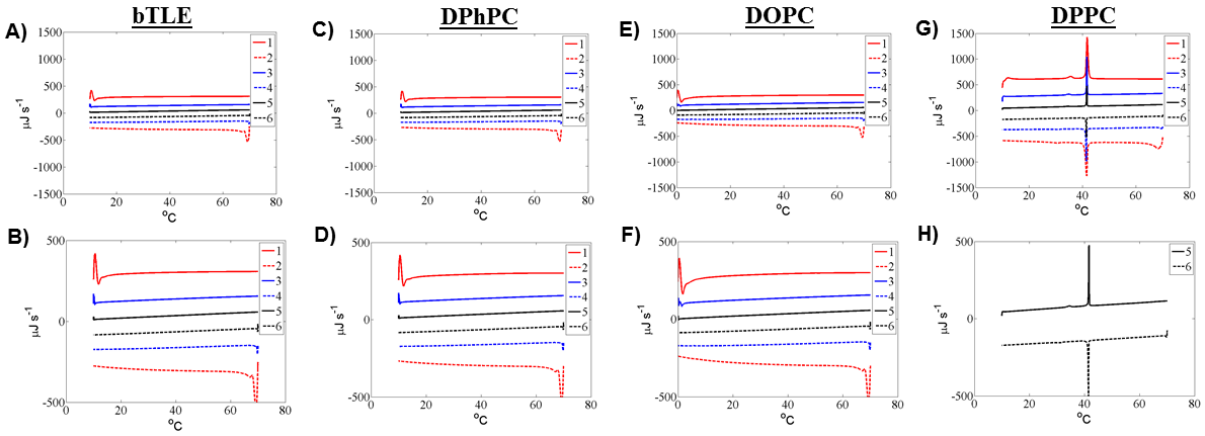

Figure 61. Differential scanning calorimetry (DSC) thermograms obtained during 3 heating and cooling cycles of multi-lamellar vesicles (MLVs) formed from A-B) bTLE, C-D) DPhPC, E-F) DOPC, or G-H) DPPC. Raw scans are shown. The bottom row shows top row data but with different y-axis limits. Legends: The DSC protocol for all trials involves heating and cooling at scan rates of 1°C/min (1,2), 0.25°C/min (3,4), and 0.1°C/min (5,6).

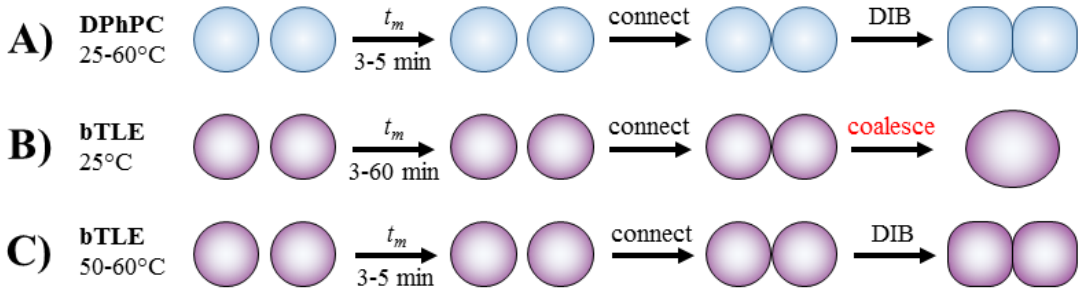

Figure 62. Illustrated outcomes from testing the ability to form DIBs using aqueous droplets infused with 100nm unilamellar liposomes made of either (A) DPhPC or (B-C) bTLE. A) DPhPC infused droplets adhere spontaneously when connected after 3-5 minutes for monolayer formation at 25°C. B) Switching from DPhPC to bTLE, droplets at room temperature coalesce when connected after up to an hour for monolayer formation. C) If bTLE infused droplets are placed in oil heated to ≥ 50°C, droplets can be connected after 3-5 minutes for monolayer formation to achieve spontaneous droplet adhesion and bilayer formation.

unsaturated fatty acids (UFA=53.3 mol%; SFA=46.7 mol%). High cholesterol content is known to reduce enthalpy and cooperativity of the main transition, and thus strongly attenuates any calorimetrically detectable phase-transitions [6, 142, 277, 314]. However, it is still possible that cholesterol-rich bTLE exhibits a higher order (i.e., not a first-order gel-fluid transition), temperature-dependent lipid phase transition similar to that encountered with other mammalian total lipid extracts [6].

DSC results suggest that bTLE does not undergo the same gel-fluid transition observed in homogenous DPPC liposomes, however, bTLE DIBs can only be formed after 3-5 minutes for monolayer assembly when the oil (tested in dodecane, hexadecane, and heptadecane) temperature is ≥ 50°C (Figure 62). Further, bTLE DIBs can be formed at 25°C as long as the droplets are heated above 50°C for several minutes before cooling to 25°C. Thus while DSC results show no detectable thermotropic transition for bTLE MLVs, the ability to form bTLE DIBS through controlled heating suggests that bTLE undergoes a phase transition between 25-50°C, and heating yields fluid-phase liposomes required to form tightly packed monolayers at the fluid interface [276]. One clear difference between DSC and DIB experiments is the presence of nonpolar alkane solvents used to assist DIB formation. However, Keller *et al*. have shown that planar bilayers formed in the presence of solvent display the same phase-behavior as their solvent-free aqueous

liposome analogs [171], thus it is unlikely that solvent is introducing or causing the suspected thermotropic behavior with bTLE lipids self-assembling at the oil-water interface.

6.3.2 Effects of Temperature on bTLE DIBs

bTLE DIBs are formed only if the droplets are first incubated in heated oil (50-60°C, Figure 62C). However, once formed they can be reversibly cooled and heated between 25°C and 60°C. This enhanced stability enables us to investigate the effects of temperature on the bTLE's electrical and physical membrane properties. Specifically, nominal membrane resistance (R), capacitance (C), and membrane area (A_M) are measured, then specific resistance (R_M) and specific capacitance (C_M) are computed, for numerous bTLE DIBs at high (60°C) and room temperatures (25°C). R_M is calculated as the product of R and A_M at each measurement temperature for each bilayer, and C_M is measured for each bilayer as described previously [10, 49]. Table 11 shows the average values, standard deviation, and number of samples for R, R_M, and C_M at each temperature with bTLE DIBs formed in hexadecane. Unlike the nominal R, which does not take into account membrane area, R_M is significantly lower in the heated state ($p < 0.05$). This finding is consistent with prior reports of temperature effects on both single-component DIBs and heterogeneous eTLE DIBs [10]. In all cases, the decreased resistance of heated bTLE DIBs is indicative of higher membrane permeability to ions.

Table 11. Summary of electrical and physical properties of bTLE DIBs formed at 60°C and after cooling to 25°C (hexadecane solvent).

Temp. Group	***R*** **(GΩ)**	***R_M*** **(MΩ*cm^2)**	***C_M*** **(μF/cm^2)**	***d_{hc}*** **(Å)**
60°C	32.3 (4.39) *n*=4	9.8 (3.26) *n*=4	0.405 (0.017) *n*=3	48.2 (2.12) *n*=3
25°C	38.1 (2.89) *n*=3	24.1 (3.47) *n*=3	0.684 (0.019) *n*=3	28.5 (0.83) *n*=3

Table 11 also shows that C_M increases upon cooling from 60°C to 25°C. Modeling the bilayer as a parallel plate capacitor, C_M is inversely proportional to the membrane hydrophobic region thickness (d_{HC}) via $C_M = \varepsilon_r\varepsilon_0/d_{HC}$, where ε_r and ε_r are the relative permittivity for the dielectric region and the permittivity of vacuum, respectively. It is common to assume a permittivity of ε_r = 2.2 for hydrocarbon rich regions such as the middle of a lipid bilayer [256, 285]. We also do not expect significant variations in the value of the hydrocarbon permittivity over the temperature range studied. Thus, the observed increase in C_M upon cooling is instead expected to be the result of a decrease in bilayer thickness, which is in contrast to what is expected when cooling solvent-free bilayers or vesicles [288]. For example, bTLE DIBs formed at 60°C show d_{HC} = 48.2 Å, but the membrane hydrocarbon region thickness decreases by 40.8% to 28.5 Å after cooling to 25°C. We recently reported that d_{HC} of DPhPC DIBs formed in hexadecane decreases by 4.0% upon cooling, from 27.5 Å at 50°C to 26.4 Å at 25°C [10]. (For a lipid like DPhPC that does not undergo a thermotropic transition, we would expect cooling to decrease the area per lipid and increase the overall solvent-free bilayer thickness due to conservation of volume: in alkane-free DPhPC vesicles, the hydrocarbon thickness increases 4.5% from 26.6 Å at 60°C to 27.8 Å at 20°C as determined via X-ray scattering [288].)

The difference between solvent-containing DIBs and solvent-free model membranes (e.g. liposomes) can be explained in terms of the increased temperature and increased solvent solubility in the hydrophobic region of the bilayer. In the absence of solvent, heating induces an increase in the flexibility of acyl chains (i.e. increased number of gauche configurations [315]) which is accompanied by membrane thinning [316]. In general, this trend is opposite to our observations of heating induced thickening. Thickening of the bilayer might be expected if there is an increase in the amount of oil that aligns parallel to, and thus packs and orders, the lipid acyl chains. Considering this possibility of solvent-induced ordering and extension of the lipids, it is possible to estimate the maximum expected thickness increase that would stem from full extension of all of the lipids. Geometrically, removal of a 30° tilt (with respect to the bilayer normal) with 16-18C acyl chains would increase the bilayer hydrophobic region thickness by 5-6 Å (from 30 Å to 34.6 Å for 16C; 37.5 Å to 43.3 Å for 18C). The fact that d_{HC} increases by almost 20 Å (Table 11) when

heating bTLE DIBs from 25°C to 60°C is an indication that a significant portion (~75%) of the heating induced thickening is associated with solvent accumulation in the midplane of the bilayer.

6.3.3 Detecting bTLE Phase Transitions via Electrical Measurements of Membrane Capacitance

During the course of cooling, we observe changes in nominal membrane capacitance of bTLE DIBs reminiscent of a temperature-dependent transition. Figure 63A shows the temperature profile and nominal membrane capacitance recorded simultaneously while cooling a bTLE DIB (hexadecane solvent) from 60°C to 25°C. Plotting the nominal capacitance versus temperature (Figure 63B) shows that nominal capacitance exhibits a sharp, non-monotonic transition at ~42°C. This response is observed (±2-3°C) in different bTLE DIB samples, while temperature cycling the same bTLE DIB, using different cooling rates (2°C/min or 0.25°C/min) , and in bTLE DIBs formed from different lots or "batches" of the culture-based total lipid extract (multiple bTLE lots were obtained from the supplier, Avanti Polar Lipids, Inc.) Taken together, our results strongly suggest that bTLE DIBs undergo a reversible thermotropic transition near 42°C.

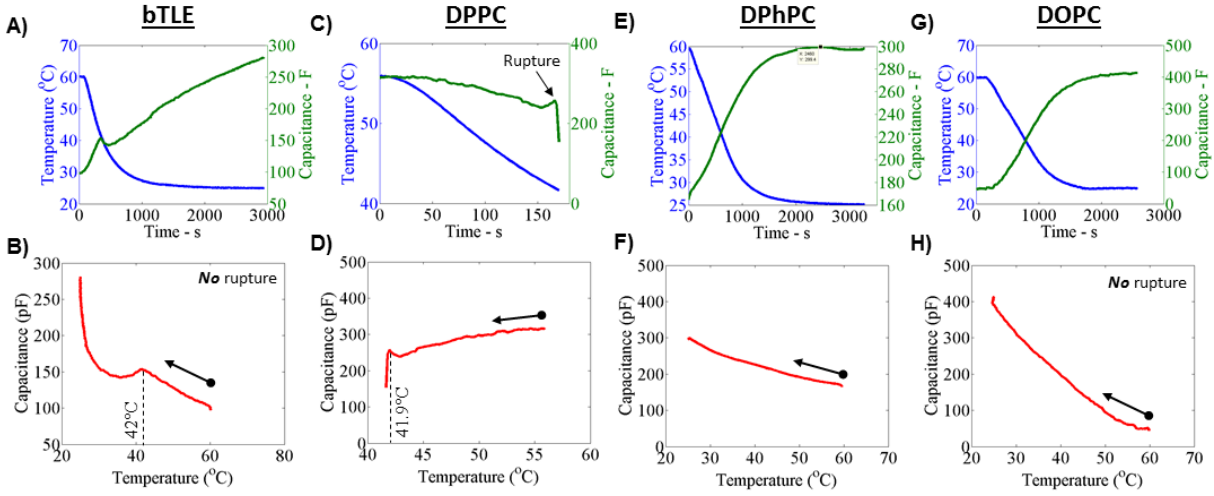

Figure 63. Nominal membrane capacitance changes with temperature for DIBs formed using bTLE (A-B), DPPC (C-D), DPhPC (E-F), and DOPC (G-H). Top: Temperature (blue) and capacitance (green) recorded as a function of time while cooling. Bottom: Capacitance as a function of temperature using the data shown in the top row. The bold arrow indicates the starting point at 60°C or 55°C. The dashed lines in (B) and (D) mark the apparent transition in the capacitance-temperature curves, and the corresponding temperature is shown.

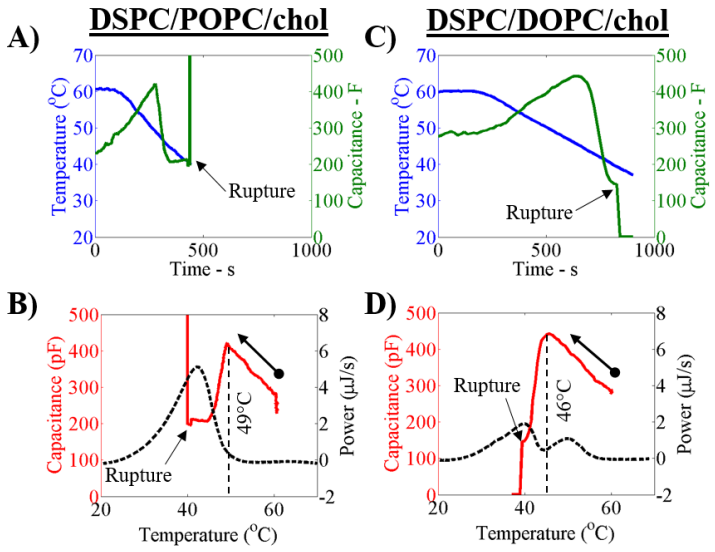

Figure 64. (A-B) Capacitance and temperature versus time (A) and capacitance versus temperature (B) while cooling a DIB formed from ternary DSPC/POPC/cholesterol liposomes. (C-D) Similar capacitance and temperature versus time (C) and capacitance versus temperature (D) while cooling a DIB formed from DSPC/DOPC/cholesterol liposomes. The black dashed lines in (B) and (D) show results of DSC scans with MLVs of each composition

To test the notion that a phase transition is the cause of the bTLE capacitance-temperature transition observed in Figure 63A-B, identical cooling experiments are performed with DPPC, DPhPC, and DOPC DIBs formed in hexadecane at 50°C. Figure 63C shows capacitance and temperature measured as a function of time for a DPPC DIB cooling experiment. Figure 63D shows the corresponding *C-T* curve. The DPPC bilayer ruptures and droplets coalesce at 41-42°C, the same transition temperature reported for DPPC solvent-free bilayers [317]. It is noted that the rupture event is almost immediately preceded by a non-linear change in the capacitance-temperature curve. This inflection occurs at ~42.5°C and likely corresponds to the onset of the lipid phase transition.

If the capacitance-temperature transitions observed while cooling bTLE DIBs are in fact due to phase transitions, we should not expect to see such capacitance-temperature transitions in DIBs formed from lipids that do not undergo a phase change when cooled from 60°C to 25°C. Figure 63E-F and Figure 63G-H show the resulting capacitance, temperature, and *C-T* curves for DPhPC and DOPC, respectively. For these, we see that capacitance changes only monotonically as a

function of temperature across the same range of temperatures. Moreover, the fact that measured capacitance inflections occur near 42°C with both bTLE and DPPC DIBs is not merely a coincidence; ongoing experiments with DIBs formed from ternary mixtures of synthetic lipids (DSPC/POPC/cholesterol and DSPC/DOPC/cholesterol) that undergo transitions (confirmed via DSC) and yield phase separation at T_m ~40-50°C [173] show a similar capacitance change at their respective transition temperatures (see representative capacitance-temperature curves in Figure 64).

The combined results from Figure 63 and Figure 64 strongly support the conclusions that: 1) thermotropic phase transitions are observed in solvent-containing DIBs upon cooling through T_m; 2) DIB phase transitions are detected using membrane capacitance measurements; and 3) bTLE DIBs undergo a phase transition around 39-42°C. As observed in heterogeneous eTLE bilayers [10], bTLE DIBs remain intact during multiple cooling and heating cycles, while single-component saturated lipid DIBs rupture when cooled through their main phase transition temperature [10, 90]. While the mechanisms governing the temperature dependent rupture or coalescence of DIBs fall outside the scope of this work, the ability of bTLE bilayers to withstand rupture may be linked to the lack of a measurable first-order transition (when studied with DSC), indicative of a weakly enthalpic and low cooperativity transition [6] (Figure 61). In comparison, DSC scans of DPPC bilayers exhibit a sharp and significant increase in heat capacity near the transition temperature (Figure 62G-H). Upon heating, bilayers that undergo a first order phase transition are believed to experience increased fluctuations and excess specific heat [289]. These fluctuations and excess are accompanied by an increased probability of pore-formation [289] which may explain the rupture of DPPC, DSPC/POPC/chol, and DSPC/DOPC/chol DIBs on cooling through their respective thermotropic transitions.

6.3.4 Specific Capacitance Measurement of the bTLE Phase Transition

Given that bTLE DIB capacitance undergoes a transition upon cooling, we are motivated to determine if the changes in capacitance stem from changes to A_M, C_M, or both. If there is no change to the bilayer C_M (and thus d_{HC}), any change in C must be a result of an increase in A_M. Figure 65A and Figure 65B show nominal C and A_M values measured as a function of temperature while

cooling a bTLE DIB from 55°C to 25°C. The *C*-*T* curve in Figure 65A shows that nominal capacitance increases with initial cooling to ~42°C, at which point there is a sudden transition and *C* begins to decrease. The area-temperature (A_M-*T*) curve in Figure 65B shows that bilayer area remains relatively unaltered through the transition, with changes taking place only as capacitance starts to rebound (≤ 30°C). Normalization of the *C*-*T* and A_M-*T* curves allows for a direct comparison of the change in capacitance and area. Figure 65C shows the normalized change in capacitance (C/C_0) and area (A_M/A_{M0}) with the initial heated state values of each used as a normalization factor. In this representation, we clearly see that the relative change in area does not account for the relative change in capacitance, implying that C_M and d_{HC} change nonlinearly as a function of decreasing temperature.

The data in Figure 65A and Figure 65B can be used to calculate C_M in a discrete fashion, i.e. by dividing each *C* value by the corresponding A_M value. However, a more-accurate approach involves mechanically varying area and capacitance as described in Chapter 0 and elsewhere [10, 49, 50]. This has the advantage of reducing error via multiple *C* versus A_M data pairs for each C_M measurement. To measure C_M as a function of temperature, a DIB is formed at 60°C and C_M is measured by dynamically varying bilayer capacitance and area as described elsewhere [10, 49]. The DIB is then cooled and equilibrated at 50°C before measuring C_M again. The process is then

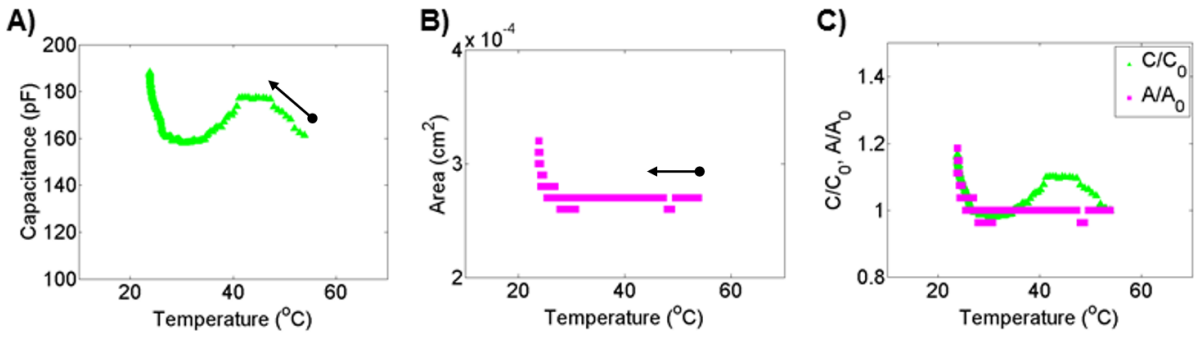

Figure 65. A) Capacitance-temperature curve obtained while cooling a bTLE DIB formed at 55°C in hexadecane. Capacitance increases as temperature decreases from 60°C to 40°C. Below 40°C, capacitance decreases sharply. B) Bilayer area-temperature curve for the same bTLE DIB. Area does not increase between 60°C and 40°C. C) Normalized capacitance and bilayer area: C_0 = capacitance at 60°C, A_{M0} = area at 60°C. Between 60°C and 40°C, increasing capacitance is not accounted for by increasing bilayer area. This result implies that membrane specific capacitance is changing. Bold arrows indicate starting points.

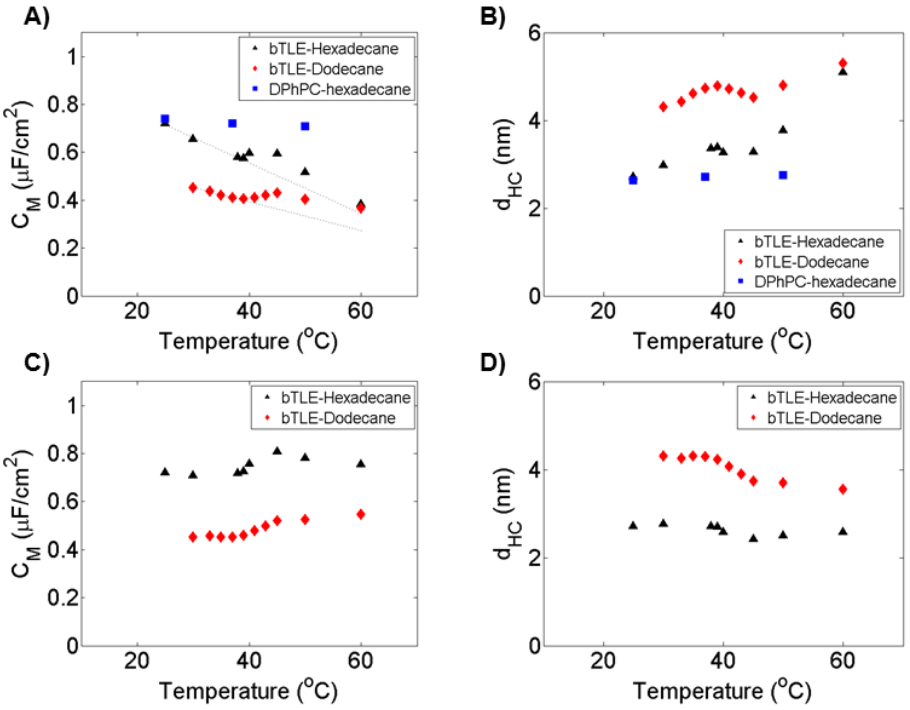

Figure 66. A) C_M measured as a function of temperature for bTLE DIBs formed in a hexadecane or a dodecane oil phase, and DPhPC DIBs formed with hexadecane as the oil phase. All DIBs are initially formed at 60°C, and C_M is measured by varying DIB area after cooling (rate ≤ 2°C/min) and equilibrating (> 5 min) the DIB at each temperature. Dashed lines show linear least squares fits to the linear region of C_M below the transition temperature around 40°C. B) The bilayer hydrophobic region thickness, d_{HC}, is calculated from the C_M data shown in (A), with an assumed relative permittivity $\varepsilon_r = 2.2$. C) Data from (A) after removing the monotonic changes not attributed to lipid phase change. D) Bilayer hydrophobic thickness change during the phase transition at 40°C, calculated from the adjusted C_M data shown in (C).

repeated to obtain measurements of C_M at temperatures as low as 25°C. The C_M values of bTLE DIBs measured at each temperature are shown in Figure 66A, and the calculated hydrophobic region thicknesses as a function of temperature are shown in Figure 66B. Solvent-dependent effects on bTLE DIB thickness versus temperature are explored by measuring C_M for bTLE DIBs formed separately in pure hexadecane and pure dodecane. These results are compared to results from DPhPC-hexadecane DIBs obtained previously [10].

Hexadecane formed bTLE DIB C_M values are higher than those formed in decane, for all temperatures studied. At 30°C, bTLE bilayers formed in hexadecane have a hydrophobic thickness of 28.6 Å. Decreasing alkane chain length by four carbons, from C16 hexadecane to C12 dodecane,

results in a 38.5 % increase in bilayer thickness (39.6 Å). This increase indicates the increased solubility of the shorter dodecane alkane chain in the bilayer's hydrophobic region, consistent with previous reports of alkanes in planar lipid bilayers [242]. Increasing the amount of dodecane associated with the lipid acyl chains is expected to disorder and thin the membrane [242], however thickness actually increases (by 11 Å) upon switching from C16 to C12 alkane solvent. The 11 Å increase in d_{HC} is too large to be accounted for by solvent induced extension of the lipid acyl chains, thus it is concluded that dodecane accumulates in the midplane of the bilayer. Despite the differences in the amount of oil accumulated at the mid-plane of the bilayer, dodecane and hexadecane trials both result in monotonically increasing d_{HC} upon heating bTLE DIBs from 25°C to ~40°C, and from ~45°C to 60°C. As reasoned earlier (Table 11 data), the increase in d_{HC} upon heating from 25°C to 60°C is too large (15-20 Å) to be accounted for solely by the straightening of the lipid acyl chains. This observation holds true when either pure dodecane or pure hexadecane is used as the solvent, and this result confirms that heating generally induces the accumulation of both alkanes in the hydrophobic interior of bTLE DIBs. In the case of single component DPhPC DIBs formed in hexadecane, the 1.1 Å increase in d_{HC} upon heating from 25-50°C (26.4 Å to 27.5 Å) is well within the window expected for possible solvent-driven straightening of the acyl chains. Thus, there is not enough evidence to conclude that C16 hexadecane solvent accumulates in the hydrophobic region of the DPhPC bilayer upon heating. According to McIntosh *et al.*, alkanes begin to collect in the bilayer when their length is four carbons less than the lipid acyl chain length ($n_{solvent} \leq n_{acyl}$-4) [242]. Thus the different responses to temperature between bTLE and DPhPC DIBs (using 12-carbon and 16-carbon alkanes) may stem from the longer acyl chains present in bTLE DIBS (GCMS of bTLE fatty acids: 30% is 18-carbon, 10% is ≥ 20-carbon) compared to the 16-carbon acyl chains making up DPhPC DIBs.

With bTLE DIBs formed in hexadecane and dodecane, C_M (Figure 66A) and d_{HC} (Figure 66B) undergo almost step-wise changes around 40°C that deviate from the monotonic trends observed when heating. Specifically, C_M increases suddenly (thus d_{HC} decreases) as temperature increases from ~40-42°C. Heating-induced thinning of the hydrophobic region at the transition would be expected for a thermotropic phase transition from an ordered to a disordered state in a solvent-free membrane. Through the C_M-T transitions, each curve includes a component that continues to

change monotonically with temperature due primarily to increasing solvent solubility in the bilayer's hydrophobic region, as discussed above. To disentangle the change in C_M and d_{HC} contributing to the sharp transition from the monotonically changing component due to increased solvent solubility, a least squares linear regression fit is applied to portions of each C_M curve below the transition temperature (<38°C). The resulting fits, shown as dashed lines in Figure 66A, are used to subtract this linearly changing component of the C_M-temperature curve. Adjusted C_M-temperature curves are shown in Figure 66C, with corresponding d_{HC} values shown in Figure 66D. In this format, we observe hydrophobic thickness of a bTLE lipid bilayer formed in hexadecane decreases from 26.4 Å at 38°C to 24.1 Å at 45°C due to the transition. With dodecane solvent, the phase transition results in a 5.1 Å decrease in bilayer thickness, from 39.5 Å at 37C to 34.4 Å at 45C. It is noted that the magnitude of the non-monotonic thickness decrease around 45°C is larger in the case of dodecane compared to hexadecane. Interestingly, increasing the alkane chain length decreased the magnitude of the observed thickness change. This finding introduces the possibility that the amount of solvent in the bilayer plays a role in the ability to detect the thermotropic transition via C_M-T measurements with DIBs.

6.3.5 Electrowetting Experiments to Measure the Effects of Temperature on bTLE DIB Surface Tension

In order to further investigate the mechanism behind the temperature dependent transitions in bTLE DIB capacitance and C_M, an electrowetting experiment was performed to measure the DIB monolayer and bilayer tensions as a function of temperature. The multi-part electrowetting experiment was performed as described in Chapter 3, however in this trial, the temperature of the DIB was varied throughout the test. The bTLE DIBs was first formed at 60°C (hexadecane as the oil phase) before measuring C_M (by mechanically varying DIB capacitance and area, see Chapter 3) and running a dc voltage step routine and measuring the steady-state contact angle at each voltage. After completing the full multi-part C_M and electrowetting measurement at 60°C, the DIB temperature was decreased at a constant rate of 1°C/min to 50°C before repeating the full multi-part experiment. This process was repeated to obtain measurements of monolayer and bilayer tension at 60, 50, 45, 43, 41, 39, 35, and 30°C. The resulting measured values for monolayer tension and bilayer tension at each temperature are shown in Figure 67A.

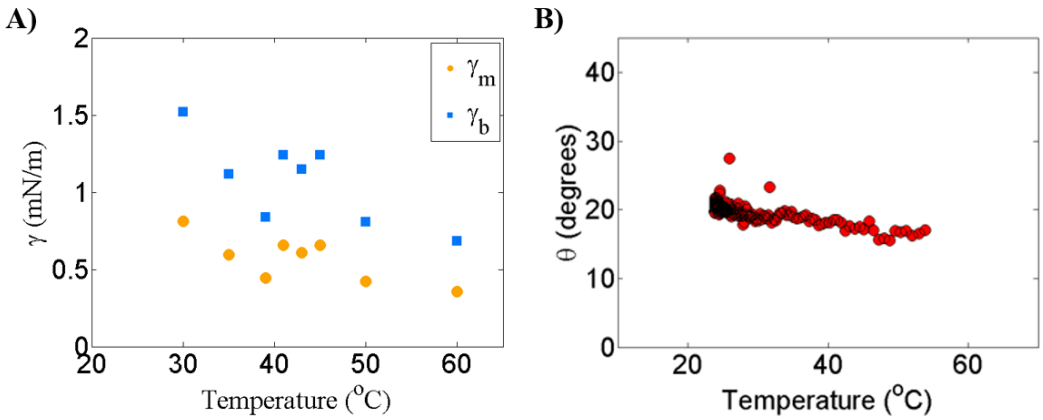

Figure 67. A) Monolayer tension and bilayer tension of a bTLE DIB formed in hexadecane as a function of temperature. Tensions at each temperature were measured using the multi-part electrowetting-based method introduced in Chapter 3 while cooling a bTLE DIB initially formed at 60°C. B) Measured contact angle while continuously cooling a bTLE DIB formed in hexadecane from 60°C towards ambient temperature.

As with capacitance and C_M (but not area), bTLE DIB monolayer and bilayer tensions are observed to undergo a transition between 40-45°C. In the initial heated state, values of 0.81 mN/m and 1.52 mN/m are obtained for monolayer ad bilayer tensions, respectively. Tension increases only marginally upon cooling until the temperature reaches 45°C at which point both monolayer and bilayer tension increase. Monolayer and bilayer tensions remain elevated, around 0.65 mN/m and 1.25 mN/m respectively, as temperature continues to decrease from 45 to 41°C. As temperature falls to 39°C, the monolayer and bilayer tensions reduce sharply to the values observed at 50 and 60°C. With further cooling, both tensions increase by about 0.3-0.6 mN/m.

The Young-Dupre equation (provided in Chapter 1 and Chapter 3) provides a relationship between bilayer tension, monolayer tension, and the contact angle, thus analysis of the change in contact angle as a function of temperature should reveal transitions that result from significant changes in the ratio of $\gamma_b/2\gamma_m$. Figure 67B shows the contact angle measured while cooling a bTLE DIB formed in hexadecane from 60°C towards room temperature, and there is no sign of the transition observed via tension measurements around 40-45°C. The lack of any clear transition in the contact angle is consistent with featureless area-temperature curves (Figure 65) and suggests that even if monolayer and bilayer tensions are changing, they are changing in a way such that the ratio of

$\gamma_b/2\gamma_m$ (per the Young-Dupre equation) remains fairly constant. This finding suggests that, in solvent-containing cases and across the 25-60°C temperature range tested, general temperature dependent changes in tension are similar in both the monolayer and the bilayer.

It is noted from Figure 67B that the contact angle increases gradually as temperature decreases, and this result suggests that the ratio $\gamma_b/2\gamma_m$ is decreasing slightly in a monotonic fashion with temperature. From this, the bilayer appears to be progressively more relaxed relative to the monolayer upon cooling, and this could be explained by the monotonic temperature dependence of solvent solubility in the bilayer observed via C_M-T measurements (i.e. heating leads to increased amounts of solvent and increased disorder, thus more exposure of water to oil and higher bilayer tension).

6.3.6 The bTLE DIB Phase Transition Affects Solvent Solubility in the Bilayer

bTLE DIBs formed in heptadecane display different behavior, compared to those formed in hexadecane, upon cooling from 60°C towards room temperature. Both heptadecane and hexadecane are linear hydrocarbon alkanes, however heptadecane has 17 carbons compared to the 16 carbons of hexadecane. Nominal capacitance of the bTLE DIB in heptadecane undergoes a non-monotonic transition around 42°C as encountered with hexadecane (Figure 68A) and

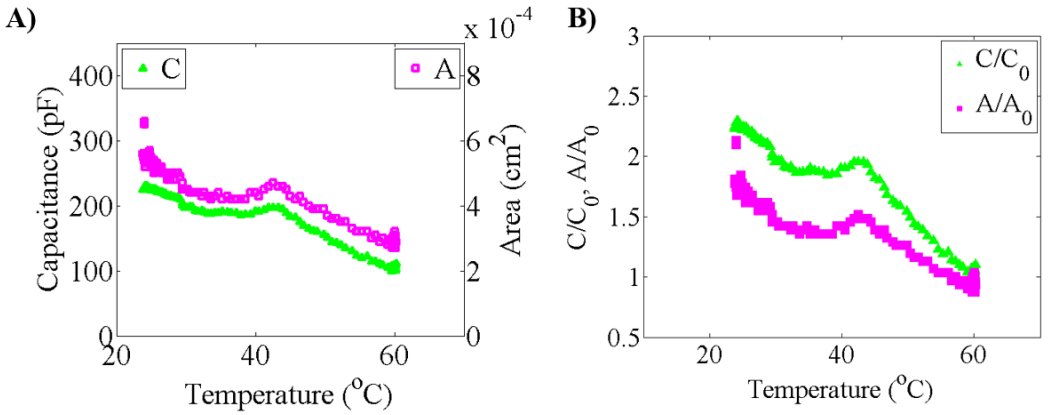

Figure 68. A) Capacitance and area while cooling bTLE DIB formed in heptadecane from 60°C to 25°C. B) Capacitance and area data from (A) normalized by their respective heated-state values: C_0 = capacitance at 60°C, A_0 = area at 60°C.

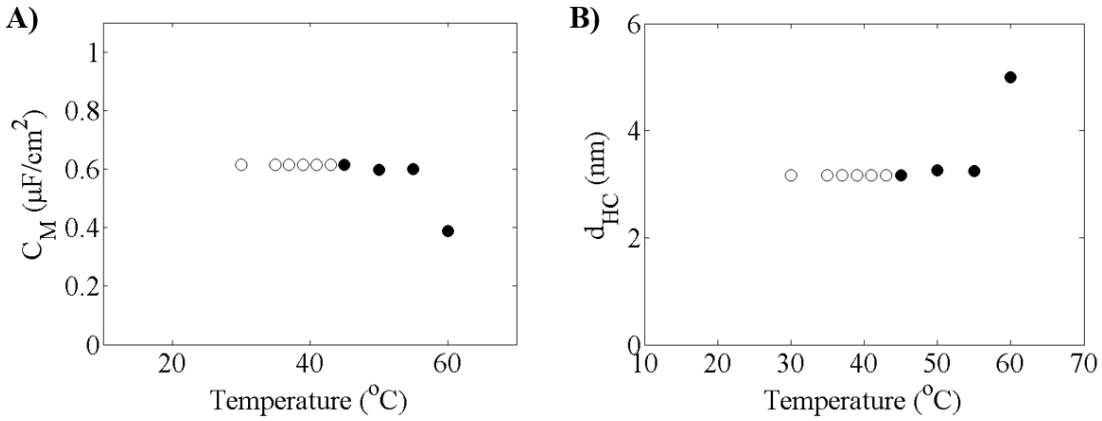

Figure 69. A) C_M measured as a function of temperature with a bTLE DIB formed in heptadecane. Measurements were performed as described for bTLE-hexadecane (data shown in Figure 66). Filled-circles represent values obtained via the method of mechanically varying capacitance and area. Open circles at T < 45°C represent assumed values of C_M and the corresponding d_{HC} values (refer to text for details) B) Hydrophobic thickness as a function of temperature, calculated using C_M values shown in (A).

dodecane. However, the use of heptadecane as the oil phase produces a transition in the area-temperature curve around 42°C. Recall that the area-temperature curve for bTLE DIBs in hexadecane shows no such transition near 42°C (Figure 65). The fact that area undergoes a transition is a strong indication that the balance between monolayer and bilayer surface tensions ($\gamma_b/2\gamma_m$) changes sharply upon cooling the bilayer through 42°C. A better comparison of the relative change in capacitance and area is obtained by normalizing capacitance and area by their initial heated-state values. The resulting values for C/C_0 and A/A_0 as a function of temperature are shown in Figure 68B. During the initial cooling leg from 60°C down to 42°C, capacitance increases in a way that is not fully accounted for by area. This observation suggests that the bilayer hydrophobic thickness decreases with temperature (i.e., lower C_M) which is attributed to a reduction in the amount of heptadecane solvent in the bilayer. Further cooling below ~40°C drives continued increase in capacitance, however the slope of the C/C0 and A/A0 curves are now approximately equal which suggests the changes in capacitance occur at a constant hydrophobic thickness. This could be explained by a complete exclusion of the solvent from the bilayer during the transition; this possibility is explored further below.

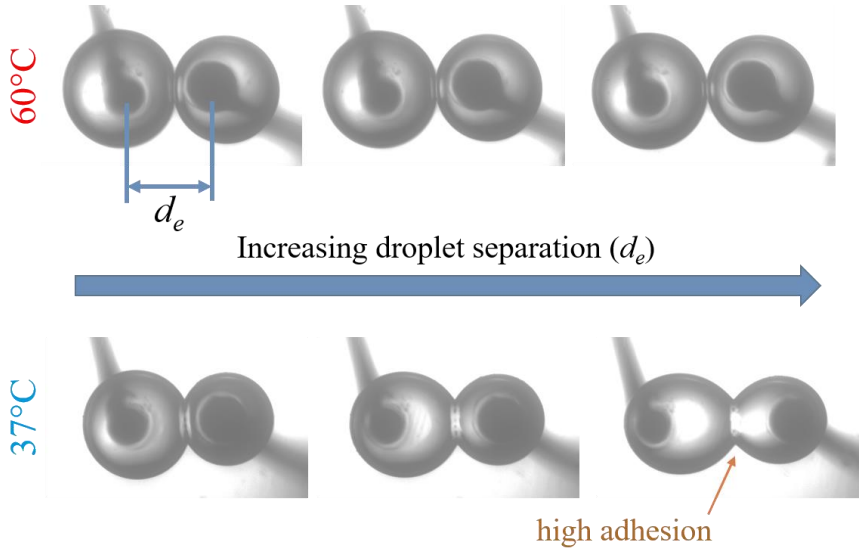

Figure 70. Micrographs showing a bTLE DIB in heptadecane as electrodes are pulled apart to increase droplet separation, d_e. At temperature below the transition temperature, droplets are highly adhesive (bottom right) and neither capacitance nor area change in response to changes in d_e.

As described above, membrane specific capacitance is often more accurately determined by mechanically varying the droplet separation distance to obtain multiple capacitance-area data points (as opposed to using one single capacitance-area data point). An experiment was thus performed to directly measure C_M as a function of temperature while cooling a bTLE DIB formed in heptadecane. The resulting C_M values are shown in Figure 69A, and bilayer hydrophobic thickness is calculated (again assuming ε_r = 2.2) and shown in Figure 69B. Compared to trials using hexadecane (16-carbon), the use of the longer chain (17-carbon) hexadecane alkane is expected to yield lower amounts of solvent in the membrane which is confirmed by the fact that C_M is higher with heptadecane, compared to hexadecane trials, at temperatures above ~42°C. It is important to note that upon cooling below 45°C, bTLE DIBs in heptadecane become highly adhesive. Even after significantly increasing or decreasing the distance between electrodes to "pull" or "push" the droplets apart, bTLE DIBs in heptadecane will not change size in this cooled, highly adhesive state (representative images are provided in Figure 70). The inability to change the bilayer capacitance and area by mechanical manipulation hinders the ability to accurately measure C_M near and below the apparent transition temperature, thus Figure 69 shows C_M values obtained via the mechanical manipulation (of capacitance and area) method only for $T \geq 45$°C.

Given that both capacitance and area are not affected by mechanical manipulation at $T < 45$°C, it seems reasonable to assume that C_M achieves a stable constant maximum representing a solvent-free bilayer at $T < 45$°C (specifically when using heptadecane as the oil phase). Figure 69 shows the assumed limiting value of C_M and the corresponding calculated values for d_{HC} as open circles.

Given prior reports that the energy of adhesion increases as bilayers become more solvent-free [226], the strong adhesion of bTLE DIBs at low temperatures supports the assumption that C_M plateaus at a stable maximum representing a solvent-free bilayer. A series of electrowetting measurements are performed to directly probe the temperature-dependent solvent-content of bTLE DIBs formed in hexadecane and heptadecane. Figure 71 shows the electrowetting constants (refer to Equation 19 and Equation 20 in section 3.2.6) for capacitance (α), area (β), and C_M ($B = \beta$-α) obtained by performing a dc voltage step routine on bTLE DIBs formed in hexadecane (C16) and heptadecane (C17) after equilibrating at various temperatures [49]. In the case of heptadecane, upon cooling to $T < 42$-45°C, all three electrowetting constants fall to around zero. Since area changes are driven by changes in tension, the low beta value implies that voltage has little effect on tension. The B value provides a measure of the ability to decrease bilayer thickness through the application voltage and resulting electrocompression. A membrane rich in solvent yields large B values, however in the case of bTLE DIBs in heptadecane at $T < T_m$, B values are almost zero. This result serves as a direct confirmation, in addition to the evidence from high adhesion and a plateau in C_M, that bTLE DIBs become virtually solvent-free as temperature falls below ~42°C. A more important conclusion is drawn from the fact that solvent-free bTLE bilayers show no C_M-T transition like that encountered using dodecane or hexadecane. It appears that the alkane solvent serves to "amplify" the change in DIB hydrophobic thickness owing to the phase transition.

Figure 70 depicts the high adhesion encountered with bTLE DIBs in heptadecane at temperatures below the transition, and it is important to consider whether the exclusion of alkane solvent is driven by changing lipid phase or is rather somehow simply related to the properties of the 17C alkane. Experiments were conducted to test the adhesion of fluid-phase DIBs formed in heptadecane at room temperature. Both DOPC and DPhPC DIBs formed in heptadecane at room temperature can be repeatedly connected and disconnected, thus they do not display the same high

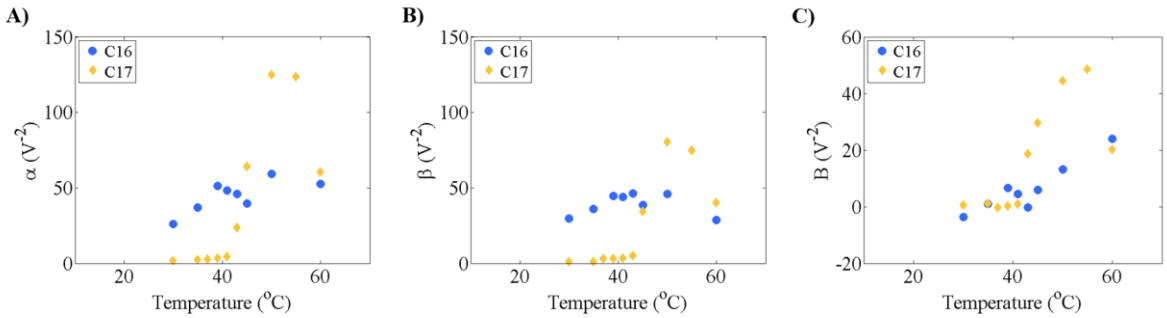

Figure 71. Electrowetting constants describing the voltage-dependence of capacitance (α), area (β), and specific capacitance (B) as a function of temperature for bTLE DIBs formed in hexadecane (C16) and heptadecane (C17). A) α. B) β. C) B.

adhesion encountered upon cooling through 42°C with bTLE (data not shown). In other words, single-component fluid-phase membranes comprised of PC lipids containing 16C or 18C acyl chains is *not* free of 17C alkane solvent at 25°C. This confirms that the reason for heptadecane solvent exclusion with bTLE DIBs is not simply cooling the alkane to T < 42°C, but rather due to the thermotropic transition achieved upon cooling the mixture of lipids in bTLE to T < 42°C.

Results of bTLE-heptadecane testing show that the membrane contains little or no solvent at temperatures near and below ~45°C, yet it is important to note that the transition in the are-temperature curve suggests that the ratio $\gamma_b/2\gamma_m$ changes non-monotonically. Perhaps the most

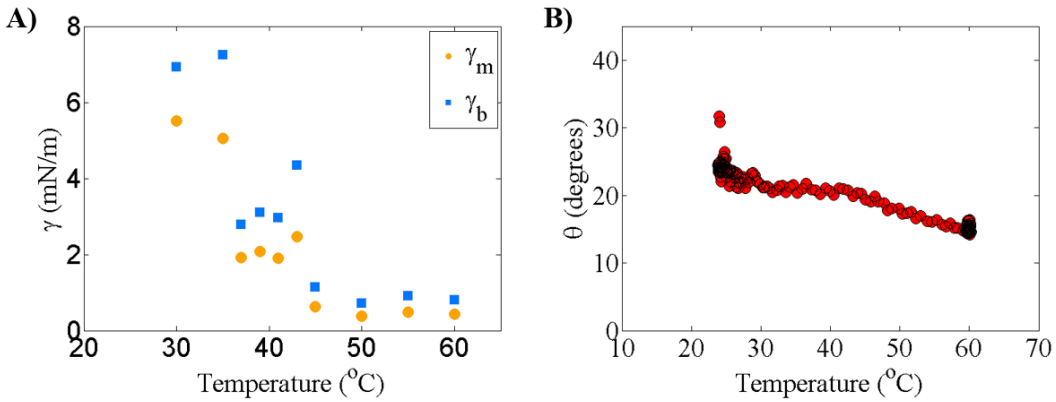

Figure 72. A) Monolayer tension and bilayer tension of a bTLE DIB formed in heptadecane (C17) as a function of temperature. Tensions at each temperature were measured using the multi-part electrowetting-based method used to measure tension shown in Figure 67. B) Measured contact angle while continuously cooling a bTLE DIB in heptadecane from 60°C towards ambient temperature.

important conclusion to be made is the fact that lipid packing and tension undergo a sharp non-monotonic transition around 42°C in bilayers that are virtually solvent-free. This provides additional evidence that solvent is not the cause of the phase transition, but it can be displaced in response to phase transitions. Experiments were performed to directly measure bTLE monolayer and bilayer surface tension as a function of temperature in heptadecane. Figure 72A shows the resulting measured values for both tensions which change drastically upon cooling through and below T < 45°C. This data shows that even at low-temperature and with bTLE DIBs containing little or no solvent, monolayer and bilayer tension are affected by temperature. In summary, while C_M-T measurements are less able to detect the transition that occurs in solvent-free bTLE bilayers, it is still possible to observe the transition via simple C-T or A-T measurements due to transition-related changes in lipid packing, organization, and tension.

6.3.7 Alamethicin Insertion and Temperature Sensitivity in bTLE DIBs

Electrophysiological measurements of alamethicin (Alm) insertion into bTLE DIBs provide a means of studying peptide insertion and organization in heterogeneous model membranes. Single channel measurements are obtained with DIBs, including a relatively low peptide concentration (100 nM Alm, P/L ratio ~1/20000) to promote stochastic channel activity, which provides single-molecule resolution of the gating behavior. After forming the DIB, an applied dc voltage (V_{dc}) is

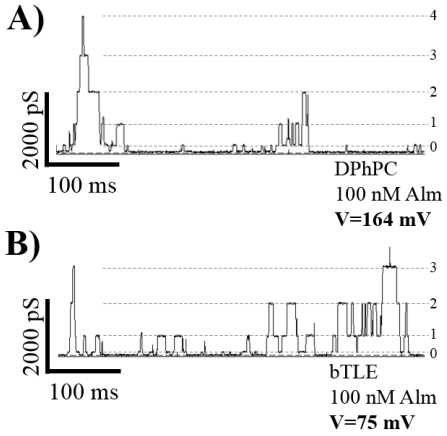

	DPhPC	bTLE
	G (pS)	G (pS)
B	0.0	0.0
L0	169.3	82.1
L1	768.9	529.7
L2	1658.1	1471.8
L3	2695.9	2519.8
L4	3826.2	3655.0

'B': baseline bilayer conductance

Figure 73. Single channel Alm gating at 25°C in DPhPC (A) and bTLE bilayers (B). The Alm concentration in each droplet = 100 nM. Buffer contains 1M NaCl. The applied dc voltage (listed) required for stochastic peptide insertion is almost 90 mV lower in the case of bTLE. The dashed lines in (A) and (B) correspond to the conductance levels listed in the table for each lipid type. 'B' – the baseline current in the absence of peptide pores.

increased until the current (*I*) measurement shows signs of peptide insertion and gating. Figure 73 shows the resulting step-wise gating pattern, here in terms of conductance ($G=I/V_{dc}$), for which Alm is known. [290, 318] Figure 73A shows the gating observed in DIBs formed from DPhPC, while Figure 73B shows the insertion behavior with bTLE DIBs (both at 25°C with hexadecane as the oil phase). A key observation is that Alm inserts at lower magnitude of V_{dc} in the case of bTLE, compared to DPhPC bilayers. This result is similar to the reduced voltage required for Alm insertion into eTLE DIBs compared to DPhPC DIBs at room temperature [10]. Histograms of multiple gating events like those in Figure 73 are used to determine the conductance levels of the peptide for each lipid composition. The table of Alm conductance levels in Figure 73 shows slightly different values for bTLE DIBs, compared to DPhPC DIBs. Despite the slight differences in conductance, we see similar gating behaviors and Alm-pore formation (peptide monomers associating and dissociating quickly to form oligomeric channels) in DPhPC and bTLE bilayers.

While bTLE DIBs in the absence of peptide were shown herein to undergo a temperature dependent transition via measurements of membrane capacitance, specific capacitance, and tensions, the temperature dependence of Alm insertion has not yet been studied in bTLE membranes. A series of CV measurements were performed to determine the threshold voltage needed to drive Alm insertion in bTLE DIBs at different temperatures (both upon heating and cooling the membrane). Single channel measurements do allow for quantitative analysis, but the stochastic nature of the method creates challenges for rapid real-time analysis of a DIB being actively cooled or heated. Alternatively, CV scans can be conducted quickly (i.e., seconds) and enable repeatable and reliable measurements of V^*, which can then be further analyzed to determine thermodynamic parameters describing peptide insertion. Several experiments are conducted where droplets used to form the DIBs contained bTLE liposomes and symmetric Alm concentrations of 1, 0.5, or 0.25 μM (P/L ratios of ~1/2000, ~1/4000, and ~1/8000 respectively). Each experiment involved forming a bTLE DIB in hexadecane at 60°C, performing several CV sweeps, cooling and equilibrating at 25°C, repeating several CV sweeps, then heating and scanning again at 30°C, 40°C, and 50°C. Figure 74A shows representative current-voltage (*I*-*V*) curves from a bTLE DIB exposed to 1 μM Alm at different temperatures (25, 30, 40, 50, and 60°C). As voltage increases during a CV sweep – for a given temperature – current remains close to zero until the

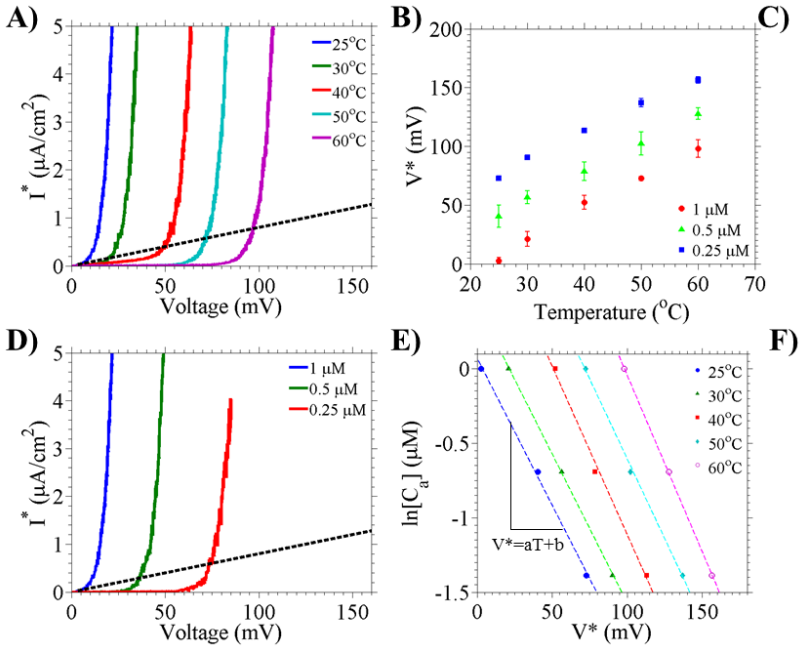

Temp. Group	V* (mV) *1µM Alm*	V* (mV) *0.5µM Alm*	V* (mV) *0.25µM Alm*
25°C	2.6 (2.63) *n*=4	40.6 (9.44) *n*=5	72.8 (1.08) *n*=2
30°C	21.0 (6.33) *n*=3	56.6(5.64) *n*=3	90.3 (1.07) *n*=2
40°C	52.2 (6.06) *n*=3	78.7 (8.02) *n*=4	113.2 (1.03) *n*=2
50°C	72.6 (1.71) *n*=2	102.4 (10.00) *n*=3	137.2 (3.50) *n*=3
60°C	98.0 (7.50) *n*=6	127.7 (5.01) *n*=6	156.5 (2.70) *n*=5

Temp. Group	a (uM/mV)	b (µM)	Va (mV)	C_0* (µM)
25°C	-0.017	0.045	58.5	1.05
30°C	-0.018	0.382	54.9	1.47
40°C	-0.025	1.283	40.7	3.61
50°C	-0.027	2.072	37.0	7.94
60°C	-0.224	2.190	4.5	8.94

Figure 74. Results from cyclic voltammetry measurements with bTLE DIBs as a function of temperature and Alm concentration (C_a) in DIBs. A) Current-voltage curves at different temperatures; C_a = 1 µM. Note that current is normalized by membrane area. The voltage threshold, V*, is the voltage at which membrane conductance exceeds a fixed conductance threshold (black dashed line). B) V* as a function of temperature after multiple experiments, such as those in (A), with varying peptide concentrations. C) Table displaying average and standard deviation of V* for each temperature and Alm concentration, as well as the number of trials (n). D) Current-voltage curves at 25°C with varying peptide concentrations. E) The log of the aqueous Alm concentration as a function of V*. Dashed lines show least-squares fits for each series, allowing for the calculation of the thermodynamic parameters shown in (F). F) 'a' and 'b' are coefficients for the linear fits shown in (E). V_a and C_0 represent a characteristic voltage and the concentration threshold for Alm insertion, respectively (see text). The conductance threshold used in all tests is 8 µS/cm^2.

increasing voltage approaches *V**. Once the voltage exceeds the threshold for peptide insertion, the current increases exponentially with respect to voltage as the membrane is populated by peptide-stabilized pores. The shifting of an *I-V* curve to the left in Figure 74A thus indicates that peptide insertion is more favorable since it occurs at a lower voltage. In contrast, the *I-V* curves in Figure 74A move continually to the right as temperature increases. Thus it appears that Alm

insertion is less favorable at higher temperatures, a trend which is consistent with Alm insertion in eTLE and DPhPC DIBs [10]. In the case of bTLE DIBs, V^* is strongly affected by changes in temperature. For example, in bTLE DIBs exposed to symmetric 1 μM Alm, V^* increases by almost 100mV upon heating from 25°C (V^* = 2.6 mV) to 60°C (V^* = 98.0 mV). We previously found that V^* increases by 64.6 and 14.4 mV when heating eTLE and DPhPC DIBs, respectively, from 25°C up to 50°C [10]. Here, using bTLE DIBs and the same 1uM Alm concentration, a similar temperature change leads to a 70 mV increase in V^* which is comparable to the sensitivity seen with eTLE DIBs. It should be noted, however, that V^* is lower with bTLE DIBs compared to previously tested DPhPC and eTLE DIBs [10] at all temperatures. Somehow, Alm is able to insert more easily into bTLE bilayers despite their large hydrophobic thicknesses and the large fraction of cholesterol (~50%), which generally reduces the ability of Alm to insert and increases V^* [56].

Figure 74B portrays the average V^* values as a function of temperature from CV measurements with bTLE DIBs containing 1, 0.5, and 0.25 μM Alm. Each data series in Figure 74B corresponds to tests conducted at a fixed Alm concentration across a range of temperatures. The average and standard deviation for given V^* values are tabulated in Figure 74C. Curves move in the positive direction along the voltage-axis as the Alm concentration decreases. Each curve is well fit using a linear least squares regression (R >0.9 for all) across the temperature range studied. It is also possible to use V^* results to extract additional relevant thermodynamics parameters describing the bTLE-Alm interaction. V^* is expected to decrease with increasing peptide concentration according to the following established empirical relationship [56, 293, 319]:

$$V^* = -V_a \ln(C_a/C_0). \qquad \text{Equation 32}$$

Equation 32 includes two variables that can be controlled and measured experimentally, namely the concentration of Alm in solution (C_a) and V^*. V_a and C_0 are parameters that vary with changing lipid type, temperature, and other factors [293]. V_a represents the decrease in V^* that can be expected with an *e*-fold increase in peptide concentration. According to Equation 32, continuously increasing the peptide concentration is expected to reduce V^* to zero. Indeed, at sufficiently high peptide concentrations, Alm insertion occurs spontaneously in the absence of voltage. The minimum peptide concentration that results in Alm insertion in the absence of any potential is

referred to as the concentration threshold (C_0). Rearranging Equation 32 as follows, experimentally obtained values of V^* across a range of peptide concentrations can be used to estimate V_a and C_0 for a given temperature or lipid composition:

$$\ln(C_a) = -(1/V_a)V^* + \ln(C_0). \qquad \text{Equation 33}$$

V_a and C_0 values can be determined via Equation 33 provided V^* values are known for a range of peptide concentrations. Figure 74D shows representative *I-V* curves from separate room temperature CV experiments conducted with bTLE DIBs infused with either 1, 0.5, or 0.25 μM Alm. As expected, *I-V* curves shift to the right on the voltage axis with decreasing peptide concentration. Figure 74E shows the log of the aqueous peptide concentration as a function of measured V^* values, at a given temperature. Least-squares linear regression of the data shown in Figure 74E allows for the calculation of V_a and C_0 for bTLE membranes as a function of temperature (via Equation 33). The resulting values are listed in Figure 74F (along with the raw regression coefficients: *a*, *b*).

Basic characterization of V^* as a function of temperature (Figure 74B) reveals no signs of the transition observed in *C-T* and C_M-T curves obtained while cooling Alm-free bTLE DIBs (Figure 63 and Figure 66). We consider the possibility that this difference may be a result of the different experimental approaches taken – Figure 63 and Figure 66 shows capacitance measurements while *cooling* DIBs, yet Figure 74B shows V^* values obtained while primarily *heating* bTLE DIBs. In order to check for hysteresis as a function of cooling and heating on Alm insertion, we performed an experiment in which V^* is measured periodically while slowly cooling (2°C/min) a bTLE DIB containing 1μM Alm (hexadecane as the oil phase). The DIB remains intact through the cooling period in spite of regular voltage sweeps that induce macroscopic pore-formation and elicit several nA of current. Figure 75A shows V^* as a function of temperature during the initial cooling scan from 60 to 25°C (triangles), a 10 minute holding period at 25°C (diamonds), and a heating scan back to 60°C (squares) at a rate of 2°C/min (the data stops around 37°C as the droplets fell off the electrodes). V^* values obtained during the slow heating leg of the process are approximately linear with respect to temperature and align well with the V^*-*T* curve for 1 μM Alm in Figure 74B. Conversely, values of V^* obtained during the cooling scan show a sharp decrease in the voltage

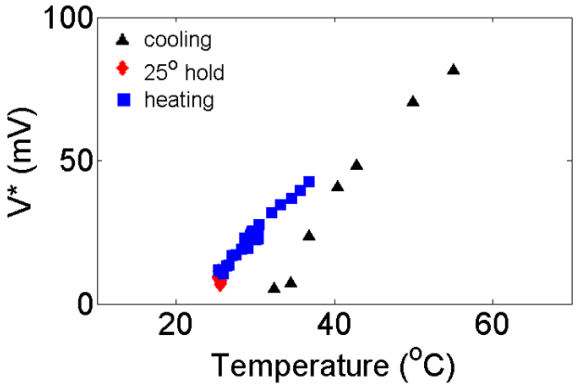

Figure 75. Voltage threshold measured while thermally cycling a bTLE DIB between 60°C and 25°C (triangles). CV sweeps were initiated after forming the bTLE DIB at 60°C, and sweeps were performed periodically as the DIB was cooled and heated. At low temperature, the sample was held at 25°C for 20 minutes (diamonds) before heating again back towards 60°C. The measurement ended when the droplets fell off the electrodes around 40°C. Alm was present at 1 μM in each droplet used to form the bTLE DIB. V* sharply decreases below 40°C during the cooling cycle.

threshold around 40°C. The relationship between concentration and V* suggests that Alm is either laterally concentrated or otherwise spatially reorganized in bTLE membranes upon cooling through 40°C. Thus, the local organization and insertion kinetics of Alm peptides are affected by the bTLE transition.

6.3.8 Tests for the Occurrence of Phase Separation

The results from attempts to form bTLE DIBs and subsequent electrical measurements of capacitance and alamethicin insertion, while cooling and heating, provide strong evidence that DIBs formed from a natural brain lipid mixture (brain total lipid extract, bTLE) exhibit a thermotropic phase transition near 40°C that is not detected by DSC (i.e. low enthalpy due to cholesterol). bTLE is rich in cholesterol and contains sphingolipids and phospholipids with saturated and unsaturated acyl chains [301]. Phase separation into coexisting liquid-ordered (L_o) and liquid-disordered (L_d) domains is often observed in model membrane mixtures containing a combination of cholesterol, unsaturated lipids, and saturated lipids or sphingomyelin [166, 168, 170, 320, 321].

Considering the fact that we observe clear reversible thermotropic transitions with heterogeneous bTLE DIBS, and considering also the occurrence of lateral reorganization of Alm as inferred from the transition in *V** upon cooling bTLE DIBs (Figure 75), it is reasonable to hypothesize that the thermotropic transition in bTLE yields coexisting L_d/L_o phases or some form of structural rearrangement. Two previously established measurement techniques are used to inspect for macroscale phase separation: confocal fluorescent microscopy with bTLE giant unilamellar vesicles (GUVs) and a FRET-based spectroscopic method utilizing bTLE large unilamellar vesicles (LUVs). Figure 76A shows images of a GUV formed using a DSPC/DOPC/chol mixture known to yield macroscopic phase-separation. Naphthopyrene (blue) and C12:0-DiI (red) fluorescent dyes are included to assist visualization of domains since naphthoprene and C12:0-DiI are known to localize preferentially to the liquid-ordered (blue) and liquid-disordered (red) phases, respectively [322]. The merged-color images shows large micron-scale patches of both L_d and L_o phases in DSPC/DOPC/chol GUVs. In contrast GUVs formed using bTLE (Figure 76B) display more evenly distributed fluorescence without any visible subdomains or signs of phase separation. Figure 76B is representative of our results with all bTLE GUVs studied to date. It should be noted, however, that macroscopic phase separation (large domains) observed in GUVs are somewhat misleading—they only form with extremely disordered low-melting lipids like DOPC and DPhPC (lipids that are not found in mammalian plasma membrane). When more biologically relevant low-melting lipids like SOPC or POPC are used, we do not see phase separation in GUVs. However, methods that are sensitive to small length scales (FRET, SANS, etc.) detect domains in both types of mixtures.

Heberle *et al*. have developed FRET-based spectroscopic methods for detecting miscibility differences and phase separation in lipid compositions that yield nanoscopic domains [167, 323]. The FRET-based method has an increased spatial sensitivity and is able to resolve domains with radii as small as 5 nm (i.e. domains that otherwise fall below the typical resolution limit of optical microscopy). For example, Figure 76C-D show the FRET probe-pair efficiencies in vesicles comprised of either DSPC/POPC/cholesterol (39/39/22) or DSPC/DOPC/chol (39/39/22) as a function of temperature. As before, ternary mixtures with DSPC/POPC/chol or DSPC/DOPC/chol show a miscibility gap. Prior studies have established understanding that the POPC mixture yields

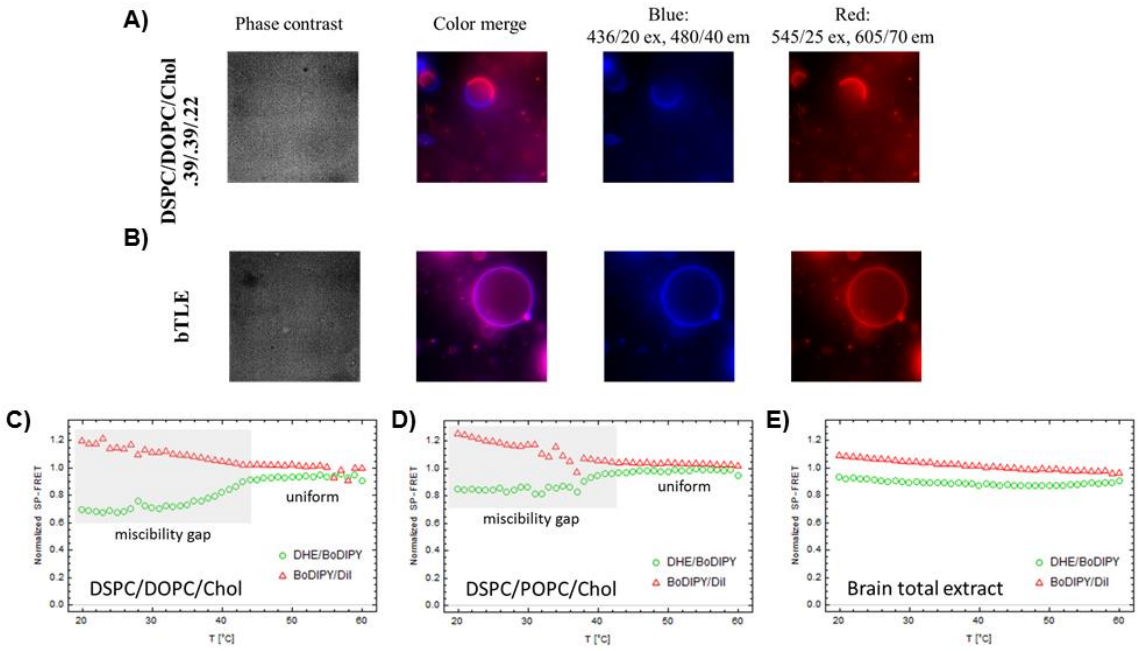

Figure 76. Results from microscopic investigation of GUVs, and FRET with LUVs, formed using bTLE and ternary mixtures known to phase-separate. A, B) GUVs formed from a ternary mixture of DSPC/DOPC/cholesterol (A) or the complex mixture of total lipids extracted from porcine brain (B). Fluorescent naphthopyrene (blue) and C12:0-DiI (red) dyes are included at ratios of 1/1500 and 1/3000 (dye/lipids) in each case. Distinct phase separation into micron-sized patches is observed only in (A). Images obtained at room temperature. C-E) Normalized efficiency of two FRET probe pairs mixed into LUVs formed from DSPC/DOPC/chol (A), DSPC/POPC/chol (B), or bTLE (C). Separation of FRET efficiencies reveals miscibility gaps below ~44°C for both ternary mixtures.

nanoscopic domains while the DOPC mixture yields larger macroscopic domains [323]. The result from a FRET experiment with bTLE vesicles is provided in Figure 76E. Interestingly FRET with bTLE shows no clear miscibility gap. It should be noted that the FRET based method is limited to detecting domains larger than the Förster radius for the probe pair used. Therefore, an open question is whether nanoscopic (at length scales below the Förster resonance distance of several angstroms) domain formation in bTLE DIBs causes the *C-T* transition (Figure 63A) and spatial reorganization of the transmembrane peptide alamethicin revealed by CV measurements (Figure 75). "Domains" that are not detectable by FRET should be very small, only a few nanometers in diameter. At the molecular level, "ultrananodomains" [170] of this size and scale are likely transient clusters comprised of less than 5-10 lipid and/or cholesterol molecules (1 lipid ~ 70Å^2, radius 8-9 Å^2, diameter ~1.6-1.8Å^2). Such clusters would more accurately be described as nonideal mixing within a single fluid phase.

6.3.9 Chapter Summary and Conclusions

Our study provides new evidence that bTLE DIBs, and likely bTLE vesicles or liposomes, undergo a thermotropic phase transition at around 42°C. bTLE DIBs can only be formed by heating droplets in oil to 50°C – room temperature droplets coalesce upon contact and do not form DIBs. The role of heating-enabled monolayer assembly is confirmed via the ability to form bTLE DIBs at room temperature as long as adequate monolayers are first assembled at a heated state. Nominal capacitance measurements of bTLE DIBS during cooling from the incubation temperature show a non-monotonic thermotropic transition near 40°C. Specific capacitance measurements yield non-monotonic changes in bTLE membrane specific capacitance (and thus thickness) versus temperature. These results can be de-convoluted to separate a stepwise change in membrane thickness at ~40°C (due to phase transition) from a monotonic change in membrane thickness (due to solvent absorption in the bilayer hydrophobic region). The magnitude of thickness change upon heating from 25°C to 60°C justifies reasoning that heating induces accumulation of alkane solvents in a pure phase at the bilayer midplane. Given the simplicity and ease of forming DIBs and measuring capacitance, this method shows great potential as a new tool for studying and characterizing phase transitions and the related effects on thermotropic reorganization of non-polar solvent in membranes.

Alamethicin insertion in bTLE DIBs was found to be highly temperature dependent (include results of all ALM testing vs. temp and conc.), and our results at RT show that alamethicin inserts into heterogeneous bTLE membranes more favorably, at much lower voltages, than eTLE or even DPhPC DIBs. Characterization of alamethicin insertion versus temperature exhibited a sharp decrease in the voltage threshold at a temperature near 40°C. The known relationship between Alm concentration and voltage threshold suggests that Alm is concentrated laterally in bTLE membranes upon cooling through 40°C (very similar to findings with eTLE DIBs). These results provide additional evidence that DIBs formed from a natural brain lipid mixture exhibit a thermotropic phase transition near 40°C that is not detected by DSC (i.e. low enthalpy, possibly due to large amounts of cholesterol). However, there are no signs of macroscopic phase separation in bTLE GUVs inspected via confocal fluorescence microscopy, nor is there any evidence of phase

separation related miscibility gaps in bTLE LUVs as measured via a FRET-based spectroscopic assay. Taken together, these measurements indicate that bTLE membranes undergo a thermotropic transition at a temperature near 40°C, which causes the membrane to undergo changes in membrane thickness and, possibly, lead to the presence of ultrananoscopic domains (<5 nm radius, low enthalpy and cooperativity) at physiological temperatures in membranes reconstituted from a natural source.

CHAPTER 7

SUMMARY AND CONCLUSIONS

7.1 Research Overview

This dissertation describes efforts to increase the utility and physiological relevance of DIBs as tools for recreating and studying cell membranes, measuring physical properties related to membrane structure, and characterizing the interactions between membranes and membrane-active entities. Chapters 3 and 4 present the theory and development of a new method for measuring the specific capacitance and tensions in a DIB, which was applied to study the effects of small-molecules and nanoparticles on membrane specific capacitance (bilayer hydrophobic thickness) and the surface tensions of the monolayer and bilayer. The method is established and validated as a useful approach to quantitatively characterize the interactions of membrane-active species that do not necessarily affect membrane conductance. Chapter 5 demonstrated that heating is required to enable DIB formation using eTLE liposomes. Further, Chapter 5 provides initial evidence that physiologically relevant and heterogeneous membrane composition can significantly affect the behavior of membrane-associating peptides. Chapter 6 builds on the findings presented in Chapter 5, first by applying controlled heating to form DIBs using a eukaryotic total lipid extract, and secondly by demonstrating that membrane capacitance and peptide insertion behaviors provide evidence of thermotropic reorganization that does not occur in single-component DIBs. Further, Chapter 6 establishes the capability of detecting and characterizing high- and low-enthalpy thermotropic transitions simply by tracking DIB capacitance as a function of temperature. More importantly, the DIB-based method for studying phase transitions enables future investigation of weak-enthalpy phase transitions and non-ideal mixing in membranes constructed using physiologically relevant mixtures of lipids derived from a natural source; such investigation is not otherwise easily achieved given the inability to detect the transition behavior using other well

established methods for studying phase transitions and phase separation phenomena (DSC, fluorescence with GUVs, immiscibility assay with FRET probe pairs).

7.2 Conclusions

This section presents conclusions and contributions generated by each research objective and which aim to address the scientific gaps identified in Chapter 1 (objectives are restated here again for reference).

7.2.1 *Objective 1*

Develop new methods to directly measure physical properties of DIBs beyond resistance/conductance including specific capacitance (thus bilayer hydrophobic thickness) and monolayer and bilayer surface tensions (a measure of lipid packing and order).

- Developed and validated a three-part experimental technique based on the Young-Lippmann and Young-Dupre relationships for measuring specific capacitance, monolayer tension, and bilayer tension in a single DIB experiment. The method was shown to enable measurements of steady-state monolayer tension at similar resolution as the pendant drop method. However, it uniquely enables measurement of bilayer tension. Outside of the work presented herein, this method was recently applied to the characterization of the tensions of droplets stabilized by amphiphilic copolymers that yield tensions too low for measurement using a goniometer [324].

7.2.2 *Objective 2*

Apply and validate measurement capability of the method developed in Objective 1 by characterizing the effects of non-permeabilizing cholesterol and nonpolar solvent molecules, as well as mixed-monolayer protected cell-penetrating nanoparticles, on DIB specific capacitance, thickness, equilibrium surface tensions, and lipid packing and order in the monolayers and bilayer.

- Applied the newly developed method for measuring specific capacitance and tensions in a DIB through studies of the effects of cholesterol and nonpolar solvents on membrane

thickness and tension. The measured values of thickness and tension for bilayers containing these molecules were in agreement with values obtained elsewhere, which validates the accuracy of the technique.

- Observed 2-3Å changes in DIB hydrophobic region thickness, 0.1-0.5 mN/m changes in bilayer tension, and 0.1-0.2 mN/m changes in monolayer tension as a result of the incorporation of cholesterol or the exclusion of nonpolar solvent residing in the bilayer hydrophobic region.
- Applied specific capacitance measurements to determine that mixed-monolayer protected gold nanoparticles do not accumulate in the lipid bilayer of a DIB. Instead, these nanoparticles were confirmed to adsorb at the oil-water interface corresponding to the monolayers stabilizing the DIB. These results suggest that the nanoparticles are excluded from the bilayer, and this result contradicts measurements made by other groups on the same type of nanoparticles.

7.2.3 *Objective 3*

Explore DIB formation methods using aqueous liposome solutions containing multi-component lipid mixtures and native cellular lipid extracts.

- Developed a feedback-controlled heating platform that allows regulated heating of model membranes, from ambient temperature up to at least 80-90°C, with the RAM and other DIB approaches.
- Demonstrated for the first time the assembly of eTLE and bTLE model membranes by heating the droplets in oil to a temperature where self-assembly is kinetically favorable. In summary, droplets containing liposomes that possess a thermotropic transition temperature above ambient temperature must be heated to $T > T_m$ in order to promote monolayer assembly, after which the droplets can be connected in the heated state or cooled down and connected. The described technique for heating-assisted monolayer formation permits the use of other high transition temperature lipids, including single-component and ternary-component mixtures of synthetic lipids, for “lipid-in” DIB formation. The technique increases access to the variety of lipid compositions that can be considered for assembling model membranes.

7.2.4 *Objective 4*

Objective 4 (addressing Gap 3). Apply methods and knowledge established via Objective 2 to study the effects of increasing compositional heterogeneity on DIB resistance, specific capacitance (thickness), monolayer and bilayer tensions (packing and order), and also the interactions of membrane-active peptides.

- Measured the resistance of DIBs formed using DPhPC, eTLE, and bTLE, ultimately to find no significant difference across these three compositions. This subtle result further motivates the fact that non-ionic methods are important for characterizing structural differences when the hydrophobic composition of the membrane is altered by the organization and interactions of lipids or other species.
- Measured C_M for DIBs formed from DPhPC, eTLE, and bTLE. The results suggest that lipid bilayers formed from natural lipid mixtures display higher hydrophobic region thickness compared to bilayers formed from DPhPC, and the result is in part due to lipid composition driven increase in the amount of solvent accumulated in the bilayer midplane.
- Obtained measurements of monolayer and bilayer tension in bTLE DIBs.
- Identified significantly enhanced sensitivity of eTLE and bTLE DIBs to the insertion of an antimicrobial peptide (alamethicin) compared to single-component DIBs.

7.2.5 *Objective 5*

Investigate temperature dependence of DIB resistance, specific capacitance, surface tensions, and membrane-active peptide interactions in simple and complex multicomponent DIBs.

- Experimentally studied the effects of changing temperature on properties of simple and complex multicomponent DIBs. Membrane properties studied include resistance, rupture potential, specific capacitance, and solvent solubility in the hydrophobic region.
- Established the ability to detect strong- and weak-enthalpy phase transitions in simple and multicomponent DIBs by tracking membrane capacitance and specific capacitance as a function of temperature.

- Separated temperature-dependent changes in a) the solubility of nonpolar hydrocarbon solvents in the hydrophobic region of DIBs, and b) lipid bilayer hydrophobic thickness due to a phase transition and resulting reorganization in the membrane.
- Measured monolayer and surface tension of bTLE DIBs as a function of temperature while cooling through a thermotropic phase transition. Monolayer and bilayer tension both generally decrease with temperature, however a transition is encountered near the T_m of ~ 40°C. Additionally, results show that bTLE DIB monolayer and bilayer tensions both change by similar relative magnitudes upon cooling through $T_{m,}$ and this finding provides insight to the fact that both monolayer and bilayer tensions are affected almost equally by changing temperature.
- Discovered through CV measurements that the voltage-threshold required to drive alamethicin insertion decreases significantly near a thermotropic transition. This relationship suggests that measurements of peptide insertion can be used to detect reorganization in complex membranes, and this method constitutes yet another new tool for studying phase transitions in lipid bilayers. The fact that peptide insertion is significantly affected by membrane composition further motivates the need for considering composition when studying interactions between membranes, proteins, and other membrane-active species.
- Obtained insight to the fact that alamethicin peptide is laterally reorganized or concentrated upon cooling the bilayer through its T_m. This finding suggests the occurrence of lateral phase separation or restructuring of membrane components in response to temperature changes.

7.3 Research Products and Output

7.3.1 Journal Publications

1. Taylor, G.J., Venkatesan, G.A., Collier, C.P., and Sarles, S.A., Direct in situ measurement of specific capacitance, monolayer tension, and bilayer tension in a droplet interface bilayer. *Soft Matter* 2015, **11**(38):7592-7605**.**

2. Mruetusatorn, P., Polizos, G., Datskos, P.G., Taylor, G.J., Sarles, S.A., Boreyko, J.B., Hayes, D.G., and Collier, C.P., "Control of membrane permeability in air-stable droplet interface bilayers. *Langmuir* 2015, **31**(14): 4224-4231.
3. Taylor, G.J. and Sarles, S.A.,Heating-enabled formation of droplet interface bilayers using *Escherichia coli* total lipid extract. *Langmuir* 2015, **31**(1): 325-337.
4. Tamaddoni, N.T., Taylor, G.J., Hepburn, T., Kilbey, S.M. II, Sarles S.A., Reversible, voltage-activated formation of biomimetic membranes between triblock copolymer-coated aqueous droplets in oil, *Under review.*
5. Taylor, G.J., Heberle, Seinfeld, J. S., Katsaras, J., F. A., Collier, C. P., and Sarles S.A., Detecting weak-enthalpy phase transitions in brain total lipid extract droplet interface bilayers, *Manuscript in preparation.*
6. Taylor, G.J., Heberle, Seinfeld, J. S., Katsaras, J., F. A., Collier, C. P., and Sarles S.A., Alamethicin responds to phase transitions in droplet interface bilayers, *Manuscript in preparation.*
7. Taylor, G.J., Heberle, Seinfeld, J. S., Katsaras, J., F. A., Collier, C. P., and Sarles S.A., Electrical and optical tracking of phase separation transitions in droplet interface bilayers. *Manuscript in preparation.*
8. Taylor, G.J., Venkatesan, G. V., Collier, C. P., Sarles S.A., Evaporation assisted monolayer packing for reliable droplet interface bilayer formation. *Manuscript in preparation.*

8.1.1 Peer-Reviewed Conference Proceedings

†DENOTES ORAL PRESENTATION GIVEN, ‡ POSTER

1. †Tamaddoni, N., Taylor, G.J., and Sarles, S.A., Robust sensing and reversible actuation using triblock copolymer stabilized intradroplet interfaces. ASME 2015 Conference Proceedings, 2015 SMASIS conference, Fort Collins, Colorado, September 21-23, 2015.
2. †Taylor, G.J. and Sarles, S.A., Model neural membrane droplet interface bilayers from brain total lipid extract for studying membrane-peptide interactions with amyloid-β. MRS Conference Proceedings, Cambridge University Press, 2014 MRS Fall Meeting and Exhibit, Boston, Massachussetts, November 30 - December 5, 2014.

3. ‡Taylor, G.J. and Sarles, S.A., Using cell-free expression to create light-activated proteins in situ in droplet interface bilayer networks. MRS Conference Proceedings, Cambridge University Press, 2014 MRS Fall Meeting and Exhibit, Boston, Massachussetts, November 30 - December 5, 2014.

8.1.2 Other Conference Papers and Presentation

†DENOTES ORAL PRESENTATION GIVEN, ‡ POSTER

1. ‡Taylor, G.J., Heberle, F.A., Seinfeld, J.S., Katsaras, J., Collier, C.P., Sarles, S.A., Electrophysiological measurement of thermotropic lipid phase transitions and enhanced peptide insertion in droplet interface bilayers. 2016 Biophysical Society Annual Meeting, Los Angeles, California, February 27 – March 2, 2016.
2. ‡Taylor, G.J., Bekdemir, A., Stellaci, F., and Sarles, S.A., Effects of mixed-monolayer protected gold nanoparticles on model membranes formed from droplet interface bilayers. 2015 MRS Fall Meeting and Exhibit, Boston, Massachussetts, November 30 – December 4, 2015.
3. ‡Tamaddoni, N., Taylor, G.J., and Sarles, S.A., Voltage controlled electro-wetting networks by low tension copolymer stabilized interfaces. MRS Fall Meeting and Exhibit, Boston, Massachussetts, November 29 – December 4, 2015.
4. ‡ **AWARDED BEST POSTER (TOP 5 OF > 1000)** - Taylor, G.J., and Sarles, S.A., Screening small-molecule membrane interactions using droplet interface bilayers. BMES 2015 Annual Meeting, Tampa Bay, Florida, October 7-10, 2015.
5. †Taylor, G.J. and Sarles, S.A., Feedback controlled bilayer heating within the regulated attachment method. ASME 2013 Conference Proceedings, 2013 SMASIS conference, Snowbird, Utah, September 16-18.
6. †Taylor, G.J. and Sarles, S.A., Detection of botulinum neurotoxin/A using an encapsulated interface bilayer (EIB). ASME 2012 Conference Proceedings, 2012 SMASIS conference, Stone Mountain, GA, September 19-21.

8.1.3 Intellectual Property

1. Taylor, G. J., Sarles, S. A. Droplet based measurement of specific capacitance and interfacial tensions. Provisional Patent Disclosure, University of Tennessee Research Foundation, April 2015.
2. Tamaddoni, N., Taylor, G. J., Sarles, S. A. Voltage-tunable copolymer emulsions. Provisional Patent Disclosure, University of Tennessee Research Foundation, March 16, 2015.

LIST OF REFERENCES

1. Sud, M., E. Fahy, D. Cotter, A. Brown, E.A. Dennis, C.K. Glass, A.H. Merrill Jr, R.C. Murphy, C.R.H. Raetz, D.W. Russell, and S. Subramaniam, *LMSD: LIPID MAPS structure database.* Nucleic Acids Research, 2007. **35**(SUPPL. 1): p. D527-D532.
2. Sarles, S.A., *Physical encapsulation of interface bilayers*. 2010, Virginia Polytechnic Institute and State University.
3. Singer, S.J. and G.L. Nicolson, *The fluid mosaic model of the structure of cell membranes.* Science, 1972. **175**(4023): p. 720-731.
4. Lodish H, B.A., Zipursky SL, et al. , *Molecular Cell Biology*. 2000, W. H. Freeman: New York.
5. Hansen, C.M., *Hansen Solubility Parameters: A User's Handbook, 2nd Edition*. 2nd ed. 2007, Boca Raton, FL: CRC Press.
6. McElhaney, R.N., *The use of differential scanning calorimetry and differential thermal analysis in studies of model and biological membranes.* Chemistry and physics of lipids, 1982. **30**(2): p. 229-259.
7. Matharu, Z., A.J. Bandodkar, V. Gupta, and B.D. Malhotra, *Fundamentals and application of ordered molecular assemblies to affinity biosensing.* Chemical Society Reviews, 2012. **41**(3): p. 1363-1402.
8. White, S.H., *Phase transitions in planar bilayer membranes.* Biophysical Journal, 1975. **15**(2, Part 1): p. 95-117.
9. Bechinger, B., *Lipid multilayers: Domains stack up.* Nat Mater, 2012. **11**(12): p. 1005-1006.
10. Taylor, G.J. and S.A. Sarles, *Heating-Enabled Formation of Droplet Interface Bilayers Using Escherichia coli Total Lipid Extract.* Langmuir, 2015. **31**(1): p. 325-337.
11. Creasy, M.A. and D.J. Leo. *Modeling the Conductance of the Peptide Alamethicin With and Without Ion Gradients*. in *ASME 2011 Conference on Smart Materials, Adaptive Structures and Intelligent Systems*. 2011. American Society of Mechanical Engineers.
12. Hwang, W.L., M. Chen, B.d. Cronin, M.A. Holden, and H. Bayley, *Asymmetric Droplet Interface Bilayers.* Journal of the American Chemical Society, 2008. **130**(18): p. 5878-5879.
13. Sarles, S.A., *The use of virtual ground to control transmembrane voltages and measure bilayer currents in serial arrays of droplet interface bilayers.* Smart Materials and Structures, 2013. **22**(9): p. 094023.
14. Sarles, S.A., P.G. Bavarsad, and D.J. Leo, *Incorporation and characterization of biological molecules in droplet-interface bilayer networks for novel active systems*. 2009.
15. Sarles, S.A. and D.J. Leo, *Tailored Current—Voltage Relationships of Droplet-Interface Bilayers Using Biomolecules and External Feedback Control.* Journal of Intelligent Material Systems and Structures, 2009. **20**(10): p. 1233-1247.
16. Sarles, S.A. and D.J. Leo, *Physical encapsulation of droplet interface bilayers for durable, portable biomolecular networks.* Lab on a Chip, 2010. **10**(6): p. 710-717.
17. Sarles, S.A. and D.J. Leo, *Regulated Attachment Method for Reconstituting Lipid Bilayers of Prescribed Size within Flexible Substrates.* Analytical Chemistry, 2010. **82**(3): p. 959-966.
18. Sarles, S.A. and D.J. Leo, *Membrane-based biomolecular smart materials.* Smart Materials and Structures, 2011. **20**(9): p. 094018.

19. Sarles, S.A., J.D.W. Madden, and D.J. Leo, *Hair cell inspired mechanotransduction with a gel-supported, artificial lipid membrane.* Soft Matter, 2011. **7**(10): p. 4644-4653.
20. Sarles, S.A., J.L. Stiltner, C.B. Williams, and D.J. Leo, *Bilayer Formation between Lipid-Encased Hydrogels Contained in Solid Substrates.* ACS Applied Materials & Interfaces, 2010. **2**(12): p. 3654-3663.
21. Sarles, S.A., V.B. Sundaresan, and D.J. Leo. *'Electrical Impedance Analysis of Phospholipid Bilayer Membranes for Enabling Engineering Design of Bio-Based Devices*. in *MRS Fall Meeting*. 2007. Cambridge Univ Press.
22. Tamaddoni, N.J., C.P. Stephens, and S. Sarles. *Fabricating neuromast-inspired gel structures for membrane-based hair cell sensing*. in *SPIE Smart Structures and Materials+ Nondestructive Evaluation and Health Monitoring*. 2012. International Society for Optics and Photonics.
23. Taylor, G. and A. Sarles. *Feedback Controlled Bilayer Heating Within the Regulated Attachment Method*. in *ASME 2013 Conference on Smart Materials, Adaptive Structures and Intelligent Systems*. 2013. Snowbird, Utah, USA: ASME.
24. Taylor, G., A. Sarles, and D.J. Leo. *Detection of Botulinum Neurotoxin/A using an Encapsulated Interface Bilayer (EIB)*. in *ASME SMASIS Conference Proceedings*. 2012. Stone Mountain, GA: ASME.
25. Creasy, M.A. and D.J. Leo, *Non-invasive measurement techniques for measuring properties of droplet interface bilayers.* Smart Materials and Structures, 2010. **19**(9): p. 094016.
26. Creasy, M.A. and D.J. Leo, *Droplet interface bilayer characteristics formed over a synthetic porous substrate.* 2009: p. 72910D-72910D.
27. Sarles, S.A. and D.J. Leo. *Encapsulated Interface Bilayers for Durable Biomolecular Materials*. in *ASME 2010 Conference on Smart Materials, Adaptive Structures and Intelligent Systems*. 2010. American Society of Mechanical Engineers.
28. Sarles, S.A. and D.J. Leo. *Durable Biomolecular Assemblies for Protein-Powered Device Concepts*. in *ASME 2009 Conference on Smart Materials, Adaptive Structures and Intelligent Systems*. 2009. American Society of Mechanical Engineers.
29. Sarles, S.A. and D.J. Leo. *Biomolecular material systems with encapsulated interface bilayers*. in *MRS Proceedings*. 2011. Cambridge Univ Press.
30. Sarles, S.A., V.B. Sundaresan, and D.J. Leo, *Electrical Impedance Analysis of Phospholipid Bilayer Membranes for Enabling Engineering Design of Bio-based Devices.* MRS Online Proceedings Library, 2007. **1061**: p. null-null.
31. Tamaddoni, N.J., C.P. Stephens, and S.A. Sarles. *Fabrication and Characterization of a Membrane Based Hair Cell Sensor That Features Soft Hydrogel Materials*. in *SMASIS*. 2012. Stone Mountain, GA, USA: ASME.
32. Creasy, M. and D. Leo, *Non-invasive measurement techniques for measuring properties of droplet interface bilayers.* Smart materials and structures, 2010. **19**(9): p. 094016.
33. Boreyko, J.B., G. Polizos, P.G. Datskos, S.A. Sarles, and C.P. Collier, *Air-stable droplet interface bilayers on oil-infused surfaces.* Proceedings of the National Academy of Sciences, 2014. **111**(21): p. 7588-7593.
34. Elani, Y., X. Niu, and O. Ces, *Novel technologies for the formation of 2-D and 3-D droplet interface bilayer networks.* Lab on a Chip, 2012. **12**(18): p. 3514-3520.

35. Heron, A.J., J.R. Thompson, B. Cronin, H. Bayley, and M.I. Wallace, *Simultaneous Measurement of Ionic Current and Fluorescence from Single Protein Pores.* Journal of the American Chemical Society, 2009. **131**(5): p. 1652-1653.
36. Heron, A.J., J.R. Thompson, A.E. Mason, and M.I. Wallace, *Direct Detection of Membrane Channels from Gels Using Water-in-Oil Droplet Bilayers.* Journal of the American Chemical Society, 2007. **129**(51): p. 16042-16047.
37. Leptihn, S., O.K. Castell, B. Cronin, E.-H. Lee, L.C.M. Gross, D.P. Marshall, J.R. Thompson, M. Holden, and M.I. Wallace, *Constructing droplet interface bilayers from the contact of aqueous droplets in oil.* Nat. Protocols, 2013. **8**(6): p. 1048-1057.
38. Lein, M., J. Huang, and M.A. Holden, *Robust reagent addition and perfusion strategies for droplet-interface bilayers.* Lab on a Chip, 2013. **13**(14): p. 2749-2753.
39. Martel, A. and B. Cross, *Handling of artificial membranes using electrowetting-actuated droplets on a microfluidic device combined with integrated pA-measurements.* Biomicrofluidics, 2012. **6**(1): p. 012813.
40. Maglia, G., A.J. Heron, W.L. Hwang, M.A. Holden, E. Mikhailova, Q. Li, S. Cheley, and H. Bayley, *Droplet networks with incorporated protein diodes show collective properties.* Nature nanotechnology, 2009. **4**(7): p. 437-440.
41. Wauer, T., H. Gerlach, S. Mantri, J. Hill, H. Bayley, and K.T. Sapra, *Construction and Manipulation of Functional Three-Dimensional Droplet Networks.* ACS Nano, 2013. **8**(1): p. 771-779.
42. Vijayvergiya, V., S. Acharya, J. Poulos, and J. Schmidt, *Single channel and ensemble hERG conductance measured in droplet bilayers.* Biomedical Microdevices, 2015. **17**(1): p. 1-7.
43. Najem, J.S., M.D. Dunlap, I.D. Rowe, E.C. Freeman, J.W. Grant, S. Sukharev, and D.J. Leo, *Activation of bacterial channel MscL in mechanically stimulated droplet interface bilayers.* Scientific reports, 2015. **5**.
44. *Cellular Biology*. [cited 2015 2/1/2015]; Available from: http://faculty.ccp.edu/faculty/wberman/bio109/cells.html.
45. Pietzsch, J. *Mind the membrane*. in *Horizon Symposia, Nature*. 2004.
46. Hanai, T., D.A. Haydon, and J. Taylor, *The variation of capacitance and conductance of bimolecular lipid membranes with area.* Journal of Theoretical Biology, 1965. **9**(3): p. 433-443.
47. Carney, R.P., Y. Astier, T.M. Carney, K. Voïtchovsky, P.H. Jacob Silva, and F. Stellacci, *Electrical Method to Quantify Nanoparticle Interaction with Lipid Bilayers.* ACS Nano, 2012. **7**(2): p. 932-942.
48. Verma, A., O. Uzun, Y. Hu, Y. Hu, H.-S. Han, N. Watson, S. Chen, D.J. Irvine, and F. Stellacci, *Surface-structure-regulated cell-membrane penetration by monolayer-protected nanoparticles.* Nat Mater, 2008. **7**(7): p. 588-595.
49. Taylor, G.J., G.A. Venkatesan, C.P. Collier, and S.A. Sarles, *Direct in situ measurement of specific capacitance, monolayer tension, and bilayer tension in a droplet interface bilayer.* Soft Matter, 2015. **11**(38): p. 7592-7605.
50. Gross, L.C.M., A.J. Heron, S.C. Baca, and M.I. Wallace, *Determining Membrane Capacitance by Dynamic Control of Droplet Interface Bilayer Area.* Langmuir, 2011. **27**(23): p. 14335-14342.

51. Mecke, A., D.-K. Lee, A. Ramamoorthy, B.G. Orr, and M.M. Banaszak Holl, *Synthetic and Natural Polycationic Polymer Nanoparticles Interact Selectively with Fluid-Phase Domains of DMPC Lipid Bilayers.* Langmuir : the ACS journal of surfaces and colloids, 2005. **21**(19): p. 8588-8590.
52. Alberts, B., A. Johnson, J. Lewis, M. Raff, K. Roberts, and P. Walter, *The lipid bilayer.* 2002.
53. Mueller, P., D.O. Rudin, H. Ti Tien, and W.C. Wescott, *Reconstitution of Cell Membrane Structure in vitro and its Transformation into an Excitable System.* Nature, 1962. **194**(4832): p. 979-980.
54. Mueller, P., D.O. Rudin, H. Ti Tien, and W.C. Wescott, *Reconstitution of Excitable Cell Membrane Structure in Vitro.* Circulation, 1962. **26**(5): p. 1167-1171.
55. Lee, J. and H. Bayley, *Semisynthetic protein nanoreactor for single-molecule chemistry.* Proceedings of the National Academy of Sciences, 2015. **112**(45): p. 13768-13773.
56. Stankowski, S., U.D. Schwarz, and G. Schwarz, *Voltage-dependent pore activity of the peptide alamethicin correlated with incorporation in the membrane: salt and cholesterol effects.* Biochimica et Biophysica Acta (BBA) - Biomembranes, 1988. **941**(1): p. 11-18.
57. Escribá, P.V., J.M. González-Ros, F.M. Goñi, P.K.J. Kinnunen, L. Vigh, L. Sánchez-Magraner, A.M. Fernández, X. Busquets, I. Horváth, and G. Barceló-Coblijn, *Membranes: a meeting point for lipids, proteins and therapies.* Journal of Cellular and Molecular Medicine, 2008. **12**(3): p. 829-875.
58. Eeman, M. and M. Deleu, *From biological membranes to biomimetic model membranes.* Biotechnologie, Agronomie, Société et Environnement, 2010. **14**(4): p. 719.
59. White, S.H., D.C. Petersen, S. Simon, and M. Yafuso, *Formation of planar bilayer membranes from lipid monolayers. A critique.* Biophysical Journal, 1976. **16**(5): p. 481-489.
60. Montal, M. and P. Mueller, *Formation of Bimolecular Membranes from Lipid Monolayers and a Study of Their Electrical Properties.* Proceedings of the National Academy of Sciences, 1972. **69**(12): p. 3561-3566.
61. Nicolson, G.L., *The Fluid—Mosaic Model of Membrane Structure: Still relevant to understanding the structure, function and dynamics of biological membranes after more than 40 years.* Biochimica et Biophysica Acta (BBA) - Biomembranes, 2014. **1838**(6): p. 1451-1466.
62. Dixit, S.S., H. Kim, A. Vasilyev, A. Eid, and G.W. Faris, *Light-driven formation and rupture of droplet bilayers.* Langmuir, 2010. **26**(9): p. 6193-6200.
63. Dixit, S.S., A. Pincus, B. Guo, and G.W. Faris, *Droplet Shape Analysis and Permeability Studies in Droplet Lipid Bilayers.* Langmuir, 2012. **28**(19): p. 7442-7451.
64. Castell, O.K., J. Berridge, and M.I. Wallace, *Quantification of Membrane Protein Inhibition by Optical Ion Flux in a Droplet Interface Bilayer Array.* Angewandte Chemie International Edition, 2012. **51**(13): p. 3134-3138.
65. Portonovo, S.A. and J. Schmidt, *Masking apertures enabling automation and solution exchange in sessile droplet lipid bilayers.* Biomedical microdevices, 2012. **14**(1): p. 187-191.

66. Poulos, J., S. Portonovo, H. Bang, and J. Schmidt, *Automatable lipid bilayer formation and ion channel measurement using sessile droplets.* Journal of Physics: Condensed Matter, 2010. **22**(45): p. 454105.
67. Syeda, R., M.A. Holden, W.L. Hwang, and H. Bayley, *Screening Blockers Against a Potassium Channel with a Droplet Interface Bilayer Array.* Journal of the American Chemical Society, 2008. **130**(46): p. 15543-15548.
68. Watanabe, H. and R. Kawano, *Channel Current Analysis for Pore-forming Properties of an Antimicrobial Peptide, Magainin 1, Using the Droplet Contact Method.* Analytical Sciences, 2016. **32**(1): p. 57-60.
69. Wang, X., S. Ma, Y. Su, Y. Zhang, H. Bi, L. Zhang, and X. Han, *High Impedance Droplet–Solid Interface Lipid Bilayer Membranes.* Analytical Chemistry, 2015. **87**(4): p. 2094-2099.
70. Hwang, W.L., M.A. Holden, S. White, and H. Bayley, *Electrical Behavior of Droplet Interface Bilayer Networks: Experimental Analysis and Modeling.* Journal of the American Chemical Society, 2007. **129**(38): p. 11854-11864.
71. Holden, M.A., D. Needham, and H. Bayley, *Functional Bionetworks from Nanoliter Water Droplets.* Journal of the American Chemical Society, 2007. **129**(27): p. 8650-8655.
72. Sapra, K.T. and H. Bayley, *Lipid-coated hydrogel shapes as components of electrical circuits and mechanical devices.* Scientific reports, 2012. **2**.
73. Yoshikazu, I., T. Yagi, and M. Sugawara. *Evaluation method for ion transport via nanopores: Toward a neural stimulation electrode using membrane protein*. in *Biomedical Engineering International Conference (BMEiCON), 2011*. 2011.
74. Leptihn, S., J.R. Thompson, J.C. Ellory, S.J. Tucker, and M.I. Wallace, *In vitro reconstitution of eukaryotic ion channels using droplet interface bilayers.* Journal of the American Chemical Society, 2011. **133**(24): p. 9370-9375.
75. Fischer, A., M.A. Holden, B.L. Pentelute, and R.J. Collier, *Ultrasensitive detection of protein translocated through toxin pores in droplet-interface bilayers.* Proceedings of the National Academy of Sciences, 2011. **108**(40): p. 16577-16581.
76. Syeda, R., J.S. Santos, M. Montal, and H. Bayley, *Tetrameric assembly of KvLm K+ channels with defined numbers of voltage sensors.* Proceedings of the National Academy of Sciences, 2012. **109**(42): p. 16917-16922.
77. Funakoshi, K., H. Suzuki, and S. Takeuchi, *Lipid bilayer formation by contacting monolayers in a microfluidic device for membrane protein analysis.* Analytical Chemistry, 2006. **78**(24): p. 8169-8174.
78. Aghdaei, S., M.E. Sandison, M. Zagnoni, N.G. Green, and H. Morgan, *Formation of artificial lipid bilayers using droplet dielectrophoresis.* Lab on a Chip, 2008. **8**(10): p. 1617-1620.
79. Kawano, R., Y. Tsuji, K. Kamiya, T. Kodama, T. Osaki, N. Miki, and S. Takeuchi, *A Portable Lipid Bilayer System for Environmental Sensing with a Transmembrane Protein.* PLoS ONE, 2014. **9**(7): p. e102427.
80. Poulos, J.L., W.C. Nelson, T.-J. Jeon, C.-J.C. Kim, and J.J. Schmidt, *Electrowetting on dielectric-based microfluidics for integrated lipid bilayer formation and measurement.* Applied Physics Letters, 2009. **95**(1): p. 013706-013703.

81. Thapliyal, T., J.L. Poulos, and J.J. Schmidt, *Automated lipid bilayer and ion channel measurement platform.* Biosensors and Bioelectronics, 2011. **26**(5): p. 2651-2654.
82. Thutupalli, S., J.-B. Fleury, A. Steinberger, S. Herminghaus, and R. Seemann, *Why can artificial membranes be fabricated so rapidly in microfluidics?* Chemical Communications, 2013. **49**(14): p. 1443-1445.
83. Poulos, J.L., T.-J. Jeon, R. Damoiseaux, E.J. Gillespie, K.A. Bradley, and J.J. Schmidt, *Ion channel and toxin measurement using a high throughput lipid membrane platform.* Biosensors and Bioelectronics, 2009. **24**(6): p. 1806-1810.
84. Villar, G., A.D. Graham, and H. Bayley, *A Tissue-Like Printed Material.* Science, 2013. **340**(6128): p. 48-52.
85. Punnamaraju, S., *Voltage and Photo Induced Effects in Droplet-Interface-Bilayer Lipid Membranes*. 2011, School of the University of Cincinnati in partial fulfillment of the requirements for the degree of Doctor of Philosophy (Ph. D.) in the School of Electronics and Computing Systems College of Engineering and Applied Science by Srikoundinya Punnamaraju MS, University of Cincinnati, USA.
86. Punnamaraju, S. and A.J. Steckl, *Voltage Control of Droplet Interface Bilayer Lipid Membrane Dimensions.* Langmuir, 2010. **27**(2): p. 618-626.
87. Punnamaraju, S., H. You, and A.J. Steckl, *Triggered Release of Molecules across Droplet Interface Bilayer Lipid Membranes Using Photopolymerizable Lipids.* Langmuir, 2012. **28**(20): p. 7657-7664.
88. Rojko, N., B. Cronin, J.S.H. Danial, M.A.B. Baker, G. Anderluh, and M.I. Wallace, *Imaging the Lipid-Phase-Dependent Pore Formation of Equinatoxin II in Droplet Interface Bilayers.* Biophysical Journal, 2014. **106**(8): p. 1630-1637.
89. Villar, G., A.J. Heron, and H. Bayley, *Formation of droplet networks that function in aqueous environments.* Nat Nano, 2011. **6**(12): p. 803-808.
90. Yanagisawa, M., T.-a. Yoshida, M. Furuta, S. Nakata, and M. Tokita, *Adhesive force between paired microdroplets coated with lipid monolayers.* Soft Matter, 2013: p. 5891-5897.
91. Mruetusatorn, P., J.B. Boreyko, G.A. Venkatesan, S.A. Sarles, D.G. Hayes, and C.P. Collier, *Dynamic morphologies of microscale droplet interface bilayers.* Soft Matter, 2014. **10**(15): p. 2530-2538.
92. Boreyko, J.B., P. Mruetusatorn, S.A. Sarles, S.T. Retterer, and C.P. Collier, *Evaporation-Induced Buckling and Fission of Microscale Droplet Interface Bilayers.* Journal of the American Chemical Society, 2013. **135**(15): p. 5545-5548.
93. Barriga, H.M.G., P. Booth, S. Haylock, R. Bazin, R.H. Templer, and O. Ces, *Droplet interface bilayer reconstitution and activity measurement of the mechanosensitive channel of large conductance from Escherichia coli.* Journal of The Royal Society Interface, 2014. **11**(98).
94. Stanley, C.E., K.S. Elvira, X.Z. Niu, A.D. Gee, O. Ces, J.B. Edel, and A.J. deMello, *A microfluidic approach for high-throughput droplet interface bilayer (DIB) formation.* Chemical Communications, 2010. **46**(10): p. 1620-1622.
95. Thompson, J.R., A.J. Heron, Y. Santoso, and M.I. Wallace, *Enhanced Stability and Fluidity in Droplet on Hydrogel Bilayers for Measuring Membrane Protein Diffusion.* Nano Letters, 2007. **7**(12): p. 3875-3878.

96. de Wit, G., J.S.H. Danial, P. Kukura, and M.I. Wallace, *Dynamic label-free imaging of lipid nanodomains.* Proceedings of the National Academy of Sciences, 2015.
97. Tsuji, Y., R. Kawano, T. Osaki, K. Kamiya, N. Miki, and S. Takeuchi, *Droplet-based lipid bilayer system integrated with microfluidic channels for solution exchange.* Lab on a Chip, 2013. **13**(8): p. 1476-1481.
98. Kawano, R., Y. Tsuji, K. Sato, T. Osaki, K. Kamiya, M. Hirano, T. Ide, N. Miki, and S. Takeuchi, *Automated parallel recordings of topologically identified single ion channels.* Scientific reports, 2013. **3**.
99. Yasuga, H., T. Osaki, K. Kamiya, R. Kawano, N. Miki, and S. Takeuchi. *Vibration-triggered self-assembly of caged droplets to construct a droplet interface bilayer network*. in *2016 IEEE 29th International Conference on Micro Electro Mechanical Systems (MEMS)*. 2016.
100. Poulin, P. and J. Bibette, *Adhesion of water droplets in organic solvent.* Langmuir, 1998. **14**(22): p. 6341-6343.
101. Thiam, A.R., N. Bremond, and J. Bibette, *Adhesive emulsion bilayers under an electric field: from unzipping to fusion.* Physical review letters, 2011. **107**(6): p. 068301.
102. Thiam, A.R., N. Bremond, and J. Bibette, *From Stability to Permeability of Adhesive Emulsion Bilayers.* Langmuir, 2012. **28**(15): p. 6291-6298.
103. Richens, J.L., J.S. Lane, M.L. Mather, and P. O'Shea, *The interactions of squalene, alkanes and other mineral oils with model membranes; effects on membrane heterogeneity and function.* Journal of Colloid and Interface Science, 2015. **457**: p. 225-231.
104. Friddin, M.S., H. Morgan, and M.R.R. de Planque, *Cell-free protein expression systems in microdroplets: Stabilization of interdroplet bilayers.* Biomicrofluidics, 2013. **7**(1): p. -.
105. Friddin, M.S., N.P. Smithers, M. Beaugrand, I. Marcotte, P.T. Williamson, H. Morgan, and M.R. de Planque, *Single-channel electrophysiology of cell-free expressed ion channels by direct incorporation in lipid bilayers.* Analyst, 2013. **138**(24): p. 7294-7298.
106. Zagnoni, M., M. Sandison, P. Marius, and H. Morgan, *Bilayer lipid membranes from falling droplets.* Analytical and Bioanalytical Chemistry, 2009. **393**(6-7): p. 1601-1605.
107. El-Arabi, A.M., C.S. Salazar, and J.J. Schmidt, *Ion channel drug potency assay with an artificial bilayer chip.* Lab on a Chip, 2012. **12**(13): p. 2409-2413.
108. Harriss, L.M., B.d. Cronin, J.R. Thompson, and M.I. Wallace, *Imaging multiple conductance states in an alamethicin pore.* Journal of the American Chemical Society, 2011. **133**(37): p. 14507-14509.
109. Aronson, M.P. and H.M. Princen, *Contact angles associated with thin liquid films in emulsions.* Nature, 1980. **286**(5771): p. 370-372.
110. Thutupalli, S., S. Herminghaus, and R. Seemann, *Bilayer membranes in micro-fluidics: from gel emulsions to soft functional devices.* Soft Matter, 2011. **7**(4): p. 1312-1320.
111. Guzowski, J., S. Jakiela, P.M. Korczyk, and P. Garstecki, *Custom tailoring multiple droplets one-by-one.* Lab on a Chip, 2013. **13**(22): p. 4308-4311.
112. Rowland, L.P., *Stroke, Spasticity, and Botulinum Toxin.* New England Journal of Medicine, 2002. **347**(6): p. 382-383.
113. Akira, S., K. Takeda, and T. Kaisho, *Toll-like receptors: critical proteins linking innate and acquired immunity.* Nat Immunol, 2001. **2**(8): p. 675-680.

114. Cook, D.N., D.S. Pisetsky, and D.A. Schwartz, *Toll-like receptors in the pathogenesis of human disease.* Nature immunology, 2004. **5**(10): p. 975-979.
115. Wood, I.S. and P. Trayhurn, *Glucose transporters (GLUT and SGLT): expanded families of sugar transport proteins.* British Journal of Nutrition, 2003. **89**(01): p. 3-9.
116. Michalak, Z., M. Muzzio, P.J. Milianta, R. Giacomini, and S. Lee, *Effect of Monoglyceride Structure and Cholesterol Content on Water Permeability of the Droplet Bilayer.* Langmuir, 2013. **29**(51): p. 15919-15925.
117. Milianta, P.J., M. Muzzio, J. Denver, G. Cawley, and S. Lee, *Water Permeability across Symmetric and Asymmetric Droplet Interface Bilayers: Interaction of Cholesterol Sulfate with DPhPC.* Langmuir, 2015. **31**(44): p. 12187-12196.
118. Athenstaedt, K., *Neutral Lipids in Yeast: Synthesis, Storage and Degradation*, in *Handbook of Hydrocarbon and Lipid Microbiology*, K.N. Timmis, Editor. 2010, Springer Berlin Heidelberg: Berlin, Heidelberg. p. 471-480.
119. Fagerberg, L., K. Jonasson, G. von Heijne, M. Uhlén, and L. Berglund, *Prediction of the human membrane proteome.* PROTEOMICS, 2010. **10**(6): p. 1141-1149.
120. Almén, M.S., K.J. Nordström, R. Fredriksson, and H.B. Schiöth, *Mapping the human membrane proteome: a majority of the human membrane proteins can be classified according to function and evolutionary origin.* BMC Biology, 2009. **7**(1): p. 1-14.
121. Vasiliou, V., K. Vasiliou, and D.W. Nebert, *Human ATP-binding cassette (ABC) transporter family.* Human Genomics, 2009. **3**(3): p. 281-290.
122. Kozma, D., I. Simon, and G.E. Tusnády, *PDBTM: Protein Data Bank of transmembrane proteins after 8 years.* Nucleic Acids Research, 2012.
123. Epand, R.M., *Diacylglycerols, lysolecithin, or hydrocarbons markedly alter the bilayer to hexagonal phase transition temperature of phosphatidylethanolamines.* Biochemistry, 1985. **24**(25): p. 7092-7095.
124. Gaede, H.C., *H NMR MAS Investigations of Phase Behavior in Lipid Membranes*, in *NMR Spectroscopy in the Undergraduate Curriculum*. 2013, American Chemical Society. p. 245-257.
125. YashRoy, R.C., *Determination of membrane lipid phase transition temperature from 13C-NMR intensities.* Journal of Biochemical and Biophysical Methods, 1990. **20**(4): p. 353-356.
126. Cullis, P.R. and B. De Kruijff, *The polymorphic phase behaviour of phosphatidylethanolamines of natural and synthetic origin. A 31P NMR study.* Biochimica et Biophysica Acta (BBA) - Biomembranes, 1978. **513**(1): p. 31-42.
127. Engelman, D.M., *X-ray diffraction studies of phase transitions in the membrane of Mycoplasma laidlawii.* Journal of Molecular Biology, 1970. **47**(1): p. 115-117.
128. Caffrey, M., *The Study of Lipid Phase Transition Kinetics by Time-Resolved X-Ray Diffraction.* Annual Review of Biophysics and Biophysical Chemistry, 1989. **18**(1): p. 159-186.
129. Finean, J.B., *X-ray diffraction studies of lipid phase transitions in hydrated mixtures of cholesterol and diacylphosphatidylcholines and their relevance to the structure of biological membranes.* Chemistry and Physics of Lipids, 1989. **49**(4): p. 265-269.
130. Brooks, N.J. and J.M. Seddon, *High Pressure X-ray Studies of Lipid Membranes and Lipid Phase Transitions.* Zeitschrift für Physikalische Chemie, 2014. **228**(10-12): p. 987-1004.

131. Nagle, J.F., *Theory of the Main Lipid Bilayer Phase Transition.* Annual Review of Physical Chemistry, 1980. **31**(1): p. 157-196.
132. Jähnig, F., *Structural order of lipids and proteins in membranes: evaluation of fluorescence anisotropy data.* Proceedings of the National Academy of Sciences, 1979. **76**(12): p. 6361-6365.
133. Han, X. and R.W. Gross, *Nonmonotonic alterations in the fluorescence anisotropy of polar head group labeled fluorophores during the lamellar to hexagonal phase transition of phospholipids.* Biophysical Journal, 1992. **63**(2): p. 309-316.
134. Ali, S., S. Minchey, A. Janoff, and E. Mayhew, *A differential scanning calorimetry study of phosphocholines mixed with paclitaxel and its bromoacylated taxanes.* Biophysical Journal, 2000. **78**(1): p. 246-256.
135. Bach, D. and E. Wachtel, *Phospholipid/cholesterol model membranes: formation of cholesterol crystallites.* Biochimica et Biophysica Acta (BBA) - Biomembranes, 2003. **1610**(2): p. 187-197.
136. Biltonen, *The use of differential scanning calorimetry as a tool to characterize liposome preparations* Chemistry and Physics of Lipids, 1993.
137. Epand, R.M., *Cholesterol in bilayers of sphingomyelin or dihydrosphingomyelin at concentrations found in ocular lens membranes.* Biophysical journal, 2003. **84**(5): p. 3102-3110.
138. Epand, R.M., D. Bach, R.F. Epand, N. Borochov, and E. Wachtel, *A new high-temperature transition of crystalline cholesterol in mixtures with phosphatidylserine.* Biophysical Journal, 2001. **81**(3): p. 1511-1520.
139. McElhaney, R.N., *The structure and function of the Acholeplasma laidlawii plasma membrane.* Biochimica et Biophysica Acta (BBA) - Reviews on Biomembranes, 1984. **779**(1): p. 1-42.
140. McMullen, T.P., R.N. Lewis, and R.N. McElhaney, *Differential scanning calorimetric and Fourier transform infrared spectroscopic studies of the effects of cholesterol on the thermotropic phase behavior and organization of a homologous series of linear saturated phosphatidylserine bilayer membranes.* Biophysical Journal, 2000. **79**(4): p. 2056-2065.
141. McMullen, T.P. and R.N. McElhaney, *Physical studies of cholesterol-phospholipid interactions.* Current Opinion in Colloid & Interface Science, 1996. **1**(1): p. 83-90.
142. McMullen, T.P.W., R.N.A.H. Lewis, and R.N. McElhaney, *Differential scanning calorimetric study of the effect of cholesterol on the thermotropic phase behavior of a homologous series of linear saturated phosphatidylcholines.* Biochemistry, 1993. **32**(2): p. 516-522.
143. Papahadjopoulos, D., M. Moscarello, E.H. Eylar, and T. Isac, *Effects of proteins on the thermotropic phase transitions of phospholipid membranes.* Biochimica et Biophysica Acta (BBA) - Biomembranes, 1975. **401**(3): p. 317-335.
144. Pokorny, A., L.E. Yandek, A.I. Elegbede, A. Hinderliter, and P.F.F. Almeida, *Temperature and Composition Dependence of the Interaction of δ-Lysin with Ternary Mixtures of Sphingomyelin/Cholesterol/POPC.* Biophysical Journal, 2006. **91**(6): p. 2184-2197.
145. Rowe, E.S., *Lipid chain length and temperature dependence of ethanol-phosphatidylcholine interactions.* Biochemistry, 1983. **22**(14): p. 3299-3305.

146. Ruiz-Sanz, J., J. Ruiz-Cabello, P. Mateo, and M. Cortijo, *The thermal transition in crude myelin proteolipid has a lipid rather than protein origin.* European biophysics journal, 1992. **21**(1): p. 71-76.
147. Ruocco, M.J., D.J. Siminovitch, and R.G. Griffin, *Comparative study of the gel phases of ether- and ester-linked phosphatidylcholines.* Biochemistry, 1985. **24**(10): p. 2406-2411.
148. Lewis, R.N.A.H., N. Mak, and R.N. McElhaney, *A differential scanning calorimetric study of the thermotropic phase behavior of model membranes composed of phosphatidylcholines containing linear saturated fatty acyl chains.* Biochemistry, 1987. **26**(19): p. 6118-6126.
149. Taylor, K.M.G. and R.M. Morris, *Thermal analysis of phase transition behaviour in liposomes.* Thermochimica Acta, 1995. **248**: p. 289-301.
150. Ulrich, A.S., M. Sami, and A. Watts, *Hydration of DOPC bilayers by differential scanning calorimetry.* Biochimica et Biophysica Acta (BBA) - Biomembranes, 1994. **1191**(1): p. 225-230.
151. Sud, M., E. Fahy, D. Cotter, A. Brown, E.A. Dennis, C.K. Glass, A.H. Merrill, R.C. Murphy, C.R.H. Raetz, D.W. Russell, and S. Subramaniam, *LMSD: LIPID MAPS structure database.* Nucleic Acids Research, 2007. **35**(suppl 1): p. D527-D532.
152. Ames, G.F., *Lipids of Salmonella typhimurium and Escherichia coli: structure and metabolism.* Journal of bacteriology, 1968. **95**(3): p. 833-843.
153. van Meer, G., D.R. Voelker, and G.W. Feigenson, *Membrane lipids: where they are and how they behave.* Nat Rev Mol Cell Biol, 2008. **9**(2): p. 112-124.
154. Zinser, E., F. Paltauf, and G. Daum, *Sterol composition of yeast organelle membranes and subcellular distribution of enzymes involved in sterol metabolism.* Journal of Bacteriology, 1993. **175**(10): p. 2853-2858.
155. Sáenz, J.P., D. Grosser, A.S. Bradley, T.J. Lagny, O. Lavrynenko, M. Broda, and K. Simons, *Hopanoids as functional analogues of cholesterol in bacterial membranes.* Proceedings of the National Academy of Sciences, 2015. **112**(38): p. 11971-11976.
156. Welander, P.V., R.C. Hunter, L. Zhang, A.L. Sessions, R.E. Summons, and D.K. Newman, *Hopanoids Play a Role in Membrane Integrity and pH Homeostasis in Rhodopseudomonas palustris TIE-1.* Journal of Bacteriology, 2009. **191**(19): p. 6145-6156.
157. Kannenberg, E.L. and K. Poralla, *Hopanoid biosynthesis and function in bacteria.* Naturwissenschaften, 1999. **86**(4): p. 168-176.
158. Casadei, M.A., P. Mañas, G. Niven, E. Needs, and B.M. Mackey, *Role of Membrane Fluidity in Pressure Resistance of Escherichia coli NCTC 8164.* Applied and Environmental Microbiology, 2002. **68**(12): p. 5965-5972.
159. Goh, Shih L., Jonathan J. Amazon, and Gerald W. Feigenson, *Toward a Better Raft Model: Modulated Phases in the Four-Component Bilayer, DSPC/DOPC/POPC/CHOL.* Biophysical Journal, 2013. **104**(4): p. 853-862.
160. Simons, K. and E. Ikonen, *Functional rafts in cell membranes.* Nature, 1997. **387**(6633): p. 569-572.
161. Nickels, J.D., J.C. Smith, and X. Cheng, *Lateral organization, bilayer asymmetry, and inter-leaflet coupling of biological membranes.* Chemistry and physics of lipids, 2015. **192**: p. 87-99.

162. Marquardt, D., B. Geier, and G. Pabst, *Asymmetric Lipid Membranes: Towards More Realistic Model Systems.* Membranes, 2015. **5**(2): p. 180.
163. Clifton, L.A., S.A. Holt, A.V. Hughes, E.L. Daulton, W. Arunmanee, F. Heinrich, S. Khalid, D. Jefferies, T.R. Charlton, J.R.P. Webster, C.J. Kinane, and J.H. Lakey, *An Accurate In Vitro Model of the E. coli Envelope.* Angewandte Chemie International Edition, 2015. **54**(41): p. 11952-11955.
164. Daleke, D.L., *Regulation of transbilayer plasma membrane phospholipid asymmetry.* Journal of Lipid Research, 2003. **44**(2): p. 233-242.
165. Heberle, F.A. and G.W. Feigenson, *Phase separation in lipid membranes.* Cold Spring Harbor perspectives in biology, 2011. **3**(4): p. a004630.
166. Heberle, F.A., R.S. Petruzielo, J. Pan, P. Drazba, N. Kučerka, R.F. Standaert, G.W. Feigenson, and J. Katsaras, *Bilayer Thickness Mismatch Controls Domain Size in Model Membranes.* Journal of the American Chemical Society, 2013. **135**(18): p. 6853-6859.
167. Heberle, F.A., J. Wu, S.L. Goh, R.S. Petruzielo, and G.W. Feigenson, *Comparison of Three Ternary Lipid Bilayer Mixtures: FRET and ESR Reveal Nanodomains.* Biophysical Journal, 2010. **99**(10): p. 3309-3318.
168. Petruzielo, R.S., F.A. Heberle, P. Drazba, J. Katsaras, and G.W. Feigenson, *Phase behavior and domain size in sphingomyelin-containing lipid bilayers.* Biochimica et Biophysica Acta (BBA) - Biomembranes, 2013. **1828**(4): p. 1302-1313.
169. Zhao, J., J. Wu, H. Shao, F. Kong, N. Jain, G. Hunt, and G. Feigenson, *Phase studies of model biomembranes: macroscopic coexistence of Lα+ Lβ, with light-induced coexistence of Lα+ Lo phases.* Biochimica et Biophysica Acta (BBA)-Biomembranes, 2007. **1768**(11): p. 2777-2786.
170. Pathak, P. and E. London, *The Effect of Membrane Lipid Composition on the Formation of Lipid Ultrananodomains.* Biophysical Journal, 2015. **109**(8): p. 1630-1638.
171. Collins, M.D. and S.L. Keller, *Tuning lipid mixtures to induce or suppress domain formation across leaflets of unsupported asymmetric bilayers.* Proceedings of the National Academy of Sciences, 2008. **105**(1): p. 124-128.
172. Veatch, S., I. Polozov, K. Gawrisch, and S. Keller, *Liquid domains in vesicles investigated by NMR and fluorescence microscopy.* Biophysical journal, 2004. **86**(5): p. 2910-2922.
173. Veatch, S.L., K. Gawrisch, and S.L. Keller, *Closed-Loop Miscibility Gap and Quantitative Tie-Lines in Ternary Membranes Containing Diphytanoyl PC.* Biophysical Journal, 2006. **90**(12): p. 4428-4436.
174. Veatch, S.L. and S.L. Keller, *Organization in Lipid Membranes Containing Cholesterol.* Physical Review Letters, 2002. **89**(26): p. 268101.
175. Veatch, S.L. and S.L. Keller, *Separation of liquid phases in giant vesicles of ternary mixtures of phospholipids and cholesterol.* Biophysical journal, 2003. **85**(5): p. 3074-3083.
176. Veatch, S.L. and S.L. Keller, *Miscibility Phase Diagrams of Giant Vesicles Containing Sphingomyelin.* Physical Review Letters, 2005. **94**(14): p. 148101.
177. Fadeel, B. and D. Xue, *The ins and outs of phospholipid asymmetry in the plasma membrane: roles in health and disease.* Critical reviews in biochemistry and molecular biology, 2009. **44**(5): p. 264-277.
178. Newton, I., *Opticks*. 1704: Dover Press.

179. Mueller, P. and D.O. Rudin, *Bimolecular Lipid Membranes: Techniques of Formation, Study of Electrical Properties, and Induction of Ionic Gating Phenomena*, in *Laboratory Techniques in Membrane Biophysics*, H. Passow and R. Stämpfli, Editors. 1969, Springer Berlin Heidelberg. p. 141-156.
180. Hooke, R., Communications to the Royal Society, 1672: p. 28.
181. Velikonja, A., P. Kramar, D. Miklavčič, and A.M. Lebar, *Specific electrical capacitance and voltage breakdown as a function of temperature for different planar lipid bilayers.* Bioelectrochemistry, 2016.
182. Schrader, M.E., *Young-Dupre Revisited.* Langmuir, 1995. **11**(9): p. 3585-3589.
183. Bayley, H., B. Cronin, A. Heron, M.A. Holden, W.L. Hwang, R. Syeda, J. Thompson, and M. Wallace, *Droplet interface bilayers.* Molecular BioSystems, 2008. **4**(12): p. 1191-1208.
184. Bogdanov, M. and W. Dowhan, *Phosphatidylethanolamine is required for in vivo function of the membrane-associated lactose permease of Escherichia coli.* Journal of Biological Chemistry, 1995. **270**(2): p. 732-739.
185. Bogdanov, M., P. Heacock, Z. Guan, and W. Dowhan, *Plasticity of lipid-protein interactions in the function and topogenesis of the membrane protein lactose permease from Escherichia coli.* Proceedings of the National Academy of Sciences, 2010. **107**(34): p. 15057-15062.
186. Wang, X., M. Bogdanov, and W. Dowhan, *Topology of polytopic membrane protein subdomains is dictated by membrane phospholipid composition.* The EMBO Journal, 2002. **21**(21): p. 5673-5681.
187. Choucair, A., M. Chakrapani, B. Chakravarthy, J. Katsaras, and L.J. Johnston, *Preferential accumulation of Aβ(1−42) on gel phase domains of lipid bilayers: An AFM and fluorescence study.* Biochimica et Biophysica Acta (BBA) - Biomembranes, 2007. **1768**(1): p. 146-154.
188. Thakur, G., M. Micic, and R.M. Leblanc, *Surface chemistry of Alzheimer's disease: A Langmuir monolayer approach.* Colloids and Surfaces B: Biointerfaces, 2009. **74**(2): p. 436-456.
189. Curtis, H.J. and K.S. Cole, *TRANSVERSE ELECTRIC IMPEDANCE OF THE SQUID GIANT AXON.* The Journal of General Physiology, 1938. **21**(6): p. 757-765.
190. Hodgkin, A.L. and A.F. Huxley, *A quantitative description of membrane current and its application to conduction and excitation in nerve.* The Journal of Physiology, 1952. **117**(4): p. 500-544.
191. Hanai, T., D. Haydon, and J. Taylor, *The variation of capacitance and conductance of bimolecular lipid membranes with area.* Journal of theoretical biology, 1965. **9**(3): p. 433-443.
192. Taylor, J. and D.A. Haydon, *Stabilization of thin films of liquid hydrocarbon by alkyl chain interaction.* Discussions of the Faraday Society, 1966. **42**(0): p. 51-59.
193. Hanai, T., D.A. Haydon, and J. Taylor, *An Investigation by Electrical Methods of Lecithin-in-Hydrocarbon Films in Aqueous Solutions.* Proceedings of the Royal Society of London A: Mathematical, Physical and Engineering Sciences, 1964. **281**(1386): p. 377-391.
194. Andrews, D.M., E.D. Manev, and D.A. Haydon, *Composition and energy relationships for some thin lipid films, and the chain conformation in monolayers at liquid-liquid interfaces.* Special Discussions of the Faraday Society, 1970. **1**(0): p. 46-56.

195. Everitt, C.T. and D.A. Haydon, *Electrical capacitance of a lipid membrane separating two aqueous phases.* Journal of Theoretical Biology, 1968. **18**(3): p. 371-379.
196. White, S., *Formation of" solvent-free" black lipid bilayer membranes from glyceryl monooleate dispersed in squalene.* Biophysical journal, 1978. **23**(3): p. 337-347.
197. White, S.H., *A study of lipid bilayer membrane stability using precise measurements of specific capacitance* Biophysical Journal, 1970. **10**(12): p. 1127-1148.
198. White, S.H., *Temperature-dependent structural changes in planar bilayer membranes: Solvent "freeze-out".* Biochimica et Biophysica Acta (BBA) - Biomembranes, 1974. **356**(1): p. 8-16.
199. White, S.H. and T.E. Thompson, *Capacitance, area, and thickness variations in thin lipid films.* Biochimica et Biophysica Acta (BBA) - Biomembranes, 1973. **323**(1): p. 7-22.
200. Alvarez, O. and R. Latorre, *Voltage-dependent capacitance in lipid bilayers made from monolayers.* Biophysical Journal, 1978. **21**(1): p. 1-17.
201. Ohki, S., *The electrical capacitance of phospholipid membranes.* Biophysical journal, 1969. **9**(10): p. 1195.
202. Redwood, W.R., F.R. Pfeiffer, J.A. Weisbach, and T.E. Thompson, *Physical properties of bilayer membranes formed from a synthetic saturated phospholipid in n-decane.* Biochimica et Biophysica Acta (BBA) - Biomembranes, 1971. **233**(1): p. 1-6.
203. Wobschall, D., *Voltage dependence of bilayer membrane capacitance.* Journal of Colloid and Interface Science, 1972. **40**(3): p. 417-423.
204. Benz, R., O. Fröhlich, P. Läuger, and M. Montal, *Electrical capacity of black lipid films and of lipid bilayers made from monolayers.* Biochimica et Biophysica Acta (BBA) - Biomembranes, 1975. **394**(3): p. 323-334.
205. Benz, R. and K. Janko, *Voltage-induced capacitance relaxation of lipid bilayer membranes Effects of membrane composition.* Biochimica et Biophysica Acta (BBA) - Biomembranes, 1976. **455**(3): p. 721-738.
206. Mansilla, M.C., L.E. Cybulski, D. Albanesi, and D. de Mendoza, *Control of Membrane Lipid Fluidity by Molecular Thermosensors.* Journal of bacteriology, 2004. **186**(20): p. 6681-6688.
207. Mykytczuk, N.C., J.T. Trevors, S.M. Twine, G.D. Ferroni, and L.G. Leduc, *Membrane fluidity and fatty acid comparisons in psychrotrophic and mesophilic strains of Acidithiobacillus ferrooxidans under cold growth temperatures.* Archives of microbiology, 2010. **192**(12): p. 1005-1018.
208. Hazel, J.R., *Thermal adaptation in biological membranes: is homeoviscous adaptation the explanation?* Annual Review of Physiology, 1995. **57**(1): p. 19-42.
209. Morein, S., A.-S. Andersson, L. Rilfors, and G. Lindblom, *Wild-type Escherichia coli cells regulate the membrane lipid composition in a window between gel and non-lamellar structures.* Journal of Biological Chemistry, 1996. **271**(12): p. 6801-6809.
210. Petelska, A., M. Naumowicz, and Z. Figaszewski, *The interfacial tension of the lipid membrane formed from lipid-cholesterol and lipid-lipid systems.* Cell Biochemistry and Biophysics, 2006. **44**(2): p. 205-211.
211. Petelska, A.D. and Z.A. Figaszewski, *Interfacial tension of phosphatidylcholine–phosphatidylserine system in bilayer lipid membrane.* Biophysical Chemistry, 2006. **120**(3): p. 199-206.

212. Petelska, A.D., M. Naumowicz, and Z.A. Figaszewski, *The Interfacial Tension of the Lipid Membrane Formed from Lipid–Amino Acid Systems.* Cell Biochemistry and Biophysics, 2011. **61**(2): p. 289-296.
213. Li, C. and T. Salditt, *Structure of Magainin and Alamethicin in Model Membranes Studied by X-Ray Reflectivity.* Biophysical Journal, 2006. **91**(9): p. 3285-3300.
214. Wu, Y., K. He, S.J. Ludtke, and H.W. Huang, *X-ray diffraction study of lipid bilayer membranes interacting with amphiphilic helical peptides: diphytanoyl phosphatidylcholine with alamethicin at low concentrations.* Biophysical Journal, 1995. **68**(6): p. 2361-2369.
215. Carney, R.P., T.M. Carney, M. Mueller, and F. Stellacci, *Dynamic cellular uptake of mixed-monolayer protected nanoparticles.* Biointerphases, 2012. **7**(1): p. 17.
216. Leduc, C., J.-M. Jung, R.R. Carney, F. Stellacci, and B. Lounis, *Direct Investigation of Intracellular Presence of Gold Nanoparticles via Photothermal Heterodyne Imaging.* ACS Nano, 2011. **5**(4): p. 2587-2592.
217. Ebihara, L., J.E. Hall, R.C. MacDonald, T.J. McIntosh, and S.A. Simon, *Effect of benzyl alcohol on lipid bilayers. A comparisons of bilayer systems.* Biophysical Journal, 1979. **28**(2): p. 185-196.
218. Elliott, J.R. and D.A. Haydon, *The influence of n-alkanols on the capacity per unit area of planar lipid bilayers.* Biochimica et Biophysica Acta (BBA) - Biomembranes, 1984. **773**(1): p. 165-168.
219. Pope, C.G., B.W. Urban, and D.A. Haydon, *The influence of n-alkanols and cholesterol on the duration and conductance of gramicidin single channels in monoolein bilayers.* Biochimica et Biophysica Acta (BBA) - Biomembranes, 1982. **688**(1): p. 279-283.
220. Reyes, J. and R. Latorre, *Effect of the anesthetics benzyl alcohol and chloroform on bilayers made from monolayers.* Biophysical journal, 1979. **28**(2): p. 259.
221. Hung, W.-C., M.-T. Lee, F.-Y. Chen, and H.W. Huang, *The Condensing Effect of Cholesterol in Lipid Bilayers.* Biophysical Journal, 2007. **92**(11): p. 3960-3967.
222. Barrera, F.N., J. Fendos, and D.M. Engelman, *Membrane physical properties influence transmembrane helix formation.* Proceedings of the National Academy of Sciences, 2012. **109**(36): p. 14422-14427.
223. Pan, J., S. Tristram-Nagle, and J.F. Nagle, *Effect of cholesterol on structural and mechanical properties of membranes depends on lipid chain saturation.* Physical review. E, Statistical, nonlinear, and soft matter physics, 2009. **80**(2 Pt 1): p. 021931.
224. Kučerka, N., J.D. Perlmutter, J. Pan, S. Tristram-Nagle, J. Katsaras, and J.N. Sachs, *The Effect of Cholesterol on Short- and Long-Chain Monounsaturated Lipid Bilayers as Determined by Molecular Dynamics Simulations and X-Ray Scattering.* Biophysical Journal, 2008. **95**(6): p. 2792-2805.
225. McIntosh, T.J., *The effect of cholesterol on the structure of phosphatidylcholine bilayers.* Biochimica et Biophysica Acta (BBA)-Biomembranes, 1978. **513**(1): p. 43-58.
226. Needham, D. and D.A. Haydon, *Tensions and free energies of formation of "solventless" lipid bilayers. Measurement of high contact angles.* Biophysical Journal, 1983. **41**(3): p. 251-257.
227. Petelska, A.D., *Interfacial tension of bilayer lipid membranes.* Central European Journal of Chemistry, 2012. **10**(1): p. 16-26.

228. Requena, J. and D.A. Haydon, *The lippmann equation and the characterization of black lipid films.* Journal of Colloid and Interface Science, 1975. **51**(2): p. 315-327.
229. Naumowicz, M., A.D. Petelska, and Z.A. Figaszewski, *Impedance analysis of phosphatidylcholine–cholesterol system in bilayer lipid membranes.* Electrochimica Acta, 2005. **50**(10): p. 2155-2161.
230. Sriwongsitanont, S. and M. Ueno, *Effect of Freeze-Thawing Process on the Size and Lamellarity of PEG-Lipid Liposomes.* The Open Colloid Science Journal, 2010. **4**(1).
231. Traïkia, M., D.E. Warschawski, M. Recouvreur, J. Cartaud, and P.F. Devaux, *Formation of unilamellar vesicles by repetitive freeze-thaw cycles: characterization by electron microscopy and 31P-nuclear magnetic resonance.* European Biophysics Journal, 2000. **29**(3): p. 184-195.
232. Kim, S.H. and E.I. Franses, *New protocols for preparing dipalmitoylphosphatidylcholine dispersions and controlling surface tension and competitive adsorption with albumin at the air/aqueous interface.* Colloids and Surfaces B: Biointerfaces, 2005. **43**(3–4): p. 256-266.
233. Stuurman, N., A.D. Edelstein, N. Amodaj, K.H. Hoover, and R.D. Vale, *Computer control of microscopes using μManager.* Current protocols in molecular biology/edited by Frederick M. Ausubel...[et al.], 2010: p. Unit14. 20.
234. Vodyanoy, I., J. Hall, and T. Balasubramanian, *Alamethicin-induced current-voltage curve asymmetry in lipid bilayers.* Biophysical Journal, 1983. **42**(1): p. 71-82.
235. Babakov, A.V., L.N. Ermishkin, and E.A. Liberman, *Influence of Electric Field on the Capacity of Phospholipid Membranes.* Nature, 1966. **210**(5039): p. 953-955.
236. Clowes, A., R. Cherry, and D. Chapman, *Physical properties of lecithin-cerebroside bilayers.* Biochimica et Biophysica Acta (BBA)-Biomembranes, 1971. **249**(1): p. 301-317.
237. Requena, J., D.F. Billett, and D.A. Haydon, *Van Der Waals Forces in Oil-Water Systems from the Study of Thin Lipid Films. I. Measurement of the Contact Angle and the Estimation of the Van Der Waals Free Energy of Thinning of a Film.* Proceedings of the Royal Society of London. A. Mathematical and Physical Sciences, 1975. **347**(1649): p. 141-159.
238. Requena, J. and D.A. Haydon, *Van Der Waals Forces in Oil--Water Systems from the Study of Thin Lipid Films. II. The Dependence of the Van Der Waals Free Energy of Thinning on Film Composition and Structure.* Proceedings of the Royal Society of London. A. Mathematical and Physical Sciences, 1975. **347**(1649): p. 161-177.
239. Brooks, D.E., Y.K. Levine, J. Requena, and D.A. Haydon, *Van Der Waals Forces in Oil--Water Systems from the Study of Thin Lipid Films. III. Comparison of Experimental Results with Hamaker Coefficients Calculated from Lifshitz Theory.* Proceedings of the Royal Society of London. A. Mathematical and Physical Sciences, 1975. **347**(1649): p. 179-194.
240. Bamberg, E. and R. Benz, *Voltage-induced thickness changes of lipid bilayer membranes and the effect of an electric field on gramicidin A channel formation.* Biochimica et Biophysica Acta (BBA) - Biomembranes, 1976. **426**(3): p. 570-580.
241. Bach, D. and I. Miller, *Glyceryl monooleate black lipid membranes obtained from squalene solutions.* Biophysical journal, 1980. **29**(1): p. 183.
242. McIntosh, T.J., S.A. Simon, and R.C. MacDonald, *The organization of n-alkanes in lipid bilayers.* Biochimica et Biophysica Acta (BBA) - Biomembranes, 1980. **597**(3): p. 445-463.

243. Dilger, J.P., *The thickness of monoolein lipid bilayers as determined from reflectance measurements.* Biochimica et Biophysica Acta (BBA) - Biomembranes, 1981. **645**(2): p. 357-363.
244. Malmstadt, N., M.A. Nash, R.F. Purnell, and J.J. Schmidt, *Automated formation of lipid-bilayer membranes in a microfluidic device.* Nano letters, 2006. **6**(9): p. 1961-1965.
245. Gross, L.C.M., O.K. Castell, and M.I. Wallace, *Dynamic and Reversible Control of 2D Membrane Protein Concentration in a Droplet Interface Bilayer.* Nano Letters, 2011. **11**(8): p. 3324-3328.
246. Elani, Y., R.V. Law, and O. Ces, *Vesicle-based artificial cells as chemical microreactors with spatially segregated reaction pathways.* Nat Commun, 2014. **5**.
247. Elani, Y., R.V. Law, and O. Ces, *Protein synthesis in artificial cells: using compartmentalisation for spatial organisation in vesicle bioreactors.* Physical Chemistry Chemical Physics, 2015. **17**(24): p. 15534-15537.
248. Petelska, A.D. and Z.A. Figaszewski, *Interfacial tension of the two-component bilayer lipid membrane modelling of cell membrane.* Bioelectrochemistry and Bioenergetics, 1998. **46**(2): p. 199-204.
249. Shamai, R., D. Andelman, B. Berge, and R. Hayes, *Water, electricity, and between… On electrowetting and its applications.* Soft Matter, 2008. **4**(1): p. 38-45.
250. Chevalliot, S., S. Kuiper, and J. Heikenfeld, *Experimental Validation of the Invariance of Electrowetting Contact Angle Saturation.* Journal of Adhesion Science and Technology, 2012. **26**(12-17): p. 1909-1930.
251. Mugele, F. and J.-C. Baret, *Electrowetting: from basics to applications.* Journal of Physics: Condensed Matter, 2005. **17**(28): p. R705.
252. Quinn, A., R. Sedev, and J. Ralston, *Contact Angle Saturation in Electrowetting.* The Journal of Physical Chemistry B, 2005. **109**(13): p. 6268-6275.
253. Weaver, J.C. and Y.A. Chizmadzhev, *Theory of electroporation: A review.* Bioelectrochemistry and Bioenergetics, 1996. **41**(2): p. 135-160.
254. White, S. and W. Chang, *Voltage dependence of the capacitance and area of black lipid membranes.* Biophysical journal, 1981. **36**(2): p. 449.
255. Requena, J., D.A. Haydon, and S.B. Hladky, *Letter: Lenses and the compression of black lipid membranes by an electric field.* Biophysical Journal, 1975. **15**(1): p. 77-81.
256. Valincius, G., F. Heinrich, R. Budvytyte, D.J. Vanderah, D.J. McGillivray, Y. Sokolov, J.E. Hall, and M. Lösche, *Soluble Amyloid ²-Oligomers Affect Dielectric Membrane Properties by Bilayer Insertion and Domain Formation: Implications for Cell Toxicity.* Biophysical Journal, 2008. **95**(10): p. 4845-4861.
257. Brakke, K.A., *The surface evolver.* Experimental mathematics, 1992. **1**(2): p. 141-165.
258. Weaire, D. and S. Hutzler, *The physics of foams*. 1999: Clarendon Press.
259. Jackson, A.M., J.W. Myerson, and F. Stellacci, *Spontaneous assembly of subnanometre-ordered domains in the ligand shell of monolayer-protected nanoparticles.* Nat Mater, 2004. **3**(5): p. 330-336.
260. Jewell, C.M., J.-M. Jung, P.U. Atukorale, R.P. Carney, F. Stellacci, and D.J. Irvine, *Oligonucleotide Delivery by Cell-Penetrating "Striped" Nanoparticles.* Angewandte Chemie International Edition, 2011. **50**(51): p. 12312-12315.

261. Baykal-Caglar, E., E. Hassan-Zadeh, B. Saremi, and J. Huang, *Preparation of giant unilamellar vesicles from damp lipid film for better lipid compositional uniformity.* Biochimica et Biophysica Acta (BBA) - Biomembranes, 2012. **1818**(11): p. 2598-2604.
262. Karolis, C., H.G.L. Coster, T.C. Chilcott, and K.D. Barrow, *Differential effects of cholesterol and oxidised-cholesterol in egg lecithin bilayers.* Biochimica et Biophysica Acta (BBA) - Biomembranes, 1998. **1368**(2): p. 247-255.
263. Chiu, S., E. Jakobsson, R.J. Mashl, and H.L. Scott, *Cholesterol-induced modifications in lipid bilayers: a simulation study.* Biophysical Journal, 2002. **83**(4): p. 1842-1853.
264. Suzuki, Y., *Effect of protein, cholesterol, and phosphatidylglycerol on the surface activity of the lipid-protein complex reconstituted from pig pulmonary surfactant.* Journal of lipid research, 1982. **23**(1): p. 62-69.
265. Levin, I.W., E. Keihn, and W.C. Harris, *A Raman spectroscopic study on the effect of cholesterol on lipid packing in diether phosphatidylcholine bilayer dispersions.* Biochimica et Biophysica Acta (BBA)-Biomembranes, 1985. **820**(1): p. 40-47.
266. Zhang, W., H.A. Campbell, S.C. King, and W. Dowhan, *Phospholipids as Determinants of Membrane Protein Topology: Phosphatidylethanolamine is Required for the Proper Topological Organization of the γ-Aminobutyric Acid Permeae (GabP) of Escherichia coli.* Journal of Biological Chemistry, 2005. **280**(28): p. 26032-26038.
267. Mehla, J. and S.K. Sood, *Substantiation in Enterococcus faecalis of Dose-Dependent Resistance and Cross-Resistance to Pore-Forming Antimicrobial Peptides by Use of a Polydiacetylene-Based Colorimetric Assay.* Applied and Environmental Microbiology, 2011. **77**(3): p. 786-793.
268. Gether, U., *Uncovering molecular mechanisms involved in activation of G protein-coupled receptors.* Endocrine reviews, 2000. **21**(1): p. 90-113.
269. Becker, O.M., Y. Marantz, S. Shacham, B. Inbal, A. Heifetz, O. Kalid, S. Bar-Haim, D. Warshaviak, M. Fichman, and S. Noiman, *G protein-coupled receptors: in silico drug discovery in 3D.* Proceedings of the National Academy of Sciences of the United States of America, 2004. **101**(31): p. 11304-11309.
270. Farquhar, M. *Multiple pathways of exocytosis, endocytosis, and membrane recycling: validation of a Golgi route*. in *Federation proceedings*. 1983.
271. Lodish, H., A. Berk, S.L. Zipursky, P. Matsudaira, D. Baltimore, and J. Darnell, *Overview of extracellular signaling*, in *Molecular Cell Biology*, W.H. Freeman, Editor. 2000: New York.
272. Guan, Z., *Discovering novel brain lipids by liquid chromatography/tandem mass spectrometry.* Journal of Chromatography B, 2009. **877**(26): p. 2814-2821.
273. Lugtenberg, E. and R. Peters, *Distribution of lipids in cytoplasmic and outer membranes of Escherichia coli K12.* Biochimica et Biophysica Acta (BBA)-Lipids and Lipid Metabolism, 1976. **441**(1): p. 38-47.
274. Cafiso, D., *Alamethicin: a peptide model for voltage gating and protein-membrane interactions.* Annual review of biophysics and biomolecular structure, 1994. **23**(1): p. 141-165.
275. Wootton, L., *Bacterial physiology: Bacillus takes the temperature.* Nat Rev Micro, 2010. **8**(10): p. 680-680.

276. Lee, S., D.H. Kim, and D. Needham, *Equilibrium and Dynamic Interfacial Tension Measurements at Microscopic Interfaces Using a Micropipet Technique. 2. Dynamics of Phospholipid Monolayer Formation and Equilibrium Tensions at the Water−Air Interface.* Langmuir, 2001. **17**(18): p. 5544-5550.
277. Lindsey, H., N.O. Petersen, and S.I. Chan, *Physicochemical characterization of 1,2-diphytanoyl-sn-glycero-3-phosphocholine in model membrane systems.* Biochimica et Biophysica Acta (BBA) - Biomembranes, 1979. **555**(1): p. 147-167.
278. Lopes, S., C.S. Neves, P. Eaton, and P. Gameiro, *Cardiolipin, a key component to mimic the E. coli bacterial membrane in model systems revealed by dynamic light scattering and steady-state fluorescence anisotropy.* Analytical and Bioanalytical Chemistry, 2010. **398**(3): p. 1357-1366.
279. Boheim, G., W. Hanke, and H. Eibl, *Lipid phase transition in planar bilayer membrane and its effect on carrier-and pore-mediated ion transport.* Proceedings of the National Academy of Sciences, 1980. **77**(6): p. 3403-3407.
280. Cronan Jr, J.E. and P.R. Vagelos, *Metabolism and function of the membrane phospholipids of Escherichia coli.* Biochimica et Biophysica Acta (BBA) - Reviews on Biomembranes, 1972. **265**(1): p. 25-60.
281. Piggot, T.J., D.A. Holdbrook, and S. Khalid, *Electroporation of the E. coli and S. Aureus Membranes: Molecular Dynamics Simulations of Complex Bacterial Membranes.* The Journal of Physical Chemistry B, 2011. **115**(45): p. 13381-13388.
282. Malinverni, J.C. and T.J. Silhavy, *An ABC transport system that maintains lipid asymmetry in the Gram-negative outer membrane.* Proceedings of the National Academy of Sciences, 2009. **106**(19): p. 8009-8014.
283. Wu, Emilia L., Patrick J. Fleming, Min S. Yeom, G. Widmalm, Jeffery B. Klauda, Karen G. Fleming, and W. Im, *E. coli Outer Membrane and Interactions with OmpLA.* Biophysical Journal, 2014. **106**(11): p. 2493-2502.
284. White, D.A., W. Lennarz, and C.A. Schnaitman, *Distribution of lipids in the wall and cytoplasmic membrane subfractions of the cell envelope of Escherichia coli.* Journal of bacteriology, 1972. **109**(2): p. 686-690.
285. Langford, K.W., B. Penkov, I.M. Derrington, and J.H. Gundlach, *Unsupported planar lipid membranes formed from mycolic acids of Mycobacterium tuberculosis.* Journal of Lipid Research, 2011. **52**(2): p. 272-277.
286. Leonenko, Z.V., E. Finot, H. Ma, T.E.S. Dahms, and D.T. Cramb, *Investigation of Temperature-Induced Phase Transitions in DOPC and DPPC Phospholipid Bilayers Using Temperature-Controlled Scanning Force Microscopy.* Biophysical Journal, 2004. **86**(6): p. 3783-3793.
287. Pan, J., S. Tristram-Nagle, N. Kučerka, and J.F. Nagle, *Temperature dependence of structure, bending rigidity, and bilayer interactions of dioleoylphosphatidylcholine bilayers.* Biophysical journal, 2008. **94**(1): p. 117-124.
288. Kučerka, N., M.-P. Nieh, and J. Katsaras, *Fluid phase lipid areas and bilayer thicknesses of commonly used phosphatidylcholines as a function of temperature.* Biochimica et Biophysica Acta (BBA) - Biomembranes, 2011. **1808**(11): p. 2761-2771.
289. Heimburg, T., *Lipid ion channels.* Biophysical Chemistry, 2010. **150**(1–3): p. 2-22.

290. Gordon, L.G.M. and D.A. Haydon, *Kinetics and stability of alamethicin conducting channels in lipid bilayers.* Biochimica et Biophysica Acta (BBA) - Biomembranes, 1976. **436**(3): p. 541-556.
291. Eisenberg, M., J. Hall, and C.A. Mead, *The nature of the voltage-dependent conductance induced by alamethicin in black lipid membranes.* The Journal of Membrane Biology, 1973. **14**(1): p. 143-176.
292. Sakmann, B. and G. Boheim, *Alamethicin-induced single channel conductance fluctuations in biological membranes.* Nature, 1979. **282**(5736): p. 336-339.
293. Boheim, G. and H.-A. Kolb, *Analysis of the multi-pore system of alamethicin in a lipid membrane.* The Journal of Membrane Biology, 1978. **38**(1-2): p. 99-150.
294. Rizzo, V., S. Stankowski, and G. Schwarz, *Alamethicin incorporation in lipid bilayers: a thermodynamic study.* Biochemistry, 1987. **26**(10): p. 2751-2759.
295. Baba, T., Y. Toshima, H. Minamikawa, M. Hato, K. Suzuki, and N. Kamo, *Formation and characterization of planar lipid bilayer membranes from synthetic phytanyl-chained glycolipids.* Biochimica et Biophysica Acta (BBA) - Biomembranes, 1999. **1421**(1): p. 91-102.
296. Doménech, Ò., S. Merino-Montero, M.T. Montero, and J. Hernández-Borrell, *Surface planar bilayers of phospholipids used in protein membrane reconstitution: an atomic force microscopy study.* Colloids and Surfaces B: Biointerfaces, 2006. **47**(1): p. 102-106.
297. Molle, G., J.-Y. Dugas, H. Duclohier, and G. Spach, *Conductance properties of des-Aib-Leu-des-Pheol-Phe-alamethicin in planar lipid bilayers.* Biochimica et Biophysica Acta (BBA)-Biomembranes, 1988. **938**(2): p. 310-314.
298. Antonov, V., A. Anosov, V. Norik, E. Korepanova, and E. Smirnova, *Electrical capacitance of lipid bilayer membranes of hydrogenated egg lecithin at the temperature phase transition.* European Biophysics Journal, 2003. **32**(1): p. 55-59.
299. Cronan, J.E., *Bacterial membrane lipids: where do we stand?* Annual reviews in microbiology, 2003. **57**(1): p. 203-224.
300. Schlame, M., *Thematic Review Series: Glycerolipids. Cardiolipin synthesis for the assembly of bacterial and mitochondrial membranes.* Journal of Lipid Research, 2008. **49**(8): p. 1607-1620.
301. Fuchs, B., A. Nimptsch, and J. Schiller, *Analysis of brain lipids by directly coupled matrix-assisted laser desorption ionization time-of-flight mass spectrometry and high-performance thin-layer chromatography.* Journal of AOAC International, 2008. **91**(5): p. 1227-1236.
302. de Almeida, R.F.M., L.M.S. Loura, A. Fedorov, and M. Prieto, *Lipid Rafts have Different Sizes Depending on Membrane Composition: A Time-resolved Fluorescence Resonance Energy Transfer Study.* Journal of Molecular Biology, 2005. **346**(4): p. 1109-1120.
303. de Almeida, R.F.M., A. Fedorov, and M. Prieto, *Sphingomyelin/Phosphatidylcholine/Cholesterol Phase Diagram: Boundaries and Composition of Lipid Rafts.* Biophysical Journal, 2003. **85**(4): p. 2406-2416.
304. Bakrač, B., I. Gutiérrez-Aguirre, Z. Podlesek, A.F.-P. Sonnen, R.J.C. Gilbert, P. Maček, J.H. Lakey, and G. Anderluh, *Molecular Determinants of Sphingomyelin Specificity of a Eukaryotic Pore-forming Toxin.* Journal of Biological Chemistry, 2008. **283**(27): p. 18665-18677.

305. Nusshold, C., A. Uellen, E. Bernhart, A. Hammer, S. Damm, A. Wintersperger, H. Reicher, A. Hermetter, E. Malle, and W. Sattler, *Endocytosis and intracellular processing of BODIPY-sphingomyelin by murine CATH. a neurons.* Biochimica et Biophysica Acta (BBA)-Molecular and Cell Biology of Lipids, 2013. **1831**(12): p. 1665-1678.
306. Trovò, L., P.P. Van Veldhoven, M.G. Martín, and C.G. Dotti, *Sphingomyelin upregulation in mature neurons contributes to TrkB activity by Rac1 endocytosis.* Journal of cell science, 2011. **124**(8): p. 1308-1315.
307. Arispe, N., E. Rojas, and H.B. Pollard, *Alzheimer disease amyloid beta protein forms calcium channels in bilayer membranes: blockade by tromethamine and aluminum.* Proceedings of the National Academy of Sciences, 1993. **90**(2): p. 567-571.
308. Bitan, G., A. Lomakin, and D.B. Teplow, *Amyloid β-Protein Oligomerization: PRENUCLEATION INTERACTIONS REVEALED BY PHOTO-INDUCED CROSS-LINKING OF UNMODIFIED PROTEINS.* Journal of Biological Chemistry, 2001. **276**(37): p. 35176-35184.
309. Bartzokis, G., *Age-related myelin breakdown: a developmental model of cognitive decline and Alzheimer's disease.* Neurobiology of aging, 2004. **25**(1): p. 5-18.
310. Tsinman, O., K. Tsinman, N. Sun, and A. Avdeef, *Physicochemical selectivity of the BBB microenvironment governing passive diffusion—matching with a porcine brain lipid extract artificial membrane permeability model.* Pharmaceutical research, 2011. **28**(2): p. 337-363.
311. Angelova, M., S. Soleau, P. Méléard, F. Faucon, and P. Bothorel, *Preparation of giant vesicles by external AC electric fields. Kinetics and applications*, in *Trends in Colloid and Interface Science VI*. 1992, Springer. p. 127-131.
312. Buboltz, J.T. and G.W. Feigenson, *A novel strategy for the preparation of liposomes: rapid solvent exchange.* Biochimica et Biophysica Acta (BBA)-Biomembranes, 1999. **1417**(2): p. 232-245.
313. Ichihara, K.i. and Y. Fukubayashi, *Preparation of fatty acid methyl esters for gas-liquid chromatography.* Journal of Lipid Research, 2010. **51**(3): p. 635-640.
314. Pandit, S.A., G. Khelashvili, E. Jakobsson, A. Grama, and H.L. Scott, *Lateral Organization in Lipid-Cholesterol Mixed Bilayers.* Biophysical Journal, 2007. **92**(2): p. 440-447.
315. Stewart, R.R. and A.M. Berrie, *Effect of temperature on the short chain fatty acid-induced inhibition of lettuce seed germination.* Plant physiology, 1979. **63**(1): p. 61-62.
316. Kučerka, N., S. Tristram-Nagle, and J.F. Nagle, *Structure of fully hydrated fluid phase lipid bilayers with monounsaturated chains.* The Journal of membrane biology, 2006. **208**(3): p. 193-202.
317. Mannock, D.A., M.Y.T. Lee, R.N.A.H. Lewis, and R.N. McElhaney, *Comparative calorimetric and spectroscopic studies of the effects of cholesterol and epicholesterol on the thermotropic phase behaviour of dipalmitoylphosphatidylcholine bilayer membranes.* Biochimica et Biophysica Acta (BBA) - Biomembranes, 2008. **1778**(10): p. 2191-2202.
318. Boheim, G., *Statistical analysis of alamethicin channels in black lipid membranes.* The Journal of Membrane Biology, 1974. **19**(1): p. 277-303.
319. Eisenberg, M., J.E. Hall, and C. Mead, *The nature of the voltage-dependent conductance induced by alamethicin in black lipid membranes.* The Journal of membrane biology, 1973. **14**(1): p. 143-176.

320. Baumgart, T., S.T. Hess, and W.W. Webb, *Imaging coexisting fluid domains in biomembrane models coupling curvature and line tension.* Nature, 2003. **425**(6960): p. 821-824.
321. Baumgart, T., S. Das, W. Webb, and J. Jenkins, *Membrane elasticity in giant vesicles with fluid phase coexistence.* Biophysical journal, 2005. **89**(2): p. 1067-1080.
322. Baumgart, T., G. Hunt, E.R. Farkas, W.W. Webb, and G.W. Feigenson, *Fluorescence probe partitioning between Lo/Ld phases in lipid membranes.* Biochimica et Biophysica Acta (BBA) - Biomembranes, 2007. **1768**(9): p. 2182-2194.
323. Heberle, F.A., J.T. Buboltz, D. Stringer, and G.W. Feigenson, *Fluorescence methods to detect phase boundaries in lipid bilayer mixtures.* Biochimica et Biophysica Acta (BBA) - Molecular Cell Research, 2005. **1746**(3): p. 186-192.
324. Tamaddoni, N., G. Taylor, T. Hepburn, M. Kilbey, and S. Sarles, *Reversible, voltage-activated formation of biomimetic membranes between triblock copolymer-coated aqueous droplets in good solvents.* Soft Matter, <submitted>.
325. Scarlata, S., *Membrane protein structure.* Biophysics Textbook Online, 2004: p. 1-23.
326. Van der Rest, M., A.H. Kamminga, A. Nakano, Y. Anraku, B. Poolman, and W.N. Konings, *The plasma membrane of Saccharomyces cerevisiae: structure, function, and biogenesis.* Microbiological reviews, 1995. **59**(2): p. 304-322.

APPENDIX

Lipid Composition of Eukaryotic and Prokaryotic Organisms

Table 12. Lipid composition* of eukaryotic and prokaryotic organisms, including *E. coli*, organized by headgroup and acyl chain content.

Headgroup	Eukaryotic		Bacterial		Acyl Chains	Bacterial
	Human erythrocyte [225]	*S. cerevisiae* [326],+	*E. coli* K12 [152]	*E. coli* B ++,†		*E. coli* B [158],†
PC	17	17.0/16.8	-	-	12:0	5.0
PI	-	27.7/17.	-	-	14:0	6.7
PS	7	3.8/33.6	-	-	14:0-3OH	8.2
PG	-	-	19	15.1	16:1	25.5
PE	18	14.0/20.3	69	57.5	16:0 (DPPC)	31.2
CL	-	4.2/0.2	6.5	9.8	17:0/17:0-cyclo	0.2/0.7
PA	-	2.5/3.9	-	-	18:1 (DOPC)	19.4
Sphingolipids	18	30.7/0	-	-	Other	4
Other/Unknown	46**	0/6.9	6	17.6	UFA/SFA/FI***	46.0/32.4/1.4

*: Values shown for each species represent % of total content
**: Includes 23% cholesterol
***: UFA – unsaturated fatty acids, SFA – saturated fatty acids, FI – fluidity index (ratio of UFA/SFA)
+: Values separated by "/" are taken from two separate studies for *S. cerevisiae*
++: Avanti Polar Lipids, Inc. P/N 100500
†: Composition data used as the basis for an eTLE bilayer shown in Figure 45

Coalescence of eTLE Infused Droplets Below 50°C

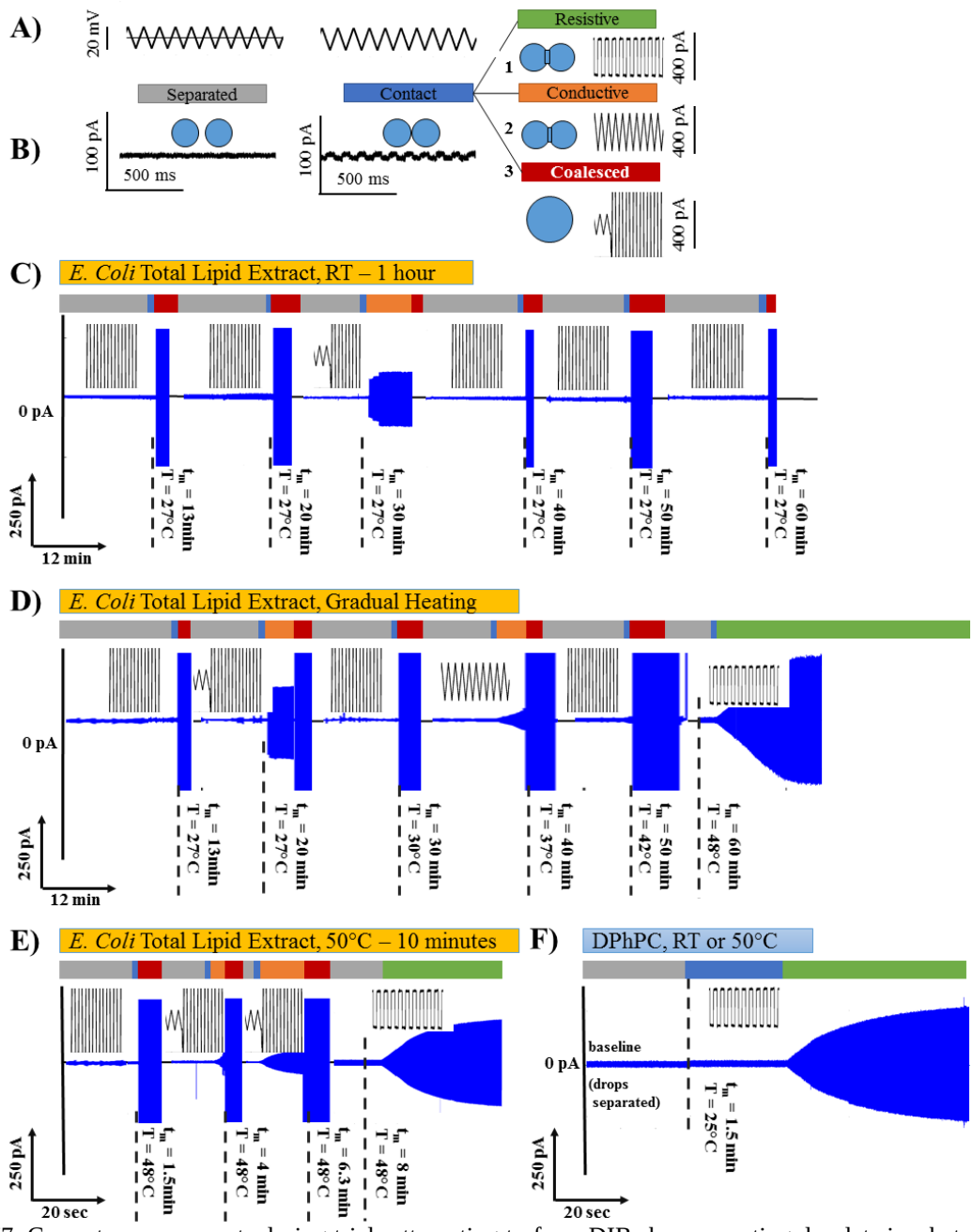

Figure 77. Current measurements during trials attempting to from DIBs by connecting droplets incubated under oil for varying amounts of monolayer formation time (t_m) and with varying temperature treatment. A) The 10 Hz, 10 mV triangular voltage waveform that is applied continuously to monitor bilayer capacitance. B) Representative current measurements obtained during a 1 second period with bilayers in various states of formation: initially separated, connected at t_m, then either resistive, conductive ("leaky"), or coalesced completely which results in saturated current signals. C-F) Current from experiments with the combination of lipid type and temperature shown for each test.

Baseline and Single Channel Alamethicin Gating with eTLE DIBs.

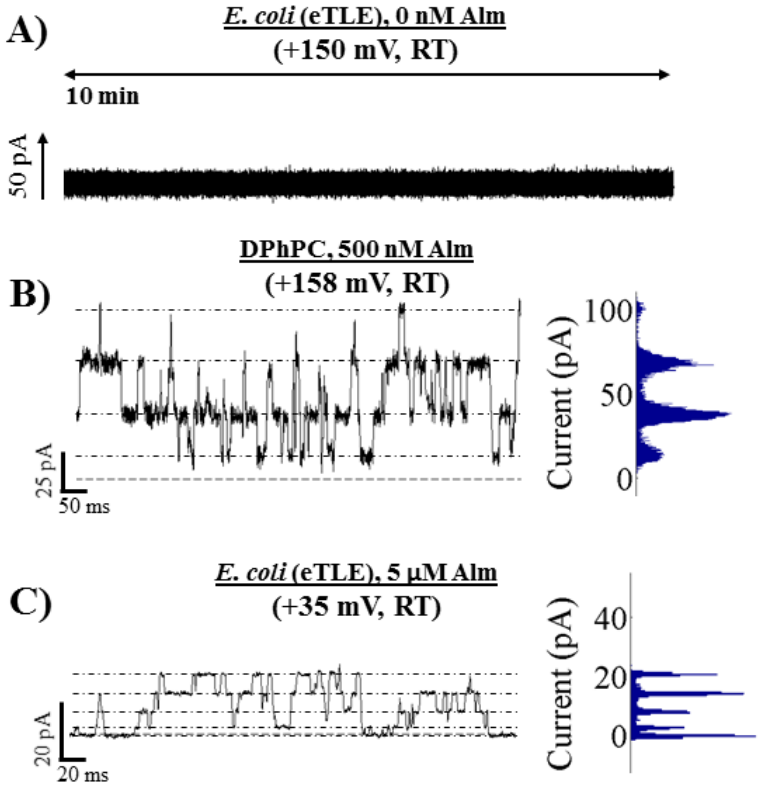

Figure 78. A) Current measured over the course of 10 minutes with an eTLE DIB (no alamethicin or peptide) held at 50°C. Fluctuations or activity with the baseline might indicate the presence of contamination or electroporation with the lipids, and there are no fluctuations or activity for 10 minutes shown. A baseline of this quality is sought at the beginning of each day or round of testing. If problems persist the setup is removed, cleaned or replaced, and set back up to test the baseline again. B-C) Representative current traces and histograms used in identifying single channel Alm conductance levels (provided in Figure 55 and the associated text). B) DPhPC DIB including 500 nM Alm at room temperature. C) eTLE DIB including 5 µM Alm at room temperature. Conductance levels are identified as peaks in a histogram of the current/conductance signal. Multiple events are analyzed for each lipid and temperature (only one typical trace is shown for each lipid type here) to obtain averages for each level, specific to each case.

VITA

Graham J. Taylor is a Tennessee native, having been born in Chattanooga to a family that is now spread across Chattanooga, Knoxville, and Nashville. He received a B.S. in Biomedical Engineering at the University of Tennessee, Knoxville, in May 2007 and is currently set to graduate in spring 2016 with a Ph.D. in Biomedical Engineering from UT.

While an undergraduate, Graham served as a research assistant in the Department of Mechanical, Aerospace, and Biomedical Engineering. He was heavily involved in the analysis of fluoroscope video and X-ray images showing the motion of prosthetic knee and hip implants during actual usage to provide data to industrial medical device manufacturers. He also took part in an NSF Research for Undergraduates program to develop tools to reliably distinguish cancer cells from healthy cells in tissues and cell cultures.

As a graduate student, his work has centered primarily on research in the field of droplet interface bilayers, thin lipid bilayers that serve as actual physical models for cell membranes. His research has resulted in two published first-author papers, with two more first-author papers in preparation. Together, these works form the basis of two provisional patent applications filed through the UT Research Foundation in 2015.

Outside of the lab, Graham co-founded a company, T&T Scientific, with colleague Nima Tamaddoni. T&T Scientific, funded in part through the Boyd Venture Challenge program, has already launched its LipX extrusion device which is the world's first single-use, fully assembled liposome extruder.

When he's not staring through the microscope and playing with droplets and bubbles, Graham enjoys whitewater kayaking, mountain biking, and hiking. Between his scientific endeavors and his love for the outdoors, Knoxville has been the perfect place for him to be.